Study on
Whistler-mode Triggered Emissions
in the Magnetosphere

Takeshi Nogi

Acknowledgements

I would like to express great gratitude to Prof. Yoshiharu Omura from Research Institute for Sustainable Humanosphere, Kyoto University. He has consistently provided me with warmful advice during my doctoral course. I admired him numerous times for his advice and supervision. International discussions in the laboratory organized by him were excellent opportunities for me. The experience powerfully has supported my study and will be an asset in my future career. I am also grateful for his continuous encouragement. I could complete the doctoral dissertation with his encouragement and consistent support over seven years.

I'm deeply grateful to Prof. Tetsuji Matsuo from Kyoto University for providing advice on my doctoral course research and the dissertation examination. He has provided fruitful feedback for the structure of the study through the discussions. The discussions triggered a deeper understanding of the phenomena, and the dissertation significantly improved.

I would also acknowledge Prof. Hirotsugu Kojima from Research Institute for Sustainable Humanosphere, Kyoto University, for his suggestions for the study. He has brought insights not only in the examination of the doctoral dissertation but also throughout the discussions in the laboratory group. The discussions on the simulation method, satellite observation, and theory have provided a deeper understanding of the results.

I would like to express my gratitude to Dr. Yusuke Ebihara from Research Institute for Sustainable Humanosphere, Kyoto University. The discussions on the initial conditions for particle simulation and magnetohydrodynamics simulations are fruitful, providing insights for the new algorithm. I also appreciate the support for the numerical simulations on the supercomputer system. With his administrative support, I could continuously work on the simulation code development and analyses of the results.

I am grateful for the discussions with Dr. Satoko Nakamura from Institute for Space-Earth Environmental Research, Nagoya University, in developing the simulation code and analyses of preliminary results. With suggestions for interpreting the simulation results from the aspects of the theory and observations, I have learned from her the methodology and knowledge of the research field throughout discussions in the doctoral course. Those discussions have brought means as a researcher, accelerating my study.

Professors, associate professors, assistant professors, lecturers, researchers, and staff in the space group laboratory are gratefully acknowledged for the fruitful discussions and suggestions from diverse viewpoints. I would appreciate Prof. Naoki Shinohara for the profound questions in the laboratory group meetings. I would also thank his encouragement in my research in my doctoral course. I am grateful to Dr. Tomohiko Mitani throughout my research and academic life. He has also provided me with questions in the group meetings in the laboratory group. I have learned a lot from him as an engineer and a researcher. I'm grateful to Dr. Satoshi Kurita for the discussions from the view point of the observation. It is helpful to associate simulation results with observational facts and theory analysis, leading to a deeper understanding of the

generation process of chorus waves. I acknowledge Dr. Yoshikatsu Ueda for the questions at a laboratory group meeting. I would like to express my gratitude to Dr. Seiji Zenitani from Kobe University for the discussions on the algorithm of particle simulations. I would like to express my gratitude to Dr. Miloslav Horky for the initial development of the simulation code with his support in the debugging of parallel processing of the simulation code. I would express special thanks to Ms. Hiroko Nitto and Ms. Etsuko Kawasaki for their consistent support throughout my doctoral course. I could always keep my concentration on my study with their kindness.

I gratefully acknowledge the discussions and support of members of the laboratory group during my doctoral course. I would express my gratitude to Dr. Naoki Hasegawa, Dr. Yikai Hsieh, Dr. Takashi Zushi, Dr. Yuko Kubota, Dr. Seishiro Kojima, Dr. Ce Wang, Dr. Bo Yang, Dr. Takashi Hirakawa, Mr. Ryo Mochiduki, and Dr. Kyle Reiter. I also thank Mr. Yuya Fujiwara for discussing the generation processes of triggered emissions. I would also be grateful to Mr. Kenta Hirahara at Karlsruhe Institute of Technology for proofreading the doctoral dissertation manuscript.

I am also deeply grateful to Mr. Christian Korf, Dr. Hironori Kiyamura, Mr. Makoto Sawada, Mr. Yoshiki Kutsuwa, Ms. Hikari Ninomiya, Dr. Taekjin Lee, and Mr. Martin Rabel at Bosch Corporation. I could complete the dissertation thanks to their warmful support on the business tasks and consistent encouragement for the doctoral degree,

I would also Prof. Kazunobu Nagasaki and Dr. Shinsuke Ohshima at Institute for Advanced Energy, Kyoto University, and Dr. Kai Masuda at National Institute for Quantum Science and Technology. During my master's course, I have learned fundamental knowledge and abilities as a researcher in electromagnetics and plasma physics through my experience in the laboratory. I also appreciate their supportive pushes for my endeavor to the different research themes from my doctoral course.

I would thank Dr. Akinori Iwai, Dr. Akito Fujita, and Dr. Ei Shigematsu for providing suggestions and encouragement throughout my academic life. I would like to acknowledge the alums of Kyoto university, Mr. Akira Kobori, Mr. Kosuke Miyaji, Mr. Kouichi Sakaguchi, Mr. Naoya Kihara, Mr. Shinsuke Fukuba, Mr. Shota Suzuki, Mr. Shotaro Taniguchi, Mr. Takashi Awamura, and Mr. Takeshi Sakai for always providing me with stimuli for the study for over a decade.

I would also express my gratitude to my parents, Kiyoshi and Ikue, for their continuous warm advice and support. Thanks to their encouragement, I could always concentrate on the research activities.

The computer simulations in the dissertation were performed on the A-KDK computer system at Research Institute for Sustainable Humanosphere, Kyoto University.

Abstract

Full-particle simulations have been conducted for the study on the generation processes of whistler-mode triggered emissions in the magnetosphere. Rising-tone and falling-tone triggered emissions are reproduced in the simulations. The parallel propagation of whistler-mode waves to a geomagnetic field is assumed, and the one-dimensional parabolic model is used in the simulations. Triggering whistler-mode waves with a constant frequency are injected from the magnetic equator by oscillating external currents at the magnetic equator with right-handed circular polarization. Minor revisions of algorithms have been applied to Kyoto University electromagnetic particle code (KEMPO). We have proposed an initialization algorithm for the phase space distribution of a superparticle to suppress the instabilities, which are caused by the difference in magnetic field intensity with respect to space. We generate particle distribution in velocity space at the magnetic equator and distribute superparticles in space, satisfying the conservation of kinetic energy and adiabatic invariants of charged particles in the mirror motion.

The triggering process of whistler-mode rising-tone emissions is studied. By injecting a wave with a fixed frequency at the equator, rising-tone emissions are generated from triggering waves. Rising-tone elements with multiple subpackets with monotonically increasing frequencies are generated from the triggering wave. Generation regions of the subpackets move upstream or downstream depending on the group velocities and resonance velocities for different frequencies. Because of the motion of a source region to the upstream, a long rising-tone subpacket is generated self-sustainingly through the formation of an electron hole in velocity phase space stretched over the generation region. The long rising-tone subpacket is modulated with increasing magnitude, splitting into smaller subpackets through propagation. Two different processes generate the amplitude modulations in the subpacket; resonant trapping oscillation of electrons at the equatorial region and enhancement of amplitude variations through propagation in the downstream region.

We have performed a series of simulation runs for whistler-mode wave-particle interaction in a parabolic magnetic field with 12 different triggering wave frequencies and three different plasma frequencies specifying cold plasma densities. Under a given plasma condition, a specific frequency range of the triggering wave can generate rising-tone emissions. The generation region of rising-tone emission shifts upstream. The velocity of the wave generation region is dependent on the duration of the subpacket, which is controlled by the formation of the resonant current in the generation region. When the source velocity, which is a sum of the resonance and group velocities, is approximately the same as the velocity of the wave generation region, a long-sustaining rising-tone emission is generated. When the spatial and temporal gap between subpackets exists due to the damping phase of short subpacket generation, resonant electrons in the gap of the subpackets are carried at the resonance velocity to the upstream region, and the velocity of the wave generation region becomes large in magnitude. When the formation of resonant currents is delayed, the velocity of the generation region becomes smaller than the source velocity in magnitude. Below one-quarter of the cyclotron frequency, the coalescence of subpackets takes place, suppressing the formation of the resonant current in the generation region. Since a gradual upstream shift of the generation region is necessary for the wave to grow locally, the source velocity should be a small negative value.

We perform a one-dimensional electromagnetic full particle simulation for triggered falling-tone emissions in the Earth's magnetosphere. The equatorial region of the magnetosphere is modeled with a parabolic magnetic field approximation. The short whistler mode waves with a large amplitude are excited and propagate poleward from an artificial current oscillating with a constant frequency and amplitude. Following the excited waves, clear emissions are triggered with a falling frequency. Without the inhomogeneity of the background magnetic field, no triggered emission appears. The falling tone has several subpackets of amplitude and decreases the frequency in a stepwise manner. The positive resonant current formed by resonant electrons in the direction of the wave magnetic field clearly shows that an electron hill is formed in the phase space and causes the frequency decrease. The entrapping of the resonant electrons at the front of the packets and the decrease of the amplitude at the end of packets are essential for the generation of falling-tone emissions. Each wavefront of the emission has a strongly negative resonant current $-J_E$, which results in wave growth. In the formation process of the resonant currents, we investigate the inhomogeneous factor S, which controls the nonlinear motion of the resonant electrons interacting with waves. The factor S consists of two terms, a frequency sweep rate and a gradient of the background magnetic field. The resonant current J_E in the wave packet changes its sign from negative to positive as the packet moves away from the equator, terminating the wave growth.

The resonant currents in the direction of the electric field and magnetic field of whistler-mode waves are always observed in cases with rising-tone, and falling-tone triggered emissions. The formation of resonant current is associated with the enhancement and depressions of resonant electrons in phase space, which corresponds with an electron hill and hole. We have found that the inhomogeneity driver in the phase space is the frequency variations of triggered waves in time. The result suggests that rising-tone and falling-tone emissions are self-sustainingly grow, and the gradient of the ambient magnetic field supports the modulation of resonant current in space. Whistler-mode chorus waves are generated in the same generation process as the triggered emissions, the present study also applies to the generation mechanisms of chorus waves in the magnetosphere. As active experiments with the same model as the present study as is planned in the future by using satellites, the present study will provide direction for the experiment design and interpretation of the results.

Contents

List of Figures

List of Tables

Nomenclature

α_{loss}	Loss cone angle
β	Loss cone parameter for subtracted Maxwellian disctribution
γ	Lorlentz factor
ζ	Phase difference between $\boldsymbol{B_w}$ and $\boldsymbol{v}_\perp$
μ_0	Magnetic permeability in a vacuum
ξ	Dimensionless parameter for plasma defined as $\xi^2 = \omega(\Omega_e - \omega)/\omega_p$ (Omura et al., 2008; Omura, 2021)
χ	Dimensionless parameter for plasma defined as $\chi^2 = 1/(1 + \xi^2)$ (Omura et al., 2008; Omura, 2021)
ω	Wave frequency
ω_0	frequency of triggering waves
Ω_{op}	Optimum amplitude multiplied by charge-to-mass ratioof electron
Ω_{th}	Threshold amplitude multiplied by charge-to-mass ratio of electron
Ω_w	Amplitude of magnetic field B_w multiplied by charge-to-mass ratio of electron
Ω_e	Electron cyclotron frequency
a	Coefficient for parabolic magnetic field model
$\boldsymbol{B_{wb}}$	Perpendicular magnetic field components for backward propagating waves
$\boldsymbol{B_{wf}}$	Perpendicular magnetic field components for forward propagating waves
$\boldsymbol{B_w}$	Perpendicular magnetic field components to ambient magnetic field
B_{eq}	Magnitude of ambient magnetic field with respect at equator

B_w	Amplitude of perpendicular magnetic field components to ambient magnetic field
c	Speed of light in a vacuum
e	Euler’s number
e	Elementary electron charge
$H(x)$	Heviside step function
i	Imaginary unit
J_B	Resonant current parallel to magnetic field
J_E	Resonant current parallel to electric field
K	Kinetic energy of electron
k	Wave number
L_D	Length of damping region
m_0	Rest mass of an electron
N_D	Number of grids for damping region
S	Inhomogeneous factor for nonlinear theory
$\boldsymbol{u}_\perp$	Perpendicular component of momenta for electron
$u_\parallel$	Pallarel component of momenta for electron
$u_\perp$	Magnitude of perpendicular component of momenta for electron
$\boldsymbol{v}_\perp$	Perpendicular velocity of electron
$v_\parallel$	Parallel velocity of electron
$v_\perp$	Magnitude of perpendicular electron velocity
V_g	Group velocity
V_p	Phase velocity
V_R	Resonance velocity
V_S	Source velocity
V_w	Velocity of wave packet generation

Chapter 1

Introduction

1.1 Magnetosphere of a planet

The magnetic field of the Earth is known from ancient and used as a compass. The magnetic field of the Earth is approximated to a dipole magnetic field. The magnetosphere of a planet is a common phenomenon. In situ observations by space exploration satellites have shown that the existence of intrinsic magnetic field for Mercury (Ness et al., 1974; Bridge et al., 1974; Anderson et al., 2010), Jupiter (Smith, Davis Jr., et al., 1974), Saturn (Smith et al., 1980; Acuña et al., 1980), Neptune (Connerney et al., 1991), and Uranus (Connerney et al., 1987). The spatial distributions of the magnetic field of those planets, including Earth, are modeled as the dipole magnetic field. The term magnetosphere is derived by Gold (1959) and defined as the region where the intrinsic magnetic fields of a planet is a key driver of physics in the vicinity of the planet (see a textbook by i.e. Maggiolo et al., 2021). The magnetic fields of the planets interact with the solar wind, forming various regions with different characteristics. Figure 1.1 shows the schematic illustration of the magnetosphere of Earth shown by National Research Council (2003). A bow shock is the boundary region to the heliosphere and magnetosphere, where solar wind decelerates, forming shock waves under collisionless plasma. The intermediate transition region from bowshock to magnetopause is magnetosheath, formed by solar wind pressure.

Geomagnetic storms and substorms are disturbances in the magnetosphere associated with solar activities. The southward interplanetary magnetic field (IMF) is typically caused by Coronal Mass Ejection (CME), which dynamically changes the environment of the magnetosphere, known as geomagnetic storms. Ring currents are formed with drifting electrons and ions during a geomagnetic storm. Substorm is associated with auroral activity and caused by the injection of charged particles by the magnetic reconnection at the magnetotail. Geomagnetic storms and substorms cause the variation of the environment over the heliosphere, the magnetosphere, and the ionosphere. Those global variations of the environment are known as space weather, which is conceptually analogous to meteorology. The satellite observation by Explorer 1 in 1958 has shown the region of high energetic ions and electrons in the inner region of Earth's magne-

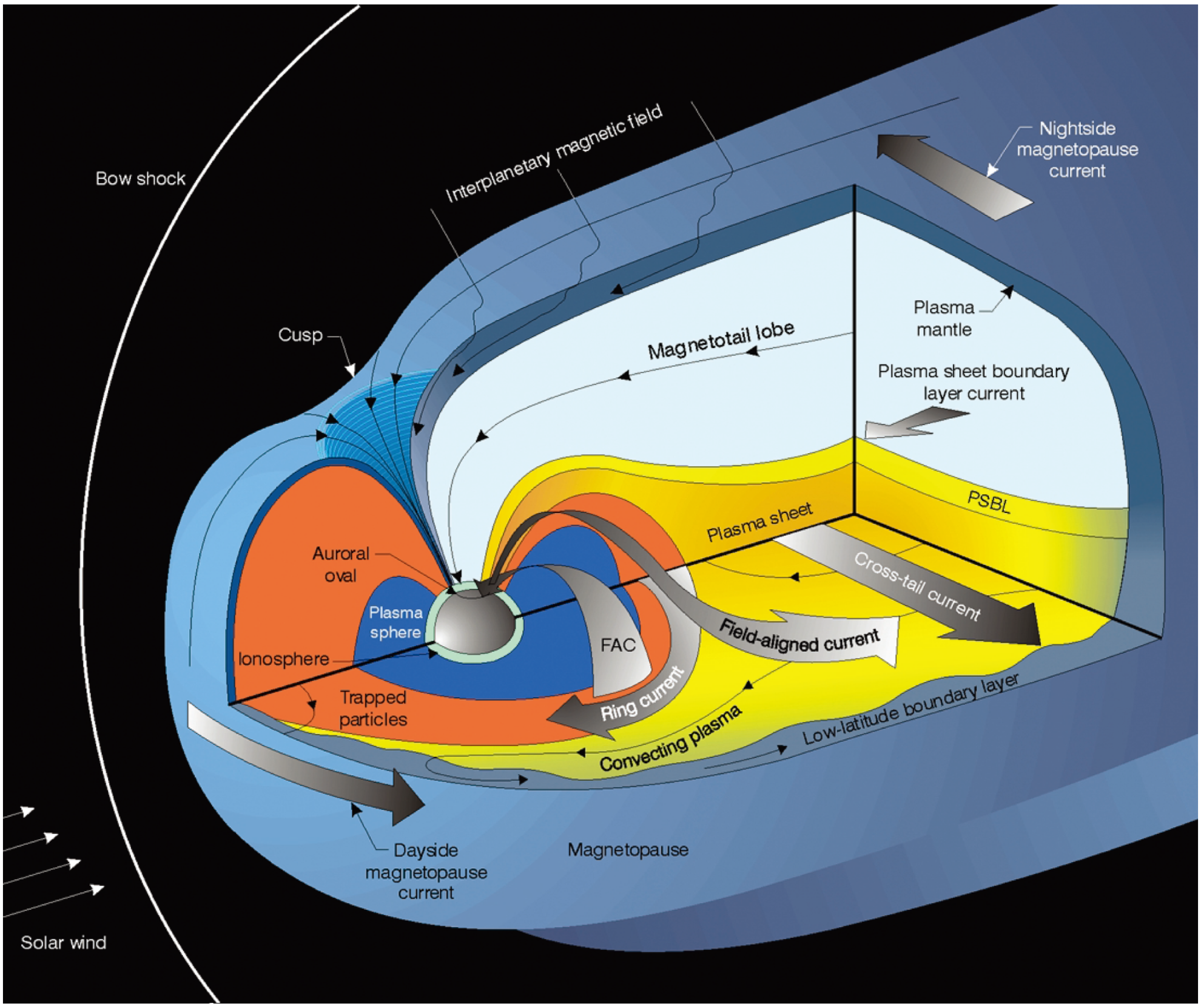

Figure 1.1: Artist's conceptional illustration of Earth's magnetosphere by National Research Council (2003).

tosphere (Van Allen et al., 1958). The formation of radiation belts is one of the significant interests in space weather.

1.2 Radiation belt of Earth

Van Allen radiation belts of Earth were first observed by the satellite (Van Allen et al., 1958). Other planets with intrinsic magnetic fields, such as Jupiter (Drake & Hvatum, 1959), Saturn (Van Allen et al., 1980; Vogt et al., 1982), Uranus (Cheng et al., 1987), and Neptune (Stone et al., 1989), also have radiation belts. Radiation belts are one of the typical characteristics of the magnetosphere of planets. The radiation belts of Earth typically form two high-energetic torus regions with relativistic charged particles; Typically, the inner and the outer radiation belts are formed as shown in Figure 1.2A. The inner radiation belts consist of several mega electron

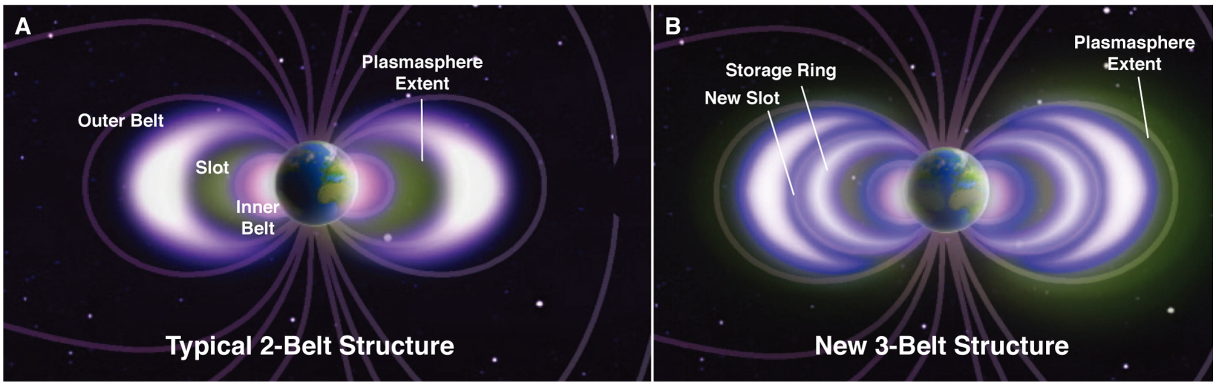

Figure 1.2: Schematic illustration of radiation belts of Earth. (A) Typical structure of radiation belts with two belts: A slot region exists between the inner and the outer belts. (B) Three-belt structure of radiation belts, forming storage ring from Baker et al. (2013). Reprinted with permission from AAAS.

volt protons with a radius below $L = 3$. The outer radiation belt is composed of relativistic electrons located from $L = 4$ to 6. Between two radiation belts, a slot region exists, where the flux of relativistic charged particles is low. Recently, three belt structures of the radiation belts are observed in the transition phase of the formation of radiation belts (Baker et al., 2013) as shown in Figure 1.2. The distance of radiation belts from Earth is a similar radius to those for geosynchronous orbits (GSO) and Global Navigation Satellite System (GNSS) orbits, and charged particles of the radiation belts lead to surface charging and degradation of satellites, and malfunction of electric circuits and semiconductors on satellites (Lanzerotti, 2001) (see a textbook by i.e. Coster et al., 2021).

The flux of the outer radiation belts dynamically changes by the solar activities, and the formation and the loss processes of the radiation belts have been discussed. Figure 1.3 shows the coupling processes of waves and electrons with different energies for the formation of relativistic electrons. Charged particles transported from the Sun interact with the magnetic fields of the Earth, and the particles are injected into the magnetosphere from the magnetotail by magnetic reconnections. Ultra Low Frequency (ULF) waves with a frequency range of several mHz are observed in the inner magnetosphere, and those waves are known as Pc4 to Pc5 pulsations (Saito, 1969). ULF waves accelerate electrons via radial transportation (Baker et al., 2016), which is known as external acceleration. Those ULF waves are generated by the Kelvin-Helmholtz instabilities in the magnetosheath and propagate as magnetohydrodynamic (MHD) waves (L. Chen & Hasegawa, 1974). The electrons in the inner magnetosphere can be accelerated via drift resonance with ULF waves (Kissinger et al., 2014; Teramoto et al., 2019), while the rapid formation of the radiation belts and their energy range can not be described only by the external acceleration.

The rapid flux variations of relativistic electrons in the energy range of several hundred keV are associated with the increase of VLF emissions in the magnetosphere. The observations

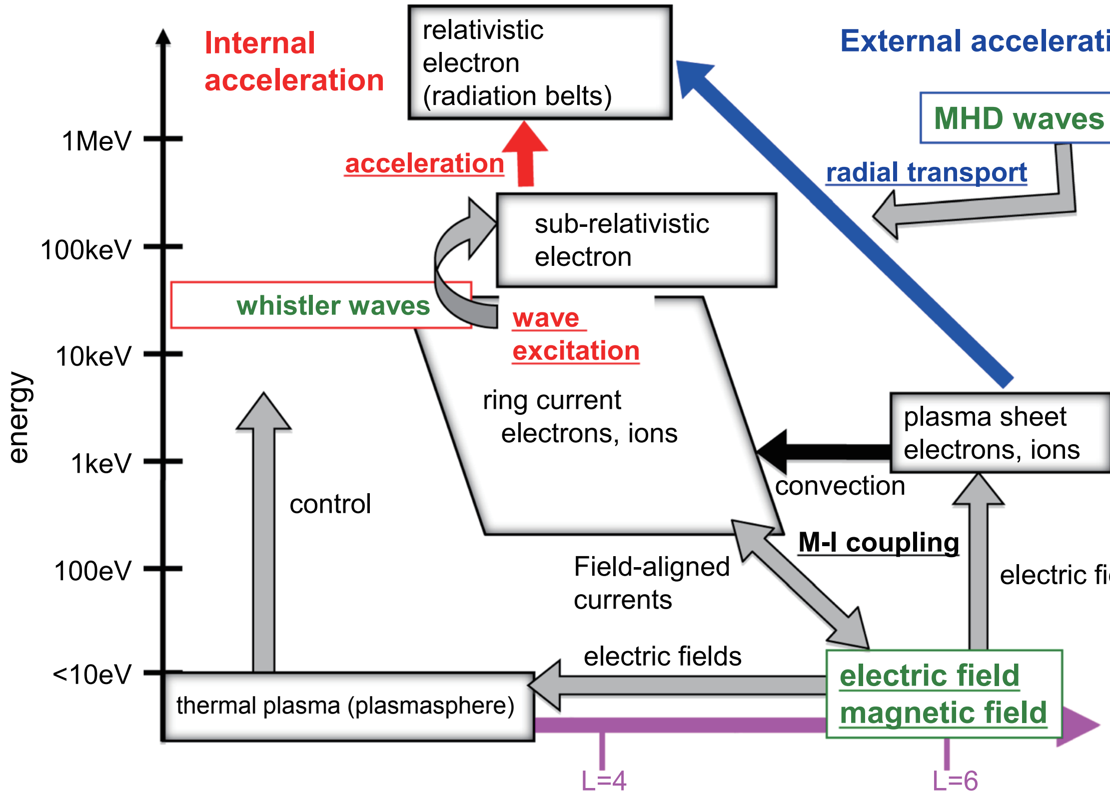

Figure 1.3: Cross energy coupling process in the inner magnetosphere (Miyoshi et al., 2012, 2018).

suggest that the electrons in the inner magnetosphere are locally accelerated (e.g., Reeves et al., 2013; Thorne et al., 2013; Foster et al., 2014; Boyd et al., 2018, and others). Whistler-mode waves and the associated increase of electron flux have been observed in the same region as the radiation belts. Whistler-mode waves are right-handed circular polarized waves below the frequency of the electron cyclotron frequency, and propagate in the quasi-parallel direction to the geomagnetic field. The characteristics of whistler-mode waves are described in Section 1.4. Figure 1.4 shows the dynamic spectrum and the time evolution of wave amplitudes and of the flux for relativistic electrons with the energy of 2.85 MeV. Whistler-mode chorus waves are the key driver of the rapid dynamics of the radiation belt by wave-particle interaction (e.g., Thorne, 2010; Reeves et al., 2013, and others). The description of whistler-mode wave-particle interactions that account for the formation of radiation belts is described in Section 1.5.

The loss of the radiation belts is caused by two different mechanisms, adiabatic radial transportation and wave-particle interactions, which are similar to the enhancement of radiation belts (Reeves et al., 2003). The electrons in the radiation belt are decelerated by adiabatic radial transportation, and the energy of relativistic electrons decreases, resulting in the temporal loss of the radiation belts. The loss of radiation belts through radial transportation is temporal, because

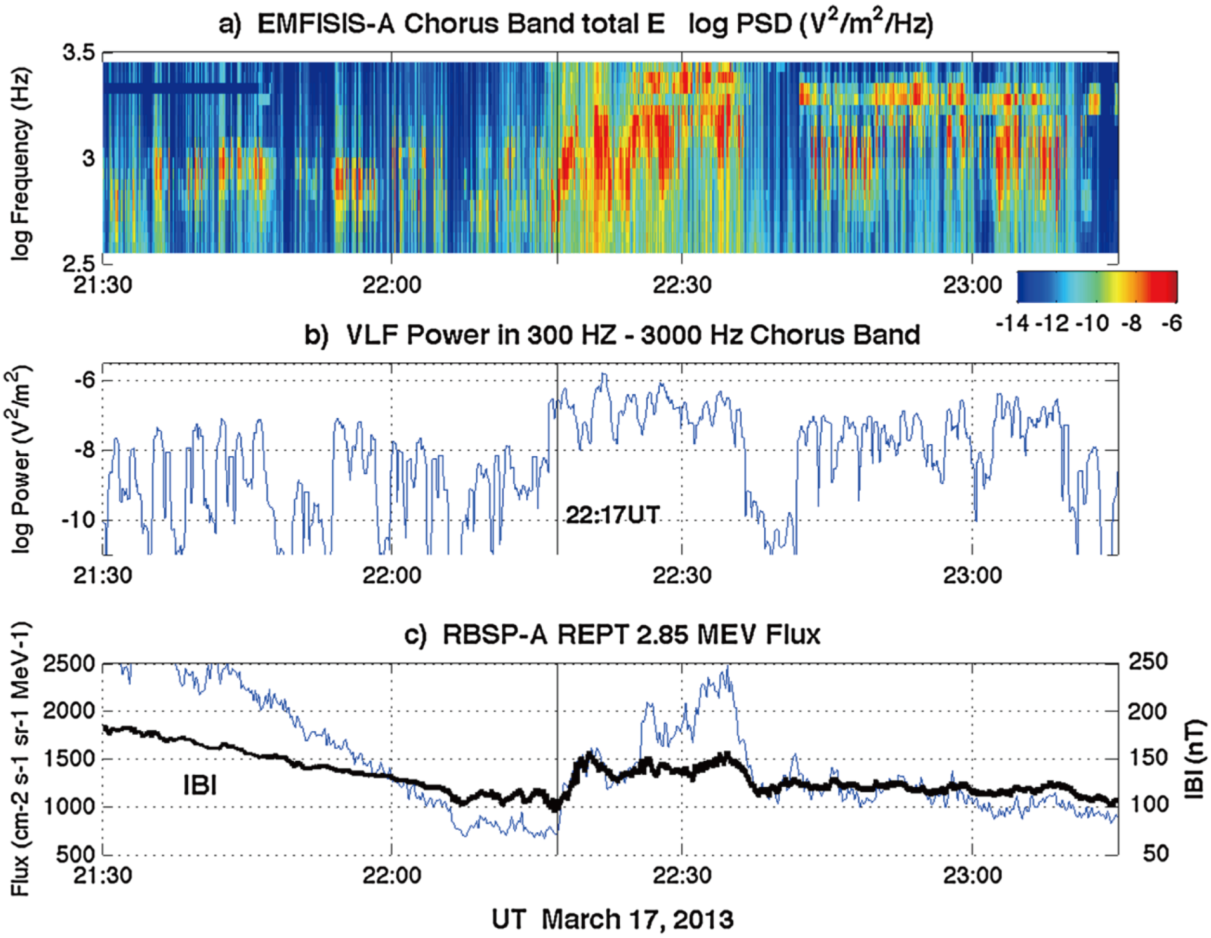

Figure 1.4: Observation result of whistler-mode chorus emission and associated flux enhancement of relativistic electrons by the Van Allen Probes (Foster et al., 2014) (a) Dynamic spectrum for electric fields observed with the EMFISIS instrument. (b) The power of VLF waves with the frequency range in 300 Hz – 3 kHz. (c) The flux of 2.85 MeVelectrons observed with the PEPT

.

the flux of relativistic electrons recovers when the magnitude of the ambient magnetic field becomes greater. The major part of the loss of the radiation belt is caused by the precipitation of relativistic electrons to the atmosphere via pitch angle scattering associated with wave-particle interactions. Electromagnetic ion cyclotron (EMIC) waves with left-handed circular polarized waves are observed when the precipitation of relativistic electrons occurs (Lorentzen et al., 2000; Miyoshi et al., 2008; Kurita et al., 2018; Nakamura et al., 2019).

1.3 Very Low Frequency triggered emissions

Very Low Frequency (VLF) radio waves are defined with the frequency range with 3 – 30 kHz, and VLF waves are used for geophysical probing, submarine communications, and global nav-

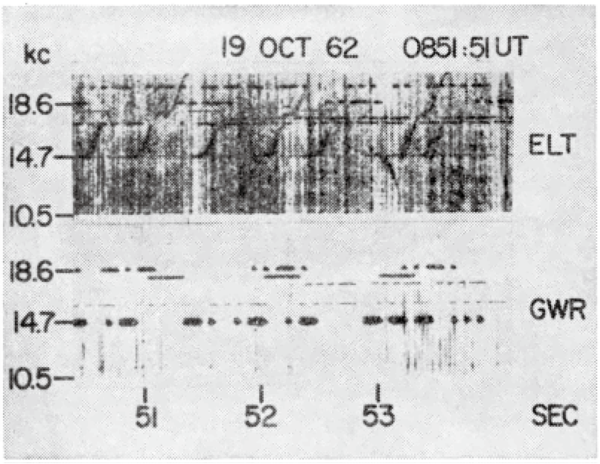

Figure 1.5: Dynamic spectrum of VLF rising-tone and falling-tone triggered emissions from Morse code, transmitted to a submarine, and received at the ground station on October 19, 1962 (Helliwell & Brice, 1964).

igation system (Casselman et al., 1959; Kasper & Hutchinson, 1978). The first report of VLF triggered emissions date back to 1964, showing the events in 1959 and 1962 where the transmitted Morse code with constant frequency are modulated, and newly generated emissions are observed with different frequencies from the original transmitted waves (Helliwell & Brice, 1964) as shown in Figure 1.5. Transmitted VLF waves from the antenna in the ground propagate in the atmosphere, and waves are injected into the magnetosphere through the ionosphere. VLF waves propagate along with the dipole magnetic field line of the Earth as whistler-mode in a duct of plasmasphere (Carpenter & Miller, 1976). VLF triggered emissions are received at a ground station in the opposite hemisphere (Helliwell, 1967; Helliwell & Katsufrakis, 1974).

Frequency variation of VLF triggered emissions are typically classified into four types; rising-tone emissions, falling-tone emissions, hooks, and inverted hocks (Helliwell, 1967; Helliwell & Katsufrakis, 1974). In the rising-tone emissions, the instantaneous frequency of the waves monotonically increases. The frequency of the falling-tone emissions decreases in time. Hooks and inverted hooks are a combination of rising-tone and falling-tone emissions, containing frequency increases and decreases. Observations of VLF triggered emission by an artificial signal injection of VLF waves have been used as an effective measure for probing the ionosphere and the magnetosphere of the Earth (Carpenter, 1988). Observations of VLF triggered emissions have shown the concept of whistler-mode propagation, showing the existence of the plasma surrounding the Earth, known as the plasmasphere. The ground observation of VLF triggered emissions suggest that the frequency variation of the VLF triggered emissions depends on the duration of the triggering waves (Helliwell & Katsufrakis, 1974). Helliwell et al. (1980) have shown that the minimum threshold amplitude of triggering wave exists for obtaining triggering emissions. The generation mechanisms of triggered emissions have been discussed over one-half of a century (see reviews by Omura et al., 1991; Gołkowski et al., 2019). Helliwell

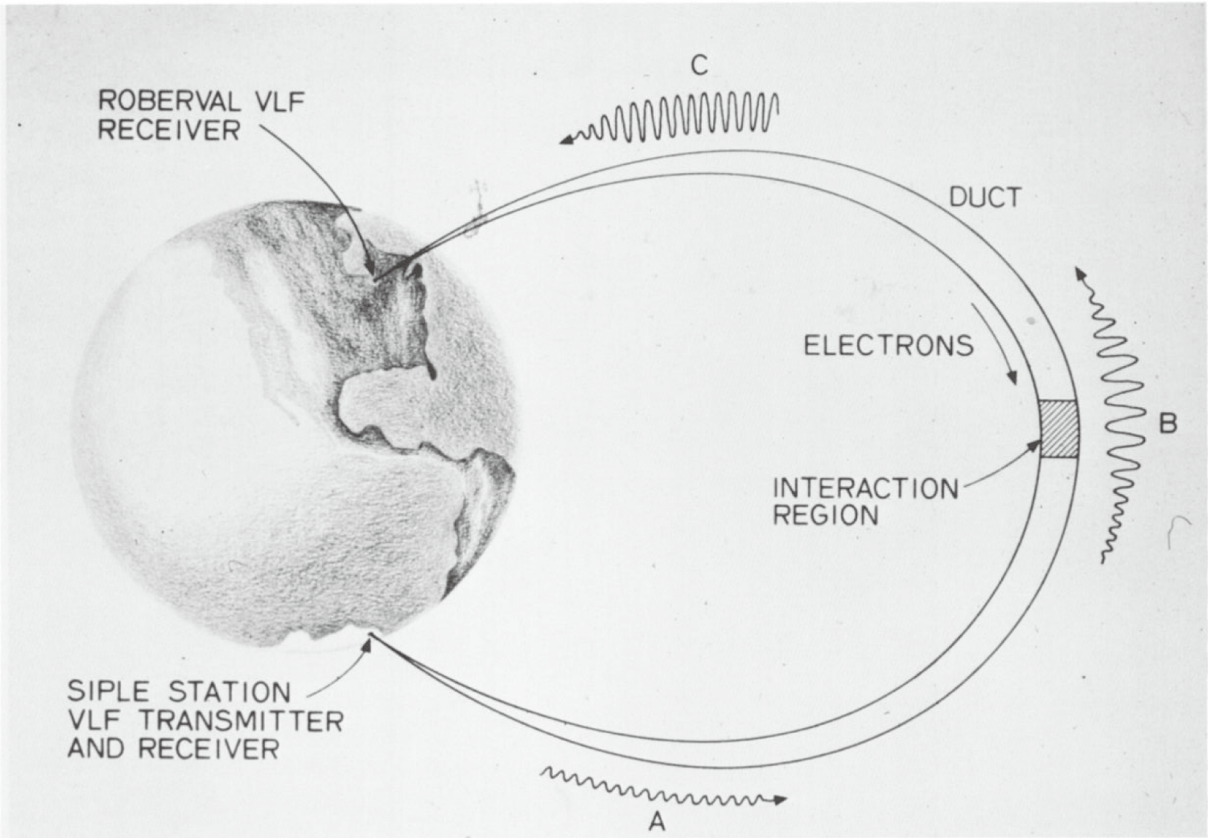

Figure 1.6: Schematic illustration of the Siple experiment (Helliwell, 1983). (A) VLF triggering waves are transmitted from the Siple station in the Antarctic and propagate along a duct in the magnetosphere. (B) VLF radio waves interact with resonant electrons in the vicinity of the magnetic equator, and triggered waves are generated (C) VLF waves propagate along with the magnetic field and are received at a ground station.

(1967) have proposed that the trajectory of the resonant electrons is not asymmetric in phase with the gradient of the ambient magnetic field. The asymmetric phase distribution of resonant electrons forms resonant currents, generating new emissions. The phase space modulation of resonant electrons generates triggered emissions, and the formation process of resonant electron distribution is caused by the parallel velocity differences between adiabatic and untrapped electrons (Roux & Pellat, 1978). Recently, Tao et al. (2021) proposed Trap-Release-Amplify (TaRA) model, untrapped electrons from the triggering wave generate resonant currents. These models suggest that untrapped resonant electrons are adiabatically transported upstream and generate triggered emissions. Katoh and Omura (2006) showed that resonant currents are generated by the formation of an electron hole in velocity phase space by using hybrid code. The formation of the resonant current is described in Section 1.5.

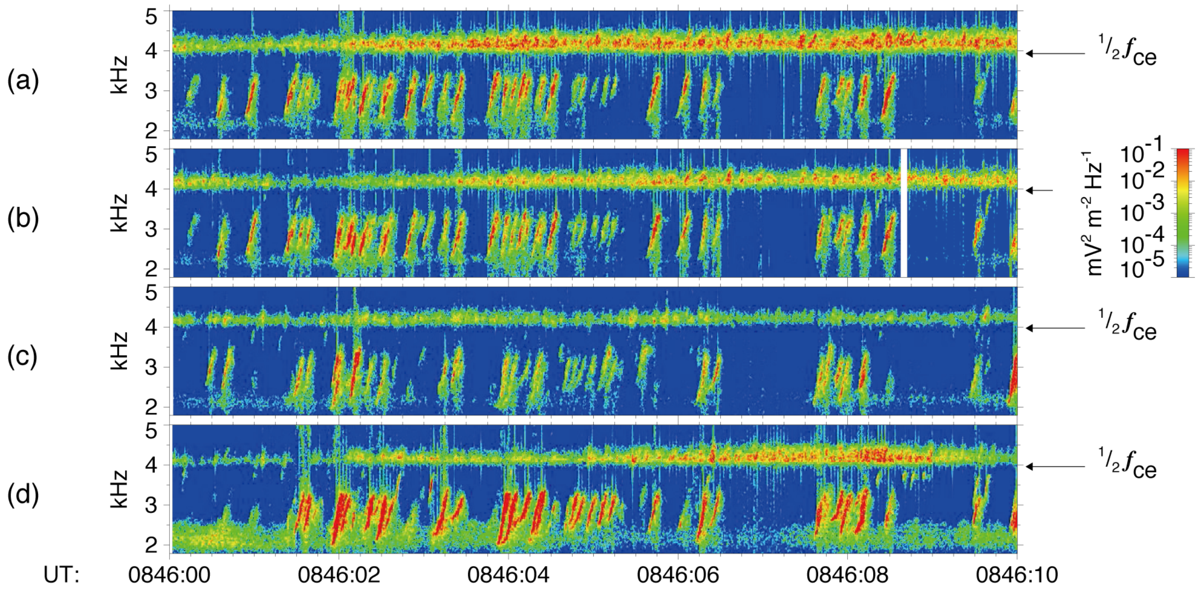

Figure 1.7: Dynamic spectra of upper-band and lower-band whistler-mode chorus emissions observed by the Wideband Data (WBD) instruments on the Cluster spacecraft (Santolík et al., 2004). (a) to (d) indicate the data from the Cluster spacecraft numbers 1 to 4, respectively.

1.4 Whistler-mode chorus emissions

Whistler-mode emissions are observed in the frequencies from several kilohertz to ten kilohertz with right-handed circular polarized waves. Whistler-mode wave is classified into three categories: Whistlers, chorus emissions, and hiss emissions. Whistlers are triggered from lightning (Storey, 1953; Carpenter, 1968; Helliwell, 1969). Lightning whistler is caused by pulsed radio wave emissions, which are triggered by lightning in the atmosphere. The frequency variation of lightning whistlers in time is observed as they propagate because of the difference in the group velocity to wave frequency. Chorus emissions are in the frequency range with $0.1 - 0.8\,\Omega_e$ of the electron cyclotron frequency and typically observed in two different frequency bands, lower-band chorus with $0.1 - 0.5\,\Omega_e$ and upper-band chorus with $0.5 - 0.8\,\Omega_e$, where Ω_e is the electron cyclotron frequency (e.g., Tsurutani & Smith, 1974; Santolík et al., 2004). Hiss emissions are in the frequency range $0.05 - 0.1\,\Omega_e$ (e.g., Smith, Frandsen, et al., 1974; Meredith et al., 2004; Nakamura et al., 2018). Fine structures of hiss emissions are observed (e.g., Summers et al., 2014; Nakamura et al., 2018). Those fine structures of hiss emissions can be generated by the same mechanism as chorus waves (Hikishima et al., 2020; Y. Liu & Omura, 2022).

The generation of the whistler-mode chorus waves is associated with magnetic storms. During a magnetic storm, charged particles are provided from the plasma sheet, forming ring currents. Protons are transported to the inner magnetosphere in the clockwise direction, and electrons are transported in the anti-clockwise direction from the bird's eye view from the Earth's north pole as shown in Figure 1.8. Whistler-mode waves are typically generated in the region of

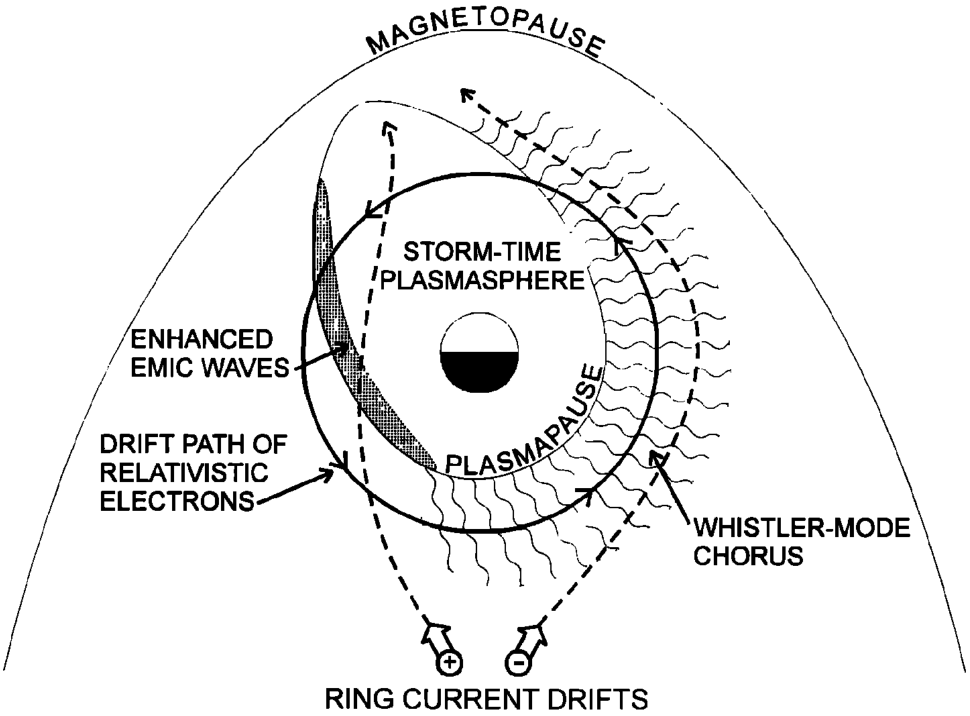

Figure 1.8: Spatial distribution of whistler-mode chorus waves and ElectroMagnetic Ion Cyclotron (EMIC) waves by the injection of electrons and ions forming ring current during magnetic storms (Summers et al., 1998)

dawn with the magnetic local time, and chorus emissions are also known as dawn chorus (W. Li et al., 2009). Global simulations have shown the formation of anisotropic electrons in the dawn region, which is responsible for the generation of whistler-mode waves (Ebihara et al., 2020).

Chorus waves are generated in the vicinity of the magnetic equator (LeDocq et al., 1998). Many studies of chorus waves have been conducted for more than half a century. (see reviews by Sazhin & Hayakawa, 1992; Tsurutani et al., 2013). Tsurutani and Smith (1974) has reported that whistler-mode chorus waves are observed during a substorm by the ground observation. W. Li et al. (2011) have conducted a statistical survey on the characteristics of rising-tone and falling-tone emissions by using THEMIS measurement data, showing the occurrence, generation region, amplitude, and propagation angle of the emissions. Rising-tone emissions are more frequently observed than falling-tone emissions, and the amplitude of rising-tone emissions is typically greater than that of falling-tone emissions. Chorus waves generally propagate in the quasi-parallel direction to the ambient magnetic field, while very oblique whistler-mode chorus waves are also observed (e.g., A. Artemyev et al., 2016). Colpitts et al. (2020) have conducted by using multiple satellites, the Van Allen Probes, and Arase. Whistler-mode waves are also observed in the magnetosheath, which locally forms a mirror-shaped magnetic field by using Multi Sattelite Mission satellites (MMS) (Kitamura et al., 2020). The satellite observations have

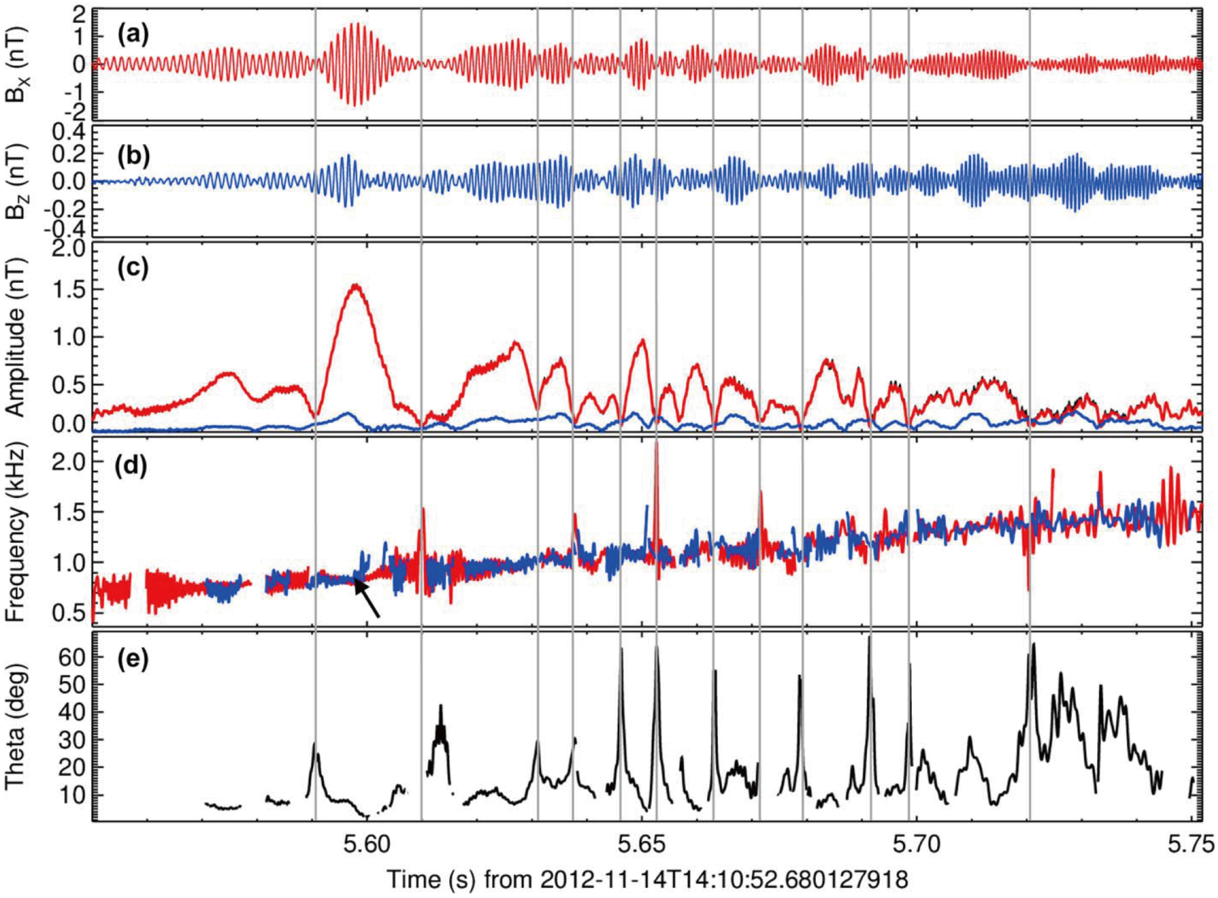

Figure 1.9: Characteristics of subpacket structures in a single rising-tone element (Santolík et al., 2014). (a) Waveform of B_x perpendicular to ambient magnetic field (b) Waveform of B_z parallel to the ambient magnetic field.(c) Time evolution of amplitudes of B_x is shown in red, and B_z is shown in blue. (d) Instantaneous frequencies of waveforms with the same color as (c). (e) Propagation wave vector of the waves.

shown that the amplitude in a single rising-tone element changes in time, forming a subpacket structure (Santolík et al., 2014; Foster et al., 2021). Figure 1.9 shows the characteristics of the subpacket structure. Tsurutani et al. (2020) has shown that the instantaneous frequency in the subpacket structure is constant. Foster et al. (2021) has shown that the instantaneous frequency smoothly increases in a subpacket for rising-tone emissions.

1.5 Whistler-mode wave-particle interaction

The generation mechanism of whistler-mode waves triggered emissions and chorus waves have been discussed for more than half a century. There exist many studies on the generation process of chorus waves, and we classify the generation mechanisms of chorus waves in those studies into two categories, linear wave growth, and resonant current. Linear wave growth is driven by the temperature anisotropy of energetic electrons. Nonlinear wave growth is caused by the

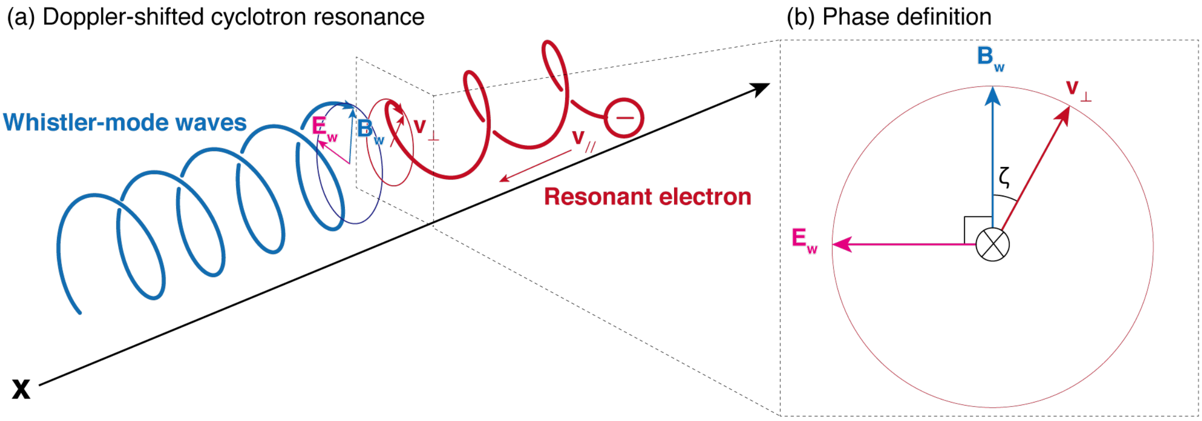

Figure 1.10: Schematic illustration of first-order doppler-shifted cyclotron resonance and definition of the phase difference between $\boldsymbol{v}_\perp$ and $\boldsymbol{B_w}$ as the frame of reference of the parallel velocity of the resonant electron.

formation of resonant current. Linear wave growth is also known as whistler instability, which is caused by the anisotropic velocity distribution of energetic electrons (Kennel & Petschek, 1966; Xiao et al., 1998). Although a positive linear wave growth rate is obtained in a certain frequency range depending on the velocity distribution function, the frequency of the generated wave packets is fixed during wave growth; Linear wave growth is not consistent with the frequency variations of rising-tone and falling-tone chorus emissions.

In the nonlinear process of the wave growth, resonant currents are formed by resonant electrons interacting with the coherent waves generated by the linear wave growth or triggering waves, leading to an effective wave growth and frequency variations (e.g., Dysthe, 1971; Nunn, 1974; Helliwell, 1967; Roux & Pellat, 1978; Vomvoridis et al., 1982; Trakhtengerts, 1999; Omura et al., 2008; Hikishima et al., 2009b; Omura, 2021, and others). Figure 1.10 shows the schematic illustration of doppler-shifter cyclotron resonance in the generation of whistler-mode waves. The wave equation and dispersion relation of whistler-mode waves are written by Omura et al. (2008) and Omura (2021) as

$$\begin{aligned} \frac{\partial B_w}{\partial t} + V_g \frac{\partial B_w}{\partial h} &= -\frac{\mu_0 V_g}{2} J_E \,, && (1.1) \\ c^2k^2 - \omega^2 - \frac{\omega\omega_p^2}{\Omega_e - \omega} &= \mu_0 c^2 k \frac{J_B}{B_w} \,, && (1.2) \end{aligned}$$

, where V_g, c, k, ω, ω_p, Ω_e and μ_0 are group velocity of whistler-mode waves, speed of light in a vacuum, wave frequency, plasma frequency, cyclotron frequency, and magnetic permittivity, respectively. By using the cold dispersion relation of whistler-mode waves with the wave frequency of ω_0 and equation (1.2), we obtain the frequency variation $\delta\omega$ from wave frequency ω_0 as

$$\delta\omega = -\frac{\mu_0 V_g}{2} \frac{J_B}{B_w} \ . \tag{1.3}$$

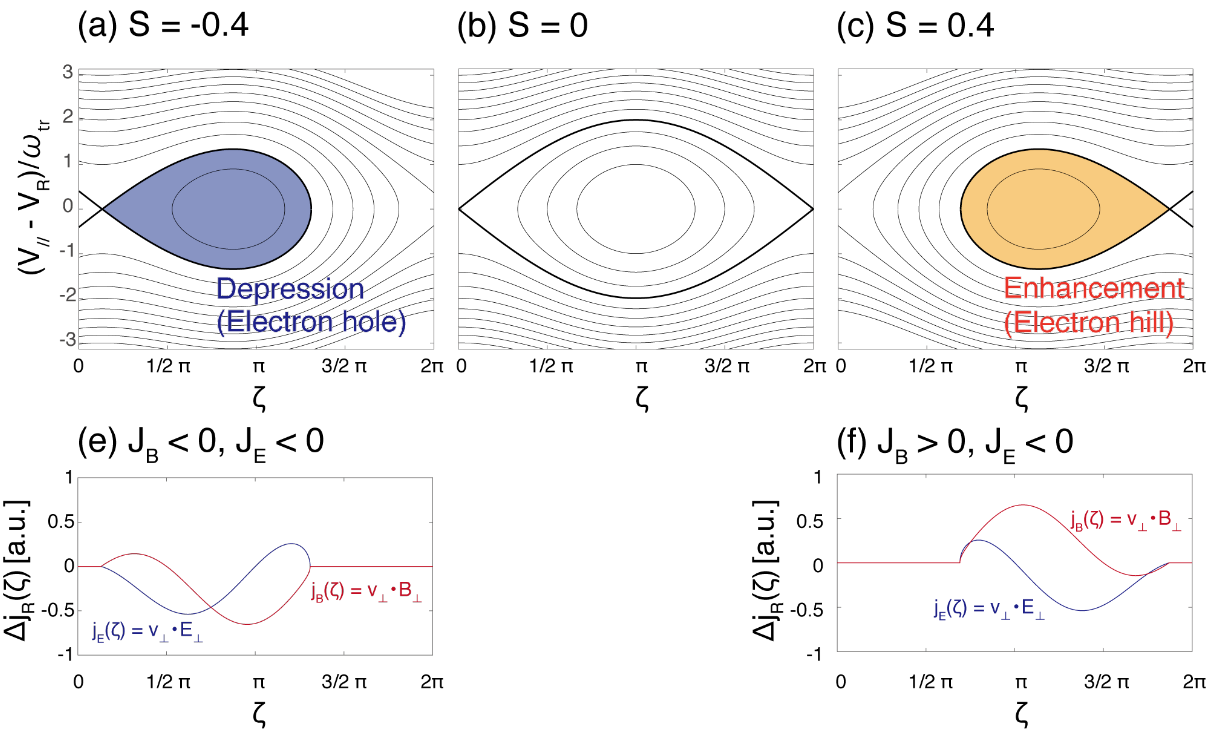

Figure 1.11: Trajectories of electrons under resonance with whistler-mode waves for different inhomogeneous factors S (Omura et al., 2008; Nunn & Omura, 2012; Omura, 2021) for (a) $S = -0.4$, (b) $S = 0$, and (c)$S = 0.4$, respectively. (e,f) Formation of resonant current for different phase angles ζ by the formation of electron hole and hill.

The formation of the resonant currents is controlled by the inhomogeneous distribution of resonant electrons in the cyclotron motion with respect to the transverse wave magnetic field. The phase difference ζ is defined as $\zeta = \phi - \psi$, where ϕ is the wave phase of the transverse magnetic field of waves, and ψ is the phase of the perpendicular velocity of resonant electrons as shown in Figure 1.10b. In the cyclotron resonance condition ζ is approximately zero. The trajectory of the resonant electrons in the phase space $(\zeta, \mathrm{d}\zeta/\mathrm{d}t)$ is given by the pendulum equation from the equation of motions, written as

$$\frac{\mathrm{d}^2\zeta}{\mathrm{d}t^2} = \omega_{tr}(\sin\zeta + S) \tag{1.4}$$

where inhomogeneous factor S is given by

$$S = -\frac{1}{s_0\omega\Omega_w}\left(s_1\frac{\partial\omega}{\partial t} + cs_2\frac{\partial\Omega_e}{\partial h}\right), \tag{1.5}$$

and

$$s_0 = \frac{\chi v_\perp}{\xi c}, \tag{1.6}$$

$$s_1 = \gamma\left(1 - \frac{V_R}{V_g}\right)^2, \tag{1.7}$$

$$s_2 = \frac{1}{2\xi\chi}\left\{\frac{\gamma\omega}{\Omega_e}\left(\frac{v_\perp}{c}\right)^2 - \left[2 + \Lambda\frac{\chi^2(\Omega_e - \gamma\omega)}{\Omega_e - \omega}\right]\frac{V_R V_p}{c^2}\right\}, \tag{1.8}$$

where ξ and χ are the dimensionless parameters given by $\xi^2 = \omega(\Omega_e - \omega)/\omega_p^2$ and $\chi^2 = 1/(1+\xi^2)$, respectively. The detailed derivation of the equations (1.1) to (1.8), are described in Omura et al. (2008) and Omura (2021). The inhomogeneous factor S is mainly controlled by two terms, frequency variation of waves in time and the spatial gradient of the ambient magnetic field, as we find in equation (1.5).

The trajectories of the resonant electrons for different inhomogeneous factor S in phase space with respect to ζ and $\mathrm{d}\zeta/\mathrm{d}t$ are shown in Figure 1.11. The trajectories of resonant electrons are symmetric to $\zeta = \pi/2$, when the inhomogeneous factor $S = 0$ as shown in Figure 1.11b. The bold solid black lines indicate separatrix between trapped and untrapped electrons, which appears in the range of inhomogeneous factor $-1 < S < 1$. When the enhancement or depression of trapped electrons takes place, resonant currents are generated, while frequency variation does not happen with $S = 0$ due to the absence of $\boldsymbol{J_B}$. When the inhomogeneous factor S becomes negative, the center of the trajectory shift to the lower phase difference ζ as shown in Figure 1.11a. In the rising-tone emissions, electron density distribution in the separatrix of the trajectory decreases, forming an electron hole. Assuming the uniform density in the separatrix, we obtain negative resonant currents by integrating resonant currents $\boldsymbol{j_B}$ and $\boldsymbol{j_E}$ with respect to wave phase ζ as shown in Figure 1.11e. With the negative resonant currents $\boldsymbol{J_B}$, the wave frequency increases in time as in equation 1.3, and wave amplitude grows with the negative resonant current $\boldsymbol{J_E}$. In the falling-tone emissions, electron hill is formed by the enhancement of electron population in the separatrix, where the inhomogeneous factor S is 0.4 as shown in Figure 1.11c. With the same assumptions as the case of rising-tone emissions applied, the resonant current $\boldsymbol{J_E}$ is negative, while the resonant current $\boldsymbol{J_B}$ is positive as shown in Figure 1.11f. With the positive resonant currents $\boldsymbol{J_B}$, the wave frequency decreases in time. Recently, Kitamura et al. (2022) have shown the formation of resonant currents and an electron hole in phase space during the generation of chorus waves by the direct satellite measurement with MMS.

The significance of the whistler-mode wave-particle interaction is not only the generation process of triggered emissions and chorus emissions but also the acceleration, diffusion, and pitch angle scattering process of an electron. With the small amplitude of whistler-mode waves, pitch angle diffusion occurs. Diffusion of resonant electrons via quasi-linear theory has also been proposed, where the amplitude of the chorus waves is low (e.g., Summers, 2005; Summers et al., 2007a, 2007b, and others). The amplitude threshold between the quasi-linear theory, including the linear theory and the nonlinear theory, is surveyed from the theoretical derivation (i.e. Omura et al., 2008) and numerical simulations (i.e. Kitahara & Katoh, 2019; Gan et al., 2020, 2022). The amplitude of chorus waves grows by the seed waves generated from temperature anisotropy (Hikishima et al., 2009b), and the observation of large amplitude chorus

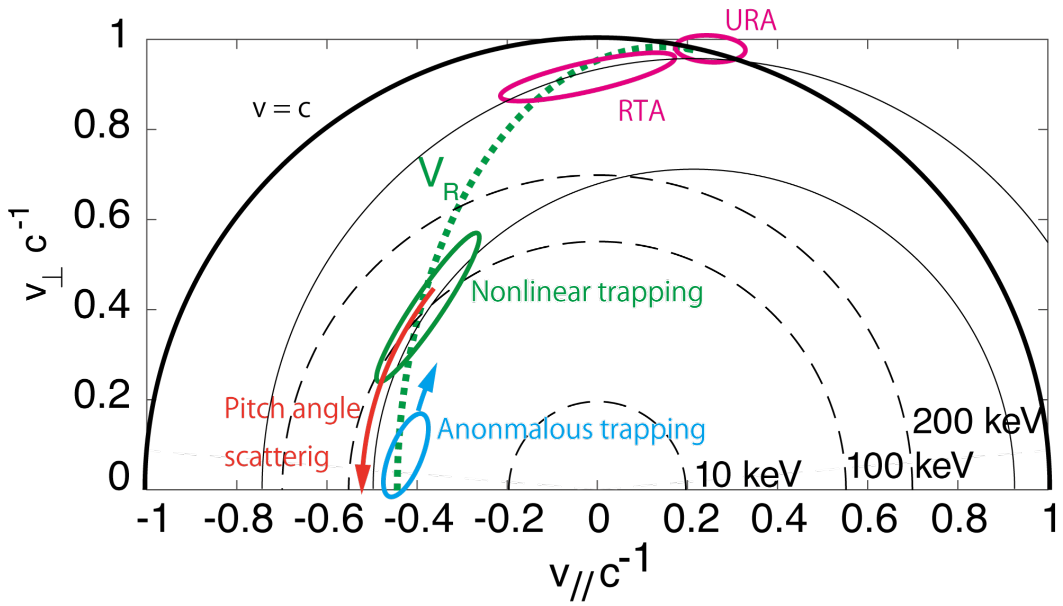

Figure 1.12: Schmatic illustration of the density population variations in the velocity distribution via cyclotron resonance for (magenta) electron acceleration (RTA, URA), (green) nonlinear trapping, (orange) pitch angle scattering, and (cyan) anomalous trapping. The cyclotron resonance velocity is shown in green dotted lines with the wave frequency of 0.3 Ω_e and the plasma frequency $\omega_p = 2.0\Omega_e$.

waves (Santolík et al., 2014), nonlinear wave-particle interactions are the key kinetic process in the inner magnetosphere. Figure 1.12 shows the whistler-mode wave-particle interactions with respect to the different pitch angles and the energy ranges. In the higher pitch angle, effective acceleration processes of electrons via trapping to wave potential occurs, which are known as Relativistic Turning Acceleration (RTA) (Omura et al., 2007) and Ultra Relativistic Acceleration (URA) (Summers & Omura, 2007). Whistler-mode chorus waves are potential waves for the pitch angle scattering of electrons (Horne & Thorne, 1998). Pitch angle scattering is associated with the observation of chorus waves (Kasahara et al., 2018). Satellite observations show that the diffuse and pulsating aurora are caused by the precipitation of the electron by chorus waves (Ozaki et al., 2018). The pitch angle scattering of electrons occurs in the generation process of chorus waves (Hikishima et al., 2009a). With the large amplitude chorus waves, the pitch angle of the resonant electrons in the low pitch angle increases via anomalous trapping occurs (Kitahara & Katoh, 2019). The trajectories of resonant electrons in the lower pitch angle are studies showing the (Gan et al., 2020; Yoon & Bellan, 2020; A. V. Artemyev et al., 2021; Albert et al., 2022). Oblique whistler-mode waves accelerate electrons via Landau resonance (e.g. A. V. Artemyev et al., 2014; Hsieh & Omura, 2018) due to the parallel (O. V. Agapitov et al., 2016) and perpendicular electric waves.

Subpacket structures of the chorus emissions are also important issues in the nonlinear wave-particle interaction. The trapping of resonant electrons and the formation of resonant currents via nonlinear interactions are based on the assumption that the wave phase smoothly changes so that the seed waves are regarded as monochromatic coherent waves over a finite time period. Subpacket structures of the VLF triggered emissions can be observed as the side-band structures in dynamic spectra (i.e. Park, 1981; Costabile et al., 2017), and multiple frequencies in dynamic spectra for chorus waves (i.e. Foster et al., 2021). These characteristics of the subpacket structures of whistler-mode waves can affect the efficiency of the nonlinear wave-particle interactions. Test particle simulations of the electron trapping with chorus waves with subpacket structures have shown that the effective acceleration by nonlinear trapping occurs (Kubota & Omura, 2018; Hsieh et al., 2020).

1.6 Numerical simulations of VLF triggered emission and chorus emission

For the study of the kinetic process in the generation of whistler-mode triggered emissions and chorus emissions, numerical simulations have been conducted. Table 1.1 shows an overview of self-consistent simulations for whistler-mode triggered emissions and whistler-mode chorus emissions after (Gołkowski et al., 2019). In the early phase of the self-consistent simulation, wave equation and dispersion relation are solved for the electromagnetic fields. Because the wave equation and dispersion relations are solved for a specific frequency, the frequency range of the narrowband simulations is restricted, preventing the generation of triggered emissions with greater frequency variations. Nunn (1974) have shown the formation of resonant current and decreasing frequency in time. Wave growth and small frequency variations associated with the formation of an electron hole are shown (Vomvoridis & Denavit, 1980; Omura & Matsumoto, 1982). Long-time-scale (LTS) algorithm is used in the simulations of whistler-mode

Table 1.1: Self-consistent numerical simulations of whistler-mode triggered emissions and chorus emissions, modified from Gołkowski et al. (2019). Acronyms in source columns, TW and TA, stand for the wave source of triggered emissions from triggering waves and from waves grown from the temperature anisotropy, respectively.

Reference	Solver type	Dimension	Model	Source	Broadband	Feature & Key results
Nunn (1974)	Hybrid Vlasov	1D3V	Parabolic	TW		Small frequency change
Vomvoridis and Denavit (1980)	Hybrid PIC	1D3V	Linear	TW		Frequency increase
Omura and Matsumoto (1982)	Hybrid PIC	1D3V	Parabolic	TW		Wave growth
Nunn (1990, 1993)	Hybrid Vlasov	1D3V	Parabolic	TW		Rising-tone emission
Nunn and Omura (2012)	Hybrid Vlasov	1D3V	Parabolic	TW		Falling-tone emission
Harid et al. (2014)	Hybrid Vlasov	1D3V	inhomogeneity	TW		Frequency variations
Katoh and Omura (2006)	Hybrid PIC	1D3V	Parabolic	TW	X	Rising-tone emission
Katoh and Omura (2007)	Hybrid PIC	1D3V	Parabolic	TA	X	Rising-tone emission
Hikishima et al. (2009b)	Full PIC	1D3V	Parabolic	TA	X	Rising-tone emission
Hikishima et al. (2010)	Full PIC	1D3V	Parabolic	TW	X	Rising-tone emission
Tao (2014)	Hybrid δf-PIC	1D3V	Parabolic	TA	X	Rising-tone emission
Katoh and Omura (2016)	Hybrid PIC	1D3V	Parabolic	TA	X	Real parameter, Rising-tone emission
Ke et al. (2017)	Hybrid PIC	2D3V	Parabolic	TA	X	Rising-tone emission
Wu et al. (2020)	Hybrid PIC	1D3V	Homogeneous	TA	X	Rising-tone and falling-tone emissions
Wu et al. (2022)	Hybrid PIC	1D3V	Inverse parabolic	TA	X	Falling-tone emission

wave-particle interaction (Rathmann et al., 1978; Omura & Matsumoto, 1982). In the LTS scheme, equations of motion are solved only for energetic electrons, and the spatial distribution of resonant currents is calculated by integrating resonant current for each superparticle. The cold dispersion relation of whistler-mode waves is determined, and wave equations are solved with the resonant current. Finally, the spatial distribution of the electromagnetic field in the system is updated. The first successive reproductions of rising-tone emissions are done by Nunn (1990) with Vlasov Hybrid Simulation code by applying quasi-broadband approaches (i.e. Nunn & Smith, 1996; Nunn, 2021). Nunn and Omura (2012) have shown the generation of falling-tone triggered emissions in the upstream region of triggering waves. (Mourenas et al., 2022) have conducted Vlasov Hybrid Simulation and reproduced short chorus wave packets.

Since the computer performance for numerical simulation has drastically improved, particle-in-cell simulation by solving Maxwell's equations with a numerical scheme (e.g., FDTD) became possible for whistler-mode wave-particle interactions. Katoh and Omura (2006) have shown the formation of rising-tone triggered emission with hybrid particle-in-cell simulation, showing the formation of resonant currents. Katoh and Omura (2007) have successfully reproduced rising-tone chorus emission from large temperature anisotropy. Hikishima et al. (2009b) and Hikishima et al. (2010) have conducted full particle simulations for chorus emissions and triggered emissions, reproducing rising-tone emissions, respectively. Tao (2014) has shown the rising-tone emissions and the formation of an electron hole with δf PIC simulation, which enables the suppression of the thermal noise due to the randomness of superparticles. Katoh and Omura (2016) have shown the generation of rising-tone chorus emissions with the real parameters in the inner magnetosphere. Ke et al. (2017) have conducted two-dimensional simulations of rising-tone chorus emissions, showing the oblique propagation of chorus waves. Wu et al. (2020) have reported the generation of rising-tone and falling-tone emissions in a homogeneous background magnetic field. Recently, Wu et al. (2022) have conducted numerical simulations with the inverted parabolic magnetic fields and observed falling-tone emissions. H. Chen, Lu, et al. (2022) have reproduced hooked chorus waves with δf PIC simulations. Fujiwara et al. (2023) have shown the formation of rising-tone and falling-tone emissions and conducted numerical analyses of the generation of an electron hole, an electron hill, and resonant currents with the inhomogeneous ambient magnetic field.

1.7 Objectives and structure of the dissertation

The generation processes of rising-tone and falling-tone emissions have been discussed over several decades, while the generation-triggered emissions in the early phase have not been clearly understood. Chorus waves are generated in the vicinity of the magnetic equator (LeDocq et al., 1998). The main process of the chorus wave generation is controlled by nonlinear wave-particle interactions growing from the seed waves with coherent waves generated by temperature anisotropy (Hikishima et al., 2009b). For obtaining long rising-tone emissions, we use the monochromatic triggering waves as the seed waves. The triggered emissions as the study of chorus waves are advantageous because we can eliminate electromagnetic wave components in the simulation with the given frequency of triggering wave frequency by signal processing on raw waveform data. The feature is powerful for the analyses of the early phase of the generation of rising-tone and falling-tone emissions.

The transition phase from linear to nonlinear wave growth is not clear. During the generation of rising-tone emissions, the wave generation region of triggered emissions shifts in space. The wave generation region of triggered waves shifts to the downstream region of triggering wave source (Katoh & Omura, 2006), while the other sets of the simulation parameters lead to the upstream shifts of the generation region shifts with the full-particle code (Hikishima et al., 2010). The shifts of the wave generation region are not obvious in the studies of chorus emissions (Katoh & Omura, 2007; Hikishima et al., 2009b, 2010). For the investigation of the characteristics in the wave generation, we also use the monochromatic triggering waves as the seed waves.

The formation process of the subpacket structure remains unclear. (Shoji & Omura, 2013) have studied the generation models of subpacket structure of ElectroMagnetic Ion cyclotron (EMIC) waves by the repeating processes of phase space modulation and the formation of resonant current, shifting the generation region upstream. Hanzelka et al. (2020) have proposed a generation model of subpacket structure for chorus waves, which is also based on the repeating processes of phase space modulation and the formation of resonant current. By comparing the characteristics of subpackets with different duration, we investigate the characteristics of the subpacket structures.

The generation process of falling-tone triggered emissions is shown in terms of the formation of resonant currents. Falling-tone emissions have not been reproduced by the self-consistent simulation except for Nunn and Omura (2012) with the quasi-broadband method. In the present studies, continuous waves are injected into the simulation system, leading to the generation of rising-tone emissions. Ground observations that shorted triggering waves generate triggered emissions with falling frequencies Helliwell and Katsufrakis (1974), we set the duration time of triggering waves as short. Resonant current and inhomogeneous factors are calculated, and the nonlinear characteristics of falling-tone emissions are shown.

Throughout the study, we reproduce rising-tone and falling-tone triggered emissions with self-consistent particle simulations. The structure of the dissertation is as follows.

- **Chapter 2: Numerical simulation of triggered emissions**
  In this chapter, simulation methods and simulation models in the study are described. We use electromagnetic particle simulation in the study. The concept of the particle-in-cell method is described. Subsequently, a one-dimensional parabolic model of the geomagnetic field is shown. We have modified the Buneman-Boris method for the conservation

of $\nabla \cdot \boldsymbol{B} = 0$ in the cyclotron motion in the parabolic magnetic field. The generation algorithm of the particle distribution in a one-dimensional model is shown. Assuming the conservation of energy and adiabatic invariants during the mirror motion in the parabolic magnetic field, we distribute energetic electrons uniformly in the oscillation phase. The separation of forward and backward waves is shown. By using spatial helicity of whistler-mode waves, forward waves and backward waves are separated with the Discreate Fourier Transformation (DFT) with respect to space. Calculations of resonant current and phase space distribution are described.

- **Chapter 3: Nonlinear signatures of rising-tone emissions**
  In this chapter, nonlinear characteristics of whistler-mode rising-tone emissions are discussed. Rising-tone elements with multiple subpackets with monotonically increasing frequencies are generated from the triggering wave. The long rising-tone subpacket is modulated with increasing magnitude, splitting into smaller subpackets through propagation. The amplitude modulations in the subpacket are generated by the oscillation of trapping electrons at the equatorial region or the enhancement of amplitude variations through propagation in the downstream region.

- **Chapter 4: Upstream shift of generation region of rising-tone emissions**
  In this chapter, we discuss the upstream shift of wave generation region of rising-tone emissions, observed in Chapter 3. We have found that the velocity of the wave generation region depends on the duration of the subpacket, which is controlled by the formation of the resonant current. The formation process of the subpacket structure and associating velocity difference for the upstream shift of wave generation region is discussed. Below one-quarter of the cyclotron frequency, the coalescence of subpackets takes place, suppressing the formation of the resonant current in the generation region. Since a gradual upstream shift of the generation region is necessary for the wave to grow locally, the source velocity should be a small negative value.

- **Chapter 5: Generation process of falling-tone emissions**
  In this chapter, we discuss the generation process of whistler-mode falling-tone emissions. The short whistler mode waves with a large amplitude are excited and propagate poleward from an artificial current oscillating with a constant frequency and amplitude. Following the excited waves, clear emissions are triggered with a falling frequency. The falling tone has several subpackets of amplitude and decreases the frequency in a stepwise manner. The positive resonant current formed by resonant electrons in the direction of the wave magnetic field clearly shows that an electron hill is formed in the phase space and causes the frequency decrease. Each wavefront of the emission has a strongly negative resonant current $-J_E$, which results in wave growth. In the formation process of the resonant

currents, we investigate the inhomogeneous factor S, which controls the nonlinear motion of the resonant electrons interacting with waves.

- **Chapter 6: Summary**
  In this chapter, we present a summary of the study and describe future prospects beyond the study.

Chapter 2

Numerical simulation of triggered emissions

2.1 Particle-in-cell simulation

In the present study, particle-in-cell simulation is used for analyses of whistler-mode triggered emissions. This chapter describes simulation methods, initial conditions for particles, and the analysis tools for nonlinear wave-particle interactions.

We use Kyoto university electromagnetic plasma code (KEMPO) (Omura & Matsumoto, 1993; Omura, 2007) with modifications. The concept of the particle-in-cell simulation for plasma is shown in Figure 2.1.

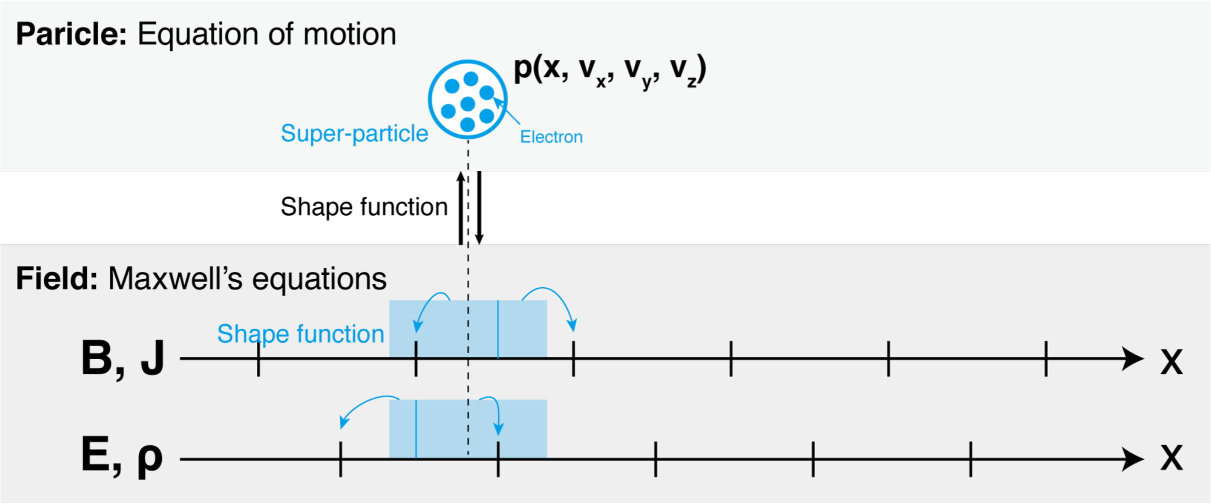

Figure 2.1: Schematic illustration of one-dimensional Particle-in-cell (PIC) simulation. Equation of motion and Maxwell's equations are solved self-consistently by using the shape function.

Electromagnetic and electrostatic components of plasma are given in the Eulerian grid and solved by using Finite Difference Time Domain (FDTD) method.

$$\begin{aligned} \nabla \times \boldsymbol{E} &= -\frac{\partial \boldsymbol{B}}{\partial t}, & (2.1)\\ \nabla \times \boldsymbol{B} &= \mu_0 \boldsymbol{J} + \frac{1}{c^2}\frac{\partial \boldsymbol{E}}{\partial t}, & (2.2)\\ \nabla \cdot \boldsymbol{B} &= 0, & (2.3)\\ \nabla \cdot \boldsymbol{E} &= \frac{\rho}{\varepsilon_0}. & (2.4) \end{aligned}$$

Electric fields and magnetic fields in a simulation system are defined at a staggered grid with the FDTD method (Yee, 1966). By taking a first-order difference with respect to time and space, the discretized Maxwell's equations (2.1) and (2.2) for numerical simulation are obtained.

The motion of charged particles in fully-ionized collisionless plasma is given by the equation of motion as

$$m_0 \frac{\mathrm{d}(\gamma \boldsymbol{v})}{\mathrm{d}t} = q(\boldsymbol{E} + \boldsymbol{v} \times \boldsymbol{B}), \tag{2.5}$$

where m_0 and q are the rest mass of a superparticle and the electron charge of the superparticle, respectively. γ is Lorlentz factor given by $\gamma = 1/\sqrt{1-(v/c)^2}$.

A cluster of electrons in plasma is treated as a superparticle in PIC simulation. The motion of superparticles is given with Lagrangian variables and solved by the Buneman-Boris method (Boris & Shanny, 1970).

The simulation requires boundary conditions for both particles and electromagnetic fields. Energetic particles are reflected at the edge of the simulation box, conserving the adiabatic momentum and randomizing the gyration phase. For electromagnetic fields, we couple the periodic condition and the absorbing boundary condition developed by Umeda et al. (2001). The first and last arrays of the grid are treated with periodic conditions, and the damping region suppresses the amplitude and retards the phase of the outgoing waves.

2.2 One-dimensional model of geomagnetic field

We set the x-axis along the field line. Near the magnetic equator, the x-component of the dipole magnetic field $B_0(x)$ is approximated by parabolic variation as

$$B_0(x) = B_{\mathrm{eq}}(1 + ax^2)\,, \tag{2.6}$$

where x is the distance along the field line from the equator, and B_{eq} and a are the equatorial magnitude of the background magnetic field and the coefficient of the parabolic variations of the background magnetic field, respectively.

The radial components of the magnetic field B_r must be taken into account for the condition $\nabla \cdot \boldsymbol{B} = 0$. The radial magnetic field B_r is given by

$$B_r = -\frac{\rho_c}{2}\frac{\partial B_0(x)}{\partial x}\,, \tag{2.7}$$

where ρ_c is the cyclotron radius of an electron.

Substituting $B_0(x)$ in equation (2.6) with equation (2.7), we have the vectors of the radial magnetic field for an individual superparticle by

$$\boldsymbol{B_r} = \frac{m\gamma(\boldsymbol{v}_\perp \times \mathbf{e_x})ax}{q(1+ax^2)} , \tag{2.8}$$

where $\mathbf{e_x}$ and $\boldsymbol{v}_\perp$ are the unit vector parallel to the ambient magnetic field and perpendicular velocity, respectively.

The radial component of the background magnetic field is dependent on the perpendicular velocity of an electron, while half time step difference exists between the temporal grid of the magnetic field and that of electron velocity. In order to obtain electron velocity at the same timing as the magnetic field, we modify the Buneman-Boris solver as follows. The radial magnetic field is given from the particle velocity as equation (2.7). The calculated radial background magnetic fields $\boldsymbol{B_r}$ are added to the wave magnetic fields, and the velocity of the particle is calculated by the normal Buneman-Boris method. The algorithm in the study is described in Appendix A.

2.3 Generation method of initial particle distribution with one-dimensional model

The model consists of three species of particles, cold electrons, cold protons, and energetic electrons. Thermal electrons and protons have a bi-Maxwellian distribution, while energetic electrons have a subtracted-Maxwellian distribution. For a marginally stable condition in the region, we define the initial velocity distribution of energetic electrons as follows.

Using the relativistic momentum $u_\parallel = \gamma v_\parallel$ and $u_\perp = \gamma v_\perp$ (the parallel and perpendicular components to the background magnetic field), we define the velocity distribution function of energetic electrons at the equator f_{eq} as

$$f_{eq}(u_\parallel, u_\perp) = C_N \exp\left\{-\frac{u_\parallel^2}{2 < u_\parallel >^2}\right\} g_{eq}(u_\perp)\ H(\arctan(\frac{|u_\perp|}{|u_\parallel|}) - \alpha_{\text{loss}}) , \tag{2.9}$$

$$g_{eq}(u_{\perp,eq}) = \frac{1}{1-\beta}\left\{\exp(-\frac{u_{\perp,eq}^2}{2u_{\perp,T}^2}) - \exp(-\frac{u_{\perp,eq}^2}{2\beta u_{\perp,T}^2})\right\} , \tag{2.10}$$

where C_N is a normalization coefficient for the distribution function, $H(x)$ is a Heviside step function, α_{loss} is a losscone angle, β is a subtraction ratio. The Heaviside function is used to eliminate electrons in the loss cone completely. Each superparticle is distributed from the magnetic equator to the mirror point with the conservation of magnetic momentum and kinetic energy, transported from the velocity distribution function at the equator. Charged particles travel with harmonic bounce oscillations along the parabolic magnetic field. The position x and the momentum in the off-equatorial region $(u_{\parallel}, u_{\perp})$ are given from the uniformly distributed phase ϕ as

$$\begin{aligned} x &= x_m \cos\phi \quad (0 \le \phi < 2\pi), && (2.11)\\ u_{\perp} &= u_{\mathrm{eq}.\perp}\sqrt{1+ax^2}, && (2.12)\\ u_{\parallel} &= u_{\mathrm{eq}.\parallel}\sqrt{1-ax^2}, && (2.13) \end{aligned}$$

where x_m is the distance from the magnetic equator to the magnetic mirror point. The initial particle distribution generation algorithm for energetic electrons is described in Appendix B.

2.4 Separation of forward and backward waves

In the present study, we define forward waves as the whistler-mode waves propagating to positive x, and backward waves as the whistler-mode waves propagating toward the negative direction, respectively. The wave separation of the direction of whistler-mode waves is important in the precise definition of wave phase for cyclotron resonance. We separate forward and backward waves by the spatial helicity of whistler-mode waves. The transverse components of whistler-mode waves B_y and B_z propagating in forward and backward direction with frequency ω and wave number k is given by

$$\begin{aligned} B_y &= B_f \mathrm{e}^{-\mathrm{i}(\omega t - kx + \frac{\pi}{2})} + B_b \mathrm{e}^{\mathrm{i}(\omega t + kx + \frac{\pi}{2})}, && (2.14)\\ B_z &= B_f \mathrm{e}^{-\mathrm{i}(\omega t - kx)} + B_b \mathrm{e}^{\mathrm{i}(\omega t + kx)}, && (2.15) \end{aligned}$$

where B_f and B_b are amplitudes for forward and backward waves with frequencyω and wave number k, respectively. By applying Fourier transformation with respect to x, we obtain equations of amplitude $\overline{B_{zk}}$ and $\overline{B_{zk}}$ with respect to wave number given by

$$\begin{aligned} \overline{B_{zk}} &= B_f \mathrm{e}^{-\mathrm{i}\omega t} + B_b \mathrm{e}^{\mathrm{i}\omega t}, && (2.16)\\ \overline{B_{yk}} &= -\mathrm{i}B_f \mathrm{e}^{-\mathrm{i}\omega t} + \mathrm{i}B_b \mathrm{e}^{\mathrm{i}\omega t}. && (2.17) \end{aligned}$$

By setting $t = 0$, and solving the equations for B_f and B_b, we obtain equations for amplitudes of forward and backward waves by

$$\begin{aligned} B_f &= \frac{1}{2}(\mathrm{i}\overline{B_{yk}} + \overline{B_{zk}}), && (2.18)\\ B_b &= \frac{1}{2}(-\mathrm{i}\overline{B_{yk}} + \overline{B_{zk}}). && (2.19) \end{aligned}$$

For the expansion to the whistler-mode waves with multiple frequencies, we substitute amplitude B_f and B_b with the wave amplitudes with respect to wave number k, $\overline{B_{fk}}$ and $\overline{B_{yk}}$ in equations (2.18) and (2.19). By taking inverse Fourier transformation on $\overline{B_{fk}}$ and $\overline{B_{yk}}$ with respect to k, we obtain waveform of forward and backward waves for whistler-mode waves.

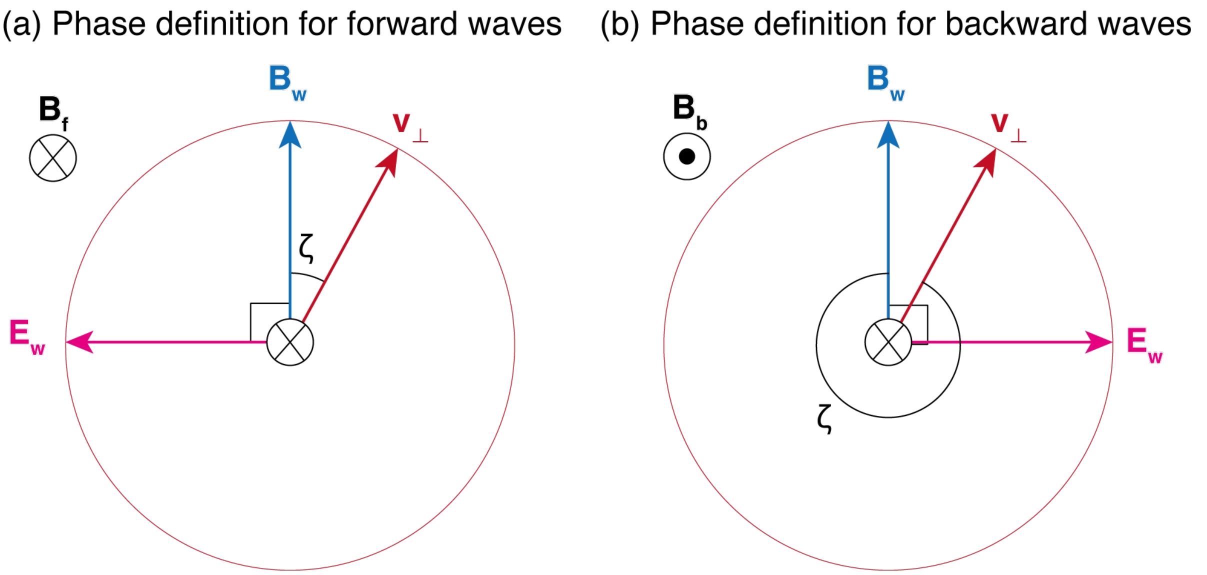

Figure 2.2: Definition of the phase difference between wave magnetic field and perpendicular velocity component of resonant electron for (a)forward (b) backward propagating waves.

Because the method is time-independent, the spatial distribution of wave components at a given time step is required, while a temporal variation of the waveform is not required. This contributes to avoiding post-processing for the calculation of resonant currents and phase space distribution by conducting wave separation during the simulation.

2.5 Calculation of resonant current and phase space distribution

We calculate the resonant current for forward waves and backward waves, which are calculated in the previous section. Resonant currents for each super particle of energetic electrons, which interact with forward waves, are given by

$$\boldsymbol{J_e} = \Sigma e \boldsymbol{v}_\perp \boldsymbol{E_f} / \Delta x, \tag{2.20}$$

$$\boldsymbol{J_b} = \Sigma e \boldsymbol{v}_\perp \boldsymbol{B_f} / \Delta x. \tag{2.21}$$

By integrating resonant current for superparticles for energetic electrons and assigning to the grid with linear shape function, we obtain resonant currents J_E and J_E in the grid.

We calculate phase space distribution for forward and backward propagating waves calculated in Section 2.4 with energetic electrons. Figure 2.2 shows the definition of phase angle ζ for forward and backward traveling waves.

Phase angle calculated from dot product and cross product of perpendicular velocity $\boldsymbol{v}_\perp$ and magnetic field $\boldsymbol{B_{wf}}$ or $\boldsymbol{B_{wb}}$. Parallel velocity and resonance velocity are used for the calculation of phase space density, which is dependent on pitch angle. The resonance velocity $V_R(\omega, v_\perp)$

is given by

$$V_R(\omega, v_\perp) = \frac{\omega^2 - \sqrt{\omega^4 + (\omega^2 + V_p^2)(1 - \omega^2 - v_\perp^2)}}{\omega^2 + V_p^2} V_p \,, \tag{2.22}$$

where V_p is the phase velocity. We count the number of energetic electrons with the same $\Delta V_\parallel$ and with different $v_\perp$ by projecting a parallel velocity $v_\parallel$ to $v_{\parallel 0}$ with $v_\perp = 0$ along the resonance velocity curve as defined by the following equation:

$$v_{\parallel 0} = V_R(\omega, 0) + v_\parallel - V_R(\omega, v_\perp) \,, \tag{2.23}$$

where we assume ω as the fixed wave frequency of triggering waves.

Chapter 3

Nonlinear signatures of rising-tone emissions

3.1 Introduction

Whistler-mode chorus emissions with rising-tone and falling-tone frequencies have been studied for more than half a century. Chorus emissions are often observed outside the plasmapause in conjunction with magnetospheric substorms (Tsurutani & Smith, 1974). Chorus emissions are essentially nonlinear phenomena induced by finite amplitude waves as evidenced by the triggered emissions from the VLF transmitters, which exhibit the same frequency spectra with varying frequencies (see a review by Omura et al. (1991); Gołkowski et al. (2019)). Recently, Demonstration and science experiments (DSX) (Scherbarth et al., 2009) was conducted for the study of whistler-mode wave-particle interactions. They injected whistler-mode wave to trigger new emissions in the magnetosphere. Propagation characteristics of the DSX waves have been studied base on ray-tracing (Reid et al., 2022). Chorus is an emission triggered by a naturally growing wave at a fixed frequency as predicted by linear growth rates (Kennel & Petschek, 1966). From the electromagnetic thermal fluctuations, a wave with the maximum linear growth rate grows to the largest amplitude, and it suppresses growth of other waves with frequencies close to its frequency through scattering of resonant electrons. The wave becomes coherent and works as a triggering wave we assume in the present study. Under a finite amplitude coherent wave, resonant electrons undergo nonlinear motion, and form either an electron hole or a hill, inducing resonant currents. The resonant currents cause variation of the wave amplitude and frequency as described by the wave equations (Nunn, 1974; Vomvoridis et al., 1982; Omura et al., 1991, 2008). A wave with a frequency different from that of the triggering wave is generated as a wave packet independent from the triggering wave. The evolution of the newly generated wave packet has not been understood completely. It has been reported that series of short wave packets are generated sequentially, forming rising and/or falling tone emissions. Each wave packet is called a subpacket of chorus elements (Santolík et al., 2014; Foster et al., 2017).

Subpacket structures of chorus waves have great importance on electron acceleration and pitch angle scattering. A simulation study has shown that efficient electron acceleration takes place by a finite packet via nonlinear electron trapping (Hiraga & Omura, 2020). Electron precipitations to the ionosphere due to chorus waves are observed by simultaneous observations between satellite and ground, which show the agreement with the pulsating aurora and each of chorus emissions with subpacket structure (Kasahara et al., 2018; Ozaki et al., 2018). A particle simulation of triggered emission (Hikishima et al., 2010) also showed each triggered chorus element has subpacket structure and the electron flux is strongly modulated by the subpackets.

The subpacket structure is also found in electromagnetic ion cyclotron (EMIC) rising-tone emissions (Nakamura et al., 2014). A model of the generation process of EMIC emissions is proposed by Shoji and Omura (2013). Based on the nonlinear wave growth process as an absolute instability and the convection of the wave packets as described by the wave equations, the fine characteristics of amplitude and frequency variations of a series of chorus subpackets are studied by Hanzelka et al. (2020). Each subpacket grows with increasing frequency because of the formation of nonlinear currents. However, it is not clear how the information of frequency of one subpacket is transferred to the next subpacket. By injecting a triggering wave with a fixed frequency, we study the formation process of subpacket structure by self-consistent particle simulations.

Tsurutani et al. (2020) have shown that the frequenency of subpacket structure is monochromatic except for the edges of the subpackets. Zhang et al. (2020) have shown that the frequency sweep rates of wave packets are dependent on lengths of wave packets. Helliwell (1967) proposed that the frequency sweep rates are determined by the nonuniform ambient magnetic field. More recently, Tao et al. (2021) refined Helliwell's model as the Trap-Release-Amplify (TaRA) model, in which the frequency sweep rate at the initial phase of chorus emissions is determined by the gradient of the background magnetic field. Since our recent particle simulations (Nogi et al., 2020) show results different from the TaRA model, it is still necessary to study the generation process of chorus emissions quantitatively by simulations to clarify the difference between these models and identify the essential physics of chorus wave generation.

In this paper, we clarify the generation process of self-sustaining emissions from the triggering wave artificially injected with a fixed frequency. In section 3.2, we describe the model of the simulation and parameters. In section 3.3, we present various analyses of the simulation results to clarify the nonlinear processes reproducing rising-tone elements successfully. Section 3.4 gives a summary and discussion.

3.2 Simulation model

We use a one-dimensional particle-in-cell code with a parabolic background magnetic field (Nogi et al., 2020). We solve particle dynamics in the cylindrical geometry formed by the parabolic magnetic field, which is approximated from the magnetic field of the Earth's dipole magnetic field near the equator. We assume that transverse electromagnetic waves propagate purely parallel to the static field, and we neglect the longitudinal electrostatic field, which is independent from the whistler-mode wave in parallel propagation. Prior to the present simulation runs, we also conducted simulations with the electrostatic field, solving Poisson's equation except for the initial thermal fluctuations. We find the generation of triggered emissions with enhanced electrostatic thermal fluctuations (Nogi et al., 2020). In the present simulation, we do not solve the electrostatic field E_x along the magnetic field in order to avoid diffusion by enhanced electrostatic fluctuations due to a limited number of superparticles in the grid spacing.

Table 3.1: Simulation parameters

parameters	Value
Time step	$0.0078125\Omega_e$
Grid spacing	$0.01\, c\Omega_e^{-1}$
Number of grids	32,768
Length of simulation region	$327.68\, c\Omega_e^{-1}$
Total number of cold electrons	1,073,741,824
Total number of energetic electrons	1,073,741,824
Plasma frequency of cold electrons ω_{pe}	$4.0\,\Omega_e$
Density ratio of energetic electrons to cold electrons n_h/n_c	0.01
Thermal momenta of cold electrons $v_{c\parallel}, v_{c\perp}$	$0.01\,c, 0.01\,c$
Thermal momenta of energetic electrons at equator $v_{h\parallel}, v_{h\perp}$	$0.25\,c, 0.30\,c$
Amplitude of triggering wave	$6.0 \times 10^{-4} B_{\mathrm{eq}}$, 0
Number of grids for damping region	2,048
Length of damping region	$20.48 c\Omega_e^{-1}$
Coefficient for parabolic magnetic field, a	$5.0 \times 10^{-6}\, c^2\Omega_e^{-2}$

We describe the simulation parameters for two simulation runs we conducted in the present study. Our simulation study basically follows the previous study by (Hikishima et al., 2010). We have changed parameters to observe the detailed process of rising-tone triggered emissions with higher resolutions and new diagnostics. The time step Δt and the grid spacing Δx are chosen to satisfy the Courant condition: $\Delta x/\Delta t = 1.28 > c$. We used a large number of superparticles for both cold and hot electrons. The averaged numbers of superparticles for the cold and hot electrons are 32,768 and 32,768 per grid, respectively, ensuring the low electromagnetic thermal fluctuation level. The physical density ratio of the hot and cold electrons $n_h/n_c = 0.01$. The ratio of the cold plasma frequency to the electron cyclotron frequency is $\omega_{pe}/\Omega_e = 4$, which is typical in the inner magnetosphere outside the plasmapause. The ions are assumed as an immobile neutralizing background. The hot electrons are initialized to form a subtracted-Maxwellian momentum distribution at the equator, and they are distributed nonuniformly in space based on the scheme described by Nogi et al. (2020).

The simulation system consists of 32,768 grid points with an equal spacing Δx, out of which

4,096 (2,048 left, 2,048 right) grids are used for the absorbing boundary (Umeda et al., 2001) for outgoing electromagnetic waves. Hot electrons going out from the boundaries are reflected back into the system with equal energies and pitch angles with randomized gyro-phases.

To inject a right-handed poralized wave, we oscillate external currents J_y and J_z at the magnetic equator. Chorus emissions are generated in the vicinity of the equator because the linear growth rate is maximized by the maximum flux of resonant electrons. The target of our research is to study the generation process of chorus emissions. Since chorus emissions are sequences of triggered emissions, it is appropriate to assume the triggering wave source at the equator for the study of chorus emissions. The external current J_y and J_z are defined as sinusoidal functions as,

$$J_y(t) = J_{\text{ext}}(t)\cos\omega t \tag{3.1}$$

$$J_z(t) = J_{\text{ext}}(t)\sin\omega t, \tag{3.2}$$

where ω is a frequency below the electron cyclotron frequency Ω_e at the equator. The external currents form an electromagnetic field with right-handed polarization. To suppress the excitation of high frequency electromagnetic R-mode waves, we change the magnitude of the currents J_{ext} gradually at the beginning of the triggering pulse as

$$J_{\text{ext}}(t) = \frac{J_0}{2}\left[\tanh\left(\frac{t-t_b}{T_J}\right)+1\right], \tag{3.3}$$

where J_0, T_J, and t_b are the amplitude of the external current, the duration for the increase of the amplitude, and the timing of the beginning of triggering pulse, respectively. The amplitude J_0 is specified so that the injected wave amplitude is $6.0\times10^{-4}B_{\text{eq}}$, where B_{eq} is the magnitude of the background magnetic field at the magnetic equator. We set $T_J = 64.1\Omega_e^{-1}$, and $t_b = 64\Omega_e^{-1}$. With these circularly polarized external currents, only whistler-mode waves are excited.

With the parameters given in Table 3.1, we calculate the linear growth rate to find the frequency of the most unstable whistler-mode wave. In Figure 3.1, we have plotted the linear growth rates computed by the linear dispersion solver KUPDAP (Sugiyama et al., 2015). The linear growth rate takes positive values in the range $0.07 - 0.46\Omega_e$ with the maximum value at $0.22\,\Omega_e$. We inject a triggering wave with a fixed frequency $0.3\,\Omega_e$. The amplitude of the triggering wave has to be greater than the threshold wave amplitude for nonlinear wave growth (Omura et al., 2009; Omura, 2021), and the wave growth saturates around the optimum wave amplitude(Omura & Nunn, 2011; Omura, 2021). The distribution of resonant particles in phase space $g(u_\parallel,\zeta)$, which generates resonant currents, is defined as

$$g(u_\parallel,\zeta) = g_0(u_\parallel) - Qg_t(u_\parallel,\zeta), \tag{3.4}$$

where g_0 is the initial unperturbed distribution function, g_t is a trapped particle distribution inside the separatrix of the trapping wave potential, and Q is the depth of the electron hole,

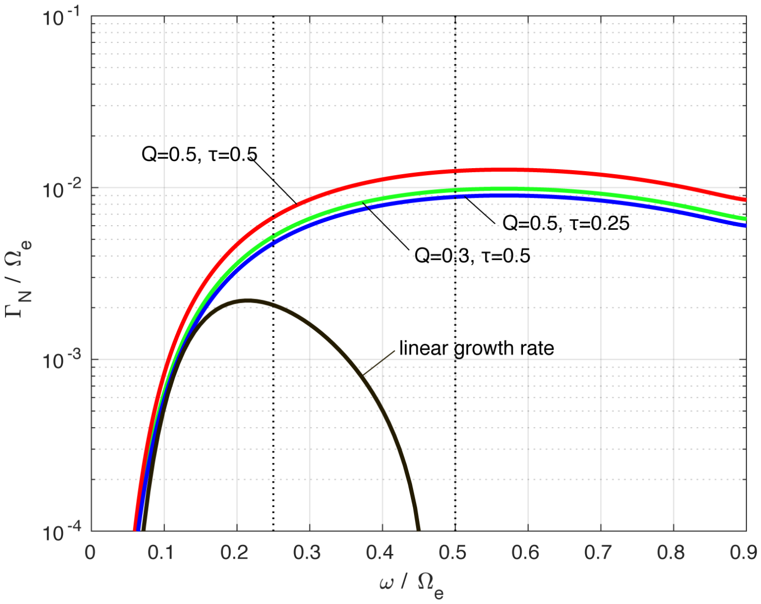

Figure 3.1: Linear growth rate and nonlinear growth rates (Omura, 2021) calculated from the simulation parameters.

respectively. The parameter τ is given by $\tau = T_N/T_{tr}$, where T_N is the nonlinear transition time necessary for the formation of resonant currents, and T_{tr} is the nonlinear trapping period. We plot the nonlinear growth rate for the optimum wave amplitudes for different values of Q and τ with red, green, and blue lines in Figure 3.1. We set J_0 that excites both forward and backward triggering waves with a wave amplitude $B_w/B_{\text{eq}} = 6.0 \times 10^{-4}$.

The linear growth rates of whistler-mode waves maximize at $0.22\,\Omega_e$. The linear growth rate for the frequency greater than $0.46\,\Omega_e$ is negative under the present simulation parameter. The frequency range of the positive linear growth rate is relatively narrow. While the linear growth rate is controlled by the temperature anisotropy and independent from the wave amplitude, the nonlinear growth rate depends on the wave amplitude. In Figure 3.1, we also plot the nonlinear growth rates for the threshold amplitude and the optimum amplitude. At the frequency of $0.35\Omega_e$, the nonlinear growth rate (Omura et al., 2009; Omura, 2021) is approximately one-order greater than the linear growth rate under the simulation parameter.

3.3 Results

3.3.1 Characteristics of rising-tone triggered emissions

We have performed two cases of simulation runs with and without the triggering wave. Figures 3.2a and 3.2b show the case with the triggering wave, and Figures 3.2c and 3.2d show the case without the triggering wave. We separated forward propagating waves and backward propagating waves by using the spatial helicities calculated from transverse wave components B_y and

B_z. We compare the two cases with and without the triggering wave with a constant frequency of $0.3\Omega_e$.

In the case with the triggering waves, large amplitude waves are triggered during $3000 - 6000\Omega_e^{-1}$ in the vicinity of the magnetic equator, forming subpackets shown in Figures 3.2a and 3.2b. The triggering wave induces the nonlinear wave growth process similar to rising-tone chorus emissions. The triggering points of the new waves shift to the upstream region from the original triggering waves.

In the case without the triggering wave, significant wave growth is not observed in Figures 3.2c and 3.2d. We find relatively small wave growth due to the linear growth rates. The wave amplitude near the equator is about 2.0×10^{-4}, which is smaller than the amplitude of the triggering wave 6.0×10^{-4}. The nonlinear wave growth does not take place without the triggering wave.

A wave growth rate is given by

$$\Gamma = \frac{V_g}{L_{12}} \log \frac{B_2}{B_1}, \tag{3.5}$$

where V_g, L_{12}, B_1, and B_2 are group velocity, the distance between points 1 and 2, and wave amplitudes at points 1 and 2 in Figure 3.2d, respectively. We calculate Γ for the wave packet in Figure 3.2d by setting $V_g = 0.143, L_{12} = 200, \log(B_2/B_1) = 2.30$, we find the linear growth rate is 1.6×10^{-3}, which is consistent to the maximum linear growth rate in Figure 3.1. Checking the case with the triggering wave, we find the triggered emissions are growing in amplitude within a short distance, indicating that the nonlinear growth rates are much greater than the linear growth rate as shown in Figure 3.1.

We analyze the wavenumbers and frequencies of the wave field B_z contained in the forward propagating waves shown in Figure 3.2b by discrete Fourier transform in space and time. We have plotted the spectra in Figure 3.3. The spectra are expanded in the direction of the wavenumbers because of the gradual variation of the electron cyclotron frequency in space. We have plotted the dispersion relation of whistler-mode waves obtained from KUPDAP with the cyclotron frequency at the equator ($x = 0$) and the off-equator ($x = 143.36\, c\Omega_e^{-1}$) plotted by dashed and solid white lines, respectively. We find that whistler-mode waves with frequencies $\omega = 0.15 - 0.75\Omega_e$ are excited. The spectra are much enhanced above $\omega = 0.3\Omega_e$, which is the frequency of the triggering wave. Waves below $0.3\Omega_e$ are due to the linear growth rate, and those above $0.3\Omega_e$ are due to the nonlinear growth rate. The bright horizontal lines from the wave numbers at the equator to those at the off-equator suggest that the excited waves at the equator propagate with fixed frequencies and the decreasing wave numbers due to the increasing cyclotron frequency in the simulation system.

To find the profile of the triggered waves in space and time, we eliminate the frequency components from $0.29\Omega_e$ to $0.31\Omega_e$ from the wave frequency spectra at each fixed position. By applying inverse discrete Fourier transform, we obtain the waveforms of triggered emissions,

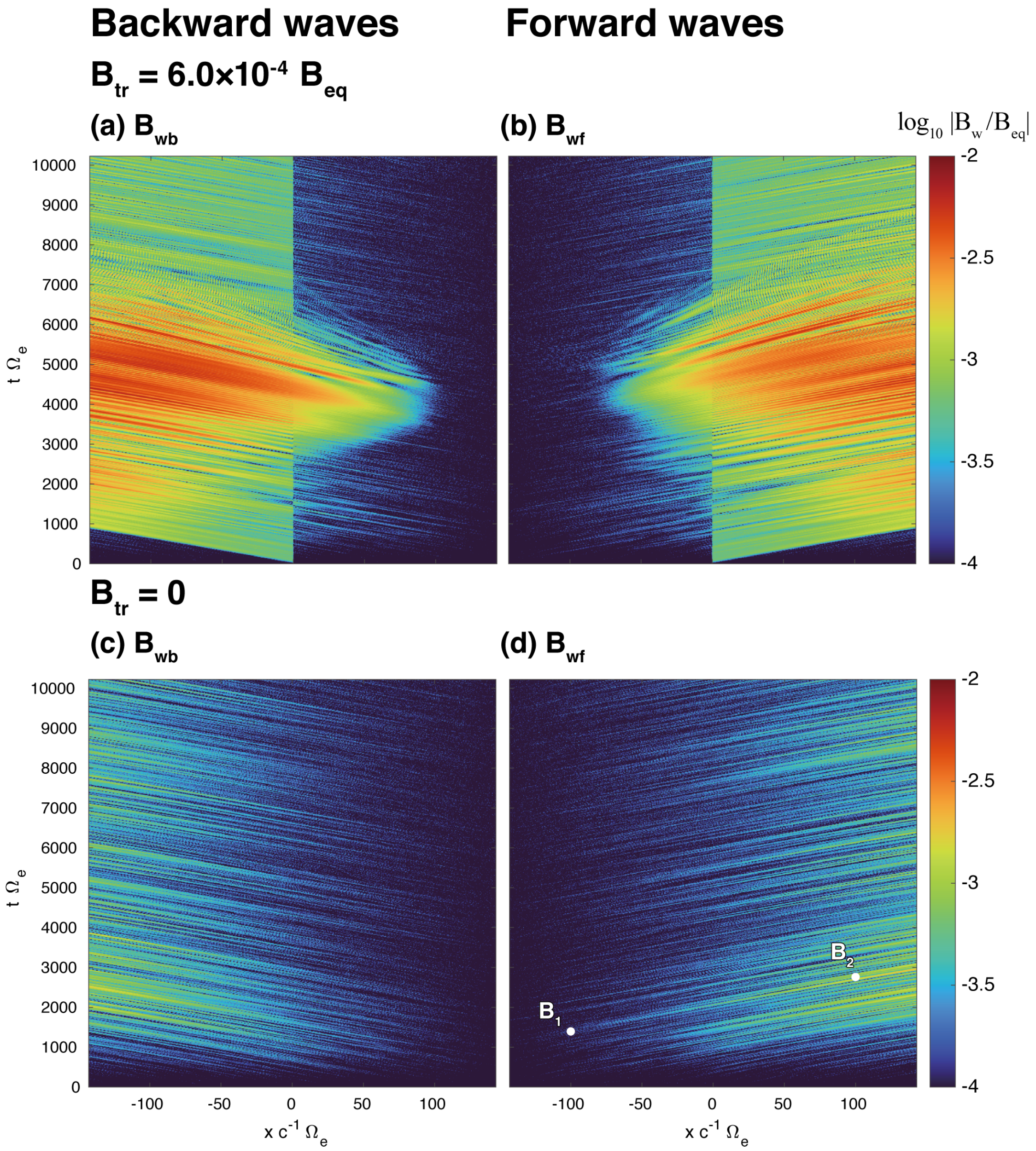

Figure 3.2: Spatial and temporal profiles of magnetic field amplitudes for forward and backward waves (a, b) with the triggering wave and (c, d) without the triggering wave.

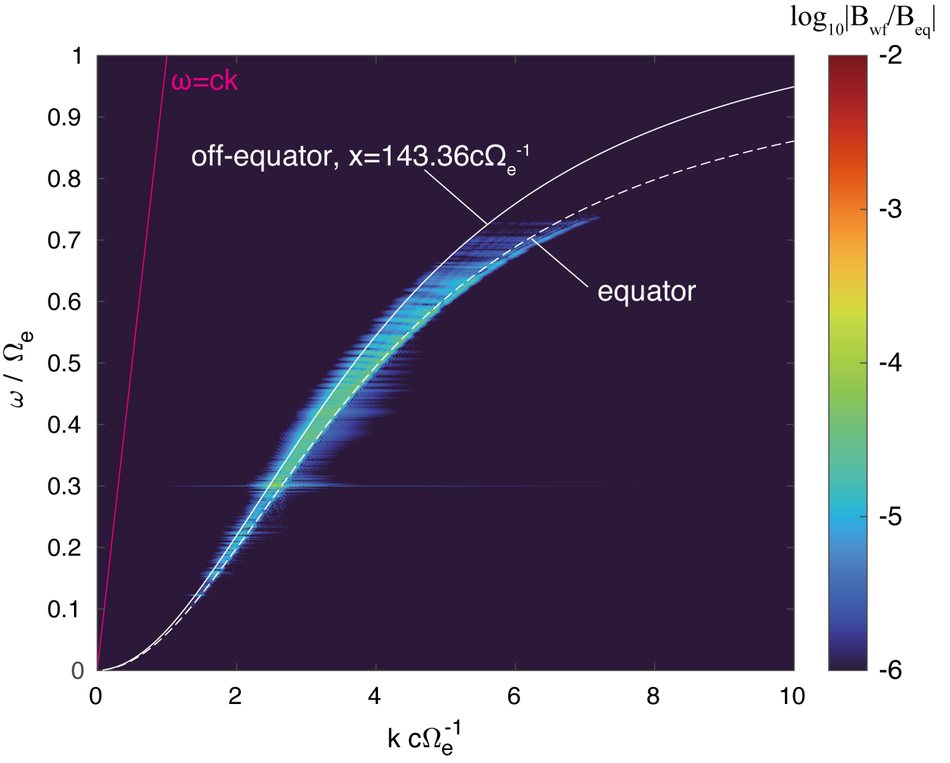

Figure 3.3: Dispersion relation of transverse magnetic field B_z in the simulation and linear dispersion relations at different positions, the equator and an off-equator $x = 143c\Omega_e^{-1}$.

and we have plotted them as a function of space and time in Figures 3.4a and 3.4b. We trace the time variation of the wave phase of the transverse fields B_y and B_z over $-\pi$ to $+\pi$ and obtain the wave period Δt, which give the instantaneous wave frequency $1/\Delta t$. In Figures 3.4c and 3.4d, we plot the instantaneous frequencies of waves with amplitudes greater than 6.0×10^{-4} of the equatorial ambient magnetic field.

In Figures 3.4a and 3.4b, we find stripes in the magnetic field amplitude profile, and the gradients of the stripes show the propagation of the subpackets. On the other hand, the contours of the instantaneous frequency in Figures 3.4c and 3.4d are continuous, showing a smooth gradual variation of frequencies. The color contour levels are approximately constant along the passage of wave propagation, which is consistent with the fact that the wave frequency does not change through propagation (Omura et al., 2009). As the frequency increases, the gradients of the stripes increase, showing smaller group velocities.

The generation region of triggered waves moves from the equator to the upstream region of the forward waves until the instantaneous wave frequency becomes approximately $0.5\,\Omega_e$. Subsequently, the generation point of triggered waves with the frequencies of the upper-band chorus moves downstream. The moving speed of the generation region is much smaller than the magnitude of the resonance velocity. This result does not agree with the hypothesis that counter-streaming particles traveling at resonant velocities generate triggered emissions.

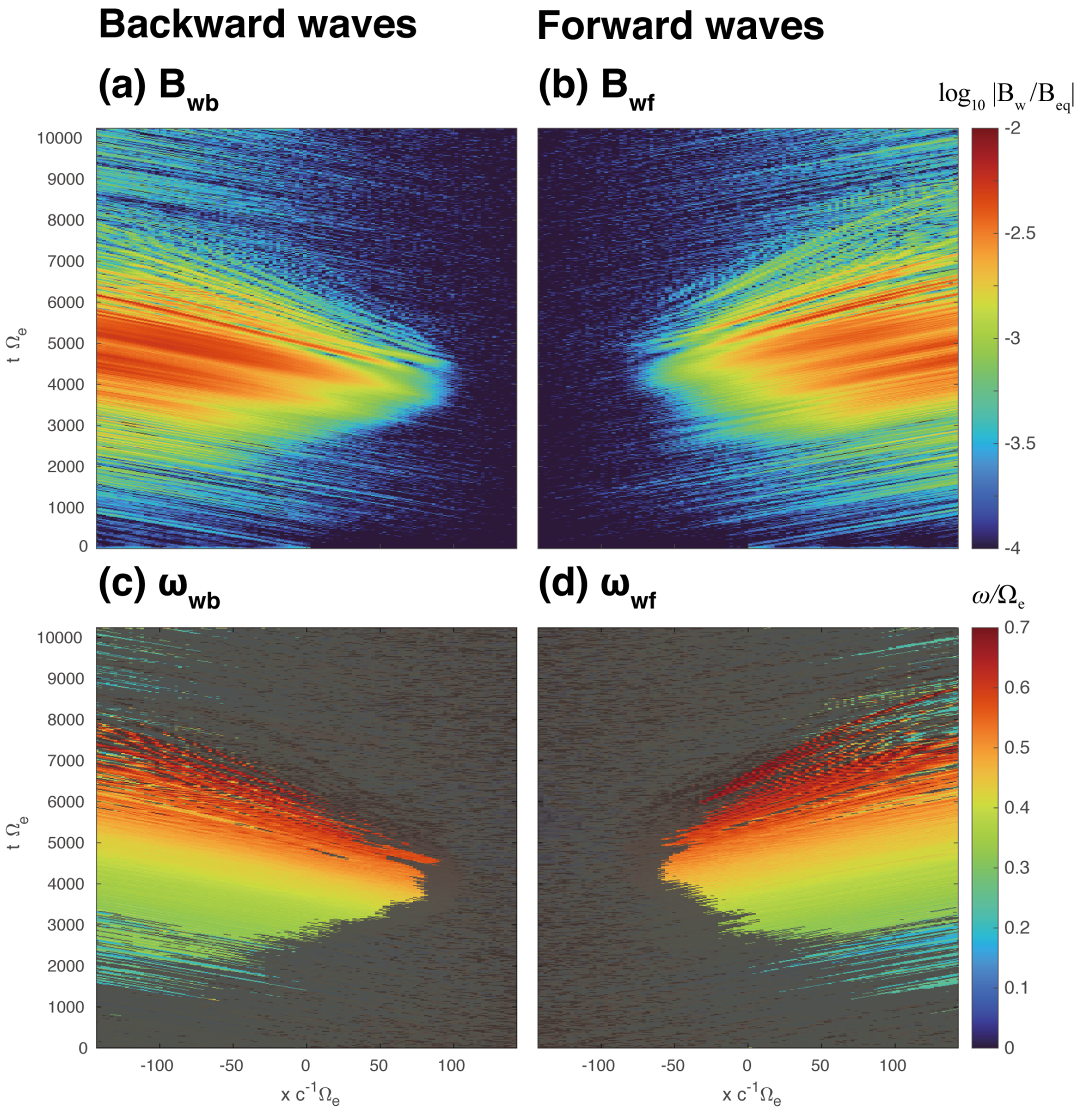

Figure 3.4: Spatial and temporal profiles of (a, b) wave amplitudes and (c, d) frequency of forward and backward propagating triggered emissions.

In Figure 3.5, we plot dynamic frequency spectra for forward and backward propagating waves with the two cases with and without triggering waves. Dynamic spectra are obtained by applying the short-time Fourier transform at five different positions ($x = -81.92$, -40.96, 2.56, 40.96, $81.92\,c\Omega_e^{-1}$). We set a window size for the short-time Fourier transform as 512 Ω_e^{-1} with 65,536 points, and shifting the window by 8,192 data points corresponding to a time resolution of $64\,\Omega_e^{-1}$. We find that clear rising-tone emissions from the frequency of $0.3\,\Omega_e$ to $0.75\,\Omega_e$ are triggered by the injected wave with a constant frequency of $0.3\,\Omega_e$ as shown in Figures 3.5a and 3.5b. We only find weak unstructured spectra grow with linear growth rates in the case without the triggering wave as shown in Figures 3.5c and 3.5d. It is noted that the seed of rising-tone emission is formed in the upstream region from the injection point of the forward

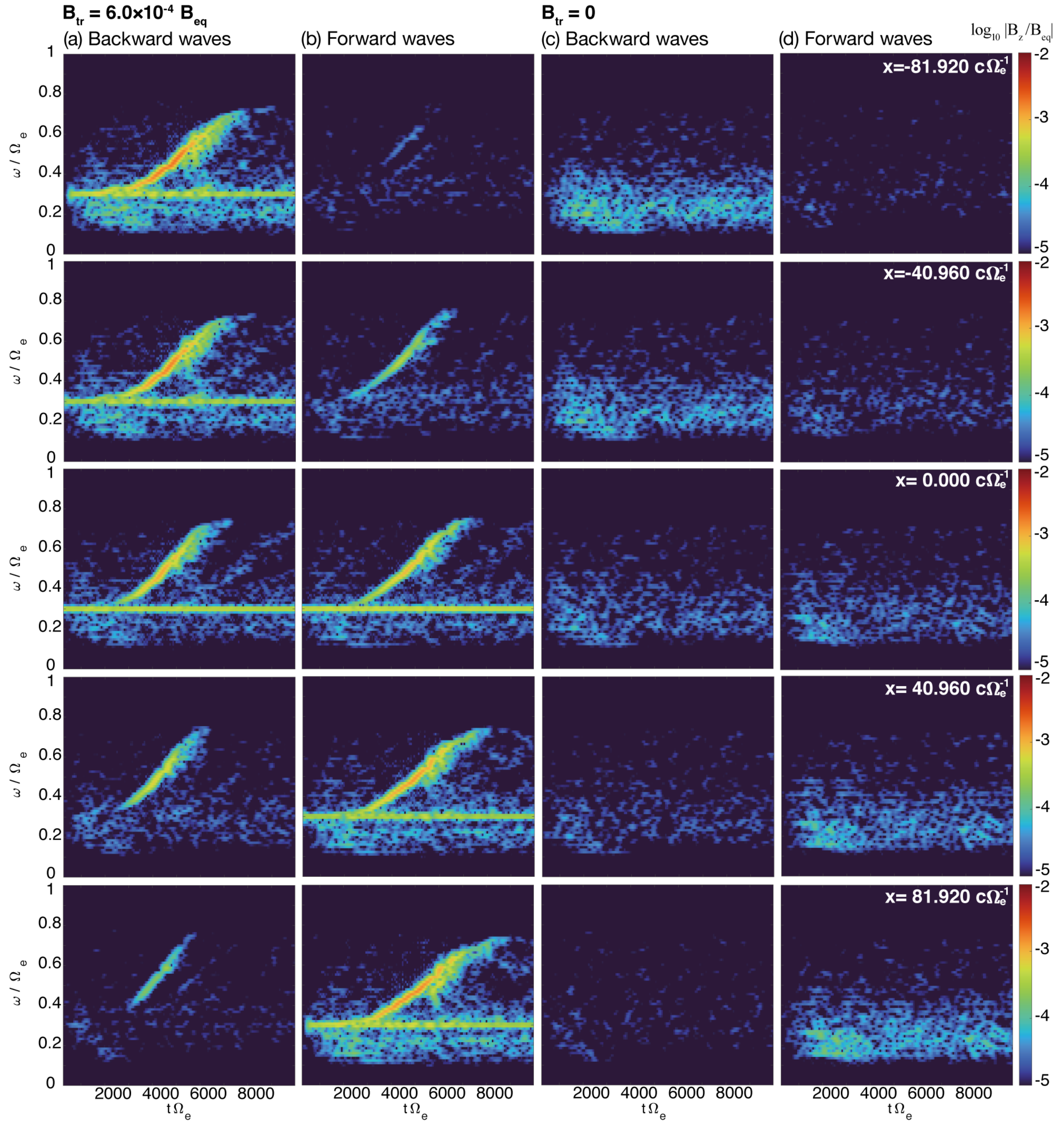

Figure 3.5: Dynamic spectra of magnetic fields of forward waves and backward waves (a, b) with the triggering wave and (c, d) without the triggering wave at different positions. (1) $x = -81.92\,c\Omega_e^{-1}$, (2) $x = -40.96\,c\Omega_e^{-1}$, (3) $x = 2.56\,c\Omega_e^{-1}$, (4) $x = 40.96\,c\Omega_e^{-1}$ and (5) $x = 81.92\,c\Omega_e^{-1}$.

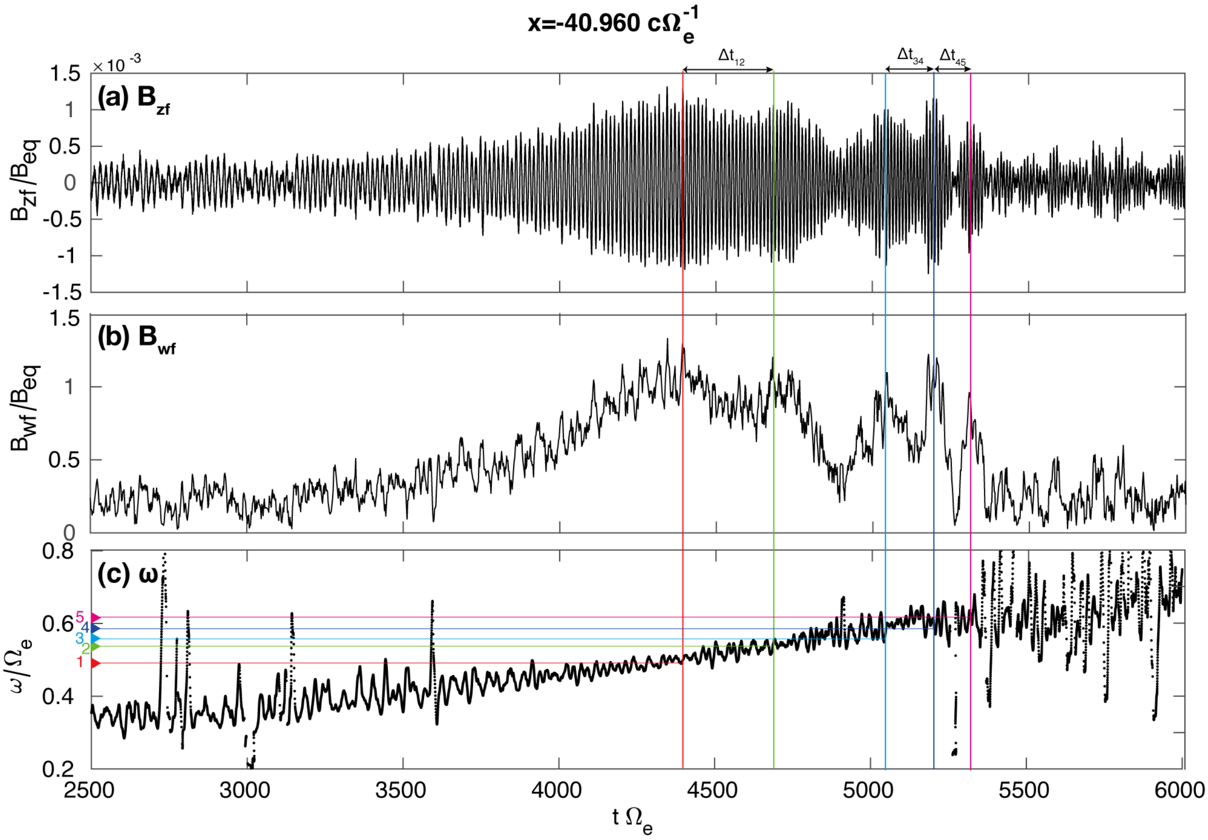

Figure 3.6: Time evolution of wave magnetic field in the upstream region of the triggering wave ($x = -40\,c\Omega_e^{-1}$): (a) forward waveform $B_{\rm zf}$ (b) amplitude of $B_{\rm wf} = \sqrt{B_{\rm yf}^2 + B_{\rm zf}^2}$ (c) instantaneous frequency. The colored lines indicate peaks of subpacket amplitudes with instantaneous frequencies, $\omega_1, \omega_2, \omega_3, \omega_4$, and ω_5, respectively.

propagating triggering waves as shown in the top two panels of Figure 3.5b. The seed wave is triggered by the energetic electrons organized in gyro-phase through the interaction with the triggering wave. Once the seed wave is generated, the rising-tone emission is gradually formed as a self-sustaining nonlinear process. The same process takes place for the waves propagating backward as shown in Figure 3.5a.

Figure 3.6 shows time histories of waveform B_z, amplitude B_w, and instantaneous frequency of the magnetic field observed at the upstream point of forward waves $x = -40\,c\Omega_e^{-1}$. We calculate the instantaneous frequency using the same method in Figures 3.4c and 3.4d. We observe subpacket structures during the triggered emissions. In the first subpacket, we find wave growth and monotonic increase of the instantaneous frequency during the period of $3800\,\Omega_e^{-1}$ to $4300\,\Omega_e^{-1}$. Throughout the emission, the nonlinear wave growth takes place as described by the chorus equations (Omura et al., 2009). Because of the thermal fluctuations contained in the waveform, the instantaneous frequency also fluctuates in time, while it shows a gradual increase of frequency. Once the wave growth of the first subpacket saturates, the wave amplitude undergoes relatively short damping and growth processes a few times. These oscillations evolve to distinct subpackets through propagation, as we find in Figure 3.7 showing the waveform, amplitude, and instantaneous frequency at the downstream point $x = 40.96\, c\Omega_e^{-1}$. To identify the subpacket evolution clearly, we eliminate the triggering waves from the waveforms as shown in Figures 3.7c and 3.7d, by applying discrete Fourier transform in time.

We choose 5 instantaneous frequencies corresponding to the 5 peaks in the wave amplitude in Figure 3.6b. Assuming that the frequencies of the wave packets do not change through propagation, we have indicated the 5 timings corresponding to the frequencies in Figure 3.7. The time intervals Δt_{12}, Δt_{34} and Δt_{45} denote those between ω_1 and ω_2, ω_3 and ω_4, and ω_4 and ω_5, respectively. Comparing the time intervals in Figure 3.6 and 3.7, we find that the time intervals of the packet become longer in the downstream of the waves. The increases of the durations, Δt_{34} and Δt_{45} are greater than that of the duration Δt_{12}. This is because the group velocities of whistler-mode waves decrease as the wave frequencies increase from $0.25\,\Omega_e$ to Ω_e. Because of the decreases of the group velocity, the convective growth rate increase in the higher frequencies, resulting in greater amplitudes for the subpackets with higher frequencies.

Comparing the time variation of the wave amplitudes in Figures 3.6b and 3.7d, we find that the wave amplitudes grow 5 times through propagation. The periods of each subpacket also increase through propagation because the group velocity decreases as the frequency increases from $0.3\,\Omega_e$ to $0.7\,\Omega_e$. Therefore, the subpacket structures are much enhanced in the downstream region.

As the wave frequency increases, the group velocity of the triggered wave decreases when the wave frequency is greater than $0.25\,\Omega_e$. In the monotonic increase of frequency, the time scale of waves is expanded due to the dispersion relation of whistler-mode waves in the downstream region, as we find in Figures 3.6 and 3.7. We also find the gradual separation of the second and third subpackets in Figure 3.4. Wave amplitudes in the downstream region exceed the nonlinear threshold amplitude in a longer duration than those in the upstream region. The low amplitude part in the subpacket does not grow much, because the amplitude is smaller than the threshold amplitude. This process of nonlinear wave growth enhances the amplitude variations of the subpacket structures in the downstream region of the triggered waves.

3.3.2 Formation of resonant current

The evolution of the wave amplitude B_w is described by the following equation (Omura et al., 2008).

$$\frac{\partial B_w}{\partial t} + V_g \frac{\partial B_w}{\partial x} = -\frac{\mu_0 V_g}{2} J_E \,, \tag{3.6}$$

where J_E is the resonant current parallel to the wave electric field, and μ_0 is the magnetic permeability in a vacuum. The frequency variation $\delta\omega$ is given by (Omura & Nunn, 2011)

$$\delta\omega = -\frac{\mu_0 V_g}{2} \frac{J_B}{B_w}. \tag{3.7}$$

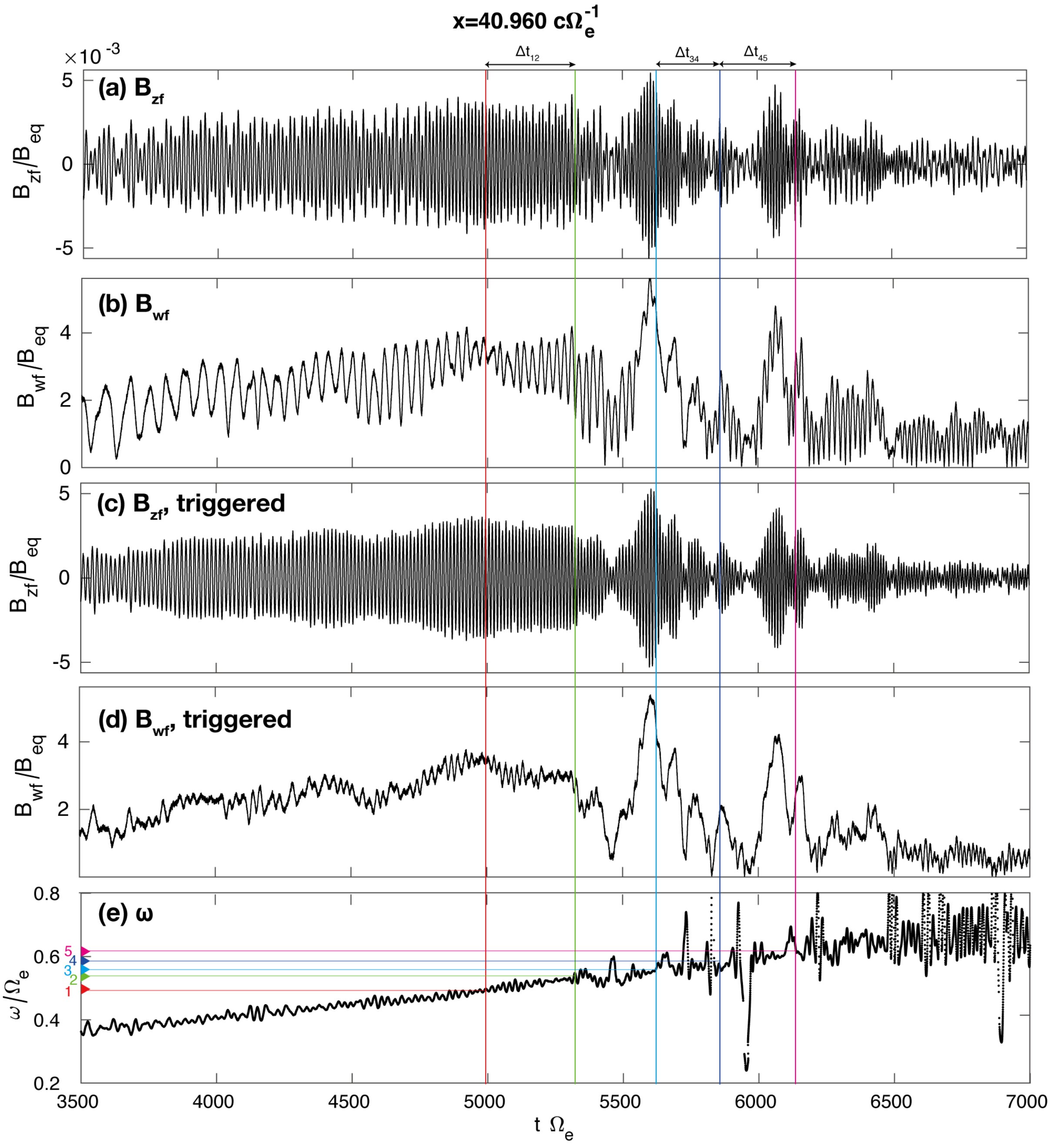

Figure 3.7: Time evolution of wave magnetic field in the downstream region of the triggering wave ($x = 40\,c\Omega_e^{-1}$): (a) waveform of B_{zf} (b) amplitude of B_{wf} (c) waveform of triggered waves (d) amplitude of triggered waves, and (e) instantaneous frequency. The colored lines indicate timings corresponding to the instantaneous frequencies $\omega_1, \omega_2, \omega_3, \omega_4$, and ω_5 as shown in Figure 3.6c. The instantaneous frequencies in Figure 3.7e are calculated from the waveforms of B_y and B_z after the elimination of triggering waves.

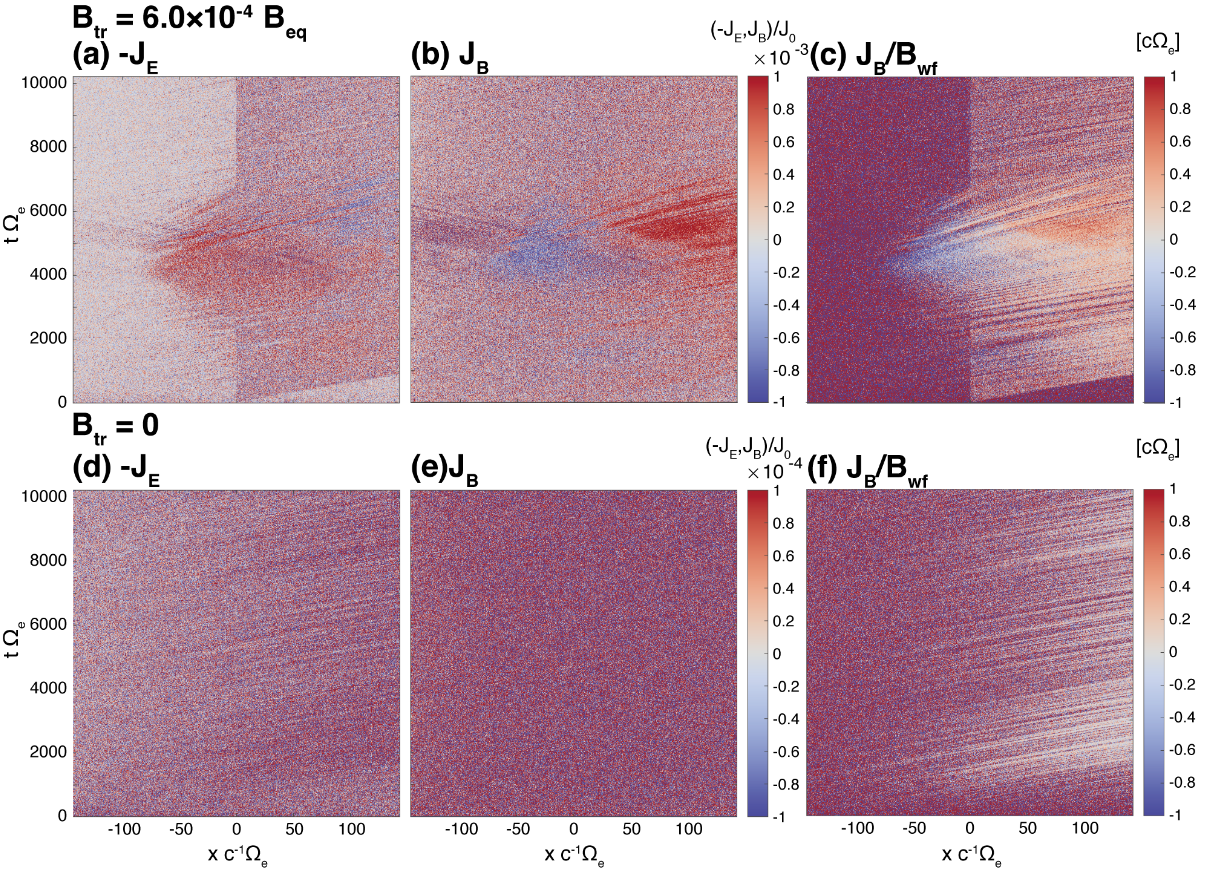

Figure 3.8: Spatial and temporal profiles of resonant currents (a) J_E and (b) J_B, and (c) $J_B/B_{\rm wf}$ with the triggering wave, and (d, e, f) without the triggering wave, respectively.

where J_B is the resonant current parallel to the wave magnetic field. The resonant currents J_E and J_B are calculated by taking dot products of electron velocity $\boldsymbol{v}_\perp$ with the electric and magnetic fields $\boldsymbol{E}_{\rm wf}$ and $\boldsymbol{B}_{\rm wf}$ of the forward propagating waves, respectively. Figures 3.8a and 3.8b show spatial and temporal profiles of J_E and J_B for the case with the triggering wave. Figure 3.8c shows J_B/B_w, which directly controls the frequency variation. We also plot the case without triggering wave in Figures 3.8d, 3.8e, and 3.8f. In the absence of the triggering wave, we only find a very small $-J_E$ which causes wave growth due to the linear growth rate. For this case, J_B is a small finite value, and in Figure 3.8f, we observe growing wave packets with white color because of the larger wave amplitudes B_w in comparison with other ambient areas which appear as the mixed color of red and blue because of the small amplitude B_w of the thermal fluctuation. In the case with the triggering wave, the red stripes found in the time period $t = 4000 - 6000\Omega_e^{-1}$ in Figure 3.8a correspond to the formation of subpackets twhich propagate with smaller V_g because of the increasing frequencies. The range of the color bar for Figures 3.8a and 3.8b is 10^{-3}, while that for Figures 3.8d and 3.8e is 10^{-4}. We find much larger resonant currents $-J_E > 0$ and $J_B < 0$, which correspond to the region where an electron hole is formed as discussed below, generating the subpacket with the increasing frequency as indicated by $J_B/B_w < 0$ in blue color in Figure 3.8c.

In the red region in Figure 3.8b with $J_B > 0$, resonant electrons are entrapped by the growing wave packet, resulting in an electron hill in the velocity phase space as shown in Figure 3.12o. The electron hill causes small segments of falling-tone emissions, as we find in Figure 3.5b, due to $J_B/B_w > 0$ in red shown in Figure 3.8c. However, it does not affect much of the rising-tone emission because of the large wave amplitude, which decreases with $J_E > 0$ as shown by the blue color in Figure 3.8a.

3.3.3 Upstream shift of wave generation region

Figure 3.9 shows a schematic illustration of the formation process of the first subpacket with a long duration. Magenta lines represent the propagation of triggered waves, and blue lines represent electron trajectories moving at resonant velocities, respectively. Bold arrows represent effective interaction regions for resonant electrons. We assume that a wave frequency is constant during the propagation, and phase-organized resonant electrons move at the resonance velocity. In Figure 3.9, we assume the magnitude of the resonance velocity V_R is greater than that of the group velocity. We also assume the resonant currents as a wave source move with the velocity

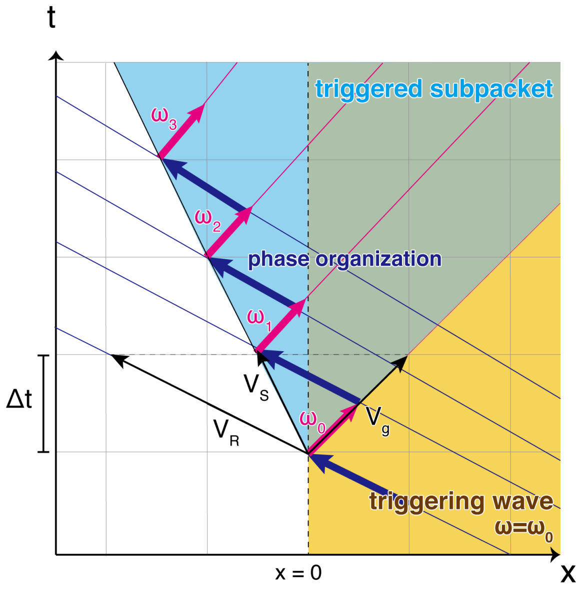

Figure 3.9: Schematic illustration of the formation process of the first subpacket. Magenta arrows represent the propagation of triggered waves with V_g, and blue arrows represent resonant electron trajectories moving at V_R, respectively. Both resonant interaction and wave propagation occur simultaneously with a gradual increase of frequency from ω_0. The source of the triggered wave moves with $V_s = V_R + V_g$.

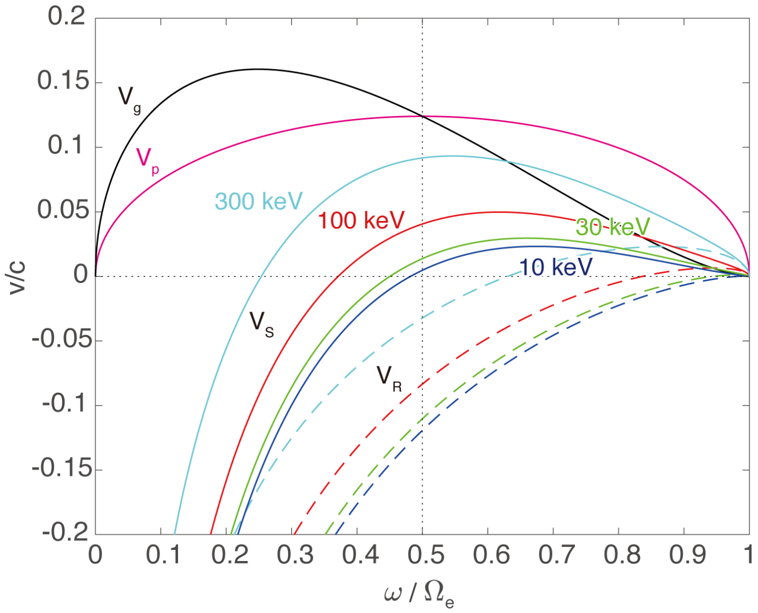

Figure 3.10: Group velocity V_g, phase velocity V_p, resonance velocities V_R, and source velocities V_s as functions of frequency for 10 keV, 30 keV, 100 keV, and 300 keV electrons, respectively.

V_s given by

$$V_s = V_g + V_R \,. \tag{3.8}$$

The resonant currents are formed by the wave packet with a notable wave amplitude moving with the group velocity and the resonant electrons moving with the resonance velocity. The phase-organized resonant electrons are formed by the triggered waves, which propagate with the group velocity. As we find in Figures 3.4b, 3.8a, and 3.8b, the upstream edges of both wave packets and resonant currents move together with V_s. Figure 3.10 shows the variation of group velocity, phase velocity, and resonance velocity for the electrons with 10 keV, 30 keV, 100 keV, and 300 keV, respectively. The source velocities are negative in the frequency range of lower-band chorus waves, which is typically generated from $10 - 30$ keV resonant electrons. In the energy range $10 - 30$keV, the frequency range with the negative source velocity is broader than those for higher energy range as shown in Figure 3.10. The same energy range is also found to be responsible for chorus emissions observed by THEMIS (Kurita, Katoh, et al., 2012). As the frequency increases, the sign of V_s changes from negative to positive around $\omega = 0.45\Omega_e$. In Figure 3.4d, we find the sign of the source velocity changes with the frequency around $0.45\Omega_e$, which corresponds to the calculated source velocity.

In the nonlinear theory, an absolute instability ($\partial\Omega_w/\partial t > 0$) is essential for the initial process of the chorus emission. Assuming that the coherent waves at different frequencies grows from nearly the same levels of thermal fluctuations and the same nonlinear growth rates, we need longer convection paths for higher frequencies so that the emission is observed locally as an absolute instability with growing wave amplitude and increasing frequency. The upward motion of the source region is necesarry for the absolute instability. At the equator, the absolute instability should take place for the formation of a wave packet with an increasing frequency. An efficient energy transfer from kinetic energy to electromagnetic energy is expected because the flux of resonant electrons maximizes at the equator. When the source velocity is negative, the interacting region between triggered waves and resonant electrons is expanded upstream region of the triggering waves. With the thermal fluctuation level nearly constant in space and the convective growth rate constant in space and frequency, the negative source velocity results in wave growth at the equator as an absolute instability. For the formation of a long subpacket wave with rising-tone frequency, the negative source velocity is required.

3.3.4 Time evolution of velocity distribution function

We obtain velocity distributions by integrating energetic electrons over the ranges $x = -40 \pm 0.32\,c\Omega_e^{-1}$ and $x = 0 \pm 0.32\,c\Omega_e^{-1}$, as shown in Figures 3.11a and 3.11b, respectively. In Figures 3.11c-3.11h, we plot the relative difference of distribution function from the initial distributions. The variation in the negative parallel velocity range is caused by the forward propagating waves, while the variation in the positive parallel velocity range is caused by the backward propagating waves. Figure 3.11d shows the formation of the initial electron holes by the forward and backward triggering waves in the negative and positive parallel velocity ranges, respectively, at $t = 2048\,\Omega_e^{-1}$. Since approximately the same processes take place for both forward and backward waves, we focus on the forward waves by plotting the resonance velocity curves for $\omega = 0.3\,\Omega_e$ and $0.7\,\Omega_e$ in green and magenta, respectively. The location of the electron hole in the velocity phase space moves to the region of the lower absolute value of parallel velocity because of the rising-tone frequency. It is also noted that the electron hole in the negative velocity range is formed at $x = -40.96\,c\Omega_e^{-1}$ in the upstream region in the absence of the forward triggering wave. The electron hole is maintained as a self-sustaining process. At $t = 6400\Omega_e^{-1}$, the frequency of the subpacket approaches $0.7\,\Omega_e$ and we find electron holes near $v_\parallel \sim 0$ for both forward and backward waves as shown in Figures 3.11g and 3.11h. Through the movement of the electron holes, significant number of resonant electrons are scattered to the lower pitch angles, while some of resonant electrons are trapped by the triggered waves via relativistic turning acceleration (RTA) (Omura et al., 2007) at higher pitch angles. Comparing Figure 3.11g with 3.11h, we find that the electron entrapping in the high pitch angle takes place in Figure 3.11g, which suggests the formation of the electron hill.

3.3.5 Formation of electron hole

Figure 3.12 shows the time evolution of the variations of velocity phase space density $\Delta g/g_0(\zeta, v_\parallel)$ of energetic electrons for different positions: (a-e) upstream of triggering waves $x = -40\,c\Omega_e^{-1}$,

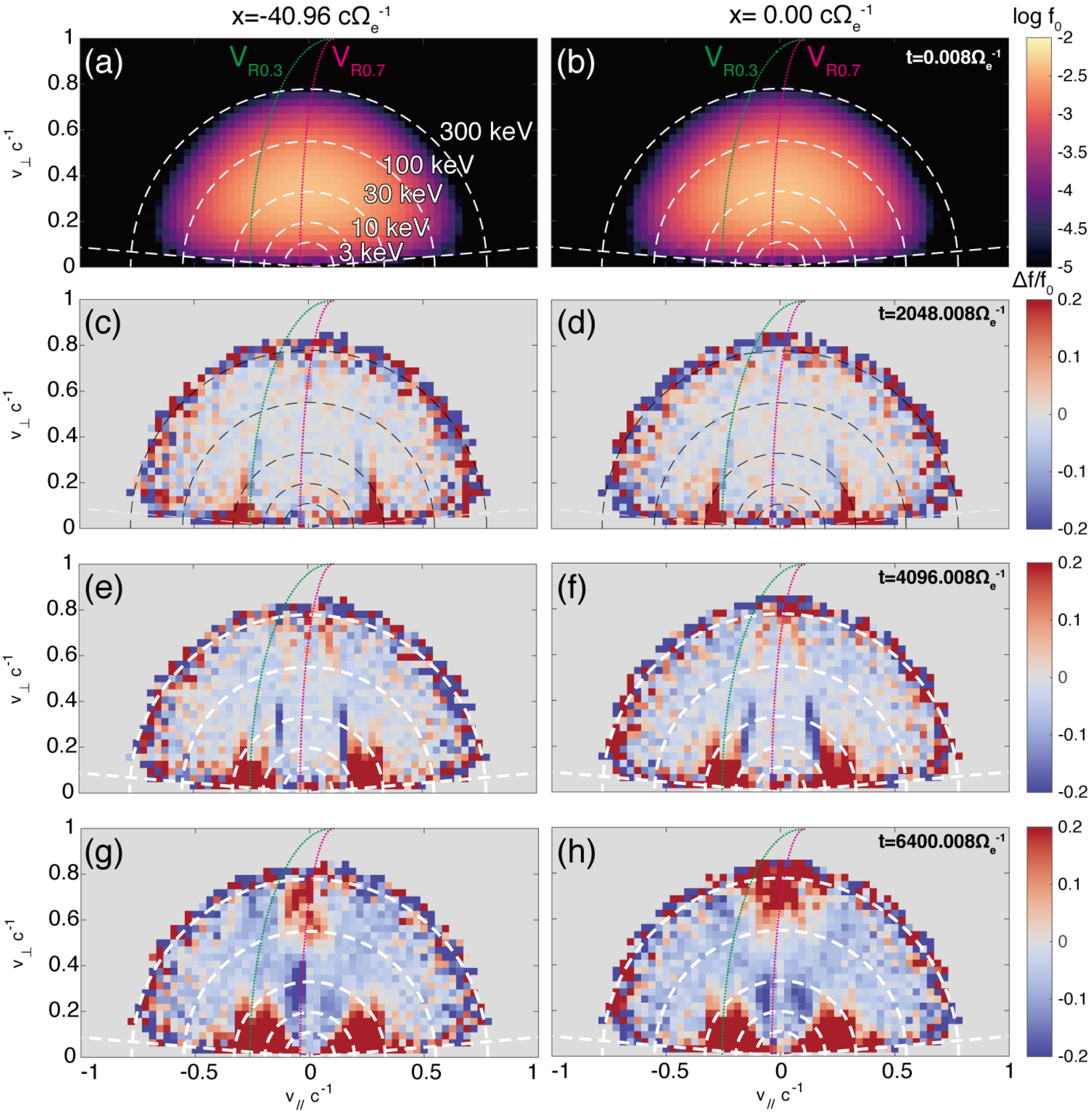

Figure 3.11: Time evolution of the velocity distribution $f(v_\parallel, v_\perp)$ of energetic electrons at $x = -40\,c\Omega_e^{-1}$ and $x = 0\,c\Omega_e^{-1}$; (a, b) the initial velocity distribution f_0, (c, d) $\Delta f = f - f_0$ at $t = 2048\,\Omega_e^{-1}$, (e, f) at $t = 4096\,\Omega_e^{-1}$, (g, h) at $t = 6400\,\Omega_e^{-1}$. The green and magenta curves are resonance velocities with frequencies $0.3\,\Omega_e$ and $0.7\,\Omega_e$, respectively.

(f-j) magnetic equator $x = 0\,c\Omega_e^{-1}$, and (k-o) downstream of triggering waves $x = 40\,c\Omega_e^{-1}$, respectively. The distribution function in velocity phase space at each position x is calculated from the energetic electrons in a finite range from $x - 0.32\,c\Omega_e^{-1}$ to $x + 0.32\,c\Omega_e^{-1}$. The structure of the velocity phase space density strongly depends on the difference between the parallel velocity and the resonance velocity $\Delta v_\parallel = v_\parallel - V_R(\omega, v_\perp)$. The resonance velocity $V_R(\omega, v_\perp)$ is given by

$$V_R(\omega, v_\perp) = \frac{\omega^2 - \sqrt{\omega^4 + (\omega^2 + V_p^2)(1 - \omega^2 - v_\perp^2)}}{\omega^2 + V_p^2} V_p \,, \tag{3.9}$$

where V_p is the phase velocity. We count the number of energetic electrons with the same $\Delta V_\parallel$ and with different $v_\perp$ by projecting a parallel velocity $v_\parallel$ to $v_{\parallel 0}$ with $v_\perp = 0$ along the resonance velocity curve as defined by the following equation:

$$v_{\parallel 0} = V_R(\omega, 0) + v_\parallel - V_R(\omega, v_\perp) \,, \tag{3.10}$$

where we assume $\omega = 0.3\Omega_e$. The resonance velocity with the frequency of $0.3\,\Omega_e$ is calculated by the cold dispersion relation with an energy of each energetic electron. The relative phase angle ζ of $\boldsymbol{v}_\perp$ to the wave magnetic field $\boldsymbol{B}_w$ is calculated for the forward propagating waves. We also take an ensemble average of the phase space density $g(\zeta, v_{\parallel 0})$ over the cyclotron period $\Delta t = 2\pi\,\Omega_e^{-1}$, and plot the results in Figure 3.12. Each of the plots in Figure 3.11 shows the difference Δg from the initial unperturbed distribution function $g_0(\zeta, v_{\parallel 0})$ at different times and positions.

In the initial phase shown in Figures 3.12a, 3.12f, and 3.12k, electron holes are gradually formed in the vicinity of the resonance velocity for the triggering waves with $\omega = 0.3\Omega_e$. We observe the formation of electron holes for triggered waves in Figures 3.12b, 3.12g, and 3.12l. Subsequently, in the downstream region shown in Figure 3.12m, the electron hole is separated into two, which correspond to the different frequencies of the triggering and the triggered waves. As the frequency of the triggered wave increases, the resonance velocity decreases in magnitude. The position of electron hole in the lower magnitude of the velocity in Figures 3.12b, 3.12g, and 3.12l are in agreement with the instantaneous frequency of the triggered wave. In the nonlinear wave growth theory (Omura, 2021), the depth of the electron hole is represented by a parameter $Q = \delta g / g_0$. From Figure 3.12h, we find the depth of the electron hole during the formation of the triggered emission is $Q = 0.3 - 0.4$.

The phase space structure shown in Figure 3.12d corresponds to the time and position of the subpacket formation due to modulation of the wave amplitude. The structure with electron depletion does not look like an electron hole anymore, as shown in Figure 3.12j, and the resonant current J_E changes its sign and oscillates in time, resulting in modulation of the wave packet. The modulated wave packet propagates to the downstream region, and the portion of the wave packet with a larger wave amplitude forms an electron hole, and it undergoes convective wave growth.

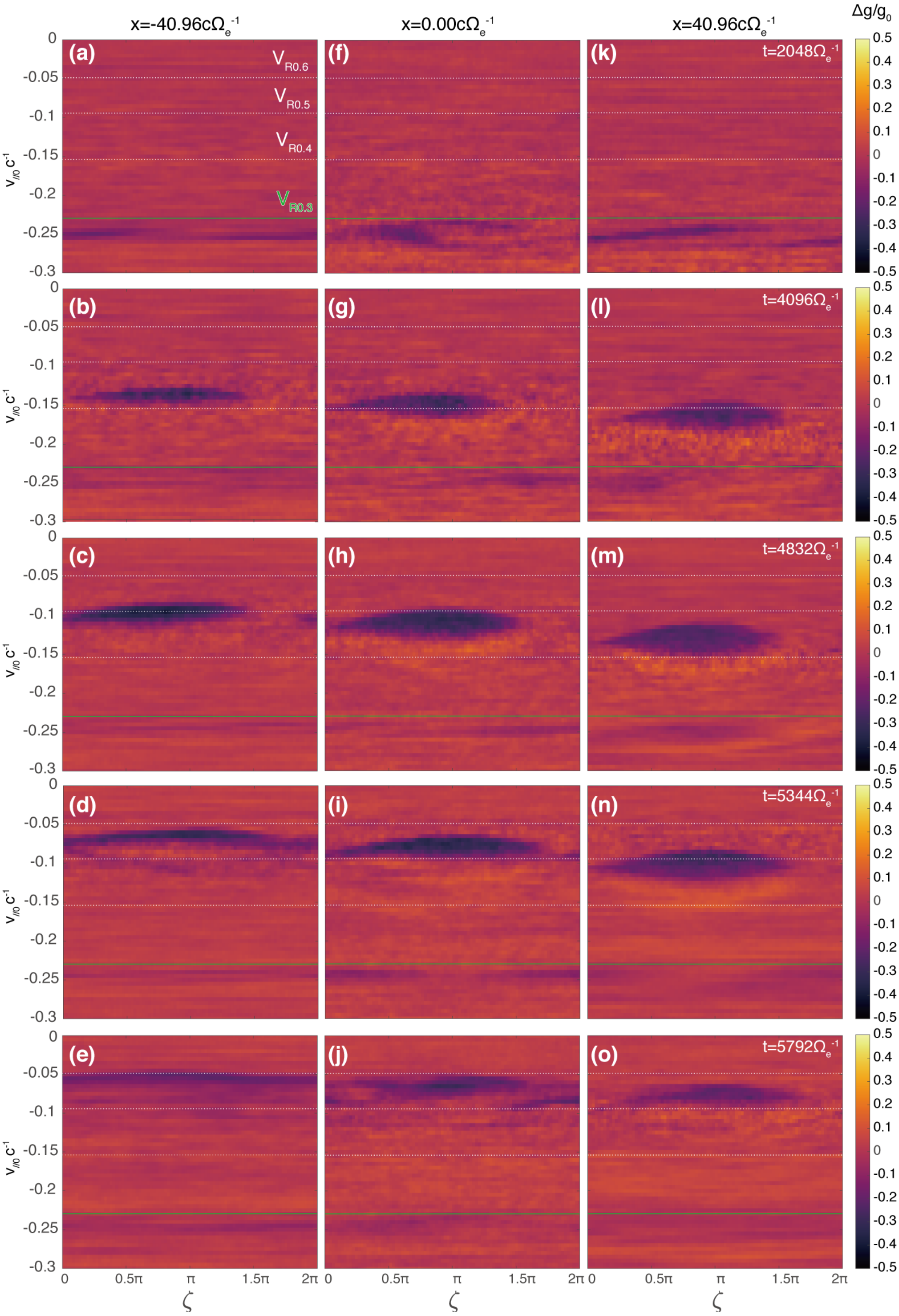

Figure 3.12: Time evolution of the velocity phase space density $\Delta g/g_0$ of energetic electrons for different positions; (a-e) upstream of the triggering wave $x = -40\,c\Omega_e^{-1}$, (f-j) magnetic equator $x = 0\,c\Omega_e^{-1}$, and (k-o) downstream of the triggering wave $x = 40\,c\Omega_e^{-1}$, respectively. The green lines show the cyclotron resonance velocity for the frequency of the triggering wave $\omega = 0.3\Omega_e$, and white dotted lines show the cyclotron resonance velocity for frequencies, $0.4\Omega_e, 0.5\Omega_e$, and $0.6\Omega_e$, respectively.

The trajectories of resonant electrons are described by the pendulum equation with a secular term S (e.g., Omura et al., 2008), which is given by

$$S = -\frac{1}{s_0\omega\Omega_w}\left(s_1\frac{\partial\omega}{\partial t} + cs_2\frac{\partial\Omega_e}{\partial x}\right), \tag{3.11}$$

where

$$s_0 = \frac{\chi v_\perp}{\xi c}, \tag{3.12}$$

$$s_1 = \gamma\left(1 - \frac{V_R}{V_g}\right)^2, \tag{3.13}$$

and

$$s_2 = \frac{1}{2\xi\chi}\left\{\frac{\gamma\omega}{\Omega_e}\left(\frac{v_\perp}{c}\right)^2 - \left[2 + \frac{\chi^2(\Omega_e - \gamma\omega)}{\Omega_e - \omega}\right]\frac{V_R V_p}{c^2}\right\}. \tag{3.14}$$

The wave amplitude B_w is normalized as $\Omega_w = qB_w/m$, ξ and χ are parameters given by the cold plasma dispersion relation $\xi^2 = \omega(\Omega_e - \omega)/\omega_{pe}^2$ and $\chi^2 = 1 - \omega^2/(c^2k^2)$, respectively. The inhomogeneity factor S determines the structure of the nonlinear trapping potential of the wave, which determines the phase of the resonant current. As we find in Figures 3.12g and 3.12h, a group of resonant electrons interacting with the triggering waveform, and the formation of the electron hole generates the negative resonant current J_B, which induces a frequency increase along with the small wave amplitude of a newly generated wave. The frequency increase makes S take a finite negative value, which changes the electron hole from the symmetric form to an asymmetric shape optimum for the maximum J_E. Under the negative J_E, the wave amplitude grows with the increasing frequency to reach the optimum wave amplitude. This process occurs as an absolute instability occurring at a fixed position. Once the wave amplitude becomes close to the optimum wave amplitude, the wave growth process saturates, while the frequency keeps increasing as shown in Figures 3.6 and 3.7. The frequency sweep rate agrees relatively well with the chorus equations (106) and (107) in Omura (2021).

In the initial phase of the triggering process, the amplitude of the triggering waves is greater than that of the triggered waves. The separatability condition of electron holes for two different frequencies between triggering waves and triggered waves is not satisfied except for the electron hole in the upstream region of the triggering wave, where the triggering wave is absent. This prevents resonant electrons from emitting their energy in the downstream region, and newly generated waves are excited in the upstream region of the triggering wave source. Subsequently, the wave growth of the triggered waves takes place in the vicinity of the equator. In those processes, phase-organized particles are continuously provided to the upstream, and continuous wave growth and frequency increase take place.

In Figure 3.13a we plot the inhomogeneity factor S, which plays a critical role in the nonlinear wave growth. It consists of two terms corresponding to the frequency sweep rate and the gradient of the magnetic field, respectively. We compare the magnitude of these terms by

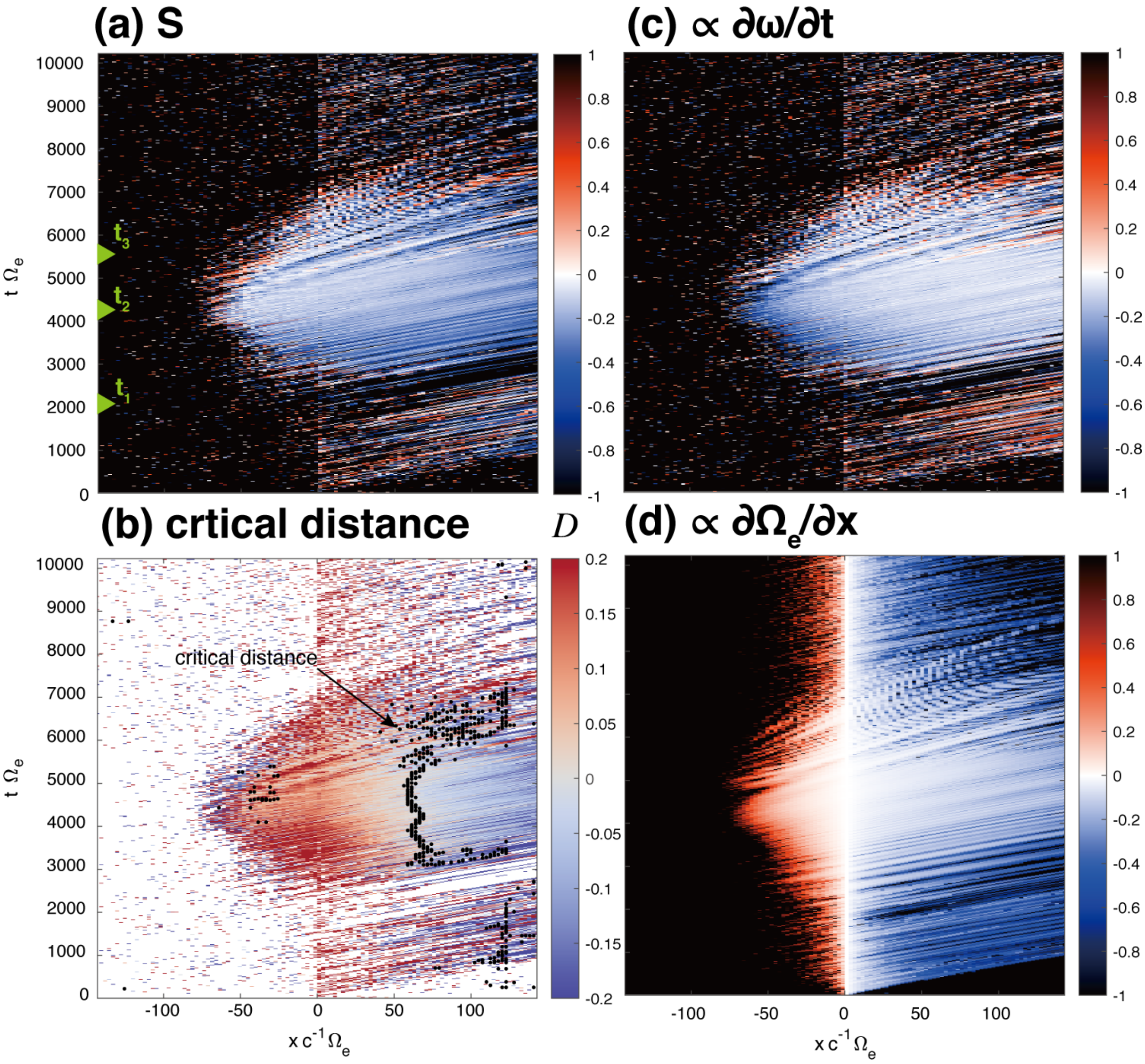

Figure 3.13: Spatial and temporal profiles of inhomogenity factor S (Omura et al., 2008) for triggered waves. (a)S parameter (b) $D = 0$ given by equation (14) and the critical distance indicated by black dots. (c) inhomogeneity due to the frequency sweep rate (d) inhomogeneity due to the magnetic field gradient.

defining

$$D = \frac{1}{s_0 \omega \Omega_w} \left(\left| s_1 \frac{\partial \omega}{\partial t} \right| - \left| c s_2 \frac{\partial \Omega_e}{\partial x} \right| \right) , \tag{3.15}$$

which is plotted in Figure 3.13b. We also plot the magnitudes of the first term and the second term in Figures 3.13c and 3.13d, respectively. We define the critical distance h_c (Omura et al., 2009) at which $D = 0$. Between the equator and the critical distance, the frequency sweep rate controls the wave growth, while at higher latitudes beyond the critical distance, the inhomogeneity factor S is determined by the gradient of the magnetic field. Figure 3.13a shows the $|S| = 0.2 \sim 0.3$ at the critical distance. Through the convective growth of the wave subpackets, the magnitude of the inhomogeneity $|S|$ is kept less than 0.4 with a smooth transition from the inhomogeneity due to the sweep rate to the inhomogeneity due to the gradient of the magnetic field. In the initial phase of triggering process, $|s_1 \partial \omega / \partial t|$ is greater than $|c s_2 \partial \Omega_e / \partial x|$ as shown in Figure 3.13b. The points where $D = 0$ are indicated by black dots in Figure 3.13b. The condition of Trap-Release-Amplify (TaRA) model is only satisfied at the small number points in the final phase of triggered emissions. Gołkowski and Gibby (2017) suggested the initiation of the triggering process start with $S = -0.9$, but we cannot find such tendency in Figure 3.13. The TaRA model assumes a group of particles that are trapped and organized in gyro-phase, and then released from the wave packet. The released particle works as an antenna to radiate a new wave packet with frequency variation matching the inhomogeneity of the background magnetic field. The similar models were proposed by Helliwell (1967) and Roux and Pellat (1978). In these models, the velocity of the wave source is close to the resonance velocity because the phase-organized particles are regarded as released from the wave packet. What we find in the present simulation, however, is clearly different. The most dominant rising-tone subpacket is generated through the formation of an electron hole consisting of untrapped resonant particles. We find the resonant currents J_B and J_E are formed by both wave packet and resonant particles. The motion of the wave source is the motion of the resonant currents, which move with the source velocity V_s. The wave packets evolve in frequency and amplitude because of the resonant currents J_B and J_E.

Figure 3.14 show gyro-phase distribution of resonant electrons in space with different parallel velocities. The phase ζ is defined as an angle between perpendicular velocity $\boldsymbol{v}_\perp$ and the forward magnetic wave components $\boldsymbol{B}_{\mathbf{wf}}$. We separate resonant electrons for different resonance energies. The parallel velocity is determined by the same projection given by equation (3.9). The velocity ranges $-0.33c \sim -0.19c$, $-0.19c \sim -0.11c$, and $-0.11c \sim -0.06c$ correspond to the wave frequency ranges $0.2 \sim 0.35\Omega_e$, $0.35 \sim 0.5\Omega_e$, and $0.5 \sim 0.6\Omega_e$, respectively. By limiting the resonance velocity ranges, we observe a clear formation of electron holes and their spatial configurations. Since the frequency gradually increases in time, the dominant resonance velocity moves to the lower velocity ranges. In each velocity range, we find the transition from electron holes to electron hill as clearly shown in Figures 3.14a-3.14b and Figures 3.14e-3.14f.

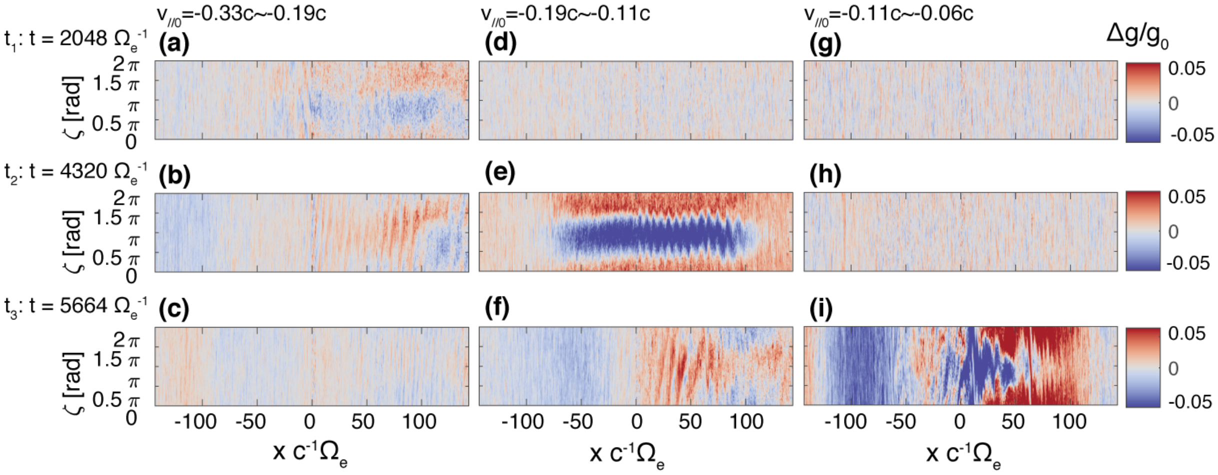

Figure 3.14: Gyrophase distribution of resonant electrons in space with different parallel resonance velocities in (a-c) $v_\parallel = -0.33 - 0.19\,c$, (d-f) $v_\parallel = -0.19 - 0.11\,c$, and (g-i) $v_\parallel = -0.11$-$- 0.06\,c$, respectively.

The wave growth induced by the electron hill makes the wave potential larger, which entraps the resonant electrons outside the wave potential. The electron hill generates a small falling tone with a decreasing wave amplitude as we observe in Figure 5b. When we find a series of subpackets, we find a distinct spatial variation of the phase space density as shown in Figure 3.14i.

3.3.6 Optimum and threshold amplitude

In Figure 3.15, we show the instantaneous wave amplitudes and frequencies at three different positions $x = -40.96, 0, 40.96\,c\Omega_e^{-1}$ by plotting colored dots indicating times in the simulation. We also plot the threshold amplitudes (Omura et al., 2009; Omura, 2021) and the optimum amplitudes (Omura & Nunn, 2011; Omura, 2021) for different values of Q and τ by dashed and solid black lines. In the wave generation region around $x = -40.96\,c\Omega_e^{-1}$ shown in Figure 6a, where no triggering wave exists, we have waves from two different sources. Waves below $0.3\,\Omega_e$ are growing from the thermal fluctuations due to the linear growth rate, and those above $0.3\,\Omega_e$ are generated from the energetic electrons organized in gyro-phase through interaction with the triggering waves in the downstream region $x > 0$. It is noted that the linear growth rate maximizes at $0.22\,\Omega_e$. The wave amplitudes with frequencies above $0.3\,\Omega_e$ increase in time with gradually increasing frequencies, and they saturate around the optimum wave amplitude. The variation of the wave amplitudes and frequencies as observed at the fixed point can be called an absolute instability described by the chorus equations (Omura et al., 2009). The wave amplitudes of the subpackets above $0.5\,\Omega_e$ gradually decrease as the frequencies increases in agreement with the variation of the optimum wave amplitude. Each of the subpackets undergoes the convective wave growth through propagation to the downstream region as shown in

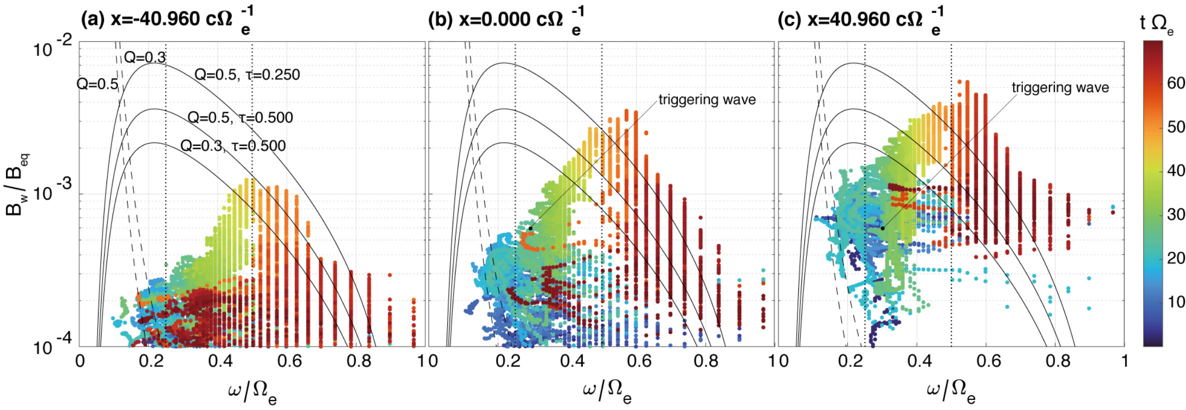

Figure 3.15: Time evolution of instantaneous frequencies and amplitudes of the triggered wave propagating forward at positions (a)$x = -40$, (b) 0, and (c) $40\,c\Omega_e^{-1}$. Black solid lines are the optimum amplitudes, and dashed lines are threshold amplitude (Omura, 2021) for $(Q, \tau) = (0.3, 0.5), (0.5, 0.5)$, and$(0.5, 0.25)$, respectively.

Figures 3.15b and 3.15c. The wave amplitudes become much greater than the optimum wave amplitudes in the downstream region.

3.4 Summary and discussion

We summarize the major nonlinear processes confirmed by the present simulation.

1. Rising-tone elements with multiple subpackets with monotonically increasing frequencies are generated from a triggering wave at the equator.
2. Generation regions of the subpackets move upstream or downstream depending on the group velocities and resonance velocities for different frequencies.
3. Because of the movement of the source region to the upstream, a long rising-tone subpacket is generated self-sustainingly through the formation of an electron hole in velocity phase space stretched over the generation region.
4. The long rising-tone subpacket is modulated with increasing magnitude, splitting into smaller subpackets through propagation.
5. The amplitude modulations in a subpacket are generated by two different processes; resonant trapping oscillation of electrons at the equatorial region and enhancement of the amplitude modulations through propagation in the downstream region.

It is not obvious that the frequency of the second subpacket starts from the frequency of the first subpacket. The information should be transferred from the first subpacket to the second subpacket via the counter-streaming resonant electrons. The resonant electrons are strongly modulated in their gyro-phase, forming a spiral structure in space, which corresponds to the distinct formation of the electron hole shown in Figure 3.14e. The pitch of the spiral has the information on the wave number. The resonant electrons with the phase modulation form a current, generating a triggering wave with the same wave number. Since the wave number and the frequency satisfy the local dispersion relation, the frequency of the first subpacket is transferred to the second subpacket.

The typical chorus spectra in observation are divided into lower and upper band chorus, whereas we do not find significant damping at $0.5\,\Omega_e$ in Figures 3.5a and 3.5b. This is because our model only allows parallel propagation, and Landau resonance does not take place. In the quasi-parallel propagation of whistler-mode waves, group velocity and phase velocity of those waves are nearly the same at $0.5\,\Omega_e$ as plotted in Figure 3.10. This makes a stationary potential structure that can trap Landau resonant electrons and accelerate them, resulting in efficient wave damping (Hsieh & Omura, 2018).

In Figure 3.5, we also find a tendency that complex frequency spectra, including short falling-tones develop around $0.5\,\Omega_e$, when the rising-tone wave packet is at the equator or in the downstream region. This tendency is in agreement with our previous simulation result (Nogi et al., 2020) showing the generation of falling-tone emissions. The short wave packet can trigger falling-tone emissions because of an efficient entrapping of resonant electrons caused by the rapid variation of the wave amplitude, resulting in an electron hill. In the frequency range above $0.5\,\Omega_e$ the source velocity becomes positive, and the generation condition for the absolute instability becomes difficult to be satisfied. Cluster observation (Pickett et al., 2004) presented a spectrogram of VLF triggered emissions, showing that falling-tones are generated from the top part of rising-tone emissions as secondary emissions. The observation and our simulation show very similar wave characteristics, but the detailed investigation is left as a future study. It would also be interesting to investigate the characteristics of triggered emissions with different positions of the triggering wave source.

Chapter 4

Upstream shift of generation region of rising-tone emissions

4.1 Introduction

Very Low frequency (VLF) triggered emissions are due to the generation of new waves with different frequencies from the VLF radio waves transmitted from the ground station (Helliwell, 1967; Helliwell & Katsufrakis, 1974), which is the manifestation of the nonlinear processes (see reviews by Omura et al., 1991; Gołkowski et al., 2019). The generation of the VLF triggered emissions is controlled by wave-particle interactions in the equatorial magnetosphere when the incident VLF waves propagate along with the geomagnetic field. The wave-particle interaction is also the key driver for generating whistler-mode chorus emissions. Recently, the Demonstration and Science eXperiments (DSX) have been conducted for a study of VLF radio wave transmission from space to space (Reid et al., 2022; McCollough et al., 2022), showing the feasibility and the capability of active experiments in the magnetosphere (McCollough et al., 2022).

Whistler-mode chorus emissions are generated near the equator, growing initially with linear growth rates due to the temperature anisotropy of energetic electrons. A coherent wave grows at a fixed frequency up to a certain level of the wave amplitude (Omura & Nunn, 2011), and new wave packets with varying frequencies are formed through nonlinear wave-particle interaction (Hikishima et al., 2009b). Therefore, we can regard chorus emissions with frequency variation as emissions triggered by wave packets naturally growing from thermal fluctuations due to an instability driven by temperature anisotropy of energetic electrons.

The generation mechanism of triggered emissions has been studied for more than half a century. Helliwell (1967) proposed that resonant electrons moving with adiabatic motion generates triggered emissions. Roux and Pellat (1978) have shown that phase space modulation of resonant electrons generates triggered emissions, which are formed by the parallel velocity differences between adiabatic and untrapped electrons. Recently, Tao et al. (2021) proposed Trap-Release-Amplify (TaRA) model, detrapped electrons from the triggering wave generate resonant currents. These models suggest that detrapped resonant electrons are adiabatically transported upstream and generate triggered emissions. Katoh and Omura (2006) showed that resonant currents are generated by the formation of an electron hole in velocity phase space by using hybrid code. Self-consistent particle-in-cell simulations of triggered rising-tone emissions also showed that the formation of an electron hole generates resonant currents inducing nonlinear wave growth and frequency increase (Hikishima et al., 2010; Hikishima & Omura, 2012). Nogi and Omura (2022) have introduced the source velocity, which describes an upstream shift of the source region for triggered emissions. Harid et al. (2022) also showed the backward propagation of the source region for whistler-mode chorus emissions by an envelope particle-in-cell code, however, the parametric dependence of the upstream shift remains unclear.

Triggered emissions and chorus waves have subpacket structures (Santolík et al., 2014). Shoji and Omura (2013) have studied the generation models of the subpacket structures of ElectroMagnetic Ion cyclotron (EMIC) waves, which have similar characteristics to whistler-mode chorus waves. Hanzelka et al. (2020) have proposed a generation model of subpacket structure for chorus waves. The wave amplitude increases rapidly by the nonlinear wave growth, and phase-organized electrons in the vicinity of the optimum amplitude generate a subsequent subpacket, showing the observation result by Van Allen Probes. Nunn et al. (2021) have shown that triggered emissions with short subpackets are generated from the triggering waves with two different frequencies by using Vlasov Hybrid Simulations. Zhang et al. (2021) have reproduced short rising-tone and falling-tone emissions with high frequency sweep rates by using four different self-consistent codes. Nogi and Omura (2022) have shown the generation of the rising-tone emissions with a long subpacket. The generation process of the subpacket and the duration time of the subpacket remain unclear.

Falling-tone triggered emissions are also generated at the termination of the triggering waves with half the electron cyclotron frequency (Nogi et al., 2020). Generation mechanisms of falling-tone emissions have been studied. Nunn and Omura (2012) have reproduced falling-tone emissions by the Vlasov Hybrid Simulation code, showing the formation of the electron hill. Falling-tone emissions are observed in the termination of the rising-tone triggered emissions when the frequency exceeds half the electron cyclotron frequency (Nogi & Omura, 2022). The frequency of the triggering waves is an important factor controlling the generation of rising-tone and falling-tone emissions. We conduct simulation runs with different frequencies of the triggering waves. We also change the background plasma frequency, which controls the frequency ranges of wave growth.

Nogi and Omura (2022) presented detailed analyses of a single PIC simulation run reproducing a long subpacket with increasing frequency (Foster et al., 2021), which is triggered by a finite amplitude wave with a constant frequency of $0.3\,\Omega_e$ under the background plasma density defined by the plasma frequency of $4.0\,\Omega_e$. They found the generation region moves with the source velocity defined by the sum of the resonance velocity and the group velocity. However, the condition for the long subpacket formation was not clear. In the present study, we analyzed the dependency of the triggering process on the frequency of the triggering wave by changing it from 0.05 Ω_e to 0.6 Ω_e with an interval of 0.05 Ω_e. We also studied the triggering process with different plasma frequencies 2.0 Ω_e and 6.0 Ω_e. The series of simulation runs with different parameters shows different processes of generation processes of subpackets forming rising-tone emissions. Simulation methods and parameters are described in section 4.2. The simulation results and characteristics of the reproduced triggered emissions are described in the first part of section 4.3. Discussions of the generation process of the triggered emissions are given in subsections of section 4.3. We give a summary and discussion in section 4.4.

4.2 Simulation parameters

We conduct particle-in-cell simulations by using Kyoto university electromagnetic plasma code (KEMPO) (Omura & Matsumoto, 1993; Omura, 2007). In this paper, our aim is to solve Maxwell's equations and relativistic equations of motion for energetic electrons undergoing cyclotron motion along the magnetic field line near the equator, which requires a code that can resolve nonlinear cyclotron resonant interaction with a time scale thousands of electron cyclotron periods. KEMPO is a code that allows us to achieve this aim since it has a good property of energy and momentum conservation by solving the equations explicitly based on central difference schemes in space aWe apply a one-dimensional parabolic model of ambient magnetic field for the generation of whistler-mode triggered emissions. We used the same model of background magnetic field as Katoh and Omura (2006). The ambient magnetic field with respect to x is given by $B_{\mathrm{eq}}(1+ax^2)$, while the radial components of the ambient magnetic field are added to the equation of motion satisfying $\mathrm{div}B = 0$. Rising-tone triggered emissions can be generated when the amplitude of the triggering wave is greater than the threshold amplitude (Omura et al., 2009). The wave can grow with an increasing frequency to an amplitude close to the optimum wave amplitude as an absolute instability (Omura, 2021). The optimum amplitude and threshold amplitude are given by

$$\Omega_{\mathrm{op}} = 0.8\pi^{-5/2}\frac{|Q|V_pV_g}{\tau\omega}\frac{U_{\perp 0}}{U_{t\parallel}}\omega_{ph}^2\left(1-\frac{V_R}{V_g}\right)^2\exp\left(-\frac{\gamma^2V_R^2}{2U_{t\parallel}^2}\right) , \tag{4.1}$$

and

$$\Omega_{\mathrm{th}} = \frac{100\pi^3\gamma^4\xi}{\omega\omega_{ph}^4U_{\perp 0}^5\chi^5}\left(\frac{as_2U_{t\parallel}}{Q}\right)^2\exp\left(\frac{\gamma^2V_R^2}{U_{t\parallel}^2}\right) , \tag{4.2}$$

where Q, V_p, V_g, V_R, τ, ω, $U_{\perp 0}$, $U_{t\parallel}$, ω_{ph}, and γ are depth of electron hole, phase velocity, group velocity, resonance velocity, trapping period, frequency, perpendicular momentum of energetic electrons, parallel momentum of trapped electrons, plasma frequency of energetic electrons, and Lorentz factor, respectively. Parameters ξ and χ are defined from the cold dispersion relation of whistler-mode waves as $\xi^2 = \omega(\Omega_e - \omega)/\omega_p^2$ and $\chi^2 = 1/(1+\xi^2)$, where ω_p

Table 4.1: Simulation parameters normalized by speed of light c and equatorial electron cyclotron frequency Ω_e

Parameters	Case 1	Case 2	Case 3
Plasma frequency of cold electrons ω_p/Ω_e	4.0	6.0	2.0
Grid spacing $\Delta x/(c\Omega_e^{-1})$	0.01	0.01	0.025
Length of simulation region $L/(c\Omega_e^{-1})$	327.68	327.68	819.2
Density ratio of energetic electrons to cold electrons n_h/n_c	0.01	3.6×10^{-3}	0.01
Thermal momenta of cold electrons $(u_{c\parallel}/c, u_{c\perp}/c)$	$(0.01, 0.01)$	$(0.01, 0.01)$	$(0.025, 0.025)$
Thermal momenta of energetic electrons at equator $(u_{h\parallel}/c, u_{h\perp}/c)$	$(0.25, 0.30)$	$(0.25, 0.30)$	$(0.20, 0.30)$
Amplitude of triggering wave B_{w0}/B_{eq}	6.0×10^{-4}	6.0×10^{-4}	2.0×10^{-4}
Length of damping region $L_D\ /(c\Omega_e^{-1})$	20.48	20.48	51.2
Coefficient for parabolic magnetic field, $a\ /(c^{-2}\Omega_e^2)$	5.0×10^{-6}	5.0×10^{-6}	8.0×10^{-7}

and ω_e are plasma frequency of cold electron, and electron cyclotron frequency, respectively. The electron cyclotron frequency at the magnetic equator is given by $\Omega_e = -eB_{\mathrm{eq}}/m_0$, where m_0 is the rest mass of an electron and $-e$ is an electron charge. The phase velocity and the resonence velocity are given by $V_p = c\chi\xi$ and $V_R = [1 - \Omega_e/(\gamma\omega)]V_p$, respectively, where c is speed of light in vacuum. The parameter τ is given by T_N/T_{tr}, where T_N and T_{tr} are the nonlinear transition time to the trapping time necessary for the formation of nonlinear resonant current and the trapping time $T_{tr} = 2\pi\sqrt{m_0\gamma/(kV_{\perp 0}eB_w)}/\chi$, respectively. The equations (1) and (2) are calculated for electrons with Maxwellian distribution in the parallel direction. The perpendicular momentum $U_\perp$ in equations (1) and (2) is an averaged momentum of energetic electrons. The averaged perpendicular momentum for subtracted bi-Maxwellian distribution (Fujiwara et al., 2022) is given by $U_{\perp 0} = U_{t\perp}\sqrt{\pi/2}(1 - \beta^{1.5})/(1 - \beta)$, where β and $U_{t\perp}$ are parameters for subtracted Maxwellian distribution assumed in the present simulation.

We have chosen different sets of parameters for three different plasma frequencies. Each set of parameters is determined so that the optimum amplitude is greater than the threshold amplitude over a frequency range of typical rising-tone chorus frequencies (O. Agapitov et al., 2019). Both threshold amplitude and optimum amplitude are derived under the assumption of an electron hole formed by the resonant electrons in the velocity phase space. We assume depth Q of an electron hole as $Q = 0.5$. The threshold amplitude is obtained by assuming a constant gradient of the wave amplitude for efficient convective wave growth in a parabolic magnetic field given by $B(x) = B_{eq}(1 + ax^2)$, where a is specified in Table 4.1.

Figure 4.1a shows optimum and threshold amplitudes at the equator. The frequency band of triggered emissions shifts to the lower frequency ranges as the plasma frequency increases. Both linear growth rate and optimum wave amplitude maximize at lower frequencies with higher plasma frequencies. The nonlinear growth rates for the optimum wave amplitudes are much greater than the linear growth rates, as shown in Figure 4.1b. The amplitudes of triggering waves are indicated by horizontal dotted lines in blue, green, and red for $\omega_p = 2.0\,\Omega_e$, $\omega_p = 4.0\,\Omega_e$ and $6.0\,\Omega_e$, respectively. When the amplitude of the triggering wave is greater

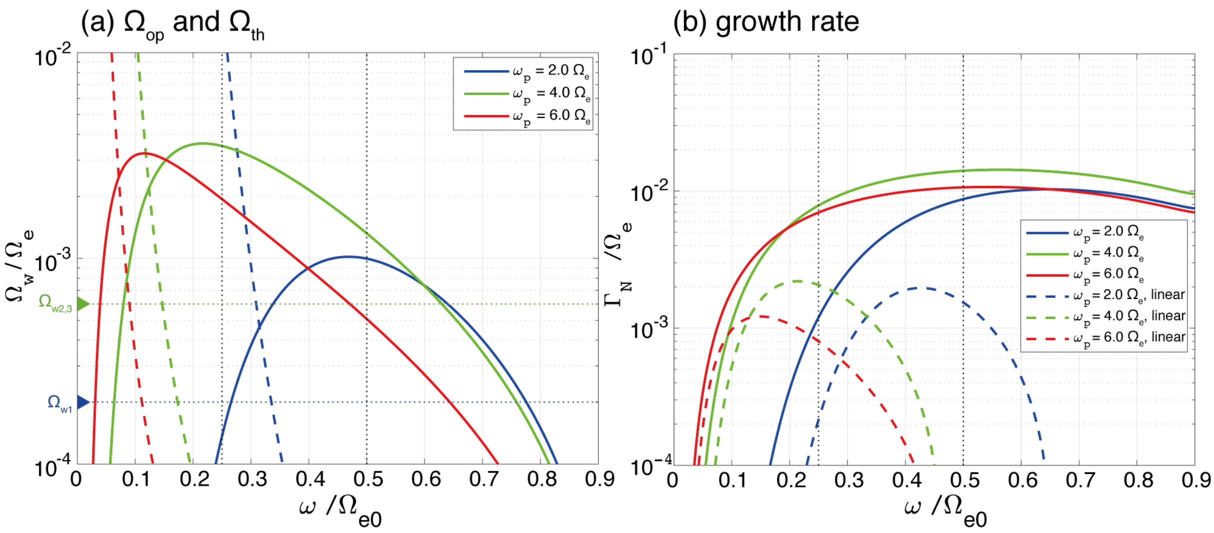

Figure 4.1: (a) Optimum amplitudes (solid lines), threshold amplitudes (dashed lines) and triggering wave amplitude (triangle marker and dotted lines) for different plasma frequencies $\omega_p = 2.0\,\Omega_e, 4.0\,\Omega_e$, and $6.0\,\Omega_e$ with $Q = 0.5$ and $\tau = 0.5$ (b) Linear growth rates (dashed lines) and nonlinear growth rates (solid lines) for the optimum amplitudes.

than the threshold wave amplitude, the wave grows to an amplitude around the optimum wave amplitudes. Based on nonlinear theory, nonlinear growth is expected if both of the following conditions are satisfied; The amplitude of the triggering wave as a seed wave is greater than the threshold amplitude Ω_{th}, and it is smaller than the optimum amplitude Ω_{op}. We inject triggering waves into the simulation system at the magnetic equator by oscillating two orthogonal external currents with right-handed polarization to the magnetic field. The amplitude of the external current J_{ext} for generating a finite amplitude of magnetic field B_w is obtained by Fujiwara et al. (2022) as $J_{\mathrm{ext}} = 2B_w/\mu_0$, where μ_0 is magnetic permeability in a vacuum.

Three different plasma frequencies, $2.0\,\Omega_e$, $4.0\,\Omega_e$, and $6.0\,\Omega_e$ are used in the simulation. Simulation parameters specific for the three cases are shown in Table 4.1 with normalization by the speed of light c and electron cyclotron frequency Ω_e. Common simulation parameters are shown in Table 4.2, which are the same parameters as in the simulations by Nogi and Omura (2022). The simulation parameters in Tables 4.1 and 4.2 are determined so that linear and non-

Table 4.2: Common simulation parameters

Parameters	Value
Time step $\Delta t/\Omega_e$	0.0078125
Number of grids	32,768
Total number of cold electrons	1,073,741,824
Total number of energetic electrons	1,073,741,824
Parameters of subtracted Maxwellian distribution ρ, β	$1, 0.3$
Number of grids for damping region	2,048

linear growth rates are positive over a frequency range. We choose plasma frequency, momenta and density of energetic electron, and amplitude of triggering wave from two conditions. We use a reduced model for the present simulation because of the limitation of computer resources, while the plasma frequency and the density ratio of energetic electrons to cold electrons are set as typical values in the inner magnetosphere with $L = 4$ to 6. The plasma frequency of the cold electrons in the present study is assumed as $2.0\Omega_e$, $4.0\Omega_e$, and $6.0\Omega_e$. The density ratio of energetic electrons to cold electrons in the present study is in the range from 0.1 to 1 percent, consistent with observations (Kubota et al., 2018; Juhász et al., 2019). The coefficient a for the parabolic magnetic field model is determined so that the critical distance for nonlinear wave growth (Omura et al., 2008) should be in the simulation region. The critical distance is given by

$$h_c = \frac{s_0 \omega \Omega_{w0}}{5 c a s_2 \Omega_{e0}}, \tag{4.3}$$

where s_0 and s_2 are given by

$$s_0 = \frac{\chi v_\perp}{\xi c} \tag{4.4}$$

and

$$s_2 = \frac{1}{2\xi\chi} \left\{ \frac{\gamma\omega}{\Omega_e} \left(\frac{v_\perp}{c} \right)^2 - \left[2 + \Lambda \frac{\chi^2(\Omega_e - \gamma\omega)}{\Omega_e - \omega} \right] \frac{V_R V_p}{c^2} \right\} . \tag{4.5}$$

By calculating the critical distance from real parameters $f_{ce} = 7000\text{kHz}$, $\Omega_w = 2 \times 10^{-3}$, $L = 6$ and the plasma frequency for Case 1 ($\omega_p = 4.0\,\Omega_e$), we obtain the critical distance in latitude as approximately 15 degrees. Nogi and Omura (2022) have shown that the critical distance for rising-tone emission is $75c\Omega_e^{-1}$, and the size of the simulation region is twice as large as the critical distance. Comparing magnetic latitude for the real values with the simulation result (Nogi & Omura, 2022), we obtain the corresponding magnetic latitude in the simulation region in the range from −30 degrees to 30 degrees. Numerical parameters Δx and Δt satisfy the Courant condition (Omura & Matsumoto, 1993) and have a sufficient temporal resolution for solving the equation of motion with the Buneman-Boris method. Under the parameter Δx, the number of grid points in space is sufficient for describing sinusoidal waveform with discrete points. We use absorbing boundaries at both edges of the simulation region with a masking method (Umeda et al., 2001). The size of the absorption region L_D and damping coefficients are the same as those in Nogi and Omura (2022). We set momentum distribution functions for cold electrons and energetic electrons as the bi-Maxwellian distribution and the subtracted bi-Maxwellian distribution, respectively. The ratio of triggering amplitude to the ambient magnetic field is of the order of 10^{-4}.

The amplitude of the triggering wave is between the optimum amplitude and the threshold amplitude. The linear growth rate is positive for the frequency range, where the nonlinear growth is positive. As we find in Figure 4.2, the group and resonance velocities are greater in Case 3. We expand the interaction region taken over a longer distance along the magnetic

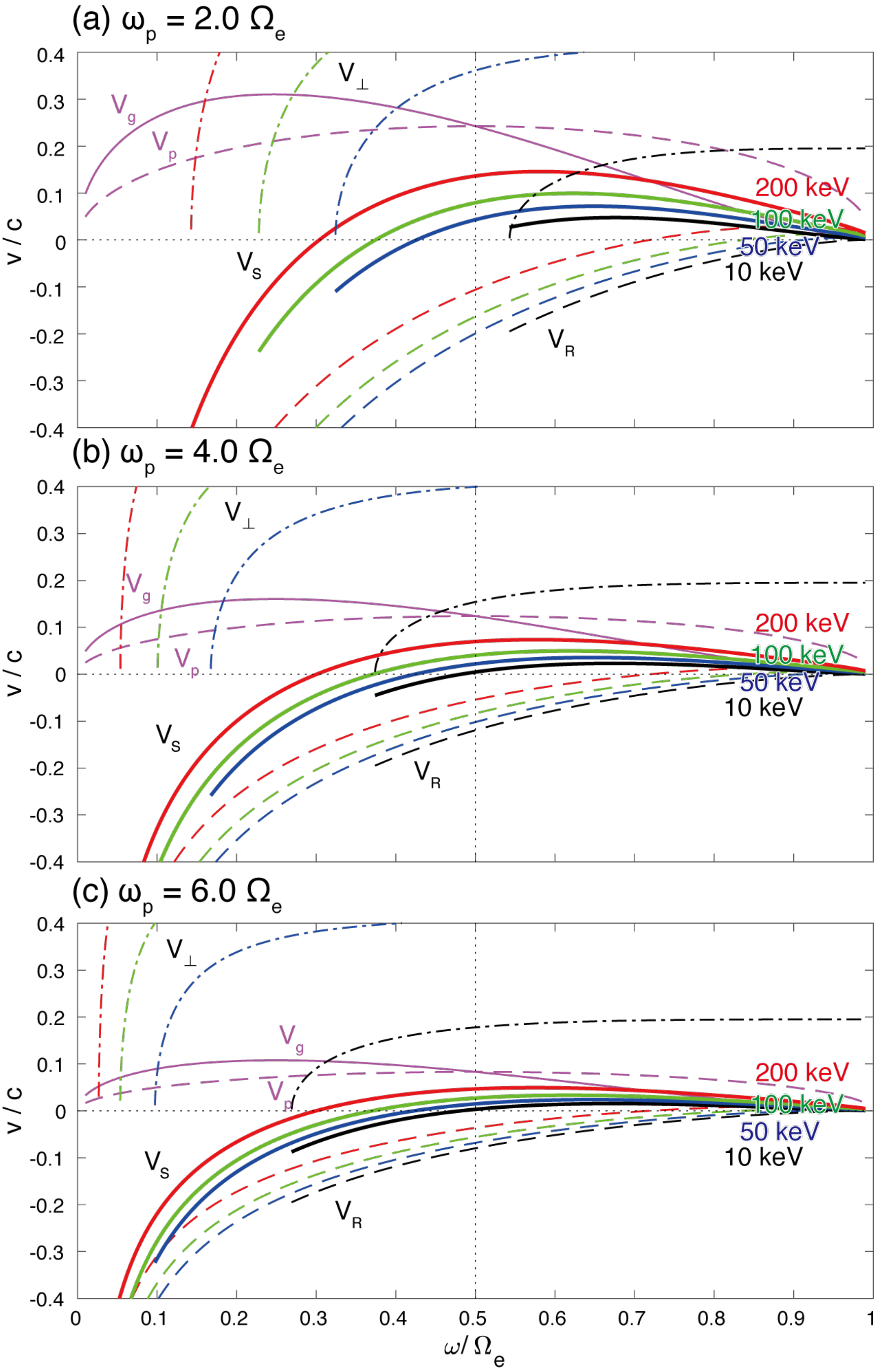

Figure 4.2: Group velocity V_g, phase velocity v_p, resonance velocities V_R, perpendicular velocities $v_\perp$, and source velocity V_S as functions of frequeny for 10, 50, 100, and 200 keV electrons with plasma frequencies (a) $\omega_p = 2.0\,\Omega_e$, (b) $4.0\,\Omega_e$, and (c) $6.0\,\Omega_e$, respectively.

field line for effective wave-particle interaction within the same time scale. Therefore, we have chosen the greater value for the grid spacing to make the system length longer and specified the smaller magnetic field gradient. Nogi and Omura (2022) showed that the source velocity V_S defined by $V_R + V_g$ represents the motion of the triggering points for a new wave packet in Case 1. In Figure 4.2, we plot V_S in solid lines for $\omega_p = 2.0\,\Omega_e$, $4.0\,\Omega_e$, and $6.0\,\Omega_e$. In the present study, source velocity is defined as the shifts of the wave generation region in a single subpacket, which is given by $V_S = V_g + V_R$ (Nogi & Omura, 2022), and the source region is the area where the single whistler-mode triggered emission is generated. We expand the concept to the multiple subpackets, and we define the wave generation velocity V_W as the shifts of the multiple subpacket generation region. The wave generation region is used for the area where the whistler-mode triggered emissions are generated.

4.3 Results

Figure 4.3 shows spatial and temporal profiles of magnetic field for forward waves with different triggering wave frequencies from (a) $\omega_0 = 0.05\,\Omega_e$ to (l) $0.60\,\Omega_e$ for the plasma frequency $\omega_p = 4.0\,\Omega_e$. The propagation directions of whistler-mode waves are separated by applying discrete Fourier transformation to B_y and B_z with respect to x. Triggered emissions are observed in the cases of the triggering wave frequency with $0.20\,\Omega_e$, $0.25\,\Omega_e$, and $0.30\,\Omega_e$ in Figures 4.3d, 4.3e, and 4.3f, respectively. Long subpacket structures are observed during the triggered emissions and the generation region of triggered emissions shifts upstream. Figures 4.4a-4.4l show spatial and temporal profiles of instantaneous frequencies for forward propagating triggered emissions for the plasma frequency $\omega_p = 4.0\,\Omega_e$. We separate triggered emissions from triggering waves by applying discrete Fourier transformation with respect to time. Instantaneous frequency is calculated by the inverse of the period of the wave phase of magnetic fields from $-\pi$ to π.

In Figure 4.4, we plot instantaneous frequencies for triggered emissions with amplitudes greater than 6.0×10^{-4} of the equatorial background magnetic field. We find that triggered emissions in Figures 4.4d, 4.4e, and 4.4f are rising-tone emissions. The instantaneous frequency of those cases smoothly increases from the frequency of triggering waves.

Figure 4.5 shows spatial and temporal profiles of magnetic field for forward waves with different triggering wave frequencies from (a) $\omega_0 = 0.05\,\Omega_e$ to (l) $0.60\,\Omega_e$ for the plasma frequency $\omega_p = 6.0\,\Omega_e$. Triggered emissions are observed in the cases of the triggering wave frequency with $0.15\,\Omega_e$ and $0.20\,\Omega_e$ in Figures 4.5c and 4.5d. A shorter subpacket is generated repeatedly, and the generation region of the subpackets moves upstream. Figures 4.6a-4.6l show spatial and temporal profiles of instantaneous frequency for forward propagating triggered emissions for the plasma frequency $\omega_p = 6.0\,\Omega_e$. We find that triggered emissions in Figures 4.5c and 4.5d are rising-tone emissions. The instantaneous frequencies of these cases smoothly

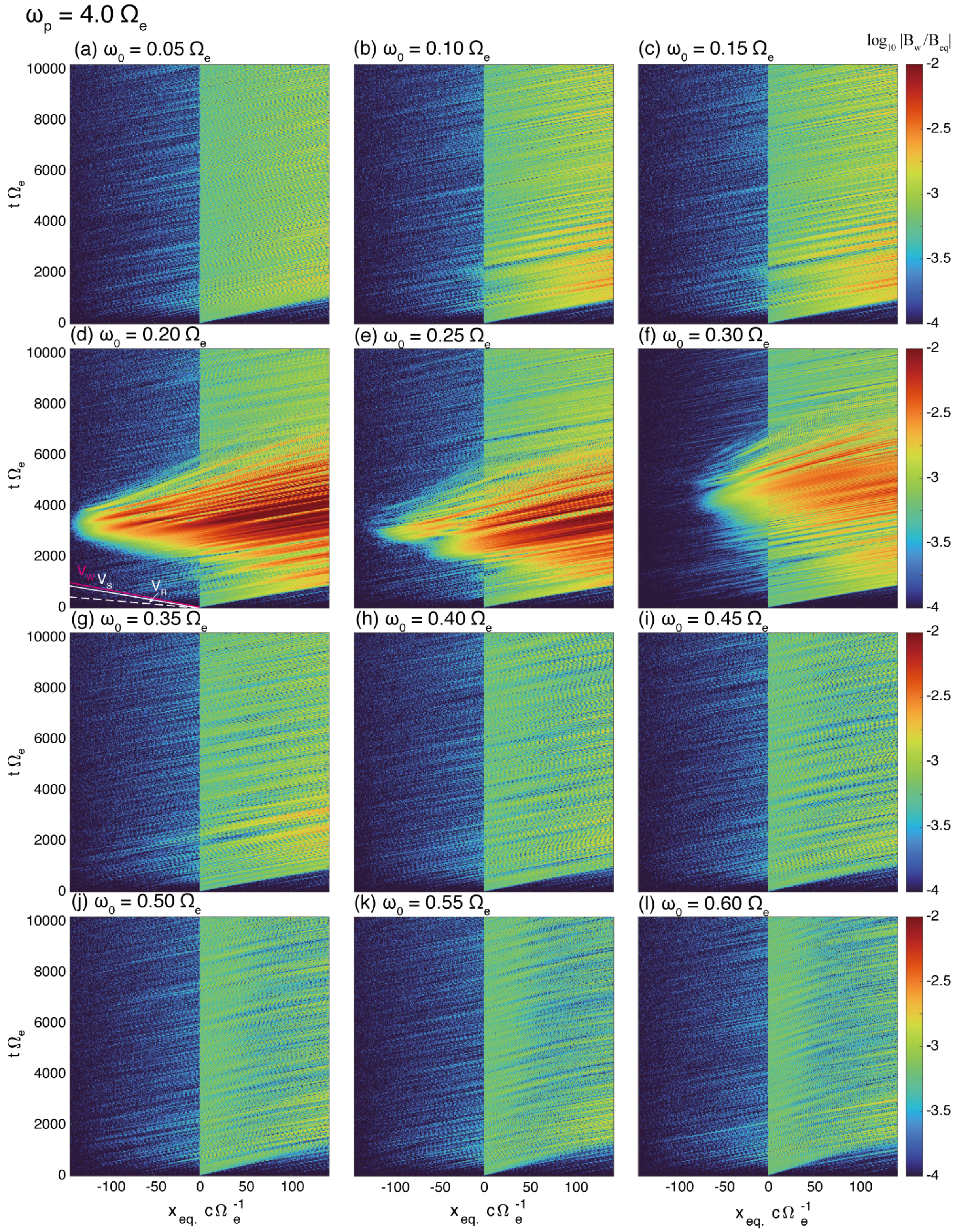

Figure 4.3: Spatial and temporal profiles of magnetic fields for forward waves for Case 1 with plasma frequency $\omega_p = 4.0\,\Omega_e$ and triggering wave frequencies ω_0 from (a) $0.05\,\Omega_e$ to (i) $0.60\,\Omega_e$, respectively. (d) (solid magenta line) The velocity of wave generation V_W, (dashed white line) the resonance velocity for 100 keV electrons at the magnetic equator, (solid white line) the source velocity V_S for 100 keV electrons at the magnetic equator.

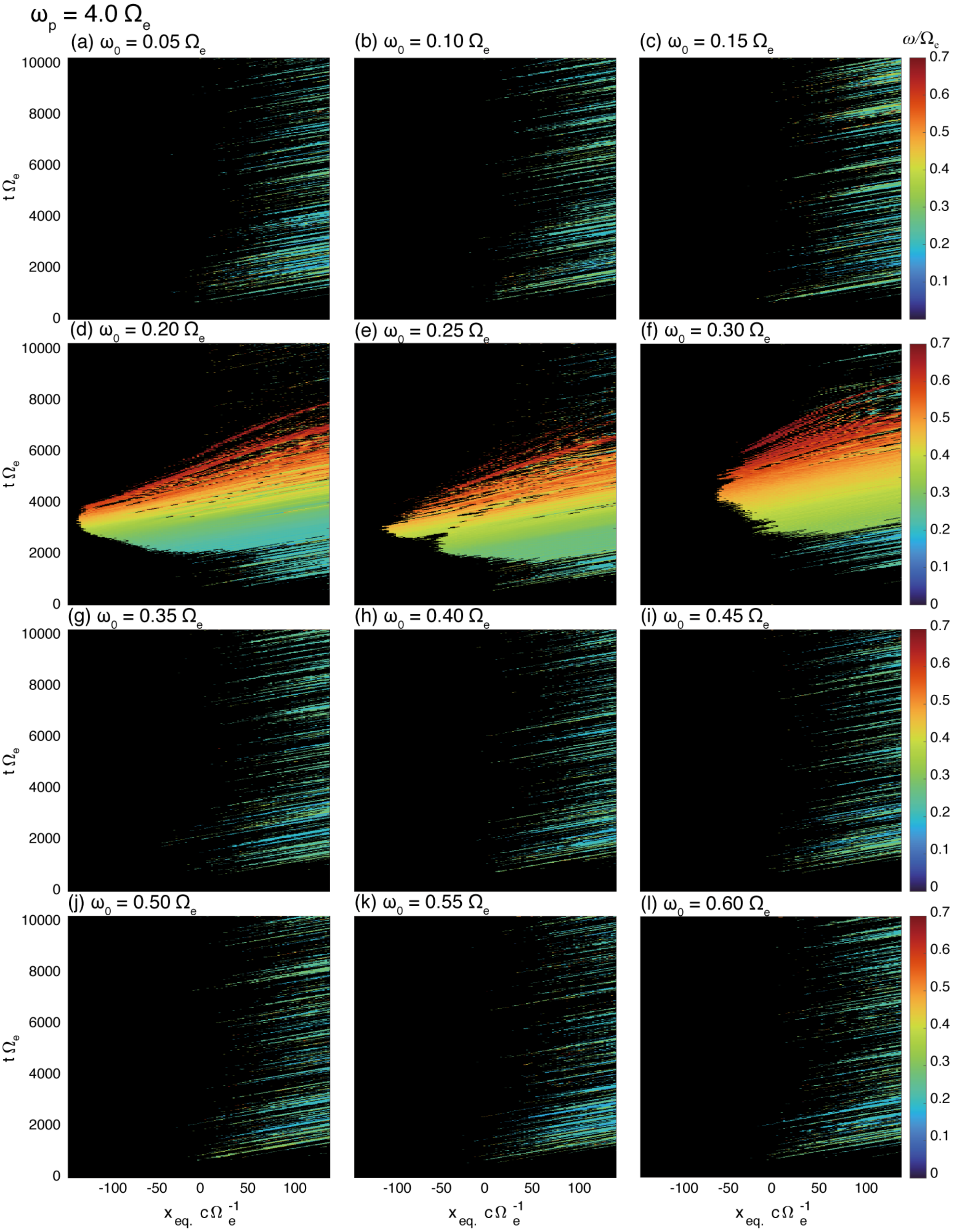

Figure 4.4: Spatial and temporal profiles of instantaneous frequency of triggered emissions for Case 1 with the plasma frequency $\omega_p = 4.0\,\Omega_e$ and different triggering wave frequencies ω_0 (a) $0.05\,\Omega_e$ to (i) $0.60\,\Omega_e$, respectively.

increase from the frequencies of the triggering waves.

Figure 4.7 shows spatial and temporal profiles of magnetic fields of forward waves with different triggering wave frequencies from (a) $\omega_0 = 0.05\,\Omega_e$ to (l) $0.60\,\Omega_e$ for the plasma frequency $\omega_p = 2.0\,\Omega_e$. In the cases of the triggering wave frequency from $0.35\,\Omega_e$ to $0.50\,\Omega_e$, we observe triggered emissions as shown in Figures 4.7g-4.7j. Comparing Figure 4.7 with Figure 4.3, we find that shorter subpackets are intermittently generated, but the generation region of the subpackets smoothly moves upstream. Figures 4.8a-4.8l show spatial and temporal profiles of instantaneous frequencies for forward propagating triggered emissions for the plasma frequency $\omega_p = 6.0\,\Omega_e$. We find that triggered emissions in Figures 4.8g-4.8j are rising-tone emissions. The instantaneous frequencies of these cases smoothly increase from the frequencies of triggering waves.

Rising-tone emissions are observed in all three cases described above. The generation regions of rising-tone emissions shift upstream from the triggering waves. We have shown that the source velocity varies depending on the triggering wave frequency and the energy of resonant electrons. The source velocity dynamically changes in the formation process of the rising-tone emissions with increasing frequencies. Comparing wave generation velocities for upstream shifts of the triggered emissions in Figures 4.4, 4.6, and 4.8 with the source velocity (V_S) in Figure 4.2, we confirm the variation of the source velocity by changing the frequency of the triggering waves. The duration of the subpacket structure depends on the plasma frequency and the frequency of triggering waves. We discuss the formation process of rising-tone emissions based on the source velocity and subpacket structures in the following sections.

4.3.1 Triggering wave frequencies

Parametric surveys on plasma frequency and triggering wave frequency have shown that rising-tone triggered emissions are observed over a certain frequency range of triggering waves. This section discusses how the triggering wave frequency controls the generation of triggered emissions. Nonlinear wave growth takes place when the amplitude of the triggering wave is greater than the threshold amplitude Ω_{op}, and less than the optimum amplitude Ω_{th}. Figure 4.1a indicates that the minimum frequency satisfying the condition is $0.35\,\Omega_e$, $0.15\,\Omega_e$, and $0.12\Omega_e$ for the plasma frequencies $\omega_p = 2.0\,\Omega_e$, $4.0\,\Omega_e$, and $6.0\,\Omega_e$, respectively. We find triggered emissions with triggering waves at frequencies from $0.35\,\Omega_e$, $0.20\,\Omega_e$, and $0.15\,\Omega_e$ for plasma frequencies $\omega_p = 2.0\,\Omega_e$, $4.0\,\Omega_e$, and $6.0\,\Omega_e$ as shown in Figures 4.7, 4.3, and 4.5, respectively. The results are consistent in terms of the prerequisite of the nonlinear theory given by optimum and threshold amplitudes, supporting that nonlinear wave growth is a dominant process in the generation of rising-tone triggered emissions.

The maximum frequency of the triggering wave for generating triggered emissions are $\omega = 0.5\,\Omega_e$, $0.3\,\Omega_e$, and $0.2\,\Omega_e$ for the plasma frequency $\omega_p = 2.0\,\Omega_e$, $4.0\,\Omega_e$, and $6.0\,\Omega_e$ in Figures 4.7d, 4.3f, and, 4.5j. In frequency ranges higher than these threshold frequencies for

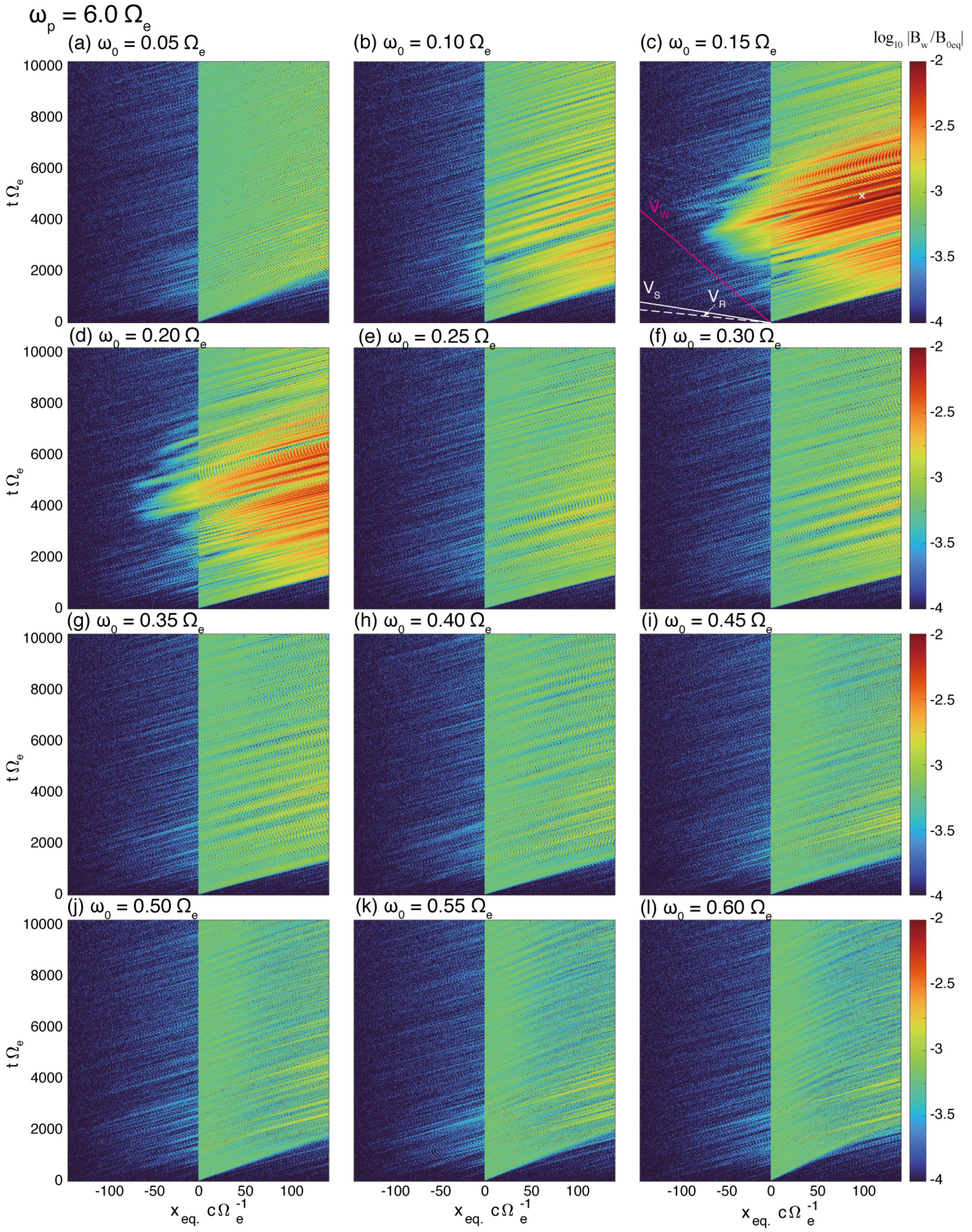

Figure 4.5: Spatial and temporal profiles of magnetic fields for forward waves for Case 2 with plasma frequency $\omega_p = 6.0\,\Omega_e$ and triggering wave frequencies ω_0 from (a) $0.05\,\Omega_e$ to (i) $0.60\,\Omega_e$, respectively. (c) (solid magenta line) The velocity of wave generation V_W, (dashed white line) the resonance velocity for 100 keV electrons at the magnetic equator, (solid white line) the source velocity V_S for 100 keV electrons at the magnetic equator.

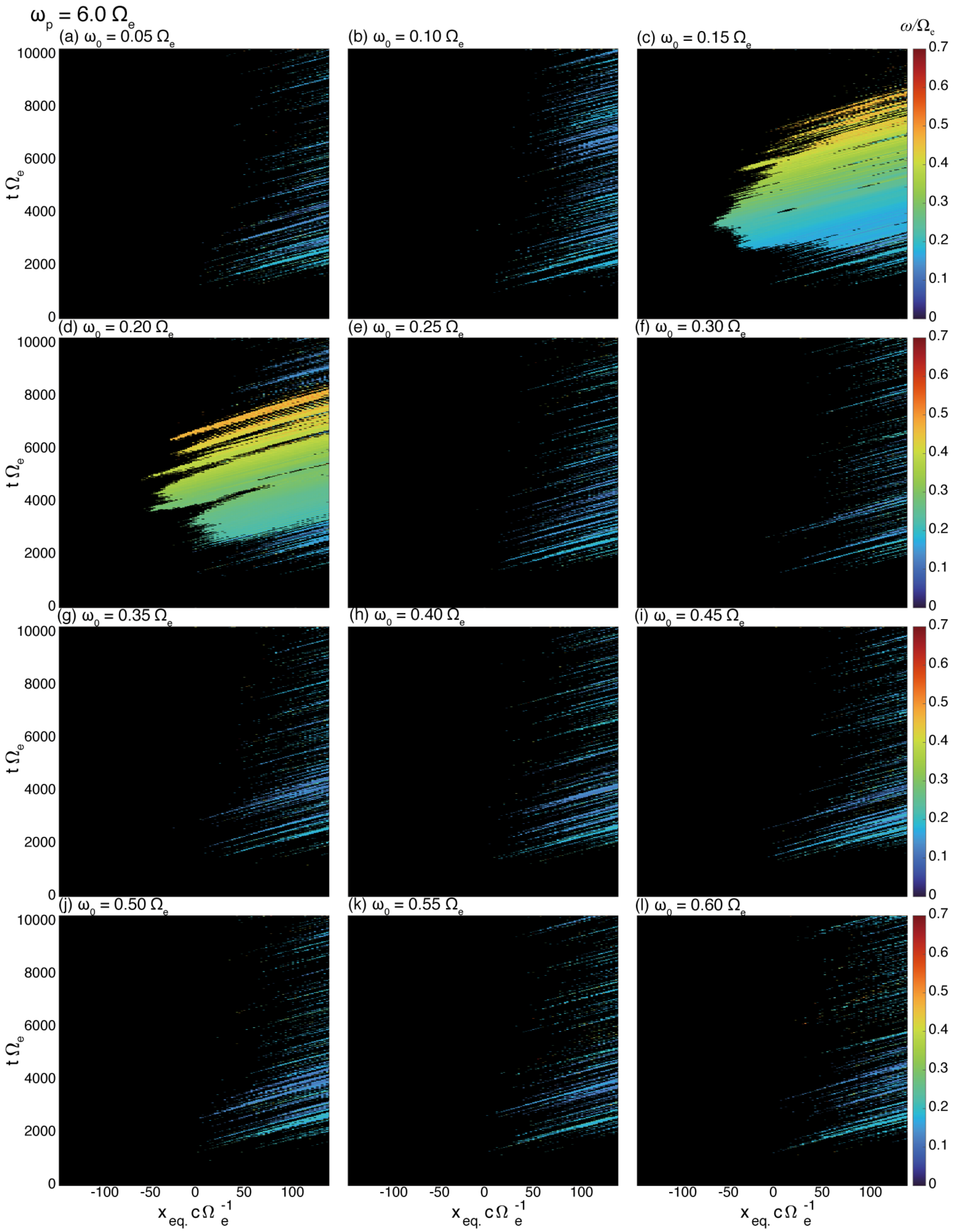

Figure 4.6: Spatial and temporal profiles of instantaneous frequency of triggered emissions for Case 2 with the plasma frequency $\omega_p = 6.0\,\Omega_e$ and different triggering wave frequencies ω_0 from (a) $0.05\,\Omega_e$ to (i) $0.60\,\Omega_e$, respectively

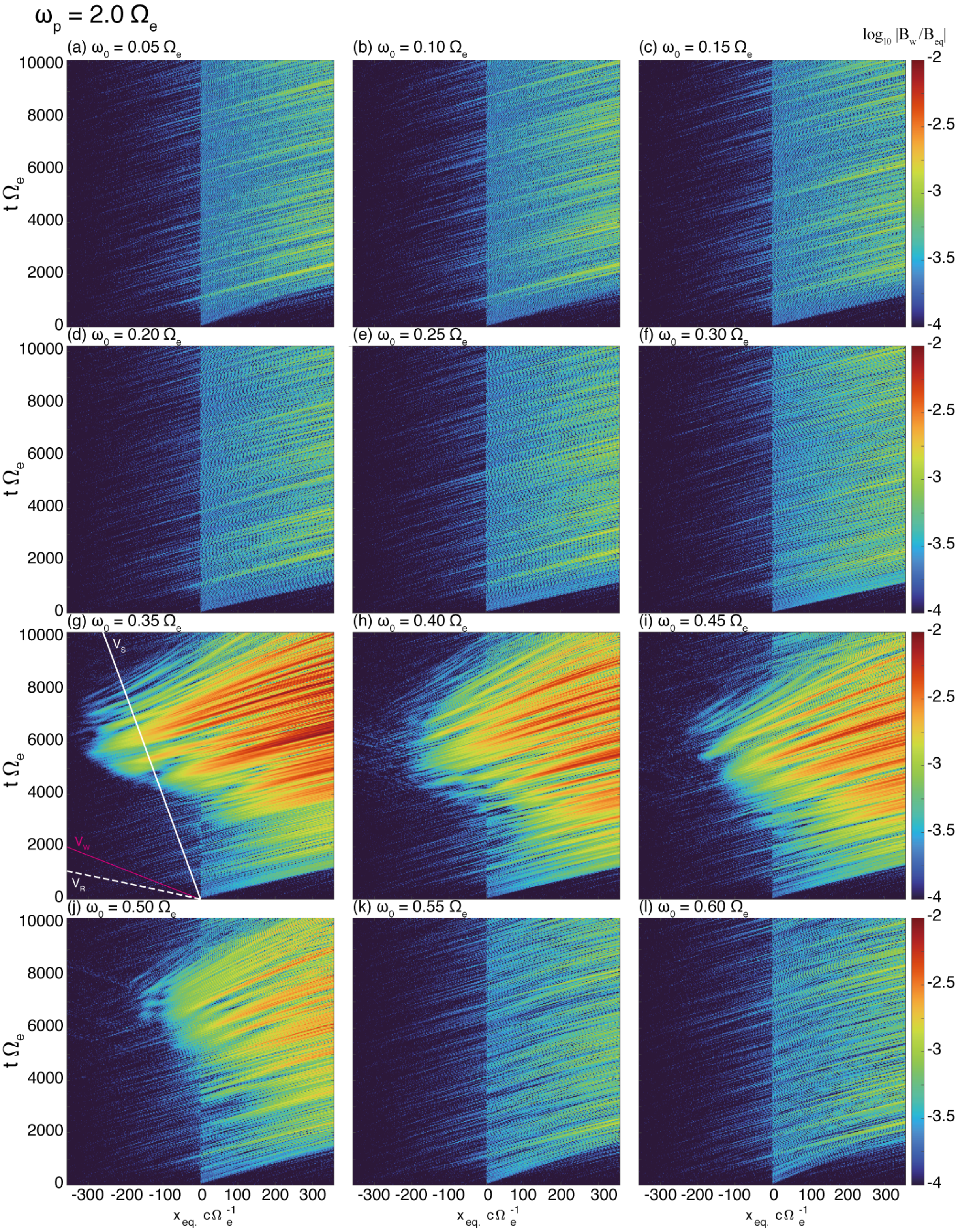

Figure 4.7: Spatial and temporal profiles of magnetic fields for forward waves for Case 3 with plasma frequency $\omega_p = 2.0\,\Omega_e$ and triggering wave frequencies ω_0 from (a) $0.05\,\Omega_e$ to (i) $0.60\,\Omega_e$, respectively. (g) (solid magenta line) The velocity of wave generation V_W, (dashed white line) the resonance velocity for 100 keV electrons at the magnetic equator, (solid white line) the source velocity V_S for 100 keV electrons at the magnetic equator.

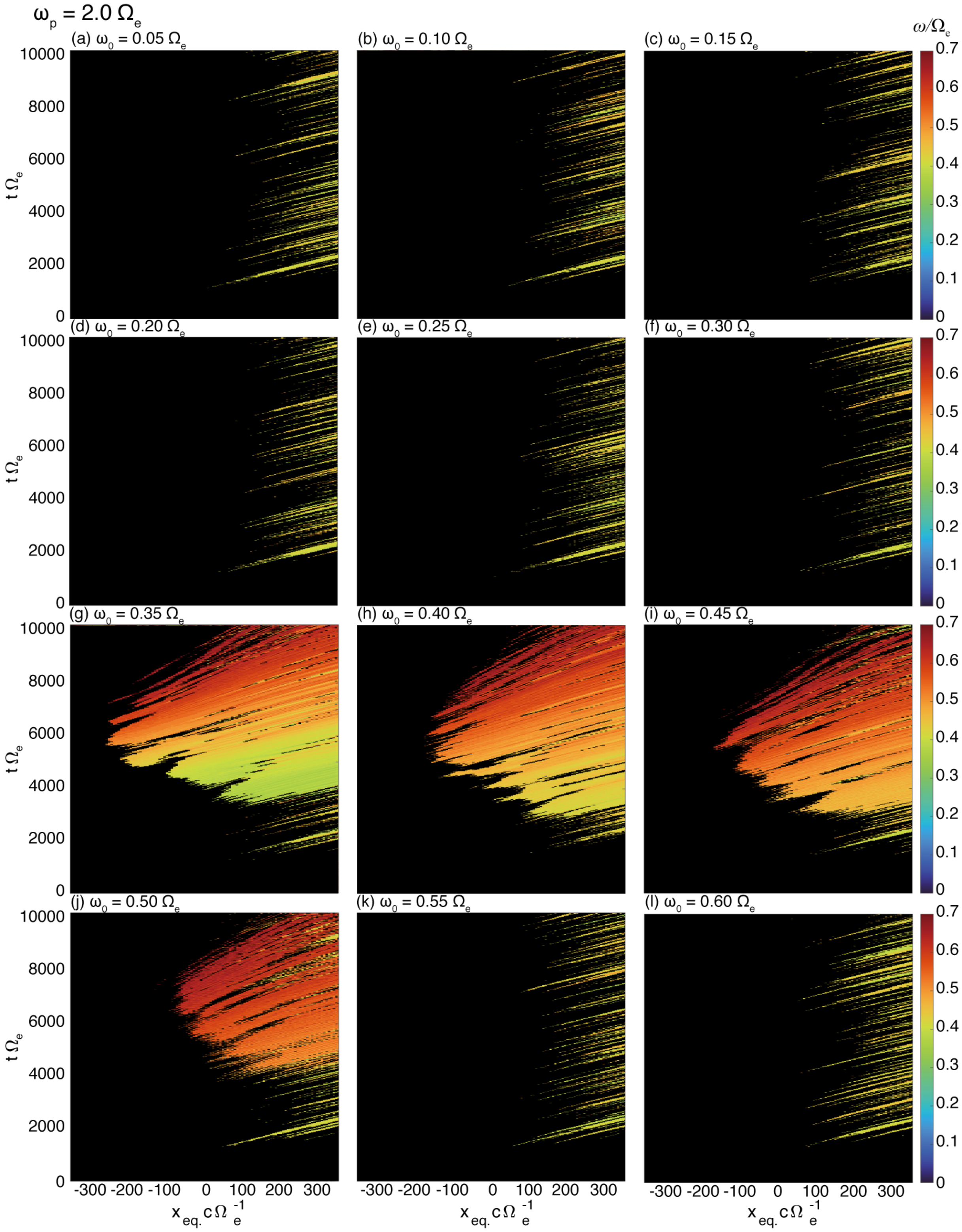

Figure 4.8: Spatial and temporal profiles of instantaneous frequency of triggered emissions for Case 3 with the plasma frequency $\omega_p = 2.0\,\Omega_e$ and different triggering wave frequencies ω_0 from (a) $0.05\,\Omega_e$ to (i) $0.60\,\Omega_e$, respectively.

triggered emissions, the conditions for optimum and threshold amplitude are satisfied. There is another condition that controls the generation of triggered emissions. Nonlinear wave growth involves two phases, which are absolute instability and convective wave growth. Absolute instability is defined as wave growth in time at a fixed position ($\frac{\partial \Omega_w}{\partial t} > 0$), which is dominant in the early phase of triggered emissions. Convective wave growth is the amplitude increase of a seed wave generated from the absolute instability in a frame of reference moving with the group velocity. Since we find no emission in the higher frequency range, the absolute instability is suppressed because the generation region for triggered emissions does not distribute over the upstream region of triggering waves. The motion of generation region is given by the source velocity V_S plotted in Figure 4.2. The source velocity is less than $-0.1\,c$ in magnitude or positive values for $10 \sim 100$keV electrons. With a small magnitude or a positive value of the source velocity, the generation region of triggered emissions does not expand over the interaction region. Assuming the constant growth rate in the vicinity of the equator, we can derive that the upstream shift of the generation region is required for obtaining the absolute instability growing from the same level of thermal fluctuations of the wave fields over the frequency range of emissions. We discuss the upstream shift of the generation region and the generation process in section 4.3.2. For obtaining continuous subpacket emissions with long duration, both nonlinear wave growth conditions $\Omega_{\text{op}} > \Omega_{\text{th}}$ and the upstream expansion of the generation region is required. The distribution and the expansion of the generation region are strongly related to the generation process of triggered emissions.

4.3.2 Upstream shift of generation region

In the present study, we define "upstream" as the opposite direction to the propagating triggering waves from the magnetic equator, and "upstream region" as the opposite area to the triggering waves through the magnetic equator in low latitude, respectively. With the plasma frequency $4.0\,\Omega_e$, we observe the generation of strong long wave packets forming rising-tone emissions in Figures 4.3d, 4.3e, and 4.3f, where the generation region of the subpackets moves to the upstream region of the triggering wave. In Figure 4.3d, the velocity of the upstream shift of the wave generation region (V_w) for forward propagating waves at the equator is equal to approximately $-0.12c$, indicated by a solid magenta line. The velocity is smaller than the resonance velocity $V_R = -0.35\,c$ in magnitude with $\omega = 0.2\,\Omega_e$ at the equator shown in white dashed line for 100 keV resonant electrons. Because the formation of the resonant current causes the generation of rising-tone emissions, it indicates that the spatial structure of the resonant current moves at a different speed from the resonance velocity. Nogi and Omura (2022) have introduced the concept of the source velocity, which describes the velocity of the spatial structure of resonant current, given by $V_S = V_R + V_g$. We find the velocity of the upstream shift of the wave generation region is in good agreement with the source velocity for 100keV electrons.

The source velocity V_S is plotted as a function of frequency for different kinetic energies

$10, 50, 100, 200\,\mathrm{keV}$ for $\omega_p = 4.0\,\Omega_e$ in Figure 4.2b. As the frequency of the triggering wave increases from $0.2\,\Omega_e$, the magnitude of the source velocity decreases, while the resonance energy decreases and compensates for the decreasing source velocity. Thus, the generation region shifts upstream with nearly a constant velocity. The condition of the absolute instability gives a necessary condition of $V_S < 0$ for triggering new emissions.

Throughout the generation of rising-tone emissions, the triggered subpacket continuously modulates the phase space distribution of counter-streaming resonant electrons, and the phase-modulated electrons form a subsequent subpacket. The process takes place repeatedly during the generation of triggered emissions. We have confirmed that the upstream motion of the generation region for the plasma frequency $4.0\,\Omega_e$ agrees with the source velocity. When the source velocity becomes positive in the generation process of a series of subpackets at progressively higher frequencies, the generation process comes to an end with the formation of small subpackets, as we find in Figures 4.3d, 4.3e, and 4.3f.

In the cases of $\omega_p = 6.0\,\Omega_e$ and $\omega_p = 2.0\,\Omega_e$, we find that the generation region of subpacket moves with different velocities from the source velocity. Figure 4.5c indicates that the velocity of the generation region shown in the solid magenta line is smaller in magnitude than the source velocity shown in the solid white line. Figure 4.7g shows an opposite tendency that the velocity of the generation region shown in the solid red line is greater than the source velocity shown in the solid white line. We also find that the duration and intensity of the subpacket in those cases are different from the case of $\omega_p = 4.0\,\Omega_e$. Comparing Figure 4.3d with Figure 4.5c and 4.7g, we find that the durations of the subpackets are different. In the next section, we discuss the discrepancy in the velocity of the wave generation region by comparing the formation processes of subpackets in the three cases.

4.3.3 Subpacket formation and motion of generation regions

The concept of the source velocity is based on the formation of the resonant current caused by the phase-organized electrons. The formation of subpacket structures of rising-tone emission gives rise to the deviation of the wave generation point from the source velocity. We extend the concept of the source velocity V_S to include the motion of the generation point of subpackets and define the velocity of the wave generation point as V_W given by

$$V_W = pV_R + qV_g, \quad \text{where} \begin{cases} p = 1 \quad \text{and} \quad q = 1\,, & \text{or} \\ 0 < p < 1 \quad \text{and} \quad q = 1\,, & \text{or} \\ p = 1 \quad \text{and} \quad 0 < q < 1\,. \end{cases} \tag{4.6}$$

When the continuous formation of a wave packet takes place as shown in Case 1 ($\omega_p = 4.0\,\Omega_e$), the velocity of wave generation V_W is identical to the source velocity, which corresponds to $p = q = 1$ in equation (4.6). When the formation of a wave packet is interrupted because of the damping phase of the wave packet after the saturation, as shown in Case 3 ($\omega_p = 2.0\,\Omega_e$),

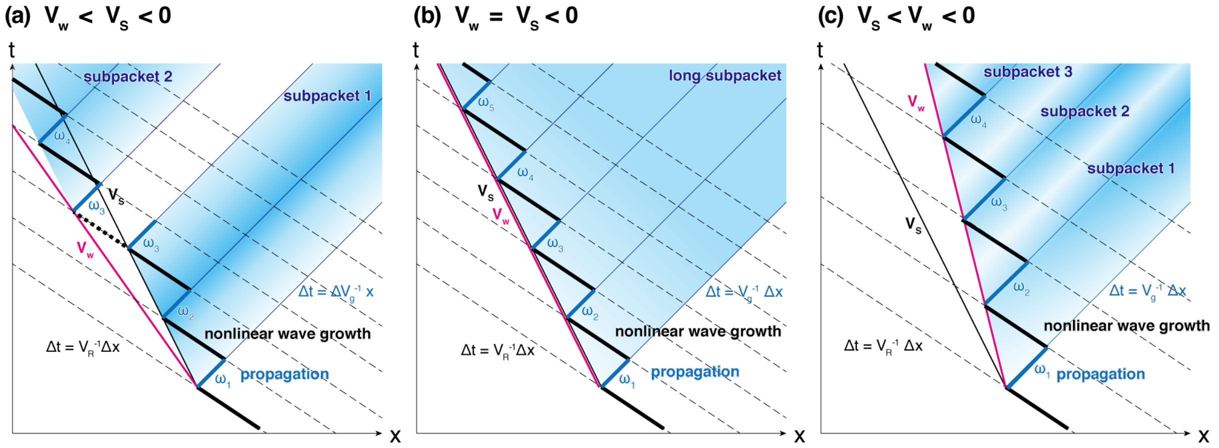

Figure 4.9: Schematic illustrations of the generation processes of subpacket structure with different velocities of wave generation; (a) The velocity of wave generation V_W is less than the source velocity $V_S = V_R + V_g$. (b) V_W is equal to V_S. (c) V_W is greater than V_S.

there arises a gap between the first wave packet and the subsequent wave packet. The results, in the absence of wave propagation over the gap, can be represented by the reduced factor q $(0 < q < 1)$ of V_g and $p = 1$. As shown in Case 2 ($\omega_p = 6.0\,\Omega_e$), the formation of the resonant current is delayed, and the period of the nonlinear wave growth is shortened. The reduction of the nonlinear wave growth period can be represented by the reduced factor p $(0 < p < 1)$ of V_R and $q = 1$. The schematic illustrations of the generation process of subpacket structure are shown in Figure 4.9.

Figure 4.10 shows spatial distributions of frequency spectra. In Figure 4.10a, three subpackets are formed with discrete frequency gaps, and the instantaneous frequency of each subpacket continuously increases as shown by arrows for sp_1, sp_2, and sp_3. Between sp_2 and sp_3, the subpackets are overlapped at $x = 200\,c\Omega_e^{-1}$. The frequency of the beginning of the latter subpacket shown as sp_3 is less than or equal to the frequency at the termination of the former subpacket as sp_2. The frequency discontinuity between subpackets remains in the later phase of triggered emissions, as shown in Figure 4.10b. Because the group velocity with the frequency greater than $0.25\,\Omega_e$ monotonically decreases as the frequency increases, the separation distance between sp_2 and sp_3 increases through propagation.

Figure 4.9a shows a schematic illustration of the generation process of short subpackets in Case 3. The dashed blue lines indicate trajectories of resonance electrons moving at the resonance velocity, and the solid blue lines indicate the propagation of triggered waves with the group velocity. The solid thin black line indicates the source velocity V_S, and the magenta line indicates the velocity of the wave packet V_W. The first subpacket is triggered from the injected triggering waves, and the generation of waves continuously takes place along V_S in a subpacket, forming a greater resonant current from ω_1 to ω_2. The wave amplitude of the triggered subpacket approaches the optimum amplitude by virtue of greater resonant current,

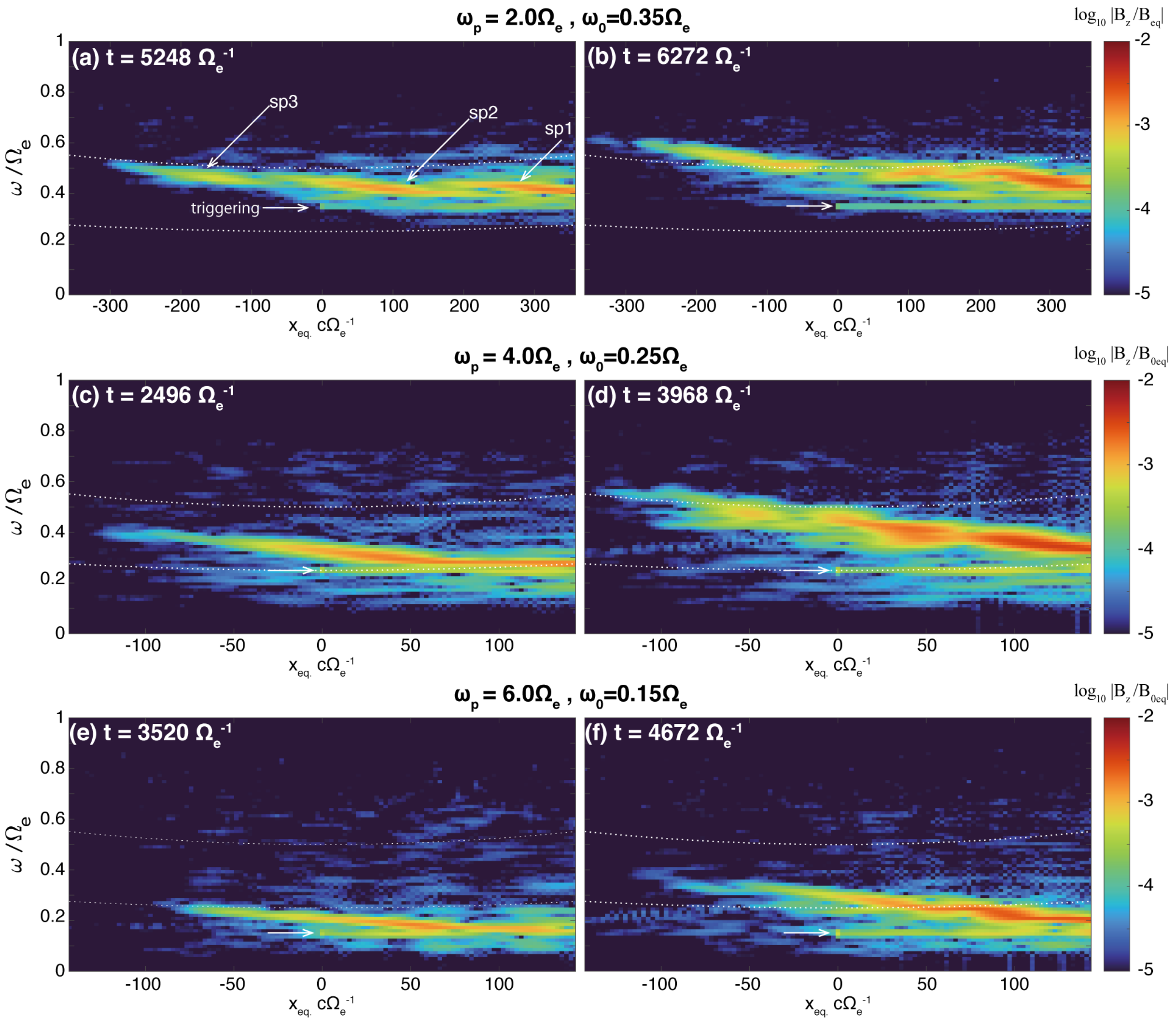

Figure 4.10: Snapshots of the spatial distribution of wave frequencies for plasma frequencies, (a,b)$\omega_p = 2.0\,\Omega_e$, (c,d) $4.0\,\Omega_e$ and (e, f) $6.0\,\Omega_e$, respectively; (dotted lines) One-quarter and one-half of the local electron cyclotron frequencies. (white arrows) the injection point and frequency of the triggering wave.

and the nonlinear wave growth is suppressed in the latter phase of the subpacket from ω_2 to ω_3. The phase organization of resonant electrons is enhanced in the vicinity of the propagation path of the wave packet with ω_2. In contrast, the release of the phase structure is suppressed due to the weak amplitude in the termination of the first subpacket, as shown in the bold black line toward ω_3. The phase-organized electrons keep their spatial structure with phase space modulation, and some of the phase-organized electrons are carried with the resonance velocity as shown in the dashed black line, and the second subpacket is generated. As a result, the velocity of the generation point over the multiple subpackets (V_W) becomes less than V_S. This generation model of the short subpacket is similar to that by Hanzelka et al. (2020), while our new model indicates that the motion of each subpacket is given by the source velocity.

When a triggered wave packet is long enough in space and time, the generation region moves with the source velocity as we find in Case 1 ($\omega_p = 4.0\,\Omega_e$) shown in Figures 4.3 and 4.4. With the plasma frequency $4.0\,\Omega_e$ and triggering wave frequency $0.25\,\Omega_e$, we observe the formation of multiple subpackets, while the spectrum analyses indicate that a single long-sustaining subpacket is generated in the vicinity of the generation region as shown in Figures 4.11c, 4.11b3, and 4.11b4. Figure 4.9b shows a schematic illustration of the generation process of a triggered emission for a long subpacket. In the long-sustaining subpacket, phase-organized particles by the triggered wave generate a subsequent wave with a slightly higher frequency, and the subsequent wave modulates fresh resonant electrons. These microscopic processes continuously take place in the vicinity of the generation region, which moves upstream from the triggering wave. For a long subpacket generation, the velocity of the wave packet (V_W) and the source velocity are approximately the same negative value so that absolute instability is maintained in the generation region. When the magnitude of the source velocity is small, the growth rate of the absolute instability at a fixed position becomes small.

When the triggering wave is injected with a frequency $0.15\Omega_e$ in Case 2 ($\omega_p = 6.0\,\Omega_e$), two long subpackets separated at $0.25\,\Omega_e$ are generated in the vicinity of the generation region in Figure 4.11c3.

The wave growth and frequency sweep rate below $0.25\,\Omega_e$ is weaker than those above $0.25\,\Omega_e$. The subpacket splits into multiple short subpackets through convective wave growth. Nonlinear wave growth in the upstream region of the equator is weaker than in other cases with $\omega_p = 2.0\,\Omega_e$ and $4.0\,\Omega_e$. Figure 4.9c shows the schematic illustration of the generation process with $\omega_p = 6.0\,\Omega_e$. The ratio of the duration of the nonlinear wave growth to the propagation time of triggered waves becomes small, and the source velocity becomes small, while its value is still negative.

The wave packets below the frequency $0.25\,\Omega_e$ are grouped together because of the variation of group velocity $\partial V_g/\partial\omega > 0$. As we find in Figure 4.2, the group velocity increases with the increasing frequency and maximizes at $\omega = 0.25\Omega_e$. When a rising-tone emission is started below $0.25\,\Omega_e$, a lower frequency packet is generated first, followed by a higher frequency

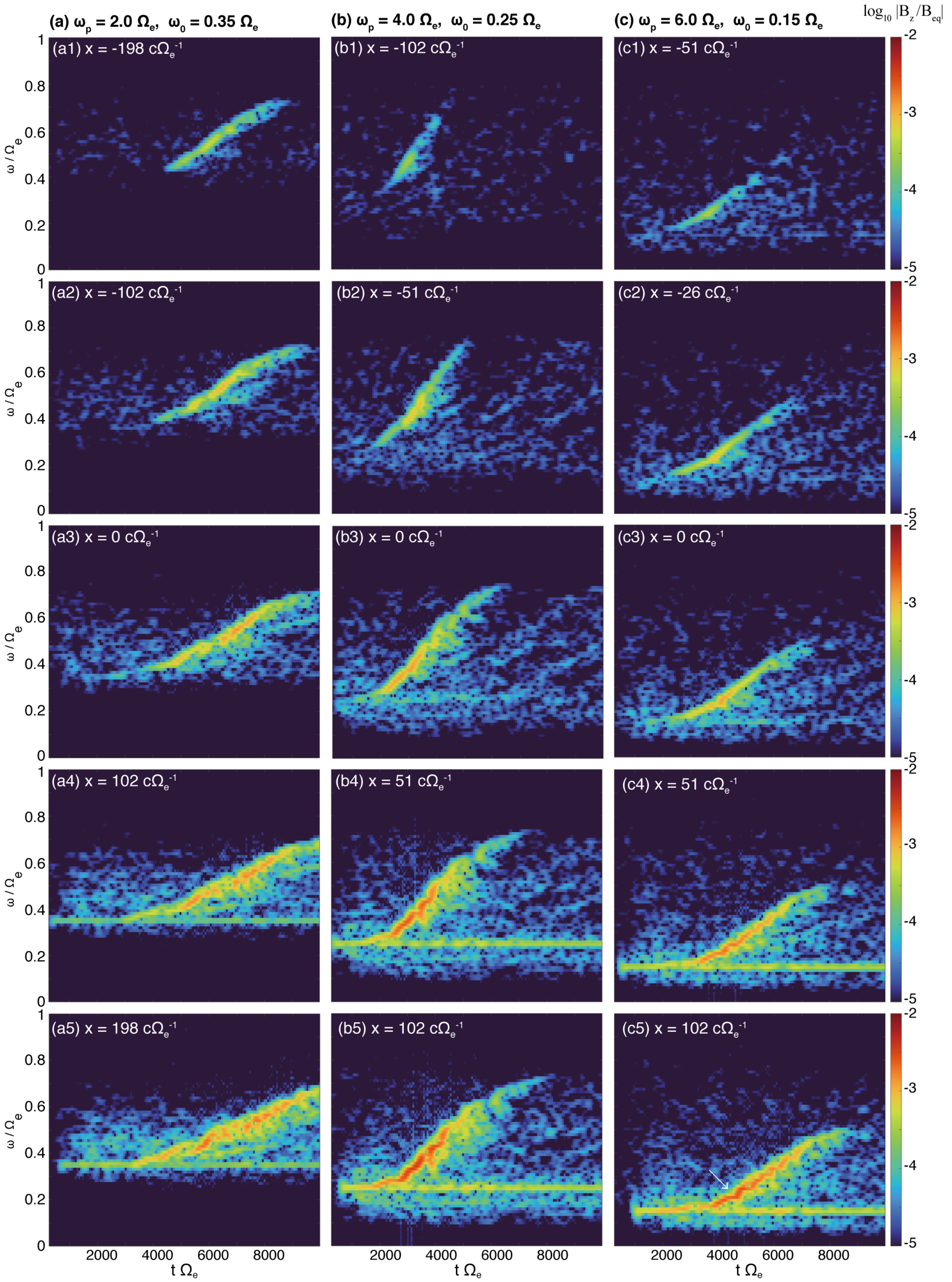

Figure 4.11: Dynamic spectra of distinct rising-tone emissions for plasma frequencies (a) $\omega_p = 2.0\,\Omega_e$, (b) $\omega_p = 4.0\,\Omega_e$, and (c) $\omega_p = 6.0\,\Omega_e$ at different positions from (1) to (5), which corresponds to positions from the upstream region to the downstream region for forward propagating waves.

packet with a higher group velocity. The wave packet with higher frequency has a tendency to catch up with the lower frequency wave packet. Because of this dispersion effect, the subpackets with frequencies below $0.25\,\Omega_e$ have a tendency to coalesce with each other, as we find in Figure 4.5c. In the corresponding spatial and temporal profile of the magnetic field, we observe that several subpackets cross at a certain point, as shown by the arrow in Figure 4.11c5. The coalescence of wave packets below $0.25\,\Omega_e$ is in agreement with the observation results reported by Foster et al. (2017).

When the electron holes are formed with two different frequency waves, while the trajectories of trapped and untrapped particles with two waves are mutually independent, we can regard each wave as coherent in terms of nonlinear wave-particle interaction (Omura, 2021). When a long triggered wave is generated as in Case 1 ($\omega_p = 4.0\,\Omega_e$), the criterion of coherence is satisfied in both the upstream region and the downstream region of the triggering waves. In Case 2 ($\omega_p = 6.0\,\Omega_e$), on the other hand, the new wave packets overtake the waves with lower frequencies in the upstream region of triggering waves, and the coherence of the waves in the generation region deteriorates. The formation of resonant currents becomes less effective, and the generation of wave packets is interrupted, resulting in the generation of a short subpacket in Case 2.

4.3.4 Dynamic frequency spectra

Figure 4.11 shows dynamic spectra observed at different positions for forward propagating waves from upstream to downstream for different plasma frequencies, (a) $2.0\,\Omega_e$, (b) $4.0\,\Omega_e$ and (c) $6.0\,\Omega_e$. We plot the dynamic spectra for the runs with the frequencies of triggering wave (a) $0.35\,\Omega_e$, (b) $0.25\,\Omega_e$, and (c) $0.15\,\Omega_e$, in which triggered emissions are observed. From the top to the bottom of each column, we plot dynamic spectra observed at different positions from the upstream region to the downstream region for forward propagating waves. We perform short-time discrete Fourier transformation for forward propagating waves with a window size $\Delta t = 512\,\Omega_e^{-1}$, which has 65,536 data points and shifting the window by $64\,\Omega_e^{-1}$, corresponding to 8,192 data points. In all cases shown in Figure 4.11, we find that triggered emissions show rising-tone frequencies. The frequency of the triggered waves increases monotonically in the generation region in Figures 4.11b1 and 4.11c1, while the frequency increase is suppressed between the subpackets in Figure 4.11a1.

In the case with $\omega_p = 2.0\,\Omega_e$ and $\omega_0 = 0.35\,\Omega_e$, relatively short subpackets are generated throughout the emission as shown in Figures 4.11a1 to 4.11a5. The generation region moves from the downstream region to the upstream region of the magnetic equator, and the frequency gap between subpackets enlarges as the triggered waves propagate, resulting in the discontinuity of the frequency variations between subpackets as shown in Figures 4.11a3 and 4.11a4.The generation of short subpackets and the frequency gap between subpackets are consistent with the generation model of the subpackets illustrated in Figure 4.9a.

Continuous long subpackets are observed in the generation region of the upstream region of triggered emissions with $\omega_p = 4.0\,\Omega_e$ and $\omega_0 = 0.35\,\Omega_e$ as shown in Figures 4.11b1 and 4.11b2. The instantaneous frequencies of triggered emissions are greater than $0.25\,\Omega_e$, and continuous formation of the resonant current takes place as illustrated in Figure 4.9b.

In the case with $\omega_p = 6.0\,\Omega_e$ and $\omega_0 = 0.15\,\Omega_e$, the weak long subpacket is generated in the upstream region as shown in Figures 4.11c1. The generation region of the subpackets with the frequency below $0.25\,\Omega_e$ exists in the vicinity of the equator in Figures 4.11c2 and 4.11c3. Figure 4.11c2 and 4.11c3 clearly show the frequency sweep rate below $0.25\,\Omega_e$ is smaller than those above $0.25\,\Omega_e$. We observe that the wave amplitude is enhanced at $0.25\,\Omega_e$ as indicated by a white arrow in Figure 4.11c5. Because the magnitude of group velocity maximizes at $0.25\,\Omega_e$, the wave packets converge in the downstream region of triggered emissions as discussed above.

Falling-tone emissions are generated from rising-tone triggered emissions in the higher frequency range in 4.11a4, 4.11a5, 4.11b4, 4.11b5, and 4.11c5. Falling-tone emissions are triggered by the termination of short rising-tone emissions in the downstream region of the subpackets. Ground observation of VLF triggered emissions have shown that shorter wave duration of injected waves leads to the generation of falling-tone emissions (Helliwell & Katsufrakis, 1974). Nogi et al. (2020) have reproduced falling-tone emissions by using similar parameters to the present paper, and the difference from the present paper is the duration period of triggering waves. Short period triggering waves around half the cyclotron frequency lead to falling-tone emissions, and long period triggering waves lead to rising-tone emissions. The generation of falling-tone emissions from a short rising-tone subpacket supports that the enhancement of trapping of resonant electrons forming electron hills is caused by short triggering waves. In the case with $\omega_p = 2.0\,\Omega_e$, falling-tone emissions are generated from rising-tone emissions with the frequency range from $0.5\,\Omega_e$ to $0.7\Omega_e$, which is upper-band chorus emissions. S. Liu et al. (2021) have shown by using Van Allen Probes that the initial frequency of distinct falling-tone subpackets gradually increases, and the sequence of the initial part of subpackets is aligned as upper-band rising-tone emissions. The present result shown in Figure 4.11a5 is similar to the observation result by S. Liu et al. (2021), except for the frequency gap between lower-band and upper-band chorus emissions. Because the parallel propagation in the one-dimensional model is assumed in the present simulation, the frequency gap due to nonlinear damping through Landau resonance cannot be formed.

4.3.5 Evolution of velocity distribution function

Figure 4.12 shows the velocity distribution of energetic electrons in the vicinity of the magnetic equator. The initial velocity distribution function f_0 is shown in Figures 4.12a and 4.12b for Case 3 ($\omega_p = 2.0\,\Omega_e$) and Case 2 ($\omega_p = 6.0\,\Omega_e$), respectively. Figures 4.12c to 4.12h show the differences from the initial velocity distribution function for (c, d) beginning of the triggered emissions, (e, f) middle phase of the triggered emissions, and (g, h) termination of the trig-

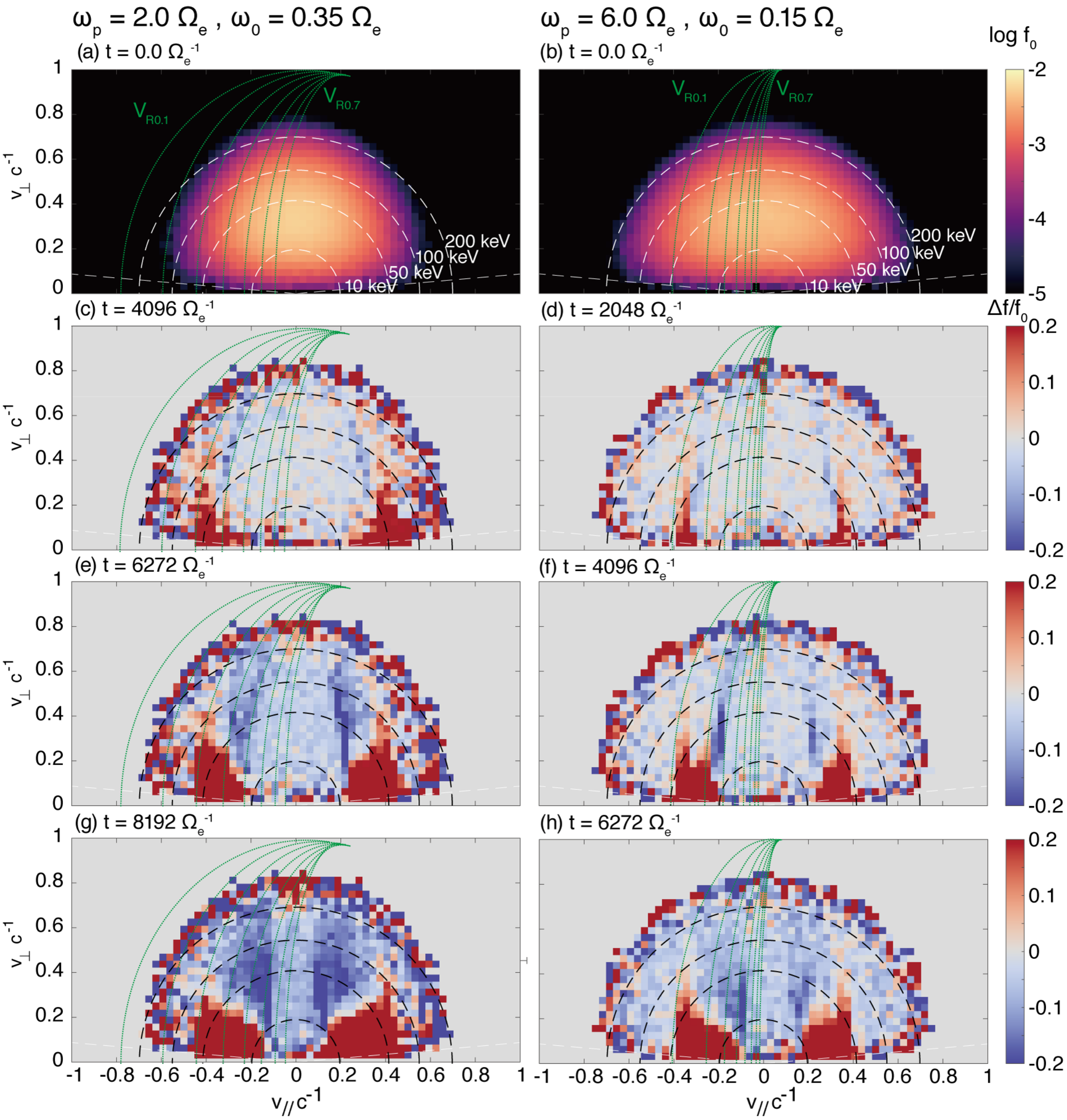

Figure 4.12: Time evolution of velocity distributions of energetic electrons at the equator for plasma frequencies, $\omega_p = 2.0\,\Omega_e$ and $6.0\,\Omega_e$ with triggering wave frequencies $\omega_0 = 0.35\,\Omega_e$ and $0.15\,\Omega_e$, respectively; (a, b) The initial distribution f_0, (c, d) f/f_0 variation from the initial distribution at the beginning, (e, f) the middle, and (g, h) the end of triggered emissions. Green lines show resonance velocities for frequencies from $0.1\,\Omega_e$ to $0.7\,\Omega_e$.

gered emissions, respectively. The variation of the velocity distribution for $\omega_p = 4.0\Omega_e$ with triggering wave $0.3\Omega_e$ is presented in Figure 3.11 in Chapter 3.

The density modulation in velocity phase space takes place in the vicinity of the resonance velocity, shown with green lines in Figures 4.12a-4.12h. In the case with the plasma frequency $2.0\,\Omega_e$, we find that the resonance velocity varies from the frequency for $0.40\,\Omega_e$, $0.45\,\Omega_e$, and $0.65\,\Omega_e$ in Figures 4.12c, 4.12e, and 4.12g, respectively. The frequencies for the resonance velocities at which the depletion of phase space density is formed are in agreement with the instantaneous frequency at the equator, as shown in Figure 4.11a3. With $\omega_p = 6.0\,\Omega_e$, we have confirmed that the frequencies for resonance velocities of the density depletion are consistent with the instantaneous frequency in Figure 4.11c3.

The energy range for the case with $\omega_p = 2.0\,\Omega_e$ is presumed from 50 keV to 100 keV in the initial phase, 10 to 50 keV in the end of triggered emissions. The effective energy range of nonlinear growth of chorus emissions is $10-100$ keV. In this energy range, we find a relatively strong depletion of electrons in Figure 4.12. Resonant electrons forming a hole in velocity phase space are scattered to lower pitch angles, and some of them get into the loss cone. In the energy range of $10-40$ keV, we can find strong precipitation due to the generation of chorus emissions. The acceleration of electrons takes place in the higher energy range as we find an enhanced electron flux around 90 degrees of pitch angle in Figure 4.12g.

Comparing Figure 4.12c with Figure 4.12d, we find the difference in the depth of the electron hole. In the case with $\omega_p = 2.0\,\Omega_e$, intense modulation of the density takes place due to a deeper electron hole (= greater Q value), leading to greater resonant current than that with $\omega_p = 6.0\,\Omega_e$. The initial difference in the intensity of the resonant current controls the absolute and convective growth rates and frequency sweep rates. In the case with $\omega_p = 6.0\,\Omega_e$, the modulation of the phase space density due to the formation of the electron hole is suppressed at the initial phase of the triggered emissions, as shown in Figure 4.12d. The forgoing subpacket at $0.20\,\Omega_e$ is overtaken by the subsequent subpacket at $0.25\,\Omega_e$, and coherent nonlinear wave-particle interaction is suppressed.

4.4 Summary and discussion

We have performed simulations of whistler-mode wave-particle interaction in a parabolic magnetic field with 12 different frequencies of triggering waves and three different plasma frequencies specifying cold plasma densities. Under a given plasma condition, specific frequency ranges of the triggering wave generate rising-tone emissions. We summarise the characteristics of triggered emissions as follows.

1. The generation regions of rising-tone emissions move upstream from the triggering waves.
2. The source velocity represents the motion of resonant current, while the velocity of the

wave generation includes formation processes of subpackets and their intervals. The velocity of wave packet generation is dependent on the duration of the subpacket controlled by the formation time of the resonant current in the generation region.

3. When the source velocity is approximately the same as the velocity of wave packet generation, the resonant current is formed continuously, leading to a long-sustaining rising-tone emission.
4. When the spatial and temporal gap between subpackets exists due to the damping phase of the generation of a short subpacket, resonant electrons in the gap of the subpacket are carried at the resonance velocity to the upstream region, forming subsequent subpacket. As a result, the velocity of wave generation increases in magnitude.
5. When the formation of resonant currents is delayed, the velocity of wave generation becomes smaller than the source velocity in magnitude. Coalescence of subpackets takes place below the frequency $0.25\,\Omega_e$, delaying the formation of the resonant current in the generation region.
6. As a condition for an absolute instability of the wave, the source velocity should be a small negative value. Namely, a gradual upstream shift of the source region is necessary for the wave to grow locally.
7. In the frequency range for the upper-band chorus of rising-tone emissions, short falling-tone packets are generated along with rising-tone packets.

In the present study, we have observed the generation of rising-tone emissions from the triggering waves below one-half of cyclotron frequency. The maximum frequency of rising-tone triggered emissions is greater than one-half of electron cyclotron frequency, while we have not observed a frequency gap at $0.5\,\Omega_e$, which is typically observed in chorus waves. Ratcliffe and Watt (2017) have proposed the model that the modulated electron distribution function is formed, and two distinct peaks of linear growth rate in frequency appear, resulting in the generation of lower-band and upper-band chorus emissions. The modulation in the velocity distribution function in frequency can be caused by Landau resonance (J. Li et al., 2019; Sauer et al., 2020; H. Chen et al., 2021; H. Chen, Gao, et al., 2022; J. Li et al., 2022). We have assumed parallel propagation of whistler-mode waves by taking the one-dimensional simulation system along the magnetic field line. Since there arises no electric field in the parallel direction, we have neglected the electrostatic field. In the real magnetosphere, the wave normal angles of the triggered emissions should deviate from the parallel direction, and there occurs effective Landau resonance at half the cyclotron frequency where the group velocity and phase velocity become equal. The rising-tone emissions crossing half the cyclotron frequency are expected to undergo damping near the local cyclotron frequency, resulting in lower-band and upper-band emissions (Omura et al., 2009; Hsieh & Omura, 2018). Self-consistent simulations in a two-dimensional system are necessary for confirmation of the gap formation in the rising-tone emissions propagating obliquely to the magnetic field. Such a two-dimensional simulation was performed by Ke et al. (2017). They did not find the formation of the gap, possibly because of the smallness of the simulation system. Two-dimensional simulations with sufficiently large spatial extent are left as a future study.

Chapter 5

Generation process of falling-tone emissions

5.1 Introduction

VLF chorus emission is one of the most significant wave phenomena in the Earth's magnetosphere. Chorus is commonly observed in the inner magnetosphere as intense whistler-mode waves, in the frequency range of 0.1-0.8 f_{ce} (f_{ce} is the equatorial electron gyrofrequency), with right-hand polarization, and propagating along the ambient magnetic field line (e.g., Oliven & Gurnett, 1968; Tsurutani & Smith, 1974; Koons & Roeder, 1990; Gurnett et al., 2001; Meredith et al., 2001, and others). They are composed of coherent wave packets with rising or falling frequency. The artificially excited rising and falling tones have also been observed from weak and monochromatic whistler wave signals, known as "triggered VLF emissions" (Helliwell & Brice, 1964; Helliwell & Katsufrakis, 1974; Helliwell et al., 1980, 1986; Helliwell, 1983). Comparisons between chorus emissions and triggered emissions have revealed that the triggered emissions have the same generation mechanism as chorus (Helliwell, 1988; Trakhtengerts et al., 1996; Nunn, 1986, 1990).

In general, the source of whistler-mode waves is associated with anisotropic energetic electrons in the equatorial region (Kennel & Petschek, 1966; Tsurutani & Smith, 1974; Tsurutani et al., 1979; LeDocq et al., 1998; Parrot et al., 2003; Santolík et al., 2004, 2005, 2008). It has been explained by both linear and quasi-linear theory (e.g., Hashimoto & Kimura, 1981; Cornilleau-Wehrlin et al., 1985; Solomon et al., 1988, and others). On the other hand, in the generation of the discrete structure of chorus, nonlinear processes play an important role. In the nonlinear growth theory, the resonant current formed by electron trapping results in the rapid growth of amplitude and the time variation of rising and falling frequencies (Nunn et al., 1997, 2009; Omura et al., 2008, 2009).

For a better understanding of these complicated nonlinear processes, many numerical simulations have been conducted, reproducing nonlinear trapping of resonant electrons. A one-dimensional Vlasov hybrid code has been developed for simulating chorus emissions (Nunn, 1974). Nunn and Omura (2012) has shown that a falling-tone emission can be excited from the upstream region by a triggering pulse with a constant frequency. Katoh and Omura (2007) and Tao (2014) have successfully reproduced rising tones by self-consistent electron hybrid codes, assuming energetic electrons with a temperature anisotropy. Hikishima et al. (2010) has developed a full-particle simulation for chorus and triggered emissions. As for the background magnetic field model, Ke et al. (2017) have expanded the electron hybrid codes from 1-D to 2-D model and also reproduced discrete rising-tone emissions. Recently, Lu et al. (2019) has reported a 2-D simulation of rising-tone emissions in the dipole magnetic field.

In this paper, we conduct a one-dimensional self-consistent full PIC calculation for simulating a triggered falling-tone emission. Section 2 describes the simulation model, initial conditions, and the method of triggering whistler-mode waves. In section 3, we show the results of exciting a triggered falling-tone emission. We discuss the generation process of the emission based on the dynamics of resonant currents in section 4. Finally, section 5 gives the conclusions.

5.2 Simulation model

To simulate triggered chorus emissions, we use a one-dimensional full particle-in-cell code, which is developed by Kyoto university ElectroMagnetic Plasma cOde (KEMPO) by Omura and Matsumoto (1993); Omura (2007). We adopt a cylindrical coordinate with the x axis along the nonuniform magnetic field. The background magnetic field is assumed axisymmetric and parabolic as a function of x. One-dimensional Maxwell's equations and three-dimensional equations of motion are solved for transverse electromagnetic fields and electrons, respectively. We assume an ideal situation of triggered emissions, which are excited from an artificial signal at the magnetic equator. The simulation system is illustrated in Figure 5.1.

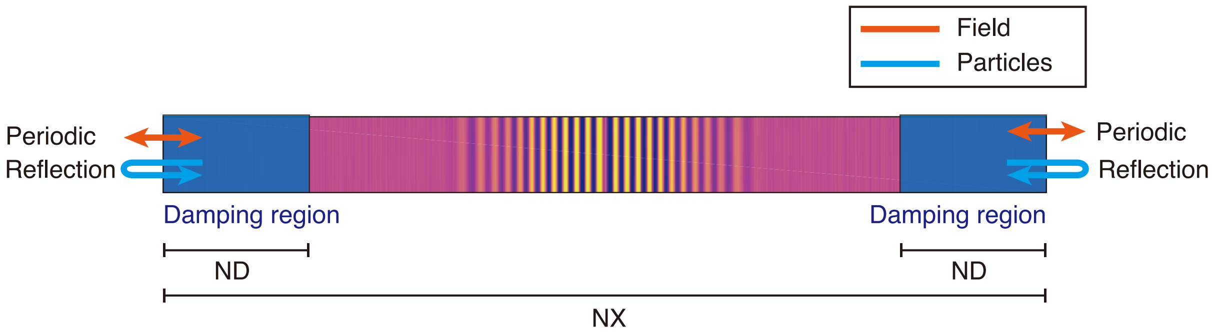

Figure 5.1: The schematic illustration of the one-dimensional simulation model. Total Simulation region (NX) includes damping region (ND).

We set the x-axis along the field line. Near the magnetic equator, the x-component of the

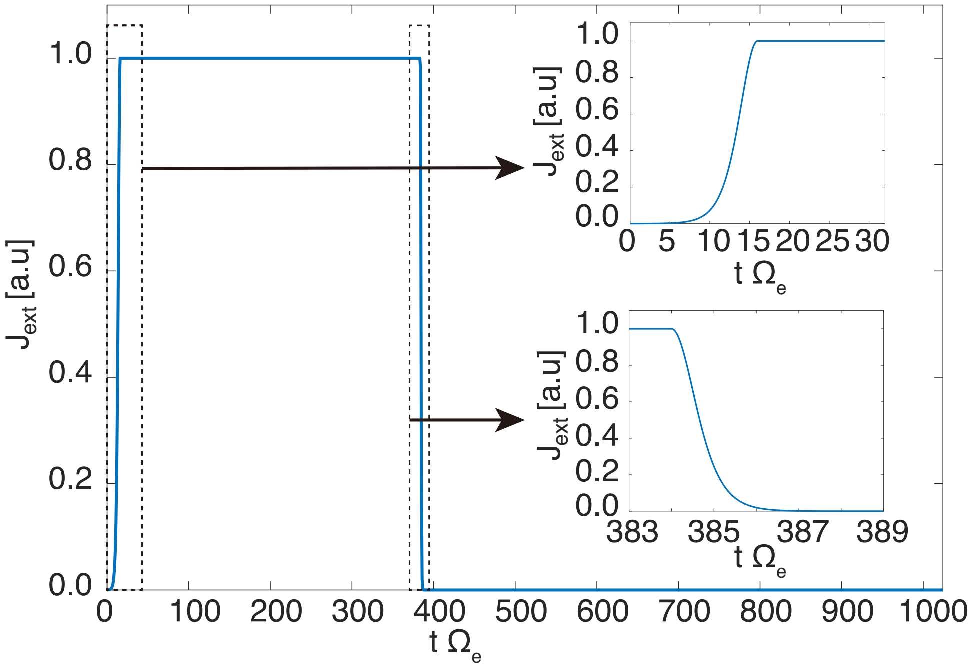

Figure 5.2: The time profile of the magnitude of the injected currents.

dipole magnetic field B_x is approximated by parabolic variation as

$$B_x(x) = B_{\mathrm{eq}}(1 + ax^2)\,, \tag{5.1}$$

where x is the distance along the field line from the equator, and B_{eq} and a are the equatorial value of B_x and the coefficient of the parabolic variatons of the background magnetic field, respectively.

At the equator, we put an external sinusoidal current J_z oscillating with a constant frequency for a finite time duration. Basically J_z generates E_z variations around the equator. The excited field propagates as whistler-mode wave packets with circular polarization in y and z as they move away from the equator. The external current J_z has nothing to do with resonant currents, which will be described in section 4. To reduce the Gibbs oscillation noise from the onset and the termination of the current, we apply the window function to the external current as $\cosh(t-\Delta t)$, where $(\Delta t) = 15\,\Omega_e^{-1}$ and $384\,\Omega_e^{-1}$ at the beginning and the end of the triggering, respectively. Figure 5.2 shows the time evolution of the magnitude of the external current.

In this paper, we report three different cases, as shown in Table 5.2. In the present paper, we compare Cases 1 and 2 to survey the generation mechanisms for different frequencies. Case 3 represents a uniform magnetic field model to compare with the effect of the parabolic background magnetic field model. In the present paper, we set the frequency as $0.51\,\Omega_e$ so that the group velocity and the phase velocity of whistler-mode waves take the same value at a certain distance from the equator. Table 5.1 shows numerical and plasma parameters in the simulations, normalized by the speed of light c in a vacuum and the electron cyclotron frequency Ω_e at the magnetic equator.

Table 5.1: Common simulation parameters in all cases

Parameter	Value
Time step	$0.007812\,\Omega_e^{-1}$
Grid spacing	$0.025\,c\Omega_e^{-1}$
Number of grids NX	8192
Length of simulation region	$204.8\,c\Omega_e^{-1}$
Total number of cold electrons, N_c	2,147,483,648
Total number of energetic electrons, N_h	2,147,483,648
Total number of protons, N_i	268,435,456
Mass ratio of proton to electrons, m_i/m_e	1600
The average plasma frequency of cold electrons, ω_{pe}	$2.0\,\Omega_e$
Density ratio of energetic electrons to cold electrons, n_h/n_c	0.02
Thermal momenta of energetic electrons at the equator, $U_{th.,\parallel}$, $U_{th/,\perp}$	$0.225\,c$, $0.250\,c$
Temperature anisotropy, $A = T_\perp/T_\parallel - 1$	0.235
Loss cone angle, α_{loss}(degrees)	5
Loss cone parameter, β in equation (2.10)	0.09
Amplitude of triggering wave at the magnetic equator (constant), B_w	$0.02\,B_{eq.}$
Number of grids for damping region (ND)	256
Length for damping region	$6.4\,c\Omega_e^{-1}$

Table 5.2: Simulation parameters for each case

Parameter	Case 1	Case 2	Case 3
coefficient of parabolic magnetic field, $a\,c^2\Omega_e^{-2}$	4.48×10^{-5}	4.48×10^{-5}	Uniform
Frequencies of triggering wave (constant), ω	$0.3\,\Omega_e$	$0.51\,\Omega_e$	$0.51\,\Omega_e$

5.3 Results

5.3.1 Wave propagation

We first show wave power profiles in space and time. Figures 5.3a-5.3f and Figures 5.3c-5.3f show magnetic field powers with the frequencies of $\omega = 0.3\,\Omega_e$ and $0.51\,\Omega_e$. For comparison, 5.3e-5.3f presents the case with uniform background magnetic field.

In all cases, triggering waves are excited from $t = 40\,\Omega_e^{-1}$ to $384\,\Omega_e^{-1}$, and propagate forward (northward) and backward (southward) in the x direction. We separate forward and backward components of parallel propagating whistler-mode waves by means of the spatial helicity along the background magnetic field. The backward waves and forward waves show symmetric results, and we focus on the forward waves in this paper.

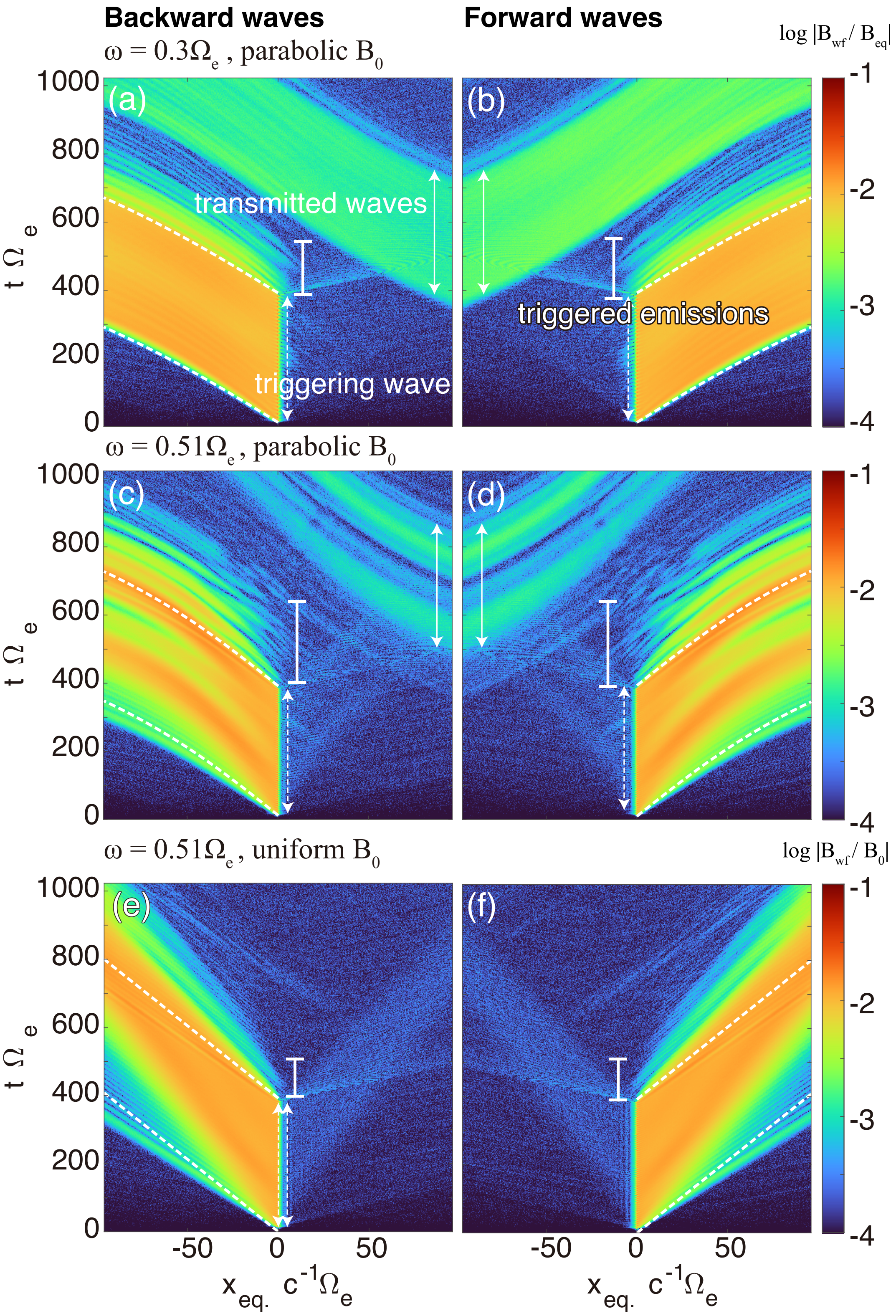

Figure 5.3: Spatial and time profiles of magnetic field magnitude for forward and backward waves with the frequencies of (a-b) $\omega = 0.3\,\Omega_e$ and (c-f) $0.51\,\Omega_e$. White dashed lines show the head and tail of the triggering wave, calculated as the waves with the triggering frequency propagate with the group velocity given by the local cold plasma dispersion relation.

After the stop of triggering, several sub-packets are triggered. The triggered emissions appear during 400−600 Ω_e^{-1}, 700 Ω_e^{-1}, and 500 Ω_e^{-1} in Figures 5.3b, 5.3d and 5.3f, respectively. We observe significant wave damping takes place at the wavefront for $\omega = 0.51\,\Omega_e$ for Figures 5.3d and 5.3f.

During $t = 400 - 700\,\Omega_e^{-1}$, weak waves are transmitted from the opposite boundary due to insufficient wave damping in the absorbing region. Those transmitted waves do not affect the physical process of our target of triggered emissions because it is second-order smaller and spatially separated from the main emissions.

5.3.2 Frequency analysis on triggering and triggered waves

Figure 5.4 shows dynamic spectrum of transverse magnetic field B_z at different locations along a magnetic field line $x = 20\,c\Omega_e^{-1}$ and $60\,c\Omega_e^{-1}$. The short-time fast Fourier transformation is applied over the magnetic field B_z with the Hamming window of one-quarter of total simulation time-shifting in $1/2048$ of simulation time. The triggering waves are indicated by solid green lines. Instantaneous frequencies of emissions are overplotted by dashed white lines. We define the emissions by the amplitude greater than 0.3% of B_{eq} and the coherence between B_y and B_z greater than 0.995. In all cases, we can see a broadband signal at the end of the triggering waves. The signal comes from the artificial termination of the injected current.

After the triggering wave with a constant frequency, triggered emissions can be seen with a small amplitude and a slightly rising frequency in Figures 5.4a-5.4b. In Figure 5.4c, the triggered emission appears during the period from $t = 500\,\Omega_e^{-1}$ to $600\,\Omega_e^{-1}$. The frequency significantly decreases from 0.51 Ω_e to 0.3 Ω_e. Figure 5.4c shows that the duration, amplitude, and frequency drop increase with the propagation. The triggered emission consists of rapid frequency modulation with a time scale of 50 Ω_e^{-1}. Figures 5.4e and 5.4f show that there occurs no significant emission in the uniform magnetic field model. There is no significant difference between Figures 5.4a and 5.4b, and Figures 5.4e and 5.4f, whereas Figures 5.4c and 5.4d show a significant evolution of the falling tone emission in space and time. Figure 5.4 clearly presents that there is neither intense wave growth nor frequency variation in the two cases with $\omega = 0.3\,\Omega_e$ and uniform magnetic field.

We also verify the frequency modulations by examining the time evolution of the electron velocity distribution. The waves should modulate the electron distribution with the resonance velocity determined by the local frequency. Figure 5.5 shows local velocity distributions of energetic electrons in the $(v_\parallel - v_\perp)$ plane at respective times with the different frequencies of the triggering waves. The blue and green lines in Figure 5.5 show the cyclotron resonance conditions for the initial and final frequencies of emissions (0.3 Ω_e and 0.35 Ω_e in Figure 5.5a, 0.35 Ω_e and 0.51 Ω_e in Figure 5.5b, and 0.51 Ω_e and 0.54 Ω_e in Figure 5.5c). On the resonance curve, the majority of energetic electrons are scattered to lower pitch angles. Figure 5.5b shows the largest variation of the resonance curve and the most effective scattering along the curves.

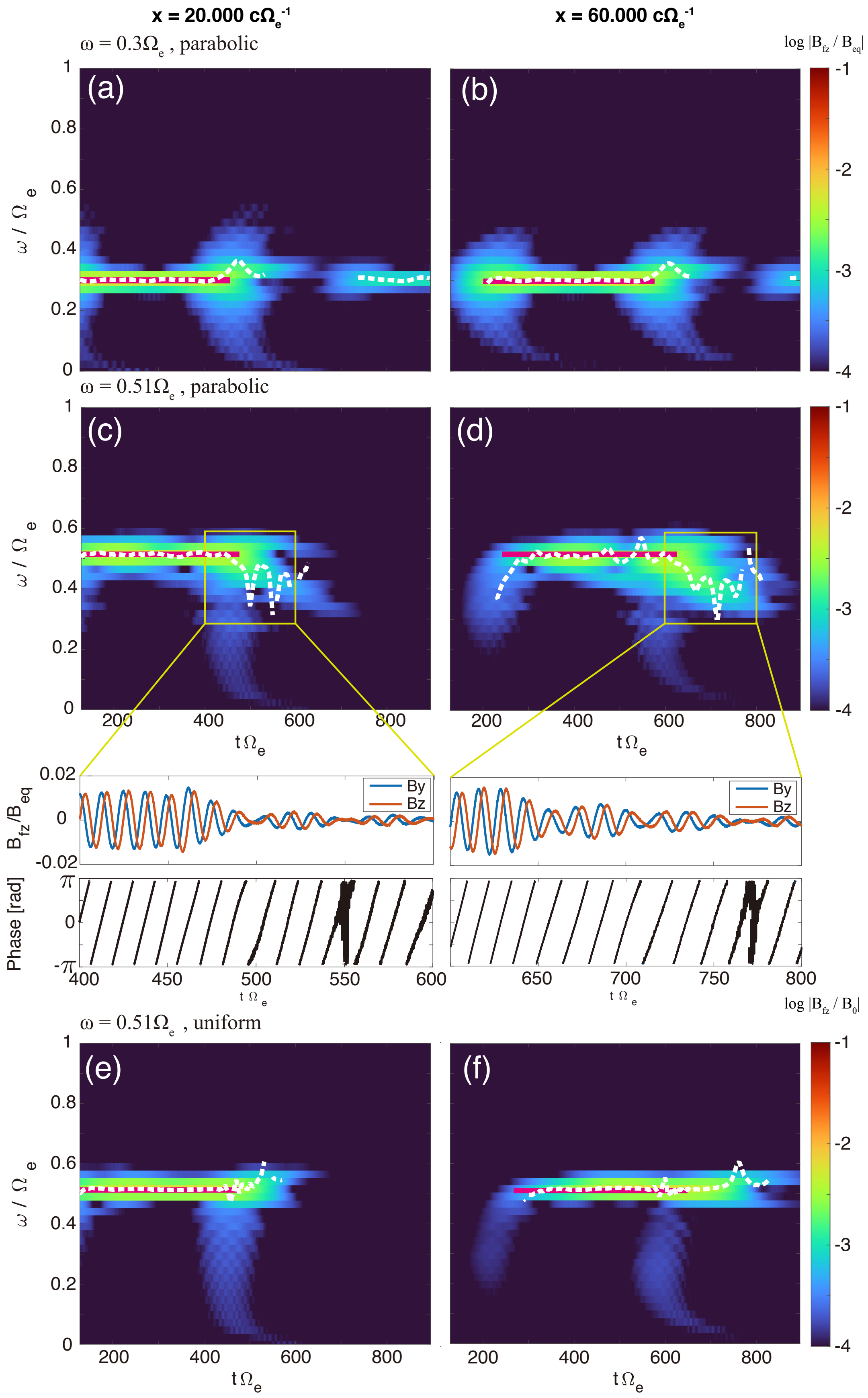

Figure 5.4: Dynamic spectra of magnetic field magnitude for forward waves with different wave frequencies and different background field models.

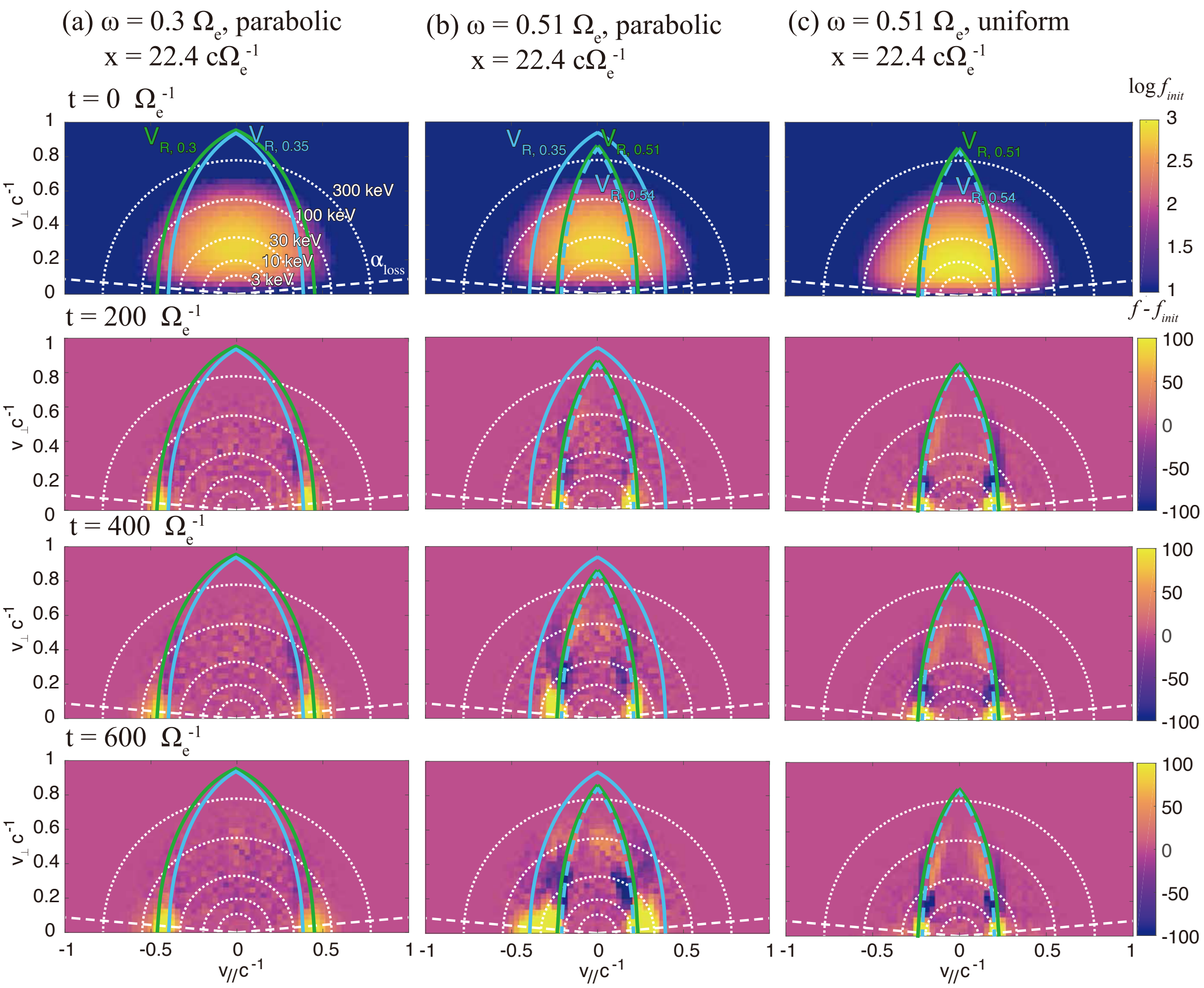

Figure 5.5: Time evolution of velocity distributions for runs with triggering wave of frequencies (a) $\omega = 0.3\,\Omega_e$ and (b, c) $\omega = 0.51\,\Omega_e$ at $x = 22.4\,c\Omega_e^{-1}$. The white dashed lines indicate the equatorial loss cone angle (5 degrees).

The solid green lines show the resonance velocity of triggering waves with $0.3\,\Omega_e$ and $0.51\,\Omega_e$, respectively, showing the part of the distribution function scattered by the falling tone. The absolute value of resonance velocity of $0.51\,\Omega_e$ is smaller than that of $0.3\,\Omega_e$. The blue solid and dashed lines show the resonance velocity with $0.35\,\Omega_e$ and $0.54\,\Omega_e$, respectively.

At $t = 200\,\Omega_e^{-1}$, the particle flux increases near the loss cone and decreases at the higher pitch angle on the resonance velocity curve. After that, Figure 5.5a shows no significant time evolution of the particle distribution. On the other hand, Figure 5.5b shows gradual modulation of the velocity distribution in a wider area of the velocity phase space. The parallel velocity range of the modulated part of the velocity distribution is shifted to larger absolute values, which corresponds to the decrease of the frequency of the emission. In addition, we can see the enhancement of higher pitch angle particles. There is a greater number of electrons scattered or energized in Figure 5.5b than in Figures 5.5a and 5.5c, corresponding to the variation range with the resonance curve.

We can see enhanced populations at higher pitch angles in Figures 5.5b, which indicates a part of electrons is transported to higher pitch angles by nonlinear resonant trapping. Without a gradient of the ambient magnetic field and a frequency variation, the trapped electrons form a symmetric hill in phase space. A symmetric hill cannot cause wave growth. Comparing Figures 5.5a and 5.5b, we find that more trapped electrons are energized to higher pitch angles in the falling tone case. Because of the broadening of the resonance velocity due to the frequency variation, the wave can interact with more particles. The trapped electrons are strongly related to the electron hill, which induces the frequency variation and the wave growth with its asymmetry in the velocity phase space.

5.4 Discussion

In the uniform magnetic field case, we found no triggered emission from the equatorial signal. On the other hand, in the parabolic model, a significant falling-tone emission is triggered at the termination of a short pulse with 0.51 Ω_e generated at the equator. The falling tone emission appears in the downstream region of the triggering signal, which is contrary to the Vlasov simulation performed by Nunn and Omura (2012). The emission consists of a series of sub-packet structures. The intense wave damping takes place at the wavefront of each packet.

To understand the generation mechanism of the emission, we analyze currents formed by energetic resonant electrons and estimate the wave growth and frequency variation via wave-particle interactions. The wave equation and dispersion relation with resonant currents can be written as equations (29) and (30) in Omura et al. (2008)

$$\frac{\partial B_w}{\partial t} + V_g \frac{\partial B_w}{\partial x} = -\frac{\mu_0 V_g}{2} J_E \,, \tag{5.2}$$

$$c^2k^2 - \omega^2 - \frac{\omega \omega_{pe}^2}{\Omega_e - \omega} = \mu_0 c^2 k \frac{J_B}{B_w} \,, \tag{5.3}$$

where μ_0 is the magnetic permittivity in a vacuum, J_B is the current parallel to the wave magnetic field, and J_E is the current parallel to the electric field, respectively. Resonant currents are formed by phase-organized electrons. Components of the resonant current parallel to the electric field and the wave magnetic field are defined by J_E and J_B, respectively. Omura et al. (2008) have proven that an amplitude variation is caused by J_E, and that a frequency variation is caused by J_B. The frequency variations for whistler-mode waves caused by the resonant current can be rewritten from equation (5.3) as Omura and Nunn (2011),

$$\Delta\omega = -\frac{\mu_0 V_g}{2} \frac{J_B}{B_w}. \tag{5.4}$$

We calculate the spatial and temporal profiles of J_B, J_B/B_w, and J_E by interacting energetic electrons with the forward propagating whistler-mode waves. In the simulation, we derive the resonant currents by integrating inner products between velocities of all energetic particles and forward-wave fields (i.e., $J_E = \Sigma \boldsymbol{v}_\perp \cdot \boldsymbol{E_{w,f}}/E_{w,f}$ and $J_B = \Sigma \boldsymbol{v}_\perp \cdot \boldsymbol{B_{wf}}/B_{wf}$). We define $\boldsymbol{B_{wf}}$ and $\boldsymbol{E_{w,f}}$ as the magnetic and electric field vectors of forward propagating waves, and we denote their amplitudes by B_{wf} and $E_{w,f}$, respectively.

We denote the characteristic areas as 1-8 in Figure 5.6. Negative J_E and positive J_B are formed in the triggering waves in region 1 in Figures 5.6a and 5.6b. Although there is a weak spatial structure around region 2, the triggering wave of $\omega = 0.3\,\Omega_e$ result in a nearly homogeneous resonant current, which causes no significant variation of the wave amplitude and the frequency.

On the other hand, Figures 5.6c and 5.6d show larger resonant currents J_E and J_B in the case of $\omega = 0.51\,\Omega_e$. We can see a sharp fluctuation of J_E changing its sign as denoted by 4-7. The stripe form of the resonant current corresponds to the group of phase-bunched electrons. The emissions have an intense positive J_B, which indicates that trapped resonant electrons form an electron enhancement referred to here as the "electron hill" in the phase space. Most electrons are trapped at the wavefront of the emission and oscillate in the wave potential, which causes an oscillating sign of J_E. The intense resonant currents are caused by the greater number of resonant electrons due to the anomalous entrapping of lower pitch angle particles, which is enhanced with larger amplitude waves with higher frequency (Kitahara & Katoh, 2019).

A remarkable feature of the falling tone emission is intense resonant currents induced by triggering waves. These resonant currents excite the sub-packet structure with falling frequencies. Figure 5.7 shows enlarged views of the triggered emission. In Figures 5.7b, 5.7c, and 5.7f, as well as in Figure 5.6f, we only plot the region that satisfies the criteria described below. The enhanced resonant current J_B at the termination of the triggering pulse has a significant effect in changing the frequency because of the large J_B/B_{wf} as we find in Figures 5.7a and 5.7b. The frequency is much decreased at the termination of the triggering pulse. We calculated the coherence of the two perpendicular forward wave components B_{yf} and B_{zf}. We only plot ω, J_B/B_{wf}, and $-J_E$ of the wave packets with coherence > 0.995 and wave amplitude > -60 dB of B_{eq} in Figure 5.7b, 5.7c, and 5.7f, respectively. We can recognize the formation of sub-packets as denoted by sp1, sp2, sp3, and sp4 in Figures 5.7b, 5.7c and 5.7d.

The sub-packets consist of falling-tone frequency because of the large J_B/B_{wf}, which causes the frequency decrease given by equation (5.4). Omura et al. (2008) have shown that the dynamics of resonant electrons are determined by the inhomogeneity factor S. The factor is controlled by two terms containing the frequency sweep rate $\partial\omega/\partial t$ and the background magnetic field gradient $\partial B_x/\partial x$. Because of the negative frequency sweep rate $\partial\omega/\partial t < 0$, the inhomogeneity factor S becomes positive, which makes the trapped particles oscillate around the phase that gives the negative J_E as shown in Figure 5.7c. The negative J_E causes the growth of the subpackets, as we find in Figure 5.7e. The sign of J_E changes depending on the sign of S. As the subpacket “sp1” propagates away from the equator, the gradient of the magnetic field

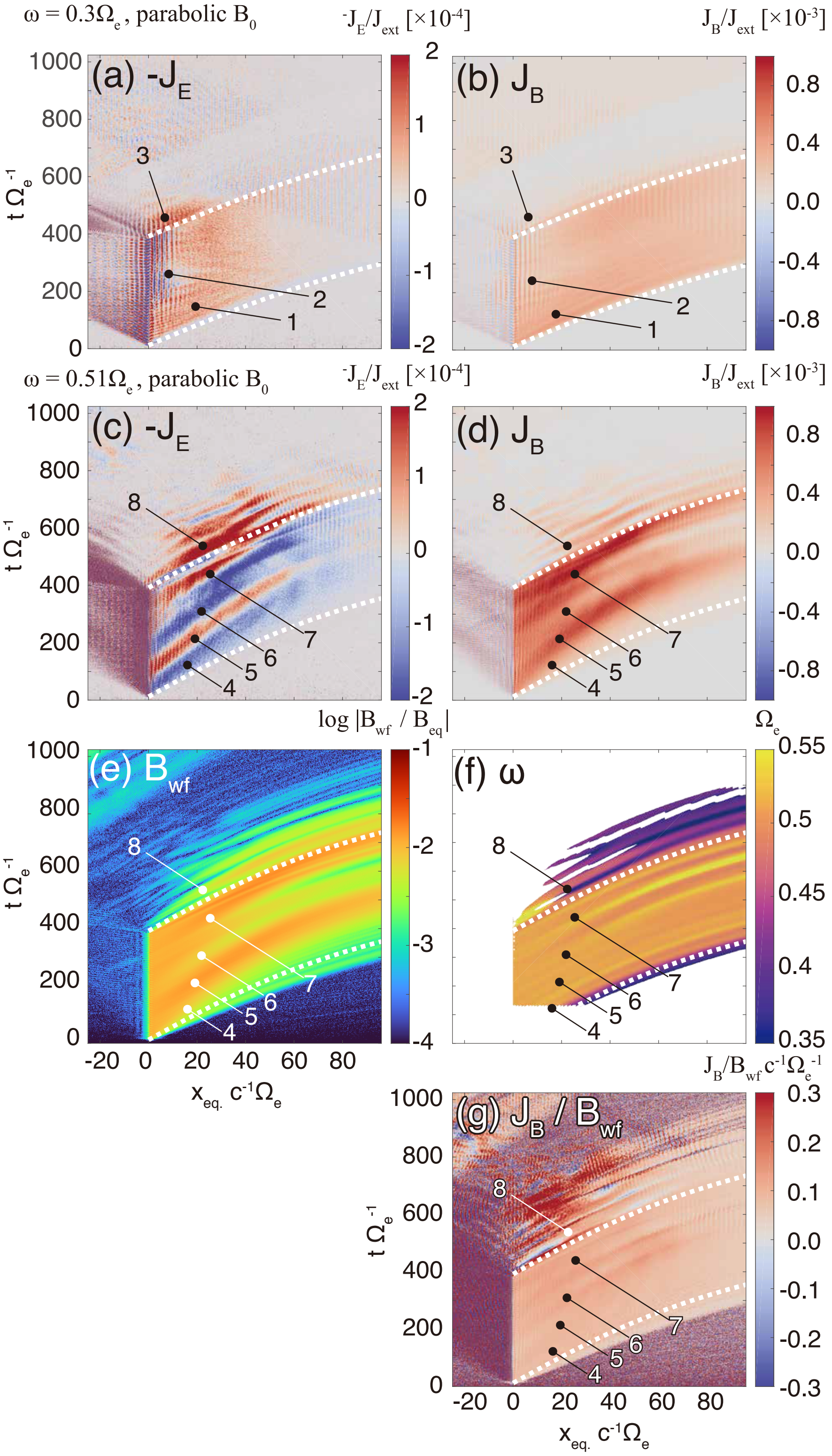

Figure 5.6: Spatial and temporal distribution of resonant current $-J_E$, J_B, and related field variables; (a, b) $-J_E$ and J_B for the frequency of 0.3 Ω_e. (c, d) $-J_E$ and J_B for the frequency of $\omega = 0.51\,\Omega_e$. (e, f, g) Magnetic field amplitude for forward waves B_{wf}, instantaneous frequency ω and J_B/B_{wf} for $\omega = 0.51\,\Omega_e$, respectively. The white dashed lines show group velocity at the frequency of the corresponding triggering frequencies using the cold plasma dispersion relation.

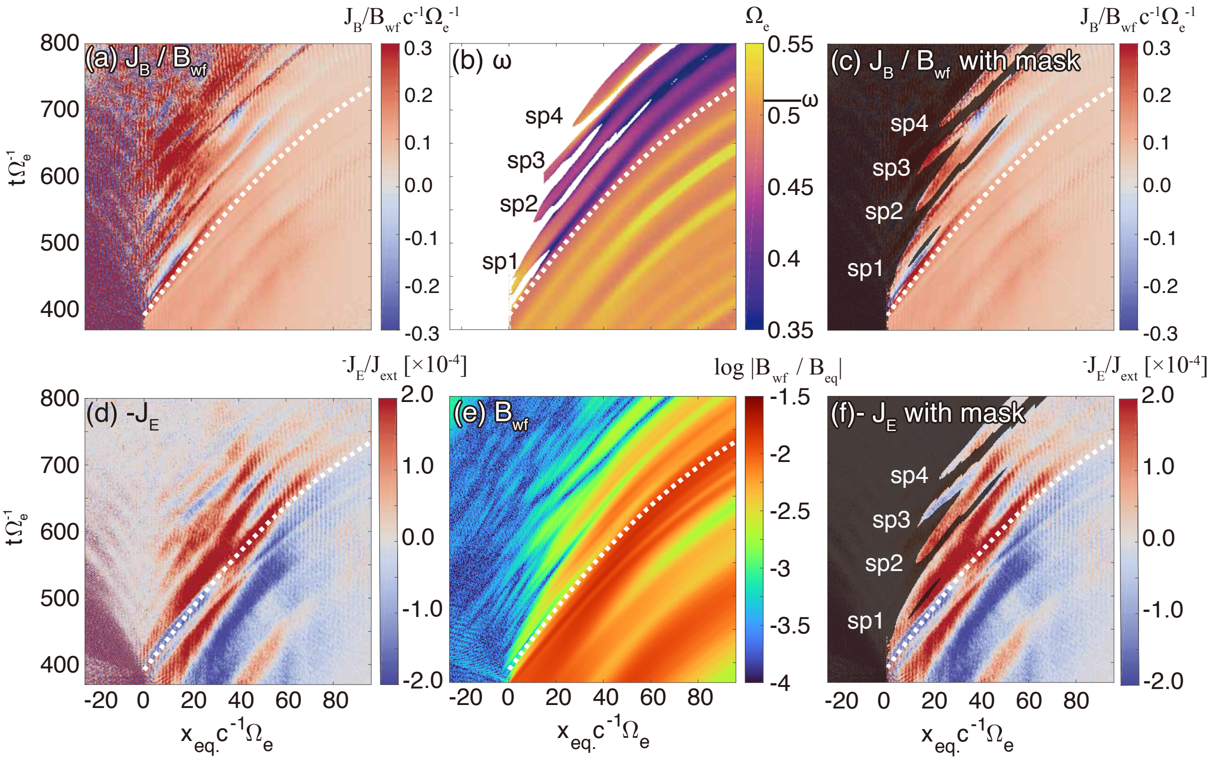

Figure 5.7: Falling-tone triggered wave packet from the run 2 with the frequency of $\omega = 0.51\Omega_e$ for (a) resonant current over the magnetic field of forward wave $J_B/B_{f,w}$, (b) wave frequency ω, (c) J_B/B_{wf} for both conditions that the amplitude is more than -60 dB and that the magnitude-squared coherence at the local instantaneous frequency is more than 0.995, (d) resonant current $-J_E$, and (e) magnetic wave power $\frac{1}{2}\mu_0 B_{wf}^2$. (f) $-J_E$ by the same method as in (c).

increases and cancels out the contribution of the negative frequency sweep rate, and S becomes negative, which makes J_E positive as shown at $x = 40\,c\Omega_e^{-1}$ and $t = 600\,\Omega_e^{-1}$ in Figure 5.7c. In the sub-packet structure, we find a rapid variation of amplitude and instantaneous frequencies. Our results are consistent with observations reported by Shoji et al. (2018), who found rapid frequency modulation in EMIC rising-tone emissions.

Figure 5.8 shows spatial and temporal profiles of inhomogeneity factor (Omura et al., 2008) for triggered falling-tone emissions. Inhomegeneity factor S (Omura et al., 2008; Omura, 2021) is given by equation (1.5). Assuming that the electron density of energetic electrons is sufficiently small for treating the dispersion relation as the cold dispersion relation, we calculate the inhomogeneity factor from the instantaneous wave frequency, amplitude, and plasma frequency of cold electrons. In Figure 5.8a, inhomogeneity factor S in the vicinity of the magnetic equator are positive values in the range with $0 < S < 1$, where the trapping potential for the pendulum equation exists. The electron hill is formed in the generation region of falling-tone emissions, and the results are consistent with the formation of resonant current in Figure 5.7. Figures

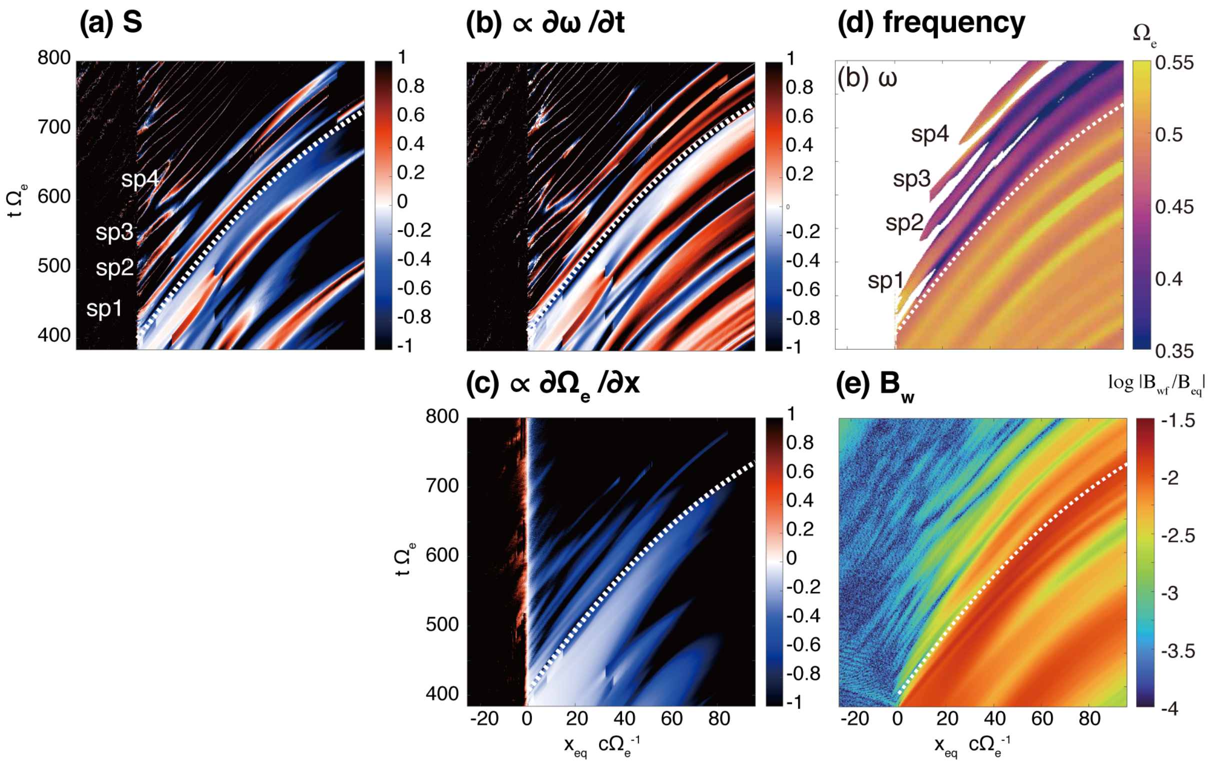

Figure 5.8: Spatial and temporal profiles of inhomogenity factor S (Omura et al., 2008) for triggered waves. (a)S parameter, (b) inhomogeneity due to the frequency sweep rate, (c) inhomogeneity due to the magnetic field gradient, (d) instantaneous frequency, and (e) spatial distribution of $\boldsymbol{B_W}$ shown in Figure 5.7.

5.8b and 5.8c show the terms in equation (1.5) proportional to the frequency sweep rate and the gradient of background magnetic field, respectively. In the early phase of the falling-tone emissions, where $x = 0 - 20c\Omega_e$, the term proportional to sweep rate has a positive value, while the term proportional to the gradient of the ambient magnetic field has a negative value. Falling-tone emissions are generated self-sustainingly by the frequency variation, and the formation process of falling-tone emissions is similar to that for rising-tone emissions in terms of the formation of resonant currents as discussed in Chapter 4.

5.5 Conclusion

We have developed a one-dimensional full PIC simulation model for studying the triggered whistler-mode emissions. We set the model so as to simulate triggered emissions from a large-amplitude wave excited artificially at the equator. With short and large-amplitude triggering waves, falling-tone emissions consisting of several sub-packets are generated in the vicinity of the magnetic equator. Each short sub-packet sequentially generates the next falling-tone sub-packet. We confirm that the falling tone is caused by a group of resonant electrons, forming a positive J_B/B_W, which is enhanced at the termination of the triggering waves. In the generation process of the falling tone, large variations of the amplitude B_W is essentially important for the strong entrapping of resonant electrons. The resonant currents are controlled by the inhomogeneous factor S. As for the propagation process of a falling-tone sub-packet, the competing relation between the negative frequency sweep rate and the positive gradient of the background magnetic field controls the sign of S and thus the convective growth of each sub-packet.

In the present paper, we compare two cases of triggering frequency $0.3\,\Omega_e$ (Case 1) and $0.51\,\Omega_e$ (Case 2) to study the generation mechanisms of triggered emissions with different ranges of frequency. Based on theoretical analysis and simulation results, we conclude that the formation of the electron hill is essential for the generation of falling tone emissions. However, the different results with the two frequency ranges may not necessarily represent a general aspect of the lower and upper band chorus. It is important to find general features of the excitation mechanism of the upper and lower band chorus by conducting the simulation with different settings, such as the frequencies and durations of the triggering pulse. In addition, the oblique propagation of whistler-mode waves, as we find in observations, is an important physics model involving Landau resonance, which results in the amplification or damping of the waves (Hsieh & Omura, 2018). To study these effects of oblique propagations, we need to extend the current model to a two-dimensional model.

Chapter 6

Summary

6.1 Summary of the study

We have conducted one-dimensional full particle simulations of whistler-mode triggered emissions in the inner magnetosphere. For enabling numerical simulations with 10 billion superparticles, we have applied the particle decomposition method to the simulation code. The generation algorithm of the initial phase space distribution of particles is proposed in the simulation. We derive equations in mirror motion. By injecting whistler-mode waves with constant frequency at the magnetic equator, rising-tone and falling-tone emissions are generated. Nonlinear signatures of rising-tone and falling-tone triggered emissions are surveyed based on the comparison with nonlinear theory for whistler-mode wave-particle interaction. The results show that resonant current is the key driver in the generation of whistler-mode triggered emissions.

In chapter 3, we reproduced long-sustaining triggered rising-tone emissions with a one-dimensional particle simulation. With an injection of continuous triggering waves from the magnetic equator, we observe rising-tone triggered emissions. Nonlinear characteristics of rising-tone emissions are observed. Throughout the formation of an electron hole in velocity phase space stretched over the generation region, long subpacket rising-tone emissions are formed by absolute instability and convective wave growth. In the generation region of the rising-tone emissions, resonant currents are formed by inhomogeneity driven by temporal frequency variations. The long rising-tone subpacket is modulated with increasing magnitude, splitting into smaller subpackets through propagation. The amplitude modulations in a subpacket are generated by two different processes: resonant trapping oscillation of electrons at the equatorial region and enhancement of the amplitude modulations through propagation in the downstream region.

The upstream shift of the generation region of rising-tone emissions and the formation processes of a subpacket structure are shown in Chapter 4. The generation regions of rising-tone emissions move upstream from the triggering waves. The source velocity represents the motion of resonant current, while the velocity of the wave generation includes the formation processes of subpackets and their intervals. The velocity of wave packet generation is dependent on the duration of the subpacket controlled by the formation time of the resonant current in the generation region. When the source velocity is approximately the same as the velocity of wave packet generation, the resonant current is formed continuously, leading to a long-sustaining rising-tone emission. When the spatial and temporal gap between subpackets exists due to the damping phase of the generation of a short subpacket, resonant electrons in the gap of the subpacket are carried at the resonance velocity to the upstream region, forming subsequent subpacket. As a result, the velocity of wave generation increases in magnitude. When the formation of resonant currents is delayed, the velocity of wave generation becomes smaller than the source velocity in magnitude. Coalescence of subpackets takes place below the frequency $0.25\,\Omega_e$, delaying the formation of the resonant current in the generation region.

Falling-tone emissions are reproduced with a particle simulation, and the generation process of falling-tone triggered emissions are shown in Chapter 5. With short and large-amplitude triggering waves, falling-tone emissions consisting of several sub-packets are generated in the vicinity of the magnetic equator. Each short sub-packet sequentially generates the next falling-tone sub-packet. We confirm that the falling tone is caused by a group of resonant electrons, forming a positive J_B/B_W, which is enhanced at the termination of the triggering waves. In the generation process of the falling tone, large variations of the amplitude B_W is essentially important for the strong entrapping of resonant electrons. The resonant currents are controlled by the inhomogeneous factor S. As for the propagation process of a falling-tone sub-packet, the competing relation between the negative frequency sweep rate and the positive gradient of the background magnetic field controls the sign of S and, thus the convective growth of each sub-packet.

Figure 6.1 shows a schematic illustration of the formation processes of rising-tone emissions with subpacket structures. Three different formation processes of the subpacket structures for rising-tone emissions have been proposed in the study. The subpacket structures with short duration of the element are classified into two different generation mechanisms as shown in 6.1a1 and 6.1a2. When the nonlinear growth rate is high, the wave amplitude rapidly grows from the threshold amplitude to the optimum amplitude. The deeper electron hole is formed in the middle phase of the generation of a single subpacket, as shown in Figures 6.1b1 and 6.1c1, causing the high growth rate of the triggered waves. After the wave growth reaches the optimum amplitude, the formation of an electron hole is suppressed, while the phase-modulated particles generate subsequent subpacket from the lower frequency. The process repeatedly occurs, and short subpackets are formed.

Another generation process of the short subpacket structure is caused by the modulations of phase space density in the vicinity of the separatrix of the trajectories in Figure 6.1a2. In the initial phase of the formation of an electron hole, the density distribution in the separatrix perturbs (Fujiwara et al., 2022) as shown in Figure 6.1c2. As the increase of the wave frequency,

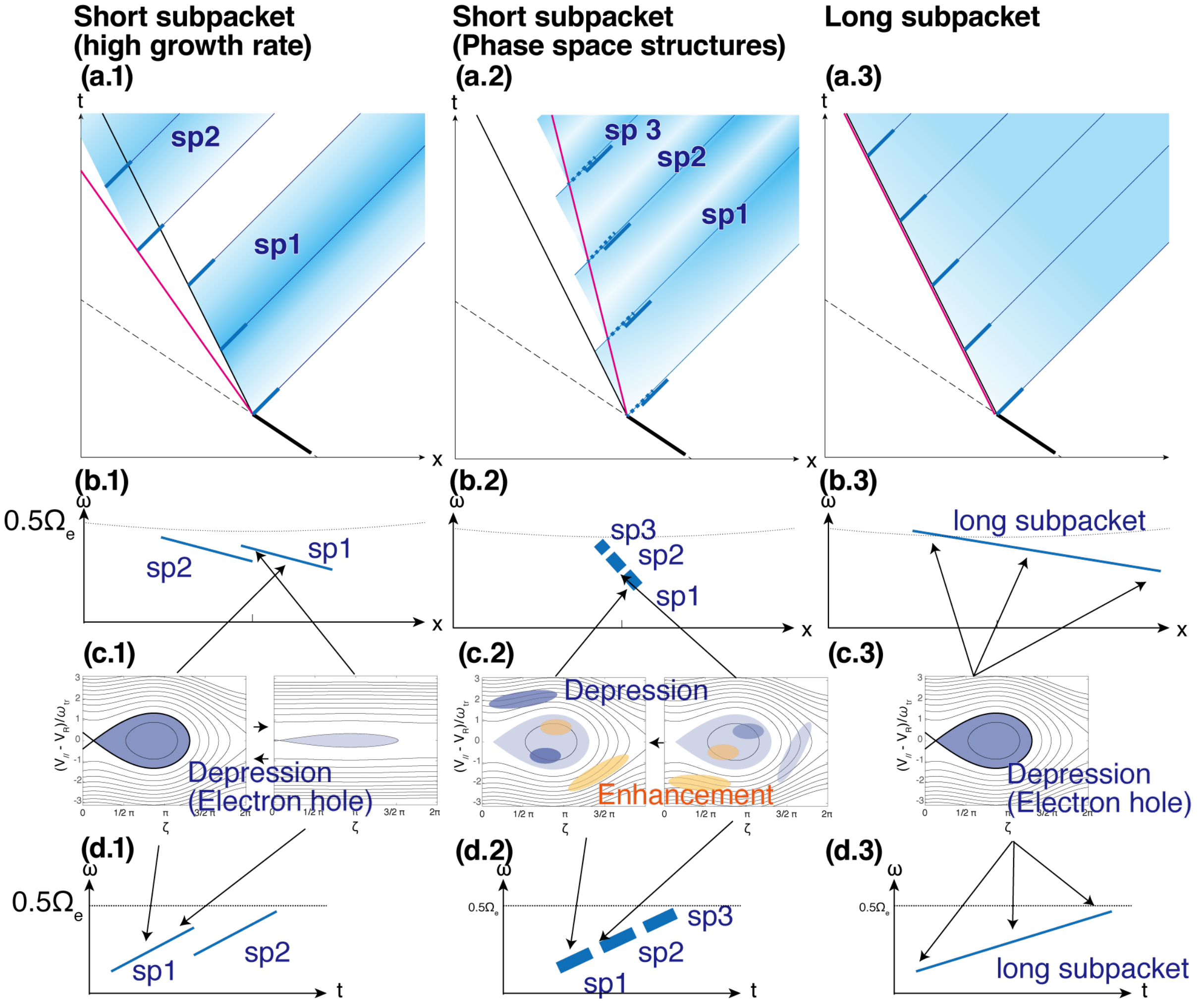

Figure 6.1: Schematic illustration of the formation processes of rising-tone emissions with subpacket structures. (a) Spatial and temporal distribution of the subpacket structures for (1) short subpackets with high growth rate, (2) perturbation of the phase space structures, and (3) a long subpacket. (b) Spatial distribution of wave frequencies for cases 1 to 3. (c) Snapshots of the phase space distribution for the formation of the electron-hole for cases 1 to 3. (d) Dynamic spectrum of rising-tone emissions for cases 1 to 3. The black arrows in (b) and (d) correspond to the formation region of the phase space structures in (c), respectively.

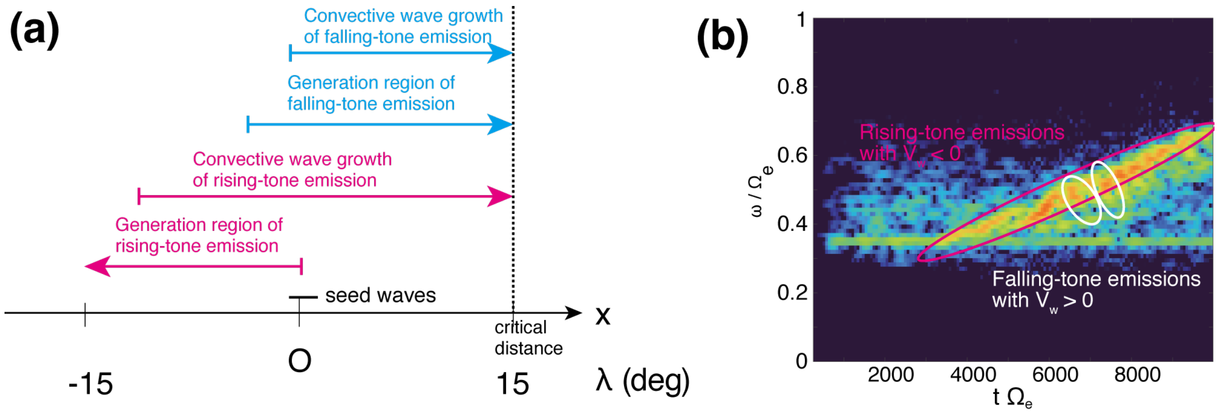

Figure 6.2: Schematic illustration of the generation of rising-tone emissions and falling-tone emissions. (a) Potential generation region of the rising-tone and falling-tone emissions, and the region for nonlinear wave growth. (b) Rising-tone emissions are triggered from the long-duration waves with constant frequency, while falling-tone emissions are triggered from rising-tone emissions with short subpacket.

the phase modulation remains moving as the untrapped particle. The major frequency of the wave frequency controlled by the global structure of the electron, while the slow rotation of the phase modulation structure generates fluctuating resonant currents. The rotation frequency of the phase space modulation is in the order of the trapping frequency. The subpacket structures with the generation process are observed as amplitude modulation with the combinations of two waves with a small frequency difference. The generation process of short subpacket structures is consistent with the study by Mourenas et al. (2022), who have reported the generation of rising-tone triggered emissions with short subpacket by injecting the waves with multiple frequencies. The short rising-tone emissions are generated with a broader spectrum in frequency range as shown in Figures 6.1b2 and 6.1d2.

The rising-tone emissions with long subpacket are generated by the continuous generation of an electron hole as shown in Figure 6.1c3. The instantaneous frequency increases monotonically in time, and the structures of electron holes stretch over the wave generation region (Nogi & Omura, 2022). Rising-tone elements with multiple subpackets with monotonically increasing frequencies are generated. A subpacket element with a long time duration is generated with the upstream shift of the source region depending on the group velocities and resonance velocities for different frequencies. Throughout the formation of an electron hole in velocity phase space stretched over the generation region, long subpacket rising-tone emissions are formed by the absolute instability and convective wave growth.

The generation region of the rising-tone and falling-tone emissions are described in Figure 6.2.

Rising-tone and falling-tone triggered emissions are reproduced in the simulations. We have analyzed resonant current in the generation region of triggered emissions and found that resonant current controls the amplitude ad frequency chirp of the triggered emissions. We have confirmed that the formation of an electron hole and hill in the generation region of rising-tone and falling-tone triggered emissions, respectively. In the generation region of rising-tone and falling-tone emissions, the absolute value of the inhomogeneous factor S kept approximately 0.4 in the generation region of triggered emissions. The dominant factor in the inhomogeneous factor is the temporal frequency variation of triggered emissions, supporting the formation of an electron hole and a hill through emissions. We observe upstream and downstream shifts of the generation region of triggered emissions for rising-tone and falling-tone emissions, respectively. The upstream or downstream shifts of the generation region are consistent with the velocity of the shifts of the spatial structure of the phase-organized structures, determined by the sum of the resonance velocity and wave group velocity.

6.2 Future prospects

The shifts in the generation region of rising-tone and falling-tone emissions have been discussed in the study. The generation region of the rising-tone emissions shifts to the upstream region of the magnetic equator, while the generation region of the falling-tone emissions shifts to the downstream region of the wave source as shown in Figure 6.2a. Throughout the present study, the frequency of the generated falling-tone is limited in the vicinity of half the electron cyclotron frequency, triggered by short injected waves and rising-tone emissions. The absence of the reproduction of strong falling-tone emissions in the study can be consistent with the lower number of observations of the lower-band falling-tone emissions than that for rising-tone emissions (W. Li et al., 2011). Although the occurrence of the lower-band falling-tone emissions is low, the generation mechanism of the falling-tone emissions in the frequency range of the lower-band chorus needs to be investigated, which is responsible for the falling-tone emission below half the cyclotron frequency. The self-consistent simulations have reported the simultaneous generation of rising-tone and falling-tone emissions with a uniform ambient magnetic field (Wu et al., 2020; Fujiwara et al., 2023). The triggering waves of the falling-tone emissions can be provided from a short rising-tone subpacket with high amplitude in the vicinity of the equator. The results agree with the observations in terms of the source region of falling-tone emissions in the vicinity of the equator (Kurita, Misawa, et al., 2012). W. Li et al. (2011) have shown that the wave normal angle of falling-tone emissions is highly oblique greater than 60 degrees, while the wave normal angle of rising-tone emissions is typically less than 30 degrees. Two-dimensional simulations of VLF triggered emissions for falling-tone emissions will be required for the survey of the generation mechanism of falling-tone emissions in the lower frequency as $0.3\Omega_e$.

We have reproduced rising-tone emissions without a frequency gap in half the cyclotron frequency. In the THEMIS observation, rising-tone emissions without a frequency gap have been observed (Kurita, Katoh, et al., 2012), while one of the typical characteristics of the chorus emissions is the frequency gap between lower-band and upper-band chorus waves. The formation process of the gap is also the missing link of the study. In the present study, we have observed the generation of rising-tone emissions from the triggering waves below half the cyclotron frequency. Ratcliffe and Watt (2017) have reported that a velocity distribution function with two distinct peaks in linear growth rate is generated, and the modulation in the velocity distribution function in caused by Landau resonance (e.g. J. Li et al., 2019; Sauer et al., 2020; H. Chen et al., 2021; H. Chen, Gao, et al., 2022; J. Li et al., 2022). Whistler-mode waves propagate obliquely as the wave propagates. With the oblique whistler-mode waves, Landau resonance and phase bunching take place (Hsieh & Omura, 2018; Hsieh et al., 2020), which can be responsible for the generation of the gap via wave damping (Habagishi et al., 2014).

A simulation technology update will also be required. The original algorithm of Particle-in-cell simulation is not suitable for parallel computing because random access to main memory happens in the Boris pusher and the current calculation, leading to performance degradation of the particle code with a large number of processes. Nakashima et al. (2009) have proposed the OhHelp algorithm for the load balancing of the calculations with the domain decomposition of the simulation region. The algorithm is effective with the dynamic variations of plasma density, such as the studies on a surface charging of a satellite (e.g. Miyake & Nakashima, 2013), while it also performs effective improvement with the hybrid simulations for the generation of chorus emissions, where the plasma density does not change significantly over a region (Katoh et al., 2018). Recently, the binning of the superparticles referring the same grids in Boris pusher have proposed, contributing to enabling the vector operation of the processors (Nakashima, 2015; Nakashima et al., 2017). In the current study, we have already implemented sorting of the superparticles for the improvement of the cache hit rate, and the binning method for a superparticle can be easily applicable to the particle code in the present study. δf-PIC is another approach for reducing stochastic noise even with a low number of superparticles. These combinations might be an enabler of large-scale two-dimensional simulation.

An in-situ experiment of whistler-mode triggered emissions is expected. DSX satellite has been launched for the active experiment, aiming at an in-situ observation of VLF triggered emissions, injected from DSX. In the active experiments, where the triggering waves are injected from the satellite in the vicinity of the equator, the same model as the study will be applied to the experiment. This study will provide active experiments with fundamental insight into the experiment design.

Appendix A

The Buneman-Boris method for the parabolic magnetic field model

In the calculation of the perpendicular components of ambient magnetic field $\boldsymbol{B_r}$ satisfying div$\boldsymbol{B} = 0$, perpendicular velocity $v_\perp$ of an electron is required. There exist half time step difference between the temporal grid of the magnetic field and that of electron velocity. Figure A.1 shows the calculation procedure in the Buneman-Boris method with the parabolic magnetic field. The radial components of the ambient magnetic field are dependent on the perpendicular velocity of a particle, while velocities are defined in the full grid, while the magnetic fields are defined in the half grid with respect to time. In order to obtain electron velocity at the same timing as the magnetic field, we modify the Buneman-Boris solver. We describe the modified scheme of the Buneman-Boris method for the better conservation of the adiabatic invariant. The equation of motion in equation (2.5) with the relativistic form is discretized with the first-order method as

$$\frac{\boldsymbol{u}^{t+\frac{\Delta t}{2}} - \boldsymbol{u}^{t-\frac{\Delta t}{2}}}{\Delta t} = \frac{q}{m}\left(\boldsymbol{E} + \frac{\boldsymbol{u}^{t+\frac{\Delta t}{2}} + \boldsymbol{u}^{t-\frac{\Delta t}{2}}}{2} \times \boldsymbol{B_W}\right), \tag{A.1}$$

where Δt, q, m, $\boldsymbol{E}$, and $\boldsymbol{B_W}$ are time step, the charge of a super particle, rest mass of the super particle, the electric field at the position of the super particle, and wave magnetic field at the position of the super particle, respectively. The electric field and magnetic field are averaged in space for the prevention of the self-force of the super particle (Omura, 2007). The velocities $\boldsymbol{u}^{t+\frac{\Delta t}{2}}$ and $\boldsymbol{u}^{t-\frac{\Delta t}{2}}$ are defined as

$$\boldsymbol{u}^{t-\frac{\Delta t}{2}} = \frac{c}{c^2 - \sqrt{c^2 - \left|\boldsymbol{v}^{t-\frac{\Delta t}{2}}\right|^2}}\boldsymbol{v}^{t-\frac{\Delta t}{2}}, \tag{A.2}$$

$$\boldsymbol{u}^{t+\frac{\Delta t}{2}} = \frac{c}{c^2 - \sqrt{c^2 - \left|\boldsymbol{v}^{t+\frac{\Delta t}{2}}\right|^2}}\boldsymbol{v}^{t+\frac{\Delta t}{2}}. \tag{A.3}$$

We define the velocities $\boldsymbol{u}^+$ and $\boldsymbol{u}^+$ as

$$\boldsymbol{u}^- := \boldsymbol{u}^{t-\frac{\Delta t}{2}} + \frac{q}{m}\boldsymbol{E}\frac{\Delta t}{2}, \tag{A.4}$$

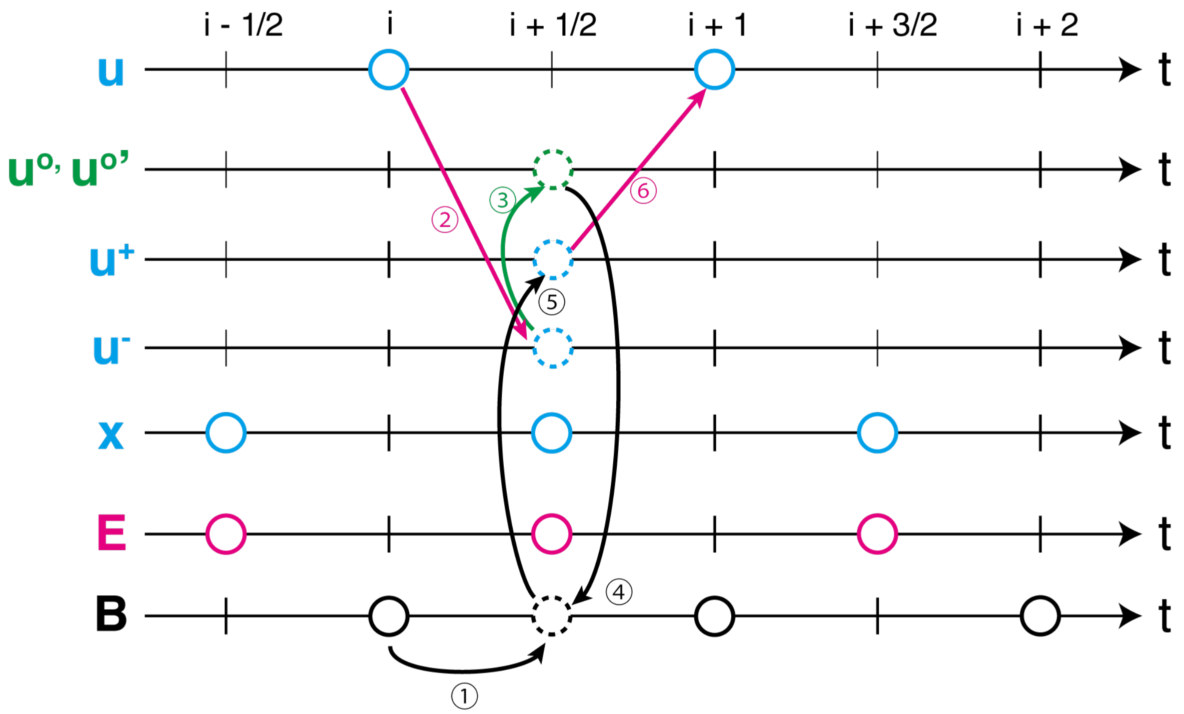

Figure A.1: Procedure of Bunneman-Boris method with the radial magnetic field correction with parabolic magnetic fields.

$$\boldsymbol{u}^{+} \quad := \quad \boldsymbol{u}^{t+\frac{\Delta t}{2}} - \frac{q}{m}\boldsymbol{E}\frac{\Delta t}{2} \,. \tag{A.5}$$

The magnitudes of the velocities $\boldsymbol{u}^-$ and $\boldsymbol{u}^+$ do not change vary during rotations, satisfying energy conservation during the rotation by the Lorentz force. With the acceleration or deceleration with the electric field by the half step, we obtain the velocity $\boldsymbol{u}^-$ from the definition of equation (A.4). For the velocity conservation with the relativistic equation of motion, magnetic fields are corrected (Omura, 2007). We add the axial component of the ambient magnetic field B_x to wave magnetic fields and obtain corrected magnetic field $\boldsymbol{B}^{\boldsymbol{O}}$ as

$$\boldsymbol{B}^{\boldsymbol{O}} = \frac{c}{\sqrt{c^2 + |\boldsymbol{u}^-|^2}}\left(\boldsymbol{B}_{\boldsymbol{W}} + \boldsymbol{B}_{\boldsymbol{x}}\right) \,. \tag{A.6}$$

By using corrected magnetic field $\boldsymbol{B}^{\boldsymbol{O}}$, we obtain the velocity components for the calculation of the radial components of ambient magnetic fields at the intermediate point of the rotation $\boldsymbol{u}^{\boldsymbol{O}'}$ by

$$\boldsymbol{u}^{\boldsymbol{O}'} = \boldsymbol{u}^- + \frac{1}{1 + \left(\boldsymbol{B}^{\boldsymbol{O}}\frac{q}{m}\frac{\Delta t}{2}\right)^2}\boldsymbol{u}^- \times \frac{q}{m}\boldsymbol{B}^{\boldsymbol{O}}\frac{\Delta t}{2} \,. \tag{A.7}$$

The coefficient of the second term is determined from the cosine of θ_0 as shown in Figure A.2. The radial components of parabolic magnetic field is derived with $\boldsymbol{u}^{\boldsymbol{O}'}$ as

$$\boldsymbol{B}_{\boldsymbol{r}} = \frac{m(\boldsymbol{u}^{\boldsymbol{O}'} \times \mathbf{e}_{\mathrm{x}})ax}{q(1 + ax^2)} \,, \tag{A.8}$$

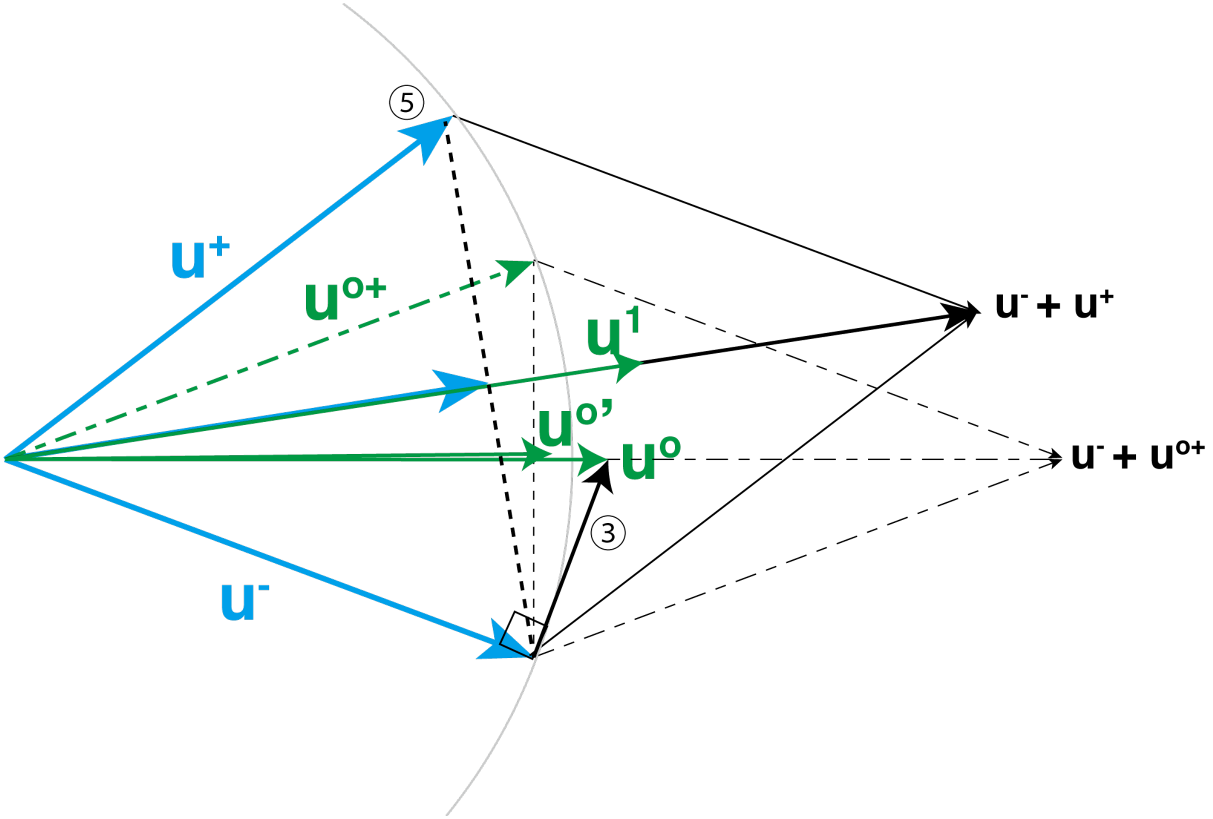

Figure A.2: Schematic illustration of the radial magnetic field correlation and $\boldsymbol{v} \times \boldsymbol{B}$ calculation.

where a is the coefficient of the parabolic magnetic field given by $B_x(x) = B_{\mathrm{eq}}(1 + ax^2)$. By adding ambient magnetic fields B_x and B_r to the wave magnetic field B_W, we obtain the effective magnetic fields interact with the super particle, corrected by relativistic effects, as

$$\boldsymbol{B}' = \frac{c}{\sqrt{c^2 + |\boldsymbol{u}^-|^2}} (\boldsymbol{B_W} + \boldsymbol{B_x} + \boldsymbol{B_r}) \ . \tag{A.9}$$

The velocity of the superparticle is calculated as the same procedure as the Buneman-Boris method with relativity. The velocity u_1 in Figure A.2 is given by

$$\boldsymbol{u}^1 = \boldsymbol{u}^- + \boldsymbol{u}^- \times \frac{q}{m} \boldsymbol{B}' \frac{\Delta t}{2} \, . \tag{A.10}$$

With the rotation by the magnetic field with tangential coefficient, we obtain the velocity after the rotation by the magnetic field as

$$\boldsymbol{u}^+ = \boldsymbol{u}^- + \frac{2}{1 + \left(\boldsymbol{B}' \frac{q}{m} \frac{\Delta t}{2}\right)^2} \boldsymbol{u}^1 \times \frac{q}{m} \boldsymbol{B}' \frac{\Delta t}{2} \, . \tag{A.11}$$

With the acceleration or deceleration with the electric field by the half step, we obtain the velocity $\boldsymbol{u}^{t+\frac{\Delta t}{2}}$ as

$$\boldsymbol{u}^{t+\frac{\Delta t}{2}} = \boldsymbol{u}^+ + \frac{q}{m} \boldsymbol{E} \frac{\Delta t}{2} \, . \tag{A.12}$$

We obtain the velocity of super particle after Δt as

$$\boldsymbol{v}^{t+\frac{\Delta t}{2}} = \frac{c}{c^2 - \sqrt{c^2 + \left|\boldsymbol{u}^{t+\frac{\Delta t}{2}}\right|^2}} \boldsymbol{u}^{t+\frac{\Delta t}{2}} \, . \tag{A.13}$$

Appendix B

Particle distribution of energetic electrons with the parabolic magnetic field

Initial phase space distribution of electrons have great influence on the generation of waves. For the analyses of the triggered emissions, instabilities except for the intended temperature anisotropy should be suppressed. In the previous studies with the same parabolic magnetic field models (e.g., Hikishima et al., 2009b, 2010, and others), conservation of the energy and adiabatic invariants are taken into account for the generation of initial phase space distribution, while emperical tuning on the pitch angle and thermal momenta of the velocity distribution function has been used. We have improved the method by adding the number modulations of the superparticles with the same momenta $u_\parallel, u_\perp$. In this chapter, we describe the generation algorithm of the initial phase space distribution function of energetic electrons with random numbers. The transverse wave electromagnetic fields generated from electrons are negligible in the equilibrium state of the superparticles. The equation of motion for the longitudinal component with ambient parabolic magnetic field in equation (2.7) is written as

$$m_0 \frac{\mathrm{d}u_\parallel}{\mathrm{d}t} = -u_\theta B_r \tag{B.1}$$

$$= -\frac{m u_\perp^2 a x}{q(1 + a x^2)}, \tag{B.2}$$

where $u_\parallel$, $u_\perp$ are parallel and perpendicular velocity with respect to x, normalized by Lorlentz factor γ as $\boldsymbol{u} = \gamma \boldsymbol{v}$, respectively. When the conservation of the magnetic momenta is satisfied, we can substitute perpendicular velocity $u_\perp$ as the parabolic function of x, and the equation (B.2) can be rewritten as

$$m_0 \frac{\mathrm{d}u_\parallel}{\mathrm{d}t} = -\frac{m}{q} u_{\perp 0}^2 a x\,. \tag{B.3}$$

The adiabatic bounce motion along the parabolic magnetic field is harmonic oscillation. Figure B.1 shows a trajectory of an electron with the conservation of energy and magnetic motion. In the generation of the phase space distribution, the equatorial velocity distribution function of energetic electrons f_{eq} is given by equation (2.10). With the stable phase space distribution

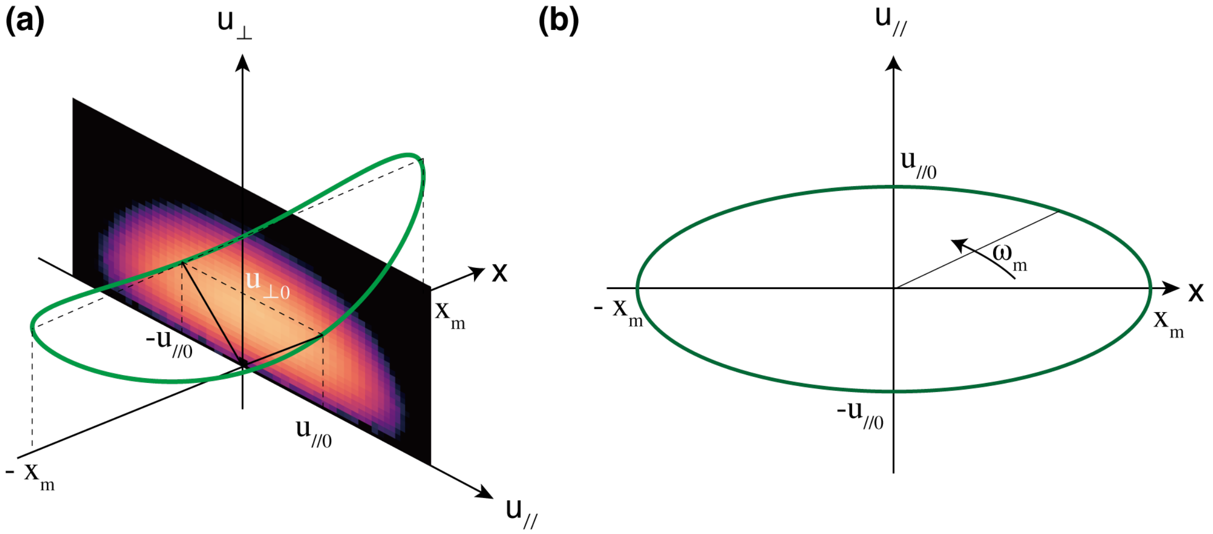

Figure B.1: Schematic illustration of electron trajectories in phase space. (a) Equatorial momenta distribution determines momentum components $u_\parallel$ and u_perp, and the trajectory of the electron at determined from the energy conservation and constant magnetic momenta. (b) The trajectory of the electron in phase space $(x, u_\parallel)$

.

of electrons, the equatorial velocity distribution is equilibrium over a long time, leading to the uniform particle density over the trajectory as shown in Figure B.1a. The trajectory of the electron in equation (B.3) is an ellipse in phase space as shown in Figure B.1b, where the semi-major radius is dependent on pitch angle. Figure B.2 shows the trajectories of bounce motion for the different distances of the mirror point in the simulation region and out of the simulation region. When the mirror point of the bounce motion exists in the simulation region, the electron moves along the arc of the ellipse as shown in Figure B.2a. When the mirror point of the bounce motion exist out of the simulation region, the electrons are reflected at the boundary with the same magnitude of momenta $u_\parallel$ and $u_\perp$, while different direction of $u_\parallel$ as shown in Figure B.2b. With the normalization of the ellips by position of mirror point x_m and equatorial parallel momenta $u_{\parallel 0}$, the trajectory of adiabatic motion is the circle as shown in Figure B.2b and B.2d, while there exist the difference in the definition range of oscillation phase ϕ. The definition range of the phase ϕ is calculated from the equatorial momenta, and the coefficient of the parabolic magnetic field as

$$x_m = \frac{|u_{\parallel 0}|}{u_{\perp 0}\sqrt{a}}, \tag{B.4}$$

$$x_{\max} = \begin{cases} x_m\,, & (x_m \leq L/2) \\ L/2\,, & (x_m < L/2)\,, \end{cases} \tag{B.5}$$

$$u_{\parallel \min} = \sqrt{u_{\parallel 0}^2 - u_{\perp 0}^2 a x_{max}^2}\,, \tag{B.6}$$

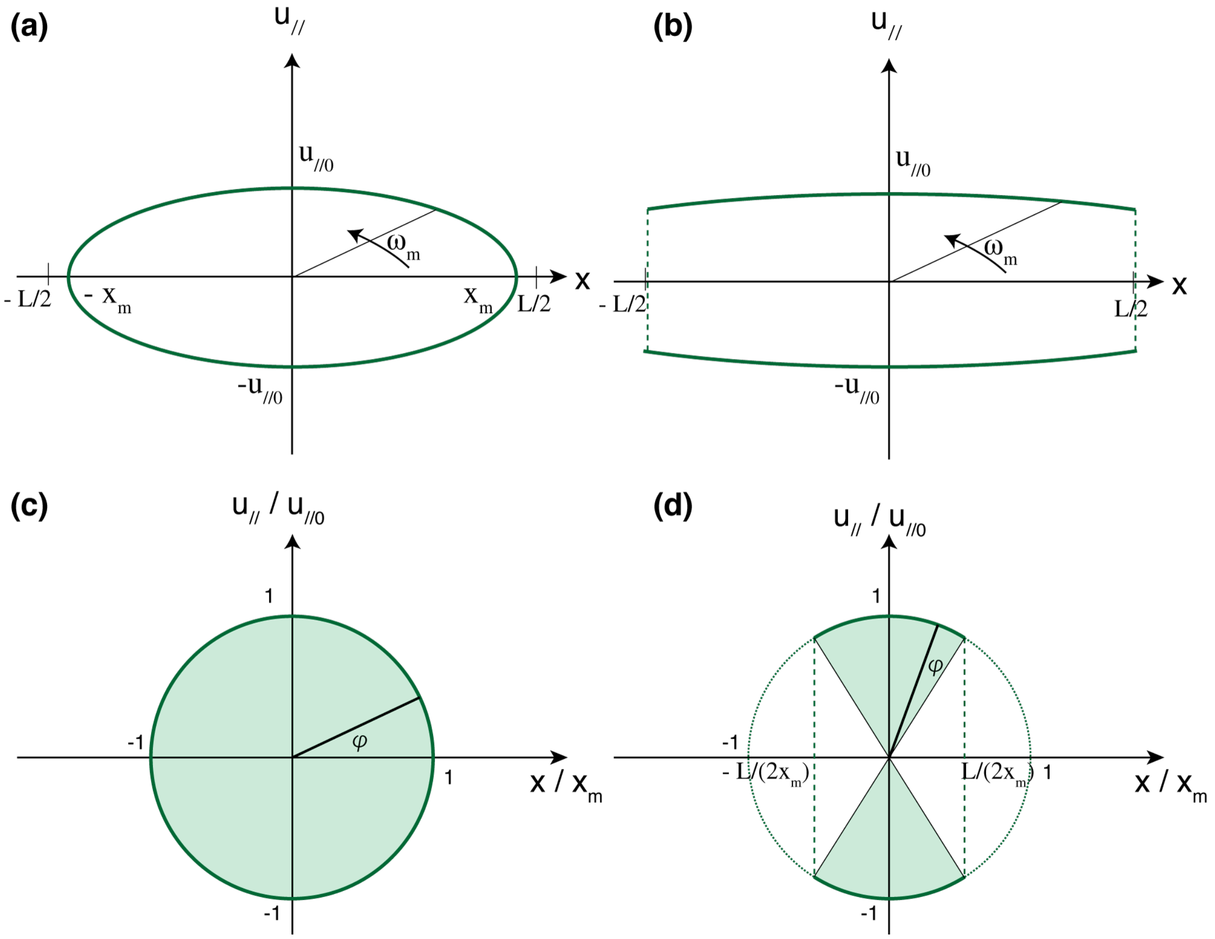

Figure B.2: Schematic illustration of the phase range of mirror motion in the simulation system. (a) The mirror point is within the simulation region. (b) The mirror point is beyond the simulation region. (c) The normalized trajectory for case (a). (d) The normalized trajectory for case (b). The solid green lines show the trajectory of a particle, and the dashed green lines indicate the reflecting boundary condition of the particle.

$$\phi_{\min} = \arctan\left(\frac{u_{\|\min} x_{\max}}{u_{\|0}/x_{\max}}\right), \tag{B.7}$$

where L is the length of the simulation region.

By distributing the position of energetic electrons by $x = x_m \cos\phi$uniform random numbers in a range with $\phi_{\min} \le \phi < \pi - \phi_{\min}$ and $\phi_{\min} + \pi \le \phi < 2\pi - \phi_{\min}$, we obtain equillibium distribution at the magnetic equator.

In the study, the charge of each superparticle for the energetic electron is fixed. When we distribute some number of superparticles with the same momenta with different positions, the number of the particle should be controlled. The number of particles with the same momenta should be proportional to the line integral of the trajectory. For normalizing the constant number of particles N_{ps}, we define the standard ellipse by setting the semi-major and the semi-minor radius as $L/2$ and $u_{\max} = 5u_{\|h}$, respectively. By normalizing the arc length of the

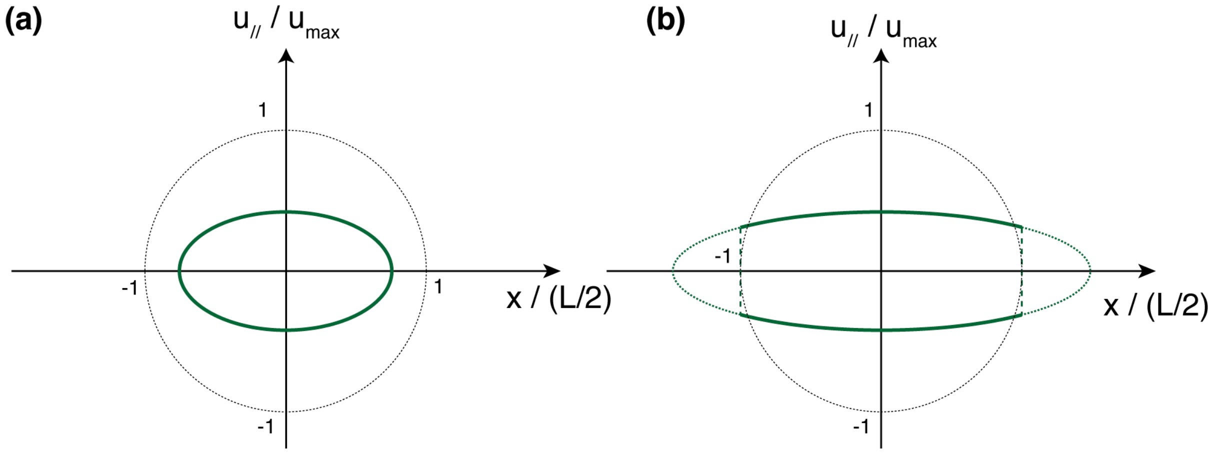

Figure B.3: Schematic illustration of the number modulation of particles with the same momenta $u_\parallel$ and $u_\perp$. (a) The mirror point is within the simulation region. (b) The mirror point is beyond the simulation region. The solid green lines show the trajectory of a particle, and dotted green lines indicate the trajectory out of the simulation region. Black dotted lines indicate the reference trajectory used for the normalization of the number of particles.

trajectory with the arc length of the standard ellipse l_{max}, we modulate a number of particles as $N_{ps} = N_{\mathrm{const.}} l_{\mathrm{arc}} / l_{\mathrm{max}}$. Figure B.3 shows the normalized ellipse for the calculation of the number modulation of the particles with the same equatorial momenta. The arc of the ellipse is given by the elliptic integrals. The processing flow described above is compiled in Figure B.4 as a flowchart.

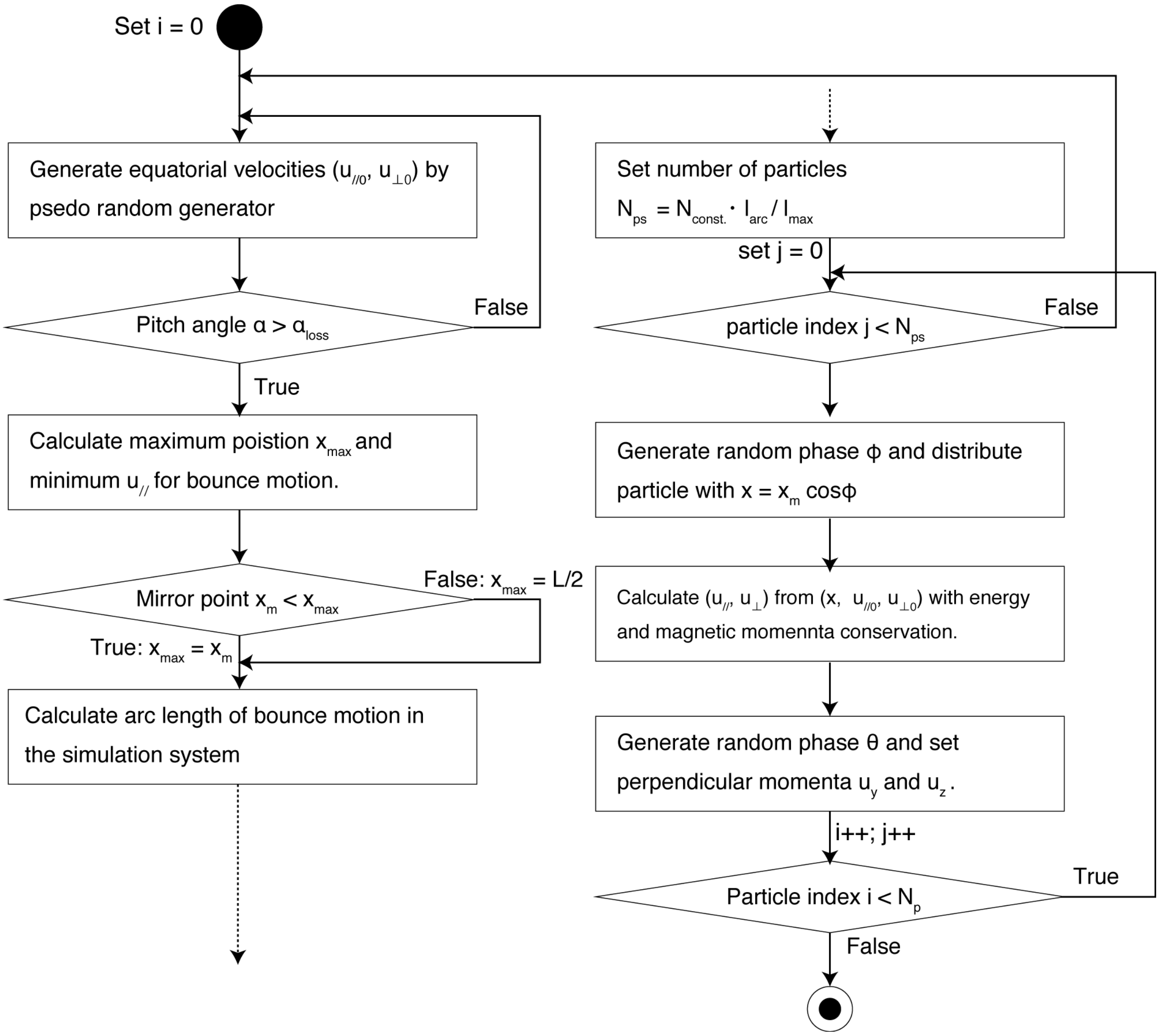

Figure B.4: Flowchart of the generation algorithm of the initial phase space distribution for energetic electrons.

References

Acuña, M. H., Ness, N. F., & Connerney, J. E. P. (1980). The magnetic field of Saturn: Further studies of the Pioneer 11 observations. *Journal of Geophysical Research: Space Physics*, *85*(A11), 5675-5678. doi: 10.1029/JA085iA11p05675

Agapitov, O., Mourenas, D., Artemyev, A., Hospodarsky, G., & Bonnell, J. (2019). Time scales for electron quasi-linear diffusion by lower-band chorus waves: The effects of ω_{pe}/Ω_{ce} dependence on geomagnetic activity. *Geophysical Research Letters*, *46*(12), 6178-6187. doi: 10.1029/2019GL083446

Agapitov, O. V., Mourenas, D., Artemyev, A. V., & Mozer, F. S. (2016). Exclusion principle for very oblique and parallel lower band chorus waves. *Geophysical Research Letters*, *43*, 11,112-11,120. doi: 10.1002/2016GL071250

Albert, J. M., Artemyev, A., Li, W., Gan, L., & Ma, Q. (2022). Analytical results for phase bunching in the pendulum model of wave-particle interactions. *Frontiers in Astronomy and Space Sciences*, *9*, 203. doi: 10.3389/FSPAS.2022.971358

Anderson, B. J., Acuña, M. H., Korth, H., Slavin, J. A., Uno, H., Johnson, C. L., … Zurbuchen, T. H. (2010). The magnetic field of Mercury. *Space Sci Rev*, *152*, 307-339. doi: 10.1007/s11214-009-9544-3

Artemyev, A., Agapitov, O., Mourenas, D., Krasnoselskikh, V., Shastun, V., & Mozer, F. (2016). Oblique whistler-mode waves in the Earth's inner magnetosphere: Energy distribution, origins, and role in radiation belt dynamics. *Space Science Reviews 2016 200:1*, *200*, 261-355. doi: 10.1007/S11214-016-0252-5

Artemyev, A. V., Agapitov, O. V., Mozer, F., & Krasnoselskikh, V. (2014). Thermal electron acceleration by localized bursts of electric field in the radiation belts. *Geophysical Research Letters*, *41*, 5734-5739. doi: 10.1002/2014GL061248

Artemyev, A. V., Neishtadt, A. I., Albert, J. M., Gan, L., Li, W., & Ma, Q. (2021). Theoretical model of the nonlinear resonant interaction of whistler-mode waves and field-aligned electrons. *Physics of Plasmas*, *28*, 052902. doi: 10.1063/5.0046635

Baker, D. N., Jaynes, A. N., Kanekal, S. G., Foster, J. C., Erickson, P. J., Fennell, J. F., … Wygant, J. R. (2016). Highly relativistic radiation belt electron acceleration, transport, and loss: Large solar storm events of March and June 2015. *Journal of Geophysical Research: Space Physics*, *121*(7), 6647-6660. doi: 10.1002/2016JA022502

Baker, D. N., Kanekal, S. G., Hoxie, V. C., Henderson, M. G., Li, X., Spence, H. E., … Claudepierre, S. G. (2013). A long-lived relativistic electron storage ring embedded in Earth's outer Van Allen belt. *Science*, *340*(6129), 186-190. doi: 10.1126/science.1233518

Boris, J. P., & Shanny, R. A. (1970). Relativistic plasma simulation-optimization of a hybrid code. In *Proceeding of 4th conference on numerical simulation of plasma* (p. 3-67). Washinton D.C: Naval Rearch Laboratory.

Boyd, A. J., Turner, D. L., Reeves, G. D., Spence, H. E., Baker, D. N., & Blake, J. B. (2018). What causes radiation belt enhancements: A survey of the Van Allen Probes Era. *Geophysical Research Letters*, *45*(11), 5253-5259. doi: 10.1029/2018GL077699

Bridge, H. S., Lazarus, A. J., Scudder, J. D., Ogilvie, K. W., Hartle, R. E., Asbridge, J. R., … Cloutier, P. A. (1974). Magnetic field observations near mercury: Preliminary results from Mariner 10. *Science*, *185*, 151-160. doi: 10.1126/SCIENCE.185.4146.151

Carpenter, D. L. (1968). Ducted whistler-mode propagation in the magnetosphere; a half-gyrofrequency upper intensity cutoff and some associated wave growth phenomena. *Journal of Geophysical Research (1896-1977)*, *73*(9), 2919-2928. doi: 10.1029/JA073i009p02919

Carpenter, D. L. (1988). Remote sensing of the magnetospheric plasma by means of whistler mode signals. *Reviews of Geophysics*, *26*(3), 535-549. doi: 10.1029/RG026i003p00535

Carpenter, D. L., & Miller, T. R. (1976). Ducted magnetospheric propagation of signals from the Siple, Antarctica, VLF transmitter. *Journal of Geophysical Research*, *81*, 2692-2700. doi: 10.1029/JA081I016P02692

Casselman, C. J., Heritage, D. P., & Tibbals, M. L. (1959). VLF propagation measurements for the radux-omega navigation system. *Proceedings of the IRE*, *47*(5), 829-839. doi: 10.1109/JRPROC.1959.287276

Chen, H., Gao, X., Lu, Q., Fan, K., Ke, Y., Wang, X., & Wang, S. (2022). Gap formation around $0.5\,\Omega_e$ in the whistler-mode waves due to the plateau-like shape in the parallel electron distribution: 2D PIC simulations. *Journal of Geophysical Research: Space Physics*, *127*(5), e2021JA030119. doi: 10.1029/2021JA030119

Chen, H., Gao, X., Lu, Q., Sauer, K., Chen, R., Yao, J., & Wang, S. (2021). Gap formation around $0.5\,\Omega_e$ of whistler-mode waves excited by electron temperature anisotropy. *Journal of Geophysical Research: Space Physics*, *126*(2), e2020JA028631. doi: 10.1029/2020JA028631

Chen, H., Lu, Q., Wang, X., Fan, K., Chen, R., & Gao, X. (2022). One-dimensional gcpic-δf simulation of hooked chorus waves in the Earth's inner magnetosphere. *Geophysical Research Letters*, *49*, e2022GL097989. doi: 10.1029/2022GL097989

Chen, L., & Hasegawa, A. (1974). A theory of long-period magnetic pulsations: 1. steady state excitation of field line resonance. *Journal of Geophysical Research (1896-1977)*, *79*(7), 1024-1032. doi: 10.1029/JA079i007p01024

Cheng, A. F., Krimigis, S. M., Mauk, B. H., Keath, E. P., Maclennan, C. G., Lanzerotti, L. J., … Armstrong, T. P. (1987). Energetic ion and electron phase space densities in the magnetosphere of Uranus. *Journal of Geophysical Research: Space Physics*, *92*(A13), 15315-15328. doi: 10.1029/JA092iA13p15315

Colpitts, C., Miyoshi, Y., Kasahara, Y., Delzanno, G. L., Wygant, J. R., Cattell, C. A., … Matsuoka, A. (2020). First direct observations of propagation of discrete chorus elements from the equatorial source to higher latitudes, using the Van Allen Probes and Arase satellites. *Journal of Geophysical Research: Space Physics*, *125*(10), e2020JA028315. doi: 10.1029/2020JA028315

Connerney, J. E. P., Acuña, M. H., & Ness, N. F. (1987). The magnetic field of Uranus. *Journal of Geophysical Research: Space Physics*, *92*(A13), 15329-15336. doi: 10.1029/JA092iA13p15329

Connerney, J. E. P., Acuña, M. H., & Ness, N. F. (1991). The magnetic field of Neptune. *Journal of Geophysical Research: Space Physics*, *96*(S01), 19023-19042.

doi: 10.1029/91JA01165

Cornilleau-Wehrlin, N., Solomon, J., Korth, A., & Kremser, G. (1985). Experimental study of the relationship between energetic electrons and ELF waves observed on board GEOS: A support to quasi-linear theory. *Journal of Geophysical Research: Space Physics*, *90*(A5), 4141-4154. doi: 10.1029/JA090iA05p04141

Costabile, J. D., Gołkowski, M., & Wall, R. E. (2017). Modulation analysis of whistler mode sidebands in VLF-triggered emissions and implications for conditions of nonlinear growth. *Journal of Geophysical Research: Space Physics*, *122*(12), 12,505-12,516. doi: 10.1002/2017JA024501

Coster, A. J., Erickson, P. J., Lanzerotti, L. J., Zhang, Y., & Paxton, L. J. (2021). Space physics and aeronomy collection: Space weather effects and applications. *Space Physics and Aeronomy Collection: Space Weather Effects and Applications*, 1-225. doi: 10.1002/9781119815570

Drake, F. D., & Hvatum, S. (1959). Non-thermal microwave radiation from Jupiter. *Astronomical Journal*, *64*, 329-330. doi: 10.1086/108047

Dysthe, K. B. (1971). Some studies of triggered whistler emissions. *Journal of Geophysical Research*, *76*, 6915-6931. doi: 10.1029/JA076I028P06915

Ebihara, Y., Ikeda, T., Omura, Y., Tanaka, T., & Fok, M.-C. (2020). Nonlinear wave growth analysis of whistler-mode chorus generation regions based on coupled MHD and advection simulation of the inner magnetosphere. *Journal of Geophysical Research: Space Physics*, *125*(1), e2019JA026951. doi: 10.1029/2019JA026951

Foster, J. C., Erickson, P. J., Baker, D. N., Claudepierre, S. G., Kletzing, C. A., Kurth, W., … Wygant, J. R. (2014). Prompt energization of relativistic and highly relativistic electrons during a substorm interval: Van Allen Probes observations. *Geophysical Research Letters*, *41*(1), 20-25. doi: 10.1002/2013GL058438

Foster, J. C., Erickson, P. J., & Omura, Y. (2021). Subpacket structure in strong VLF chorus rising tones: characteristics and consequences for relativistic electron acceleration. *Earth, Planets and Space*, *73*(1). doi: 10.1186/s40623-021-01467-4

Foster, J. C., Erickson, P. J., Omura, Y., Baker, D. N., Kletzing, C. A., & Claudepierre, S. G. (2017). Van Allen Probes observations of prompt MeV radiation belt electron acceleration in nonlinear interactions with VLF chorus. *Journal of Geophysical Research: Space Physics*, *122*(1), 324-339. doi: 10.1002/2016JA023429

Fujiwara, Y., Nogi, T., & Omura, Y. (2022). Nonlinear triggering process of whistler-mode emissions in a homogeneous magnetic field. *Earth, Planets and Space*, *74*, 95. doi: 10.1186/s40623-022-01646-x

Fujiwara, Y., Omura, Y., & Nogi, T. (2023). Triggering of whistler-mode rising and falling tone emissions in a homogeneous magnetic field. *Journal of Geophysical Research: Space Physics*, *128*(2), e2022JA030967. doi: 10.1029/2022JA030967

Gan, L., Li, W., Ma, Q., Albert, J. M., Artemyev, A. V., & Bortnik, J. (2020). Nonlinear interactions between radiation belt electrons and chorus waves: Dependence on wave amplitude modulation. *Geophysical Research Letters*, *47*, e2019GL085987. doi: 10.1029/2019GL085987

Gan, L., Li, W., Ma, Q., Artemyev, A. V., & Albert, J. M. (2022). Dependence of nonlinear effects on whistler-mode wave bandwidth and amplitude: A perspective from diffusion coefficients. *Journal of Geophysical Research: Space Physics*, *127*, e2021JA030063. doi: 10.1029/2021JA030063

Gold, T. (1959). Motions in the magnetosphere of the earth. *Journal of Geophysical Research (1896-1977)*, *64*(9), 1219-1224. doi: https://doi.org/10.1029/JZ064i009p01219

Gołkowski, M., & Gibby, A. R. (2017). On the conditions for nonlinear growth in magnetospheric chorus and triggered emissions. *Physics of Plasmas*, *24*(9), 092904. doi: 10.1063/1.4986225

Gołkowski, M., Harid, V., & Hosseini, P. (2019). Review of controlled excitation of nonlinear wave-particle interactions in the magnetosphere. *Frontiers in Astronomy and Space Sciences*, *6*, 2. doi: 10.3389/fspas.2019.00002

Gurnett, D. A., Huff, R. L., Pickett, J. S., Persoon, A. M., Mutel, R. L., Christopher, I. W., … Yearby, K. H. (2001). First results from the cluster wideband plasma wave investigation. *Annales Geophysicae*, *19*(10/12), 1259–1272. doi: 10.5194/angeo-19-1259-2001

Habagishi, T., Yagitani, S., & Omura, Y. (2014). Nonlinear damping of chorus emissions at local half cyclotron frequencies observed by geotail at $L > 9$. *Journal of Geophysical Research: Space Physics*, *119*, 4475-4483. doi: 10.1002/2013JA019696

Hanzelka, M., Santolík, O., Omura, Y., Kolmašová, I., & Kletzing, C. A. (2020). A model of the subpacket structure of rising tone chorus emissions. *Journal of Geophysical Research: Space Physics*, *125*(8), e2020JA028094. doi: 10.1029/2020JA028094

Harid, V., Gołkowski, M., Bell, T., Li, J. D., & Inan, U. S. (2014). Finite difference modeling of coherent wave amplification in the earth's radiation belts. *Geophysical Research Letters*, *41*, 8193-8200. doi: 10.1002/2014GL061787

Harid, V., Gołkowski, M., Hosseini, P., & Kim, H. (2022). Backward-propagating source as a component of rising tone whistler-mode chorus generation. *Frontiers in Astronomy and Space Sciences*, *0*, 232. doi: 10.3389/FSPAS.2022.981949

Hashimoto, K., & Kimura, I. (1981). A generation mechanism of narrow band hiss emissions above one half the electron cyclotron frequency in the outer magnetosphere. *Journal of Geophysical Research: Space Physics*, *86*(A13), 11148-11152. doi: 10.1029/JA086iA13p11148

Helliwell, R. A. (1967). A theory of discrete VLF emissions from the magnetosphere. *Journal of Geophysical Research*, *72*(19), 4773-4790. doi: 10.1029/JZ072i019p04773

Helliwell, R. A. (1969). Low-frequency waves in the magnetosphere. *Reviews of Geophysics*, *7*(1-2), 281-303. doi: 10.1029/RG007i001p00281

Helliwell, R. A. (1983). Controlled stimulation of VLF emissions from Siple Station, antarctica. *Radio Science*, *18*(06), 801-814. doi: 10.1029/RS018i006p00801

Helliwell, R. A. (1988). VLF wave-injection experiments from Siple Station, Antarctica. *Advances in Space Research*, *8*(1), 279 - 289. doi: 10.1016/0273-1177(88)90373-0

Helliwell, R. A., & Brice, N. (1964). Very low frequency emission periods and whistler-mode group delays. *Journal of Geophysical Research*, *69*(21), 4704-4708. doi: 10.1029/JZ069i021p04704

Helliwell, R. A., Carpenter, D., & Miller, T. R. (1980). Power threshold for growth of coherent VLF signals in the magnetosphere. *Journal of Geophysical Research: Space Physics*, *85*(A7), 3360-3366. doi: 10.1029/JA085iA07p03360

Helliwell, R. A., Carpenter, D. L., Inan, U. S., & Katsufrakis, J. P. (1986). Generation of band-limited VLF noise using the Siple transmitter: A model for magnetospheric hiss. *Journal of Geophysical Research: Space Physics*, *91*(A4), 4381-4392. doi: 10.1029/JA091iA04p04381

Helliwell, R. A., & Katsufrakis, J. P. (1974). VLF wave injection into the magnetosphere from Siple Station, Antarctica. *Journal of Geophysical Research*, *79*(16), 2511-2518. doi: 10.1029/JA079i016p02511

Hikishima, M., & Omura, Y. (2012). Particle simulations of whistler-mode rising-tone emissions triggered by waves with different amplitudes. *Journal of Geophysical Research: Space Physics*, *117*(A4). doi: 10.1029/2011JA017428

Hikishima, M., Omura, Y., & Summers, D. (2010). Self-consistent particle simulation of whistler mode triggered emissions. *Journal of Geophysical Research: Space Physics*, *115*(A12). doi: 10.1029/2010JA015860

Hikishima, M., Omura, Y., & Summers, D. (2020). Particle simulation of the generation of plasmaspheric hiss. *Journal of Geophysical Research: Space Physics*, *125*(8), e2020JA027973. doi: 10.1029/2020JA027973

Hikishima, M., Yagitani, S., Omura, Y., & Nagano, I. (2009a). Coherent nonlinear scattering of energetic electrons in the process of whistler mode chorus generation. *Journal of Geophysical Research: Space Physics*, *114*(A10). doi: 10.1029/2009JA014371

Hikishima, M., Yagitani, S., Omura, Y., & Nagano, I. (2009b). Full particle simulation of whistler-mode rising chorus emissions in the magnetosphere. *Journal of Geophysical Research: Space Physics*, *114*(A1). doi: 10.1029/2008JA013625

Hiraga, R., & Omura, Y. (2020). Acceleration mechanism of radiation belt electrons through interaction with multi-subpacket chorus waves. *Earth, Planets and Space*, *72*(1). doi: 10.1186/s40623-020-1134-3

Horne, R. B., & Thorne, R. M. (1998). Potential waves for relativistic electron scattering and stochastic acceleration during magnetic storms. *Geophysical Research Letters*, *25*, 3011-3014. doi: 10.1029/98GL01002

Hsieh, Y.-K., Kubota, Y., & Omura, Y. (2020). Nonlinear evolution of radiation belt electron fluxes interacting with oblique whistler mode chorus emissions. *Journal of Geophysical Research: Space Physics*, *125*(2), e2019JA027465. doi: 10.1029/2019JA027465

Hsieh, Y.-K., & Omura, Y. (2018). Nonlinear damping of oblique whistler mode waves via landau resonance. *Journal of Geophysical Research: Space Physics*, *123*(9), 7462-7472. doi: 10.1029/2018JA025848

Juhász, L., Omura, Y., Lichtenberger, J., & Friedel, R. H. (2019). Evaluation of plasma properties from chorus waves observed at the generation region. *Journal of Geophysical Research: Space Physics*, *124*(6), 4125-4136. doi: 10.1029/2018JA026337

Kasahara, S., Miyoshi, Y., Yokota, S., Mitani, T., Kasahara, Y., Matsuda, S., … Shinohara, I. (2018). Pulsating aurora from electron scattering by chorus waves. *Nature*, *554*(7692), 337–340. doi: 10.1038/nature25505

Kasper, J., & Hutchinson, C. (1978). The omega navigation system–an overview. *IEEE Communications Society Magazine*, *16*(3), 23-35. doi: 10.1109/MCOM.1978.1089729

Katoh, Y., & Omura, Y. (2006). A study of generation mechanism of VLF triggered emission by self-consistent particle code. *Journal of Geophysical Research: Space Physics*, *111*(A12). doi: 10.1029/2006JA011704

Katoh, Y., & Omura, Y. (2007). Computer simulation of chorus wave generation in the earth's inner magnetosphere. *Geophysical Research Letters*, *34*(3). doi: 10.1029/2006GL028594

Katoh, Y., & Omura, Y. (2016). Electron hybrid code simulation of whistler-mode chorus generation with real parameters in the earth's inner magnetosphere. *Earth, Planets and Space*, *68*, 1-8. doi: 10.1186/S40623-016-0568-0

Katoh, Y., Omura, Y., Miyake, Y., Usui, H., & Nakashima, H. (2018). Dependence of generation of whistler mode chorus emissions on the temperature anisotropy and density of energetic electrons in the Earth's inner magnetosphere. *Journal of Geophysical Research: Space Physics*, *123*(2), 1165-1177. doi: 10.1002/2017JA024801

Ke, Y., Gao, X., Lu, Q., Wang, X., & Wang, S. (2017). Generation of rising-tone chorus in a two-dimensional mirror field by using the general curvilinear PIC code. *Journal of Geophysical Research: Space Physics*, *122*(8), 8154-8165. doi: 10.1002/2017JA024178

Kennel, C. F., & Petschek, H. E. (1966). Limit on stably trapped particle fluxes. *Journal of Geophysical Research*, *71*(1), 1-28. doi: 10.1029/JZ071i001p00001

Kissinger, J., Kepko, L., Baker, D. N., Kanekal, S., Li, W., McPherron, R. L., & Angelopoulos, V. (2014). The importance of storm time steady magnetospheric convection in determining the final relativistic electron flux level. *Journal of Geophysical Research: Space Physics*, *119*(9), 7433-7443. doi: 10.1002/2014JA019948

Kitahara, M., & Katoh, Y. (2019). Anomalous trapping of low pitch angle electrons by coherent whistler mode waves. *Journal of Geophysical Research: Space Physics*, *124*(7), 5568-5583. doi: 10.1029/2019JA026493

Kitamura, N., Amano, T., Omura, Y., Boardsen, S. A., Gershman, D. J., Miyoshi, Y., … Burch, J. L. (2022). Direct observations of energy transfer from resonant electrons to whistler-mode waves in magnetosheath of earth. *Nature Communications 2022 13:1*, *13*, 1-12. doi: 10.1038/s41467-022-33604-2

Kitamura, N., Omura, Y., Nakamura, S., Amano, T., Boardsen, S. A., Ahmadi, N., … Burch, J. L. (2020). Observations of the source region of whistler mode waves in magnetosheath mirror structures. *Journal of Geophysical Research: Space Physics*, *125*(5), e2019JA027488. doi: 10.1029/2019JA027488

Koons, H., & Roeder, J. (1990). A survey of equatorial magnetospheric wave activity between 5 and 8 re. *Planetary and Space Science*, *38*(10), 1335 - 1341. doi: 10.1016/0032-0633(90)90136-E

Kubota, Y., & Omura, Y. (2018). Nonlinear dynamics of radiation belt electrons interacting with chorus emissions localized in longitude. *Journal of Geophysical Research: Space Physics*, *123*(6), 4835-4857. doi: 10.1029/2017JA025050

Kubota, Y., Omura, Y., Kletzing, C., & Reeves, G. (2018). Generation process of large-amplitude upper-band chorus emissions observed by Van Allen Probes. *Journal of Geophysical Research: Space Physics*, *123*(5), 3704-3713. doi: 10.1029/2017JA024782

Kurita, S., Katoh, Y., Omura, Y., Angelopoulos, V., Cully, C. M., Le Contel, O., & Misawa, H. (2012). Themis observation of chorus elements without a gap at half the gyrofrequency. *Journal of Geophysical Research: Space Physics*, *117*(A11). doi: 10.1029/2012JA018076

Kurita, S., Misawa, H., Cully, C. M., Le Contel, O., & Angelopoulos, V. (2012). Source location of falling tone chorus. *Geophysical Research Letters*, *39*(22). doi: 10.1029/2012GL053929

Kurita, S., Miyoshi, Y., Shiokawa, K., Higashio, N., Mitani, T., Takashima, T., … Otsuka, Y. (2018). Rapid loss of relativistic electrons by EMIC waves in the outer radiation belt observed by Arase, Van Allen Probes, and the PWING ground stations. *Geophysical Research Letters*, *45*(23), 12,720-12,729. doi: 10.1029/2018GL080262

Lanzerotti, L. J. (2001). Space weather effects on technologies. *Geophysical Monograph Series*, *125*, 11-22. doi: 10.1029/GM125P0011

LeDocq, M. J., Gurnett, D. A., & Hospodarsky, G. B. (1998). Chorus source locations from VLF poynting flux measurements with the polar spacecraft. *Geophysical Research Letters*, *25*(21), 4063-4066. doi: 10.1029/1998GL900071

Li, J., Bortnik, J., An, X., Li, W., Angelopoulos, V., Thorne, R. M., … Baker, D. N. (2019). Origin of two-band chorus in the radiation belt of earth. *Nature Communications*, *10*(1). doi: 10.1038/s41467-019-12561-3

Li, J., Bortnik, J., Li, W., An, X., Lyons, L. R., Kurth, W. S., … Baker, D. N. (2022). Unraveling the formation region and frequency of chorus spectral gaps. *Geophysical Research Letters*, *49*(19), e2022GL100385. doi: 10.1029/2022GL100385

Li, W., Thorne, R. M., Angelopoulos, V., Bortnik, J., Cully, C. M., Ni, B., … Magnes, W. (2009). Global distribution of whistler-mode chorus waves observed on the THEMIS spacecraft. *Geophysical Research Letters*, *36*(9). doi: 10.1029/2009GL037595

Li, W., Thorne, R. M., Bortnik, J., Shprits, Y. Y., Nishimura, Y., Angelopoulos, V., … Bonnell, J. W. (2011). Typical properties of rising and falling tone chorus waves. *Geophysical Research Letters*, *38*, 1-6. doi: 10.1029/2011GL047925

Liu, S., Gao, Z., Xiao, F., He, Q., Li, T., Shang, X., … Zhang, S. (2021). Observation of unusual chorus elements by Van Allen Probes. *Journal of Geophysical Research: Space Physics*, *126*(7), e2021JA029258. doi: 10.1029/2021JA029258

Liu, Y., & Omura, Y. (2022). Nonlinear wave growth of whistler-mode hiss emissions in a uniform magnetic field. *Journal of Geophysical Research: Space Physics*, *127*(5), e2022JA030428. doi: 10.1029/2022JA030428

Lorentzen, K. R., McCarthy, M. P., Parks, G. K., Foat, J. E., Millan, R. M., Smith, D. M., … Treilhou, J. P. (2000). Precipitation of relativistic electrons by interaction with electromagnetic ion cyclotron waves. *Journal of Geophysical Research: Space Physics*, *105*(A3), 5381-5389. doi: 10.1029/1999JA000283

Lu, Q., Ke, Y., Wang, X., Liu, K., Gao, X., Chen, L., & Wang, S. (2019). Two-dimensional gcPIC simulation of rising-tone chorus waves in a dipole magnetic field. *Journal of Geophysical Research: Space Physics*, *124*(6), 4157-4167. doi: 10.1029/2019JA026586

Maggiolo, R., André, N., Hasegawa, H., Welling, D. T., Zhang, Y., & Paxton, L. J. (2021). Magnetospheres in the solar system. *Magnetospheres in the Solar System*, 1-784. doi: 10.1002/9781119815624

McCollough, J. P., Miyoshi, Y., Ginet, G. P., Johnston, W. R., Su, Y.-J., Starks, M. J., … Langhals, J. T. (2022). Space-to-space very low frequency radio transmission in the magnetosphere using the DSX and Arase satellites. *Earth, Planets and Space*, *74*(1), 64. doi: 10.1186/s40623-022-01605-6

Meredith, N. P., Horne, R. B., & Anderson, R. R. (2001). Substorm dependence of chorus amplitudes: Implications for the acceleration of electrons to relativistic energies. *Journal of Geophysical Research: Space Physics*, *106*(A7), 13165-13178. doi: 10.1029/2000JA900156

Meredith, N. P., Horne, R. B., Thorne, R. M., Summers, D., & Anderson, R. R. (2004). Substorm dependence of plasmaspheric hiss. *Journal of Geophysical Research: Space Physics*, *109*(A6). doi: 10.1029/2004JA010387

Miyake, Y., & Nakashima, H. (2013, July). Low-cost load balancing for parallel particle-in-cell simulations with thick overlapping layers. In *2013 12th ieee international conference on trust, security and privacy in computing and communications* (p. 1107-1114). doi: 10.1109/TrustCom.2013.134

Miyoshi, Y., Ono, T., Takashima, T., Asamura, K., Hirahara, M., Kasaba, Y., … Segawa, T. T. (2012). The Energization and Radiation in Geospace (ERG) project. In *Dynamics of the earth's radiation belts and inner magnetosphere* (p. 103-116). American Geophysical Union (AGU). doi: 10.1029/2012GM001304

Miyoshi, Y., Sakaguchi, K., Shiokawa, K., Evans, D., Albert, J., Connors, M., & Jordanova, V. (2008). Precipitation of radiation belt electrons by EMIC waves, observed from ground and space. *Geophysical Research Letters*, *35*(23). doi: 10.1029/2008GL035727

Miyoshi, Y., Shinohara, I., Takashima, T., Asamura, K., Higashio, N., Mitani, T., … Seki, K. (2018). Geospace exploration project erg. *Earth, Planets and Space*, *70*, 1-13. doi: 10.1186/S40623-018-0862-0

Mourenas, D., Zhang, X. J., Nunn, D., Artemyev, A. V., Angelopoulos, V., Tsai, E., & Wilkins, C. (2022). Short chorus wave packets: Generation within chorus elements, statistics, and consequences on energetic electron precipitation. *Journal of Geophysical Research: Space Physics*, *127*, e2022JA030310. doi: 10.1029/2022JA030310

Nakamura, S., Omura, Y., Kletzing, C., & Baker, D. N. (2019). Rapid precipitation of relativistic electron by EMIC rising-tone emissions observed by the Van Allen Probes. *Journal of Geophysical Research: Space Physics*, *124*(8), 6701-6714. doi: 10.1029/2019JA026772

Nakamura, S., Omura, Y., Machida, S., Shoji, M., Nosé, M., & Angelopoulos, V. (2014). Electromagnetic ion cyclotron rising tone emissions observed by THEMIS probes outside the plasmapause. *Journal of Geophysical Research: Space Physics*, *119*(3), 1874-1886. doi: 10.1002/2013JA019146

Nakamura, S., Omura, Y., & Summers, D. (2018). Fine structure of whistler mode hiss in plasmaspheric plumes observed by the Van Allen Probes. *Journal of Geophysical Research: Space Physics*, *123*(11), 9055-9064. doi: 10.1029/2018JA025803

Nakashima, H. (2015). Manycore challenge in particle-in-cell simulation: How to exploit 1 TFlops peak performance for simulation codes with irregular computation. *Computers & Electrical Engineering*, *46*, 81-94. doi: 10.1016/j.compeleceng.2015.03.010

Nakashima, H., Miyake, Y., Usui, H., & Omura, Y. (2009). OhHelp: A scalable domain-decomposing dynamic load balancing for particle-in-cell simulations. In *Proceedings of the 23rd international conference on supercomputing* (p. 90–99). New York, NY, USA: Association for Computing Machinery. doi: 10.1145/1542275.1542293

Nakashima, H., Summura, Y., Kikura, K., & Miyake, Y. (2017). Large scale manycore-aware PIC simulation with efficient particle binning. In *2017 ieee international parallel and distributed processing symposium (ipdps)* (p. 202-212). doi: 10.1109/IPDPS.2017.65

National Research Council. (2003). *The sun to the earth – and beyond: A decadal research strategy in solar and space physics*. Washington, DC: The National Academies Press. doi: 10.17226/10477

Ness, N. F., Behannon, K. W., Lepping, R. P., Whang, Y. C., & Schatten, K. H. (1974). Magnetic field observations near Mercury: Preliminary results from mariner 10. *Science*, *185*(4146), 151-160. doi: 10.1126/science.185.4146.151

Nogi, T., Nakamura, S., & Omura, Y. (2020). Full particle simulation of whistler-mode triggered falling-tone emissions in the magnetosphere. *Journal of Geophysical Research: Space Physics*, *125*(10), e2020JA027953. doi: 10.1029/2020JA027953

Nogi, T., & Omura, Y. (2022). Nonlinear signatures of VLF-triggered emissions: A simulation study. *Journal of Geophysical Research: Space Physics*, *127*(1), e2021JA029826.

doi: 10.1029/2021JA029826

Nunn, D. (1974). A self-consistent theory of triggered VLF emissions. *Planetary and Space Science*, *22*(3), 349 - 378. doi: 10.1016/0032-0633(74)90070-1

Nunn, D. (1986). A nonlinear theory of sideband stability in ducted whistler mode waves. *Planetary and Space Science*, *34*(5), 429 - 451. doi: 10.1016/0032-0633(86)90032-2

Nunn, D. (1990). The numerical simulation of VLF nonlinear wave-particle interactions in collision-free plasmas using the vlasov hybrid simulation technique. *Computer Physics Communications*, *60*(1), 1 - 25. doi: 10.1016/0010-4655(90)90074-B

Nunn, D. (1993). A novel technique for the numerical simulation of hot collision-free plasma; vlasov hybrid simulation. *Journal of Computational Physics*, *108*, 180-196. doi: 10.1006/JCPH.1993.1173

Nunn, D. (2021). The numerical simulation of the generation of lower-band VLFchorus using a quasi-broadband Vlasov Hybrid Simulation code. *Earth, Planets and Space*, *73*, 1-16. doi: 10.1186/S40623-021-01549-3/FIGURES/8

Nunn, D., & Omura, Y. (2012). A computational and theoretical analysis of falling frequency VLF emissions. *Journal of Geophysical Research: Space Physics*, *117*(A8). doi: 10.1029/2012JA017557

Nunn, D., Omura, Y., Matsumoto, H., Nagano, I., & Yagitani, S. (1997). The numerical simulation of VLF chorus and discrete emissions observed on the geotail satellite using a vlasov code. *Journal of Geophysical Research: Space Physics*, *102*(A12), 27083-27097. doi: 10.1029/97JA02518

Nunn, D., Santolík, O., Rycroft, M., & Trakhtengerts, V. (2009). On the numerical modelling of VLF chorus dynamical spectra. *Annales Geophysicae*, *27*(6), 2341–2359. doi: 10.5194/angeo-27-2341-2009

Nunn, D., & Smith, A. J. (1996). Numerical simulation of whistler-triggered VLF emissions observed in Antarctica. *Journal of Geophysical Research: Space Physics*, *101*(A3), 5261-5277. doi: 10.1029/95JA03143

Nunn, D., Zhang, X.-J., Mourenas, D., & Artemyev, A. V. (2021). Generation of realistic short chorus wave packets. *Geophysical Research Letters*, *48*(7), e2020GL092178. doi: 10.1029/2020GL092178

Oliven, M. N., & Gurnett, D. A. (1968). Microburst phenomena: 3. an association between microbursts and VLF chorus. *Journal of Geophysical Research*, *73*(7), 2355-2362. doi: 10.1029/JA073i007p02355

Omura, Y. (2007). One-dimensional electromagnetic particle code KEMPO1: A tutorial on microphysics in space plasmas. In H. Usui & Y. Omura (Eds.), *Advanced methods for space simulations* (p. 1-21). Tokyo: Terra Scientific Publishing Company.

Omura, Y. (2021). Nonlinear wave growth theory of whistler-mode chorus and hiss emissions in the magnetosphere. *Earth, Planets and Space*, *73*(1), 95. doi: 10.1186/s40623-021-01380-w

Omura, Y., Furuya, N., & Summers, D. (2007). Relativistic turning acceleration of resonant electrons by coherent whistler mode waves in a dipole magnetic field. *Journal of Geophysical Research: Space Physics*, *112*(A6). doi: 10.1029/2006JA012243

Omura, Y., Hikishima, M., Katoh, Y., Summers, D., & Yagitani, S. (2009). Nonlinear mechanisms of lower-band and upper-band VLF chorus emissions in the magnetosphere. *Journal of Geophysical Research: Space Physics*, *114*(A7). doi: 10.1029/2009JA014206

Omura, Y., Katoh, Y., & Summers, D. (2008). Theory and simulation of the generation of whistler-mode chorus. *Journal of Geophysical Research: Space Physics*, *113*(A4). doi: 10.1029/2007JA012622

Omura, Y., & Matsumoto, H. (1982). Computer simulations of basic processes of coherent whistler wave-particle interactions in the magnetosphere. *Journal of Geophysical Research: Space Physics*, *87*(A6), 4435-4444. doi: 10.1029/JA087iA06p04435

Omura, Y., & Matsumoto, H. (1993). KEMPO1: Technical guide to one-dimensional electromagnetic particle code. In H. Matsumoto & Y. Omura (Eds.), *Computer space plasma physics: Simulation techniques and softwares* (p. 21-65). Tokyo: Terra Scientific Publishing Company.

Omura, Y., & Nunn, D. (2011). Triggering process of whistler mode chorus emissions in the magnetosphere. *Journal of Geophysical Research: Space Physics*, *116*(A5). doi: 10.1029/2010JA016280

Omura, Y., Nunn, D., Matsumoto, H., & Rycroft, M. (1991). A review of observational, theoretical and numerical studies of VLF triggered emissions. *Journal of Atmospheric and Terrestrial Physics*, *53*(5), 351 - 368. doi: 10.1016/0021-9169(91)90031-2

Ozaki, M., Shiokawa, K., Miyoshi, Y., Hosokawa, K., Oyama, S., Yagitani, S., … Shinohara, I. (2018). Microscopic observations of pulsating aurora associated with chorus element structures: Coordinated arase satellite-PWING observations. *Geophysical Research Letters*, *45*(22), 12,125-12,134. doi: 10.1029/2018GL079812

Park, C. G. (1981). Generation of whistler-mode sidebands in the magnetosphere. *Journal of Geophysical Research: Space Physics*, *86*(A4), 2286-2294. doi: 10.1029/JA086iA04p02286

Parrot, M., Santolík, O., Cornilleau-Wehrlin, N., Maksimovic, M., & Harvey, C. C. (2003). Source location of chorus emissions observed by cluster. *Annales Geophysicae*, *21*(2), 473–480. doi: 10.5194/angeo-21-473-2003

Pickett, J. S., Santolík, O., Kahler, S. W., Masson, A., Adrian, M. L., Gurnett, D. A., … André, M. (2004). Multi-point cluster observations of VLF risers, fallers, and hooks at and near the plasmapause. In J.-A. Sauvaud & Z. Němeček (Eds.), *Multiscale processes in earth's magnetosphere: From interball to cluster* (p. 307-328). Dordrecht: NATO Science Book Series, Kluwer Academic Publishers. doi: 10.1007/1-4020-2768-0_17

Ratcliffe, H., & Watt, C. E. J. (2017). Self-consistent formation of a 0.5 cyclotron frequency gap in magnetospheric whistler mode waves. *Journal of Geophysical Research: Space Physics*, *122*(8), 8166-8180. doi: 10.1002/2017JA024399

Rathmann, C., Vomvoridis, J., & Denavit, J. (1978). Long-time-scale simulation of resonant particle effects in langmuir and whistler waves. *Journal of Computational Physics*, *26*, 408-442. doi: 10.1016/0021-9991(78)90078-5

Reeves, G. D., McAdams, K. L., Friedel, R. H. W., & O'Brien, T. P. (2003). Acceleration and loss of relativistic electrons during geomagnetic storms. *Geophysical Research Letters*, *30*(10). doi: 10.1029/2002GL016513

Reeves, G. D., Spence, H. E., Henderson, M. G., Morley, S. K., Friedel, R. H. W., Funsten, H. O., … Niehof, J. T. (2013). Electron acceleration in the heart of the Van Allen radiation belts. *Science*, *341*(6149), 991-994. doi: 10.1126/science.1237743

Reid, R. A., Marshall, R. A., Starks, M. J., Usanova, M. E., Wilson, G. R., Johnston, W. R., … Galkin, I. A. (2022). Active VLF transmission experiments between the DSX and VPM spacecraft. *Journal of Geophysical Research: Space Physics*, *127*(4), e2021JA030087. doi: 10.1029/2021JA030087

Roux, A., & Pellat, R. (1978). A theory of triggered emissions. *Journal of Geophysical Research: Space Physics*, *83*(A4), 1433-1441. doi: 10.1029/JA083iA04p01433

Saito, T. (1969). Geomagnetic pulsations. *Space Science Reviews*, *10*, 319-412. doi: 10.1007/BF00203620

Santolík, O., Gurnett, D. A., Pickett, J., Parrot, M., & Cornilleau-Wehrlin, N. (2005). Central position of the source region of storm-time chorus. *Planetary and Space Science*, *53*(1), 299 - 305. doi: 10.1016/j.pss.2004.09.056

Santolík, O., Gurnett, D. A., & Pickett, J. S. (2004). Multipoint investigation of the source region of storm-time chorus. *Annales Geophysicae*, *22*(7), 2555–2563. doi: 10.5194/angeo-22-2555-2004

Santolík, O., Macusova, E., Titova, E. E., Kozelov, B. V., Gurnett, D. A., Pickett, J. S., … Demekhov, A. G. (2008). Frequencies of wave packets of whistler-mode chorus inside its source region: a case study. *Annales Geophysicae*, *26*(6), 1665–1670. doi: 10.5194/angeo-26-1665-2008

Santolík, O., Kletzing, C. A., Kurth, W. S., Hospodarsky, G. B., & Bounds, S. R. (2014). Fine structure of large-amplitude chorus wave packets. *Geophysical Research Letters*, *41*(2), 293-299. doi: 10.1002/2013GL058889

Sauer, K., Baumgärtel, K., & Sydora, R. (2020). Gap formation around $\Omega_e/2$ and generation of low-band whistler waves by landau-resonant electrons in the magnetosphere: Predictions from dispersion theory. *Earth and Planetary Physics*, *4*(2), 138-150. doi: 10.26464/epp2020020

Sazhin, S., & Hayakawa, M. (1992). Magnetospheric chorus emissions: A review. *Planetary and Space Science*, *40*(5), 681-697. doi: 10.1016/0032-0633(92)90009-D

Scherbarth, M., Smith, D., Adler, A., Stuart, J., & Ginet, G. (2009). AFRL's demonstration and science experiments (DSX) mission. In S. Fineschi & J. A. Fennelly (Eds.), *Solar physics and space weather instrumentation III.* (p. 74380B-10). San Diego, CA, USA: The International Society for Optical Engineering.

Shoji, M., Miyoshi, Y., Omura, Y., Kistler, L. M., Kasaba, Y., Matsuda, S., … Shinohara, I. (2018). Instantaneous frequency analysis on nonlinear EMIC emissions: Arase observation. *Geophysical Research Letters*, *45*(24), 13,199-13,205. doi: 10.1029/2018GL079765

Shoji, M., & Omura, Y. (2013). Triggering process of electromagnetic ion cyclotron rising tone emissions in the inner magnetosphere. *Journal of Geophysical Research: Space Physics*, *118*(9), 5553-5561. doi: 10.1002/jgra.50523

Smith, E. J., Davis Jr., L., Jones, D. E., Coleman Jr., P. J., Colburn, D. S., Dyal, P., … Frandsen, A. M. A. (1974). The planetary magnetic field and magnetosphere of Jupiter: Pioneer 10. *Journal of Geophysical Research*, *79*(25), 3501-3513. doi: 10.1029/JA079i025p03501

Smith, E. J., Davis Jr., L., Jones, D. E., Coleman Jr., P. J., Colburn, D. S., Dyal, P., & Sonett, C. P. (1980). Saturn's magnetosphere and its interaction with the solar wind. *Journal of Geophysical Research: Space Physics*, *85*(A11), 5655-5674. doi: 10.1029/JA085iA11p05655

Smith, E. J., Frandsen, A. M. A., Tsurutani, B. T., Thorne, R. M., & Chan, K. W. (1974). Plasmaspheric hiss intensity variations during magnetic storms. *Journal of Geophysical Research (1896-1977)*, *79*(16), 2507-2510. doi: 10.1029/JA079i016p02507

Solomon, J., Cornilleau-Wehrlin, N., Korth, A., & Kremser, G. (1988). An experimental study of ELF/VLF hiss generation in the earth's magnetosphere. *Journal of Geophysical*

Research: Space Physics, *93*(A3), 1839-1847. doi: 10.1029/JA093iA03p01839

Stone, E. C., Cummings, A. C., Loooper, M. D., Selesnick, R. S., Lal, N., McDonald, F. B., … Chenette, D. L. (1989). Energetic charged particles in the magnetosphere of Neptune. *Science*, *246*(4936), 1489-1494. doi: 10.1126/science.246.4936.1489

Storey, L. R. O. (1953). An investigation of whistling atmospherics. *Philosophical Transactions of the Royal Society of London. Series A, Mathematical and Physical Sciences*, *246*, 113-141. doi: 10.1098/RSTA.1953.0011

Sugiyama, H., Singh, S., Omura, Y., Shoji, M., Nunn, D., & Summers, D. (2015). Electromagnetic ion cyclotron waves in the earth's magnetosphere with a kappa-maxwellian particle distribution. *Journal of Geophysical Research: Space Physics*, *120*(10), 8426-8439. doi: 10.1002/2015JA021346

Summers, D. (2005). Quasi-linear diffusion coefficients for field-aligned electromagnetic waves with applications to the magnetosphere. *Journal of Geophysical Research: Space Physics*, *110*, 8213. doi: 10.1029/2005JA011159

Summers, D., Ni, B., & Meredith, N. P. (2007a). Timescales for radiation belt electron acceleration and loss due to resonant wave-particle interactions: 1. theory. *Journal of Geophysical Research: Space Physics*, *112*, 4206. doi: 10.1029/2006JA011801

Summers, D., Ni, B., & Meredith, N. P. (2007b). Timescales for radiation belt electron acceleration and loss due to resonant wave-particle interactions: 2. evaluation for VLF chorus, ELF hiss, and electromagnetic ion cyclotron waves. *Journal of Geophysical Research: Space Physics*, *112*, 4207. doi: 10.1029/2006JA011993

Summers, D., & Omura, Y. (2007). Ultra-relativistic acceleration of electrons in planetary magnetospheres. *Geophysical Research Letters*, *34*, 24205. doi: 10.1029/2007GL032226

Summers, D., Omura, Y., Nakamura, S., & Kletzing, C. A. (2014). Fine structure of plasmaspheric hiss. *Journal of Geophysical Research: Space Physics*, *119*(11), 9134-9149. doi: 10.1002/2014JA020437

Summers, D., Thorne, R. M., & Xiao, F. (1998). Relativistic theory of wave-particle resonant diffusion with application to electron acceleration in the magnetosphere. *Journal of Geophysical Research: Space Physics*, *103*(A9), 20487-20500. doi: 10.1029/98JA01740

Tao, X. (2014). A numerical study of chorus generation and the related variation of wave intensity using the DAWN code. *Journal of Geophysical Research: Space Physics*, *119*(5), 3362-3372. doi: 10.1002/2014JA019820

Tao, X., Zonca, F., & Chen, L. (2021). A "Trap-Release-Amplify" model of chorus waves. *Journal of Geophysical Research: Space Physics*, *126*(9), e2021JA029585. doi: 10.1029/2021JA029585

Teramoto, M., Hori, T., Saito, S., Miyoshi, Y., Kurita, S., Higashio, N., … Troshichev, O. (2019). Remote detection of drift resonance between energetic electrons and ultralow frequency waves: Multisatellite coordinated observation by Arase and Van Allen Probes. *Geophysical Research Letters*, *46*(21), 11642-11651. doi: 10.1029/2019GL084379

Thorne, R. M. (2010). Radiation belt dynamics: The importance of wave-particle interactions. *Geophysical Research Letters*, *37*, 22107. doi: 10.1029/2010GL044990

Thorne, R. M., Li, W., Ni, B., Ma, Q., Bortnik, J., Chen, L., … Kanekal, S. G. (2013). Rapid local acceleration of relativistic radiation-belt electrons by magnetospheric chorus. *Nature*, *504*, 411-414. doi: 10.1038/nature12889

Trakhtengerts, V. Y. (1999). A generation mechanism for chorus emission. *Annales Geophysicae*, *17*(1), 95–100. doi: 10.1007/s00585-999-0095-4

Trakhtengerts, V. Y., Rycroft, M. J., & Demekhov, A. G. (1996). Interrelation of noise-like and discrete ELF/VLF emissions generated by cyclotron interactions. *Journal of Geophysical Research: Space Physics*, *101*(A6), 13293-13301. doi: 10.1029/95JA03515

Tsurutani, B. T., Chen, R., Gao, X., Lu, Q., Pickett, J. S., Lakhina, G. S., … Falkowski, B. J. (2020). Lower-band "monochromatic" chorus riser subelement/wave packet observations. *Journal of Geophysical Research: Space Physics*, *125*(10), e2020JA028090. doi: 10.1029/2020JA028090

Tsurutani, B. T., Lakhina, G. S., & Verkhoglyadova, O. P. (2013). Energetic electron ($>$ 10 keV) microburst precipitation, $\sim$ 5–15 s x-ray pulsations, chorus, and wave-particle interactions: A review. *Journal of Geophysical Research: Space Physics*, *118*(5), 2296-2312. doi: 10.1002/jgra.50264

Tsurutani, B. T., & Smith, E. J. (1974). Postmidnight chorus: A substorm phenomenon. *Journal of Geophysical Research*, *79*(1), 118-127. doi: 10.1029/JA079i001p00118

Tsurutani, B. T., Smith, E. J., West, H. I., & Buck, R. M. (1979). Chorus, energetic electrons and magnetospheric substorms. In P. J. Palmadesso & K. Papadopoulos (Eds.), *Wave instabilities in space plasmas* (pp. 55–62). Dordrecht: Springer Netherlands. doi: 10.1007/978-94-009-9500-0_6

Umeda, T., Omura, Y., & Matsumoto, H. (2001). An improved masking method for absorbing boundaries in electromagnetic particle simulations. *Computer Physics Communications*, *137*(2), 286 - 299. doi: 10.1016/S0010-4655(01)00182-5

Van Allen, J. A., Ludwig, G. H., Ray, E. C., & McIlwain, C. (1958). Observation of high intensity radiation by satellites 1958 alpha and gamma. *Journal of Jet Propulsion*, *28*(9), 588-592. doi: 10.2514/8.7396

Van Allen, J. A., Thomsen, M. F., Randall, B. A., Rairden, R. L., & Grosskreutz, C. L. (1980). Saturn's magnetosphere, rings, and inner satellites. *Science*, *207*(4429), 415-421. doi: 10.1126/science.207.4429.415

Vogt, R. E., Chenette, D. L., Cummings, A. C., Garrard, T. L., Stone, E. C., Schardt, A. W., … McDonald, F. B. (1982). Energetic charged particles in Saturn's magnetosphere: Voyager 2 results. *Science*, *215*(4532), 577-582. doi: 10.1126/science.215.4532.577

Vomvoridis, J. L., Crystal, T. L., & Denavit, J. (1982). Theory and computer simulations of magnetospheric very low frequency emissions. *Journal of Geophysical Research: Space Physics*, *87*(A3), 1473-1489. doi: 10.1029/JA087iA03p01473

Vomvoridis, J. L., & Denavit, J. (1980). Nonlinear evolution of a monochromatic whistler wave in a nonuniform magnetic field. *The Physics of Fluids*, *23*, 174. doi: 10.1063/1.862836

Wu, Y., Tao, X., Zonca, F., & Chen, L. (2022). Nonlinear electron phase-space dynamics in spontaneous excitation of falling-tone chorus. *Geophysical Research Letters*, *49*, e2022GL100046. doi: 10.1029/2022GL100046

Wu, Y., Tao, X., Zonca, F., Chen, L., & Wang, S. (2020). Controlling the chirping of chorus waves via magnetic field inhomogeneity. *Geophysical Research Letters*, *47*, e2020GL087791. doi: 10.1029/2020GL087791

Xiao, F., Thorne, R. M., & Summers, D. (1998). Instability of electromagnetic R-mode waves in a relativistic plasma. *Physics of Plasmas*, *5*(7), 2489-2497. doi: 10.1063/1.872932

Yee, K. (1966). Numerical solution of initial boundary value problems involving maxwell's equations in isotropic media. *IEEE Transactions on Antennas and Propagation*, *14*(3), 302-307. doi: 10.1109/TAP.1966.1138693

Yoon, Y. D., & Bellan, P. M. (2020). Nondiffusive pitch-angle scattering of a distribution of energetic particles by coherent whistler waves. *Journal of Geophysical Research: Space Physics*, *125*, e2020JA027796. doi: 10.1029/2020JA027796

Zhang, X.-J., Demekhov, A. G., Katoh, Y., Nunn, D., Tao, X., Mourenas, D., … Angelopoulos, V. (2021). Fine structure of chorus wave packets: Comparison between observations and wave generation models. *Journal of Geophysical Research: Space Physics*, *126*(8), e2021JA029330. doi: 10.1029/2021JA029330

Zhang, X.-J., Mourenas, D., Artemyev, A. V., Angelopoulos, V., Kurth, W. S., Kletzing, C. A., & Hospodarsky, G. B. (2020). Rapid frequency variations within intense chorus wave packets. *Geophysical Research Letters*, *47*(15), e2020GL088853. doi: 10.1029/2020GL088853

Publication list

Journal papers

1. Nogi, T., Nakamura, S., & Omura, Y. (2020). Full particle simulation of whistler-mode triggered falling-tone emissions in the magnetosphere. *Journal of Geophysical Research: Space Physics*, 125, e2020JA027953. doi:10.1029/2020JA027953
2. Nogi, T., & Omura, Y. (2022). Nonlinear signatures of VLF-triggered emissions: A simulation study. *Journal of Geophysical Research: Space Physics*, 127, e2021JA029826. doi: 10.1029/2021JA029826
3. Fujiwara, Y., Nogi, T. & Omura, Y. (2022). Nonlinear triggering process of whistler-mode emissions in a homogeneous magnetic field. *Earth Planets Space*, 74, 95. doi: 10.1186/s40623-022-01646-x
4. Fujiwara, Y., Omura, Y. & Nogi, T. (2023). Triggering of whistler-mode rising and falling tone emissions in a homogeneous magnetic field. *Journal of Geophysical Research: Space Physics*, 128, e2022JA030967. doi: 10.1029/2022JA030967
5. Nogi, T., & Omura, Y. (2022). Upstream shift of generation region for whistler-mode rising-tone emission in the magnetosphere. Submitted to *Journal of Geophysical Research: Space Physics*

International conference

1. Nogi, T. & Omura, Y. (2017), Two-dimensional Simulation of Whistler-mode wave Particle Interaction, *The 32nd International Union of Radio Science General Assembly and Scientific Symposium*, Montreal, Canada, 19-26 August.
2. Nogi, T. & Omura, Y. (2018), Simulation of oblique propagation for whistler mode triggered emissions in a parabolic magnetic field, *Japan Geoscience Union Meeting 2018*, Makuhari, Chiba, Japan, 20-24 May.
3. Nogi, T. & Omura, Y. (2018), Two-Dimensional Particle Simulation of Whistler Mode Chorus Wave Damping Through Landau Resonance, *The 13th International School / Symposium for Space Simulations*, Los Angeles, CA, USA, 6-14 September.
4. Nogi, T., & Omura, Y. (2019), One-dimensional simulation of whistler mode wave packets interacting with energetic electrons, *Japan Geoscience Union Meeting 2019*, Makuhari, Chiba, Japan, 26-30 May.

5. Nogi, T. & Omura, Y. (2019), Two-Dimensional Simulation of Whistler Mode Wave Packets Interacting with nergetic Electrons, *The 16th Annual meeting Asia Oceania Geoscience Society*, Singapore, 28 July - 2 August.
6. Nogi, T., Omura, Y. & Nakamura, S. (2019), Particle Simulation of Whistler-mode Triggered Emissions in the Earth's Inner Magnetosphere, *American Geophysical Union Fall meeting 2019*, San Francisco, CA, USA, 9-13 December.
7. Fujiwara, Y., Omura, Y., Hsieh, Y., Nogi, T., & Nakamura, S. (2020), Particle Simulation of whistler mode triggered emissions in a uniform magnetic field, *VLF/ELF Remote Sensing of Ionospheres and Magnetosphere*, Virtual meeting, 16-20 November.
8. Nogi, T., Nakamura, S., & Omura, Y. (2020), Particle Simulation of Triggered Emissions from Large Amplitude Whistler-mode Waves, *Japan Geoscience Union Meeting 2020*, Virtual meeting, 12-16 July.
9. Fujiwara, Y., Omura, Y., Nogi, T., Hsieh, Y., & Nakamura, S.(2020), Electromagnetic particle simulation of whistler mode triggered emissions in the equatorial magnetosphere, *Japan Geoscience Union Meeting 2020*, Virtual meeting, 12-16 July.
10. Nogi, T., Omura, Y. & Nakamura, S. (2020), Electromangetic Particle Simulation of VLF Triggered Emissions, *VLF/ELF Remote Sensing of Ionospheres and Magnetosphere*, Virtual meeting, 16-20 November.
11. Fujiwara, Y., Omura, Y. & Nogi, T. (2020), Nonlinear triggering process of whistler mode emissions in a homogeneous magnetic field, *American Geophysical Union Fall meeting 2020*, Online, 1-17 December.
12. Nogi, T. & Omura, Y. (2020), Simulation Study of Rising-tone Emissions Triggered by a VLF Wave Packets in the Equatorial Magnetosphere, *American Geophysical Union Fall meeting 2020*, Online, 1-17 December.
13. Nogi, T. & Omura, Y. (2021), Particle Simulation of whistler-mode triggered emissions with subpacket structures, *Japan Geoscience Union Meeting 2021*, Online, 30 May - 6 June.
14. Fujiwara, Y., Omura, Y. , and Nogi, T. (2021), Simulation for wave-particle interactions of triggered emissions in a uniform magnetic field, *Japan Geoscience Union Meeting 2021*, Online, 30 May - 6 June.
15. Nogi, T. & Omura, Y. (2021), Simulation Study of Triggered Rising-tone Emissions in the Earth's Magnetosphere, *The 18th Annual meetig Asia Oceania Geoscience Society*, Virtual, 1-6 August.
16. Omura, Y., & Nogi, T. (2021), One-dimensional simulation of triggered rising-tone emissions with subpacket structure, *The 33rd International Union of Radio Science General Assembly and Scientific Symposium*, Rome, Italy, 28 August - 4 September.
17. Fujiwara, Y., Nogi, T. & Omura, Y. (2021), Particle simulation of the nonlinear triggering process by monochromatic whistler-mode waves in a homogeneous magnetic field, *The 33rd International Union of Radio Science General Assembly and Scientific Symposium*,

Rome, Italy, 28 August - 4 September.

18. Fujiwara, Y., Omura, Y., & Nogi, T. (2021), Simulation study of generation process of whistler-mode triggered emissions in a uniform magnetic field, *American Geophysical Union Fall meeting 2021*, New Orleans, LA, USA, 1-17 December.
19. Omura, Y. & Nogi, T. (2022), Effective energy range of electrons exciting whistler-mode chorus emissions, *Japan Geoscience Union Meeting 2022*, Makuhari, Chiba, Japan, 22 May - 3 June.
20. Omura, Y., Fujiwara, Y., & Nogi, T. (2022), Whistler-mode triggered emissions in a homogeneous magnetic field, *6th Asia-Pacific Conference on Plasma Physics*, on-line e-Conference, 9-14 October.
21. Omura, Y., Liu, Y., Fujiwara, Y., & Nogi, T. (2022), Nonlinear Wave Growth Process of Whistler-mode Hiss and Chorus Emissions in the Magnetosphere, *American Geophysical Union Fall meeting 2022*, Chicago, IL, USA, 12-16 December.

Awards

1. ISSS Prize Bronze Award(2018), The 13th International School/Symposium for Space Simulations, Los Angeles, CA, USA, 6-14 September.